



Experimental Studies of Premixed Flame Structure and Propagation

Suresh Menon
GEORGIA TECH RESEARCH CORPORATION

07/14/2015
Final Report

DISTRIBUTION A: Distribution approved for public release.

Air Force Research Laboratory
AF Office Of Scientific Research (AFOSR)/ RTE
Arlington, Virginia 22203
Air Force Materiel Command

REPORT DOCUMENTATION PAGE					Form Approved OMB No. 0704-0188	
<p>The public reporting burden for this collection of information is estimated to average 1 hour per response, including the time for reviewing instructions, searching existing data sources, gathering and maintaining the data needed, and completing and reviewing the collection of information. Send comments regarding this burden estimate or any other aspect of this collection of information, including suggestions for reducing the burden, to the Department of Defense, Executive Service Directorate (0704-0188). Respondents should be aware that notwithstanding any other provision of law, no person shall be subject to any penalty for failing to comply with a collection of information if it does not display a currently valid OMB control number.</p> <p>PLEASE DO NOT RETURN YOUR FORM TO THE ABOVE ORGANIZATION.</p>						
1. REPORT DATE (DD-MM-YYYY)		2. REPORT TYPE			3. DATES COVERED (From - To)	
4. TITLE AND SUBTITLE				5a. CONTRACT NUMBER		
				5b. GRANT NUMBER		
				5c. PROGRAM ELEMENT NUMBER		
6. AUTHOR(S)				5d. PROJECT NUMBER		
				5e. TASK NUMBER		
				5f. WORK UNIT NUMBER		
7. PERFORMING ORGANIZATION NAME(S) AND ADDRESS(ES)					8. PERFORMING ORGANIZATION REPORT NUMBER	
9. SPONSORING/MONITORING AGENCY NAME(S) AND ADDRESS(ES)					10. SPONSOR/MONITOR'S ACRONYM(S)	
					11. SPONSOR/MONITOR'S REPORT NUMBER(S)	
12. DISTRIBUTION/AVAILABILITY STATEMENT						
13. SUPPLEMENTARY NOTES						
14. ABSTRACT						
15. SUBJECT TERMS						
16. SECURITY CLASSIFICATION OF:			17. LIMITATION OF ABSTRACT	18. NUMBER OF PAGES	19a. NAME OF RESPONSIBLE PERSON	
a. REPORT	b. ABSTRACT	c. THIS PAGE			19b. TELEPHONE NUMBER (Include area code)	

INSTRUCTIONS FOR COMPLETING SF 298

1. REPORT DATE. Full publication date, including day, month, if available. Must cite at least the year and be Year 2000 compliant, e.g. 30-06-1998; xx-06-1998; xx-xx-1998.

2. REPORT TYPE. State the type of report, such as final, technical, interim, memorandum, master's thesis, progress, quarterly, research, special, group study, etc.

3. DATES COVERED. Indicate the time during which the work was performed and the report was written, e.g., Jun 1997 - Jun 1998; 1-10 Jun 1996; May - Nov 1998; Nov 1998.

4. TITLE. Enter title and subtitle with volume number and part number, if applicable. On classified documents, enter the title classification in parentheses.

5a. CONTRACT NUMBER. Enter all contract numbers as they appear in the report, e.g. F33615-86-C-5169.

5b. GRANT NUMBER. Enter all grant numbers as they appear in the report, e.g. AFOSR-82-1234.

5c. PROGRAM ELEMENT NUMBER. Enter all program element numbers as they appear in the report, e.g. 61101A.

5d. PROJECT NUMBER. Enter all project numbers as they appear in the report, e.g. 1F665702D1257; ILIR.

5e. TASK NUMBER. Enter all task numbers as they appear in the report, e.g. 05; RF0330201; T4112.

5f. WORK UNIT NUMBER. Enter all work unit numbers as they appear in the report, e.g. 001; AFAPL30480105.

6. AUTHOR(S). Enter name(s) of person(s) responsible for writing the report, performing the research, or credited with the content of the report. The form of entry is the last name, first name, middle initial, and additional qualifiers separated by commas, e.g. Smith, Richard, J, Jr.

7. PERFORMING ORGANIZATION NAME(S) AND ADDRESS(ES). Self-explanatory.

8. PERFORMING ORGANIZATION REPORT NUMBER. Enter all unique alphanumeric report numbers assigned by the performing organization, e.g. BRL-1234; AFWL-TR-85-4017-Vol-21-PT-2.

9. SPONSORING/MONITORING AGENCY NAME(S) AND ADDRESS(ES). Enter the name and address of the organization(s) financially responsible for and monitoring the work.

10. SPONSOR/MONITOR'S ACRONYM(S). Enter, if available, e.g. BRL, ARDEC, NADC.

11. SPONSOR/MONITOR'S REPORT NUMBER(S). Enter report number as assigned by the sponsoring/monitoring agency, if available, e.g. BRL-TR-829; -215.

12. DISTRIBUTION/AVAILABILITY STATEMENT. Use agency-mandated availability statements to indicate the public availability or distribution limitations of the report. If additional limitations/ restrictions or special markings are indicated, follow agency authorization procedures, e.g. RD/FRD, PROPIN, ITAR, etc. Include copyright information.

13. SUPPLEMENTARY NOTES. Enter information not included elsewhere such as: prepared in cooperation with; translation of; report supersedes; old edition number, etc.

14. ABSTRACT. A brief (approximately 200 words) factual summary of the most significant information.

15. SUBJECT TERMS. Key words or phrases identifying major concepts in the report.

16. SECURITY CLASSIFICATION. Enter security classification in accordance with security classification regulations, e.g. U, C, S, etc. If this form contains classified information, stamp classification level on the top and bottom of this page.

17. LIMITATION OF ABSTRACT. This block must be completed to assign a distribution limitation to the abstract. Enter UU (Unclassified Unlimited) or SAR (Same as Report). An entry in this block is necessary if the abstract is to be limited.

Experimental Studies of Premixed Flame Structure and Propagation Characteristics in Compressible Flow

Brad Ochs, Dan Fries, Tom Slais and Nathan Grady

Co-Investigators: Jeff Jagoda, Robert Pitz, and David Scarborough

Principal Investigator: Suresh Menon

FA9550-12-1-0107

June 30, 2015

Contents

1	Background and Introduction	2
2	Summary of Major Accomplishments	7
2.1	Year One Accomplishments	7
2.2	Year Two Accomplishments	7
2.3	Year Three Accomplishments	9
2.4	Major Findings	9
3	Experimental Facilities	11
3.1	Subsonic Facility	12
3.1.1	Design Concept	13
3.1.2	Detailed Design	14
3.1.2.1	Incompressible Tunnel ($M < 0.1$)	19
3.1.2.2	Compressible Tunnel ($0.1 \leq M \leq 0.6$)	21
3.1.2.3	Data Acquisition Systems	24
3.1.3	Facility Improvements	25
3.1.3.1	Particulate Filtration System	26
3.1.3.2	Test Section Access Panels and Probe Array	26
3.1.3.3	Centerline Traverse CTA Probe Sting	27
3.1.3.4	Hydrogen Torch	27
3.1.3.5	Air Line Bleed System	27
3.1.3.6	Divergent Test Section	27
3.2	Supersonic Reacting Facility	29
3.2.1	Introduction	29
3.2.2	Experimental Facility	29
3.2.3	Supersonic Tunnels	29
3.2.3.1	M=1.25 Tunnel	29
3.2.3.2	M=1.5 Variable Divergence Tunnel	30
3.2.3.3	M=1.5 Fixed Divergence Tunnel	33
3.3	Supersonic Turbulence Facility	34
3.4	Turbulence Generators	35
3.5	Laser-Induced Breakdown Plasma Ignition System	43
4	Diagnostics	45
4.1	Constant Temperature Anemometry (CTA)	45
4.2	Hydroxyl Tagging Velocimetry (HTV)	51
4.3	Particle Image Velocimetry (PIV)	56
4.4	Schlieren Photography	57
4.4.1	Schlieren Examples: Backward Facing Step	58
4.4.2	Schlieren Examples: Sonic Jet in Crossflow	59
4.5	OH and CH ₂ O Planar Laser Induced Fluorescence	59

5	Results and Discussions	61
5.1	Turbulence Generation and Evaluation	61
5.1.1	Background	61
5.1.2	Experimental Investigations of Subsonic, $M < 0.1$ Turbulence	65
5.1.2.1	Passive Grid Studies	66
5.1.2.2	Blown Grid Studies	66
5.1.2.3	Vane-Stirred Grid Studies	70
5.1.3	Experimental Investigations of Subsonic, $0.1 \leq M \leq 0.3$ Turbulence .	74
5.1.3.1	Passive Grid Studies	74
5.1.3.2	Blown Grid Studies	79
5.1.3.3	Vane-Stirred Grid Studies	86
5.1.3.4	Post Contraction Passive Grid	87
5.1.4	Numerical Investigation of Subsonic-Compressible Facility	90
5.1.4.1	Numerical Methodology	90
5.1.4.2	Geometry and Boundary Conditions	90
5.1.4.3	Channel Results	91
5.1.5	Experimental Investigations of Supersonic Turbulence	96
5.1.5.1	Flow Field Visualization	96
5.1.5.2	PIV Measurements	97
5.2	Flame Kernel Analysis	100
5.2.1	Background and Methodology	100
5.2.2	Flame Kernels in Low Speed $M < 0.1$ Turbulent Flow	102
5.2.3	Flame Kernels in Medium Speed $0.1 \leq M \leq 0.3$ Turbulent Flow . . .	104
5.2.3.1	Isotropic Turbulence	104
5.2.3.2	Anisotropic Turbulence	108
5.2.4	Flame Kernels in Supersonic $M = 1.5$ Turbulent Flow	120
5.2.4.1	Initial Studies	121
5.2.4.2	Detailed Measurements	127
5.2.5	Summary of Freely Flowing Flame Kernel Data Collected to Date . .	132
6	Conclusions and Future Work	134
7	Supported Students and Personnel	136
A	Measurements of Leading Point Conditioned Statistics of High Hydrogen Content Fuels	137
B	OH PLIF Laser Diagnostics of Turbulent, Premixed, Freely Propagating Flame Kernels	163
C	An Experimental Study of Homogeneous Anisotropic Turbulence in Chan- nel Flow	176
D	Propagation of Premixed Flame Kernels in High Speed Channel Flows with Moderate Turbulence	192

E	Characteristics of Freely Propagating Premixed Flame Kernels in Supersonic Turbulent Channel Flow	206
----------	--	------------

Program Overview

The overall research program associated with Contract No. FA9550-12-1-0107 is split into two different elements with different supported staffs and research goals. The various long-term goals and major accomplishments of each element are summarized independently in the following report. The body of this report is dedicated to the prime project titled: "Experimental studies of premixed flame structure and propagation characteristics in compressible flow," lead by Professor Suresh Menon, while the subcontract: "Measurements of Leading Point Conditioned Statistics of High Hydrogen Content Fuels," lead by Professor Timothy Lieuwen appears in Appendix A. Four papers generated under the prime contract are included in Appendices B, C, D and E.

1 Background and Introduction

Recent desires to achieve hypersonic flight require more robust designs of nearly all aircraft components. In particular, the development of air-breathing propulsion systems that can operate in hypersonic flows is critical for the success of such vehicles. In one design, a ram effect on the inlet air is used to pressurize and slow the air entering the engine. Gaseous or liquid fuel is premixed upstream and burned in the combustion chamber at supersonic conditions. A recent study [1] has used shock waves to ignite premixed mixtures obtained with such upstream injection. Scramjet engines have been flight tested on several occasions, and will likely be the desired propulsion technology for future hypersonic flight. However, challenges associated with reliability and thermo-acoustic instabilities have thus far limited the adoption of premixed propulsion designs. In addition, our fundamental understanding of the fluid dynamics of premixed reacting flows at compressible conditions is limited. Additional challenges are encountered because the nature of the premixed burning mode is a strong function of the local turbulence characteristics. Hence, elucidating premixed combustion physics in highly turbulent, compressible flows is the primary goal in this research effort.

Past studies of turbulent premixed combustion in low-speed flows have established that increasing u'/S_L can drastically alter the flame structure and burning rate [2, 3, 4]. Here, u' indicates turbulence intensity and S_L is the laminar flame speed, which is a fundamental thermophysical property of the premixed mixture. It is important to note that u' is measure of turbulence, and typically the use of a single measure suggests that turbulence is isotropic. [The reason for this point will be noted later.] Regime diagrams that relate flame and turbulent length and velocity scales have been developed to classify premixed flames. Flames that are fast relative to the turbulence may only be mildly wrinkled, while very intense turbulence can completely dissolve the premixed flame structure leading to burning as a distributed reaction zone. Between these extremes lies a regime in which the turbulence can penetrate into the flame structure but the reaction zone is still thin. To illustrate these concepts, the Borghi diagram is presented in Figure 1, which identifies the various regimes using non-dimensional parameters such as the Reynolds number (Re), Damkohler number (Da) and Karlovitz number (Ka). Various laboratory flames are identified on the Borghi diagram. In particular, B1, M1, M9, M15 are Bunsen burner flames [5, 6]. Other lines and flames identified in this figure will be discussed further below.

The existence of combustion regimes spanning from flamelets to thin reaction zones (TRZ) to broken reaction zones (BRZ) has been well known for some time [7, 3, 8, 9]. However, most of the research effort has been limited to the flamelet regime, while a few recent studies have focused on thin reaction zone problems [10, 11, 12, 13, 14, 15]. Most, if not all, studies are limited to relatively low-speed flows and employ experimental configurations in which a flame can be anchored, e.g., classical burner designs or swirl systems. Although such designs provide stationary flames allowing for long-term measurements, they make it difficult to understand the true nature of flame-turbulence interactions as the turbulence level is increased. Such designs, by their nature, impose large-scale effects (e.g., coherent structures, large-scale strain) on the flame, which make it difficult to isolate the effects of small-scale, isotropic structures. Other issues related to flame holding include heat transfer and preferential diffusion, which can also contaminate the results. Therefore, to understand

the effect of turbulence (and to study the effect of increasing turbulence intensity) on flame characteristics, we need to focus on turbulence without large-scale effects.

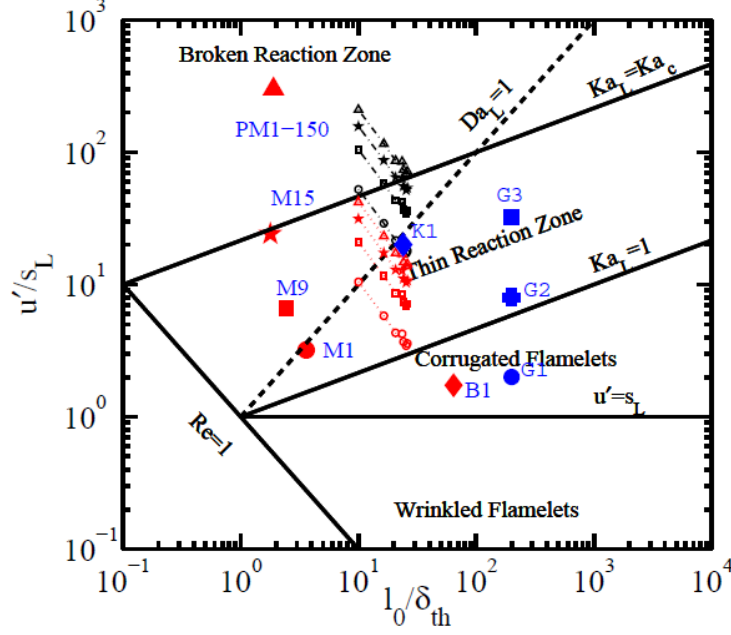


Figure 1: Borghi diagram identifying premixed turbulent combustion regimes. Both experimental Bunsen burner flames (called *B1*[16], *M1*, *M9* etc. [5, 6]) and computed flames in isotropic turbulence (identified as Flames *G* and *K*) are shown for reference. Here, the lines are data reported in Table 1 for a range of Mach numbers Ma .

Φ	Ma	u'/\bar{U}	u'/S_L	η (μm)	$\tau_\eta = \eta^2/\nu$ (μs)	$\tau_{\ell_0} = \ell_0/u'$ (ms)	Re_t	Ka	Da
1.0	0.30	0.01	3.45	60.33	234.8	7.32	911	1.3	7.383
1.0	0.60	0.01	6.9	35.87	83.0	3.66	1821	3.6	3.691
1.0	0.90	0.01	10.35	26.47	45.2	2.44	2732	6.6	2.461
1.0	1.20	0.01	13.8	21.33	29.4	1.83	3642	10.2	1.846
1.0	0.30	0.05	17.25	18.04	21.0	1.46	4553	14.2	1.477
1.0	0.60	0.05	34.49	10.73	7.4	0.73	9106	40.1	0.738
1.0	0.90	0.05	51.74	7.92	4.0	0.49	13658	73.7	0.492
1.0	1.20	0.05	68.98	6.38	2.6	0.37	18211	113.5	0.369

Table 1: Turbulent flame properties for a CH_4/Air mixture. Here, $u'/\bar{U} = 0.1$ with the mean velocity \bar{U} estimated using Mach number Ma . The integral length scale ℓ_0 is 1 cm. The Kolmogorov length scale is estimated as $\eta = \ell_0 Re_t^{-3/4}$ where $Re_t = u'\ell_0/\nu$ is the Reynolds number. The Karlovitz number is $Ka = [(u'/s_L)^3(\delta_{th}/\ell_0)]^{1/2}$, and the Damkohler number is $Da = \tau_{\ell_0}/\tau_{chem}$, where τ_{ℓ_0} is defined below and τ_{chem} is the chemical time scale.

Previous studies in low speed flows have focused on the interaction between isotropic turbulence and premixed flame kernels [11, 12, 14, 15, 17]. By employing isotropic turbulence,

these studies address some of the concerns with burner experiments mentioned above. In these studies, ignition kernels were created in a premixed mixture with isotropic turbulence. Following ignition, the propagation and growth of the kernels were studied to understand the nature of flame-turbulence interactions in flows devoid of large-scale effects. Flame and turbulence properties have been measured to understand how the burning rate is modified due to the flame-turbulence interaction. Results have shown that as the turbulence level increases, the flame surface undergoes wrinkling, resulting in fluctuations of the local kernel radius. Direct numerical simulations (DNS) have also been attempted in these low-speed regimes [18, 19, 20].

As mentioned previously, the current understanding of how flow compressibility affects flame characteristics is rather limited. Pressure oscillations are known to affect flame stability and burning processes [21], but most of these studies are limited to relatively low mean flow, with most of the pressure effects coming from long wavelength acoustics. As the flow speed increases from subsonic to supersonic, compressibility effects can change the nature of the fine-scale structures of turbulence. For example, suppression of mixing efficiency has been seen for highly compressible shear layers, and the presence of eddy shocklets has been identified in DNS of compressible turbulence [22]; however, flame characteristics in such flows are still not fully understood [23, 24]. While there have been attempts to generate compressible turbulence in the past [25, 26, 27], propagation of premixed flame kernels in compressible isotropic turbulence has not been addressed experimentally. These issues are important for next generation high-pressure gas turbine, and especially, for scramjet combustion systems.

It is also well understood that future design studies will increasingly rely upon on predictive simulations to understand design features, and to reduce the parameter space for experimental testing. The main drivers for incorporating simulations in the design process are the prohibitively expensive cost of full-scale experiments, and that data acquisition in such environments can be difficult, if not impossible. Recent development of large-eddy simulations (LES) have shown some promise [9, 28, 29, 30, 31, 32], but the accuracy of these LES approaches strongly depends on the reliability of the subgrid scale (SGS) models employed. As noted above, flamelet models [7, 3] have shown promise for some applications with low u'/S_L . However, there is still a lack of validated models that can span a wide range of flame-turbulence conditions without ad hoc adjustments. This issue becomes more critical when designing systems in which local flame-turbulence characteristics span the entire space shown in Figure 1. It is important to note that partial-premixing can occur in spray combustors, so such systems are within the scope of this discussion. Thus, an LES approach needs a validated subgrid strategy that will work in all regimes without adjustments. Since SGS closures typically couple combustion physics with small-scale turbulence, experimental data on flame-turbulence interactions without the effect of large-scale effects are highly desirable.

The effect of turbulence intensity and small scales on the flame must be incorporated into subgrid models since the LES grid cannot resolve these features. Models for the turbulent burning speed S_T have been developed using low-speed data, but there still remain uncertainties in these models [4, 2, 3, 8]. In general, $S_T = S_T(u', S_L)$, but its functional form has been shown to increase at low and decrease at very high u'/S_L (and in some cases show extinction). There is currently a large scatter in the available data, which results in a loss of confidence of the subgrid models. Furthermore, the very nature of the turbulent consumption speed in intense turbulence and in compressible flow is not fully understood. Thus,

subgrid closure models employing subgrid S_T closure remain limited in practical problems.

An advanced dynamics closure developed at Georgia Tech based on the linear-eddy mixing (LEM) model addresses many of the aforementioned issues surrounding turbulent-chemistry closures. Specifically, a multi-scale strategy has been developed that simulates the large-scales using LES, while LEM is employed as a subgrid model in order to dynamically capture the interaction of small-scale turbulence and molecular processes [33, 34, 35, 36, 37, 38, 39, 40, 41, 42]. Application to a wide range of problems, spanning from non-premixed (gaseous and spray) to premixed and to partially premixed systems, have demonstrated that this model adapts locally to any burning regimes with reasonable to excellent agreement with experimental data. However, as in any other model, LEM implicitly assumes something about the subgrid processes. LEM assumes that the unresolved small-scales are isotropic and follow Kolmogorov scaling, and that the impact of these unresolved eddies on the flame or scalar fields can be approximated using stirring events that follow simple scaling rules obeying the Kolmogorov hypothesis. Although DNS in low Re flows and experiments in low speed flows have provided supporting evidence, there are still uncertainties in using these models for very high turbulence intensities and compressible flows. For example, is it not fully established if Kolmogorov scaling is valid in high Re compressible turbulence. New quantitative data is needed to verify the assumptions of LEM and other subgrid models. This is the primary objective of the premixed flame structure portion of the research program.

Thus, to understand compressible flame characteristics and validate subgrid models, we must obtain high quality data that not only span the regimes shown in Figure 1, but also include the effect of Mach number M . Earlier studies have attempted a similar strategy for low speed flamelet regime flames [43]. Thus, in this proposed study, we will address these challenges by carrying out a comprehensive experimental study in an attempt to establish a new set of high quality experimental data for high Re and high M flows. Such data will elucidate compressible flame-turbulence physics and provide a valuable data set for LES model validation. In order to focus on these requirements certain conditions have to be achieved in the experimental design. These design requirements are (a) no large-scale structures in the burning zone in order to avoid the effect of large-scale strain on the flame, (b) an ability to vary inflow turbulence (or Reynolds number) over a wide range to cover the entire regime from flamelet to broken zone, (c) additionally an ability to vary u'/S_L by at least 2 orders of magnitude (1-100), and (d) to include the effect of compressibility by varying the uniform free stream from Mach 0.3 to 1.25. We expect to cover all regimes of interest and form a comprehensive data set that will correlate the flame propagation and structure characteristics for a wide range of Ma , Ka , Da , and Re . The data set will be archived and reported to the research community for analysis and/or for model development.

This report summarizes the efforts and accomplishments of this three-year research program:

In year one, the design and construction of major components of the new compressible subsonic facility at Georgia Tech were completed. Similarly, new diagnostic capabilities such as a new Constant Temperature Anemometry system (CTA), along with Vanderbilts advances in Hydroxyl Tagging Velocimetry (HTV) were developed and used to characterize grid turbulence in the compressible regime.

During year two, a number of infrastructure improvements were carried out. For example, continuing updates for the subsonic facility were implemented to deal with issues such as

particle contamination and water injection for hydroxyl tagging. In addition, a new diverging supersonic test section was built to account for Fanno flow deceleration due to boundary layer growth. Several investigations were made in both subsonic and supersonic regimes with passive and active turbulence generation. An in depth turbulence investigation was performed to characterize the effect of the test section nozzle. Also, a comprehensive set of OH PLIF measurements of subsonic freely propagating kernels with passive turbulence generation was collected; the results of which were presented at the 2014 Aerospace Sciences Meeting.

In year three, several new facility improvements were made to increase the quality of flame kernel measurements for both subsonic and supersonic flows. For example, windows were added to the subsonic incompressible tunnel to produce and directly compare kernels to flame bomb studies and window modifications were made to the supersonic tunnel to improve wall smoothness and reduce the significance of natural oblique shock waves. Full experimental campaigns were conducted on the subsonic facility in $M < 0.1$ and $0.1 \leq M \leq 0.3$ for passive and actively-generated turbulence. Finally, OH PLIF and PIV laser diagnostics were demonstrated as viable options for flame and turbulence measurements on premixed kernels in supersonic flows.

2 Summary of Major Accomplishments

2.1 Year One Accomplishments

The premixed flame structure group of the overall research program successfully met a number of design and development goals as part of its overall three year program. Both Georgia Tech and Vanderbilt University elements furthered both their experimental infrastructure and diagnostic methods in preparation for data collection. Early stages of data collection with regards to compressible turbulence characterization is currently in progress.

1. Georgia Tech Accomplishments

- (a) Designed new compressible subsonic reacting facility for examination of turbulence generation methods, flame kernel propagation, and diagnostic validation
- (b) Provided necessary infrastructure (air and fuel lines, ignition system)
- (c) Fabricated and assembled above facility
- (d) Performed facility check out, including its ability to reach steady state Mach numbers (0.3, 0.5, and 0.7) with varying turbulence levels
- (e) Developed hot-wire Constant Temperature Anemometry (CTA) methods for use in turbulence characterization and validation of laser-based non-intrusive methods
- (f) Began detailed design of active turbulence generation systems (currently in progress)
- (g) Began turbulence characterization and preliminary ignition studies (currently in progress)

2. Vanderbilt Accomplishments

- (a) The HTV two-photon was tested and developed at Vanderbilt University using a newly acquired lens to increase signal strength.
- (b) Optical minimizer was developed to determine the best temporal and spatial resolution possible using HTV.
- (c) New UV Raman equipment was purchased and development of methods for facility integration were conducted
- (d) Began HTV characterization of resultant grid turbulence

2.2 Year Two Accomplishments

A series of goals have been met in support of the overall goals of the program. The overall objectives of the program require a workflow that includes parallel development of facilities and capabilities, as well as reaching experimental milestones.

Developmental Accomplishments

1. Further modifications to the Subsonic Compressible Facility were performed to facilitate current and future turbulence evaluation, including:
 - Integration of a high-pressure particulate filtration system capable of filtering particles with diameters greater than $0.3\ \mu\text{m}$.
 - Incorporation of a traverse array for use with both pitot and hot-wire (Constant Temperature Anemometry) probes.
 - Development of a rigid CTA probe sting for use in streamwise turbulence evolution studies.
 - Development of a data acquisition system controlled hydrogen torch to accurately meter OH production for use with Hydroxyl Tagging Velocimetry (HTV).
 - Introduction of a main air line bleed system for use with active blown grid turbulence generation and seeding for Laser Doppler Velocimetry (LDV).
 - Development of a reliable and consistent kernel ignition system using a focused IR laser.
2. Additional improvements were made to the Supersonic Reacting Facility:
 - A variable-diverging supersonic test section was designed and built
 - Installation of an improved fuel control and measurement system.
 - Development of a reliable and consistent kernel ignition system using a focused 532 nm laser.
3. Recommissioning and demonstration of the Supersonic Turbulence Investigation Facility.
 - Development of a high-speed Schlieren system for compressible turbulence interactions.

Experimental Accomplishments

1. Completion of exploratory studies in turbulence generation using passive grids to gauge the properties of the subsonic facility.
2. Construction and testing of an active blown jet grid.
3. Obtained initial OH PLIF images of subsonic premixed flame kernels. The preliminary results showed consistent growth rates across the incompressible ($M = 0.1 - 0.3$) mean flow conditions studied.
4. Obtained OH* Chemiluminescence images of kernels evolving in a $M = 1.25$ flow. The results showed that kernels were both reliably lit and grew in the supersonic mean flow.

2.3 Year Three Accomplishments

A series of goals have been met in support of the overall goals of the program. Year three builds on major facilities developments accomplished in the previous two years of effort. Efforts were therefore primarily focused on experimental campaigns.

1. Facility Modifications:

- The incompressible-subsonic tunnel was modified to add quartz windows for flame kernel measurements. This allowed more direct comparison to flame bomb studies.
- The supersonic tunnel was modified to incorporate a fixed divergence and improved window-tunnel interface to eliminate oblique shock formation.

2. Experimental Campaigns:

- Conducted a complete evaluation of incompressible kernels ($M < 0.1$) with isotropic turbulence for comparison to flame bomb studies.
- Conducted a complete evaluation of flame kernels ($M < 0.3$) with both isotropic and anisotropic turbulence with both passive and active turbulence generators with $u'/S_L < 10$.
- Completed exploratory studies of PIV and OH PLIF laser diagnostics for use in supersonic flame kernel studies. Initial results show feasibility of these diagnostics and match chemiluminescence studies from year two. A variable-diverging supersonic test section was designed and built.

2.4 Major Findings

Subsonic Turbulence

- Corrections to the energy spectra were necessary to correct for:
 - Small tunnel dimensions cause a deviation from isotropy in center of energy containing range.

- Low wavenumber non-turbulent content
- TKE decay within range of expected values (from existing data)
- Isotropy at low Mach numbers using the active vane grid

Subsonic Flame Kernels

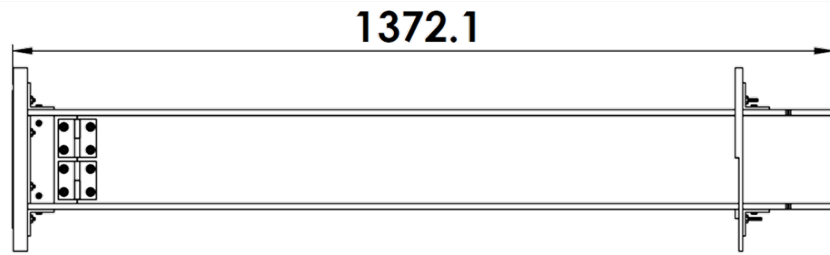
- Correction for kernel growth: influential turbulent scales and stretch effects (thermo-diffusion) necessary
- Correlations can be made across different spark energies
- With above corrections, growth is consistent with previously observed spherical, turbulent flames
- Definition of turbulent quantities influencing combustion not consistent across literature, i.e. how meaningful is Borghi-Diagram evaluation?
- Anisotropic turbulence effectively reduces S_T

Supersonic Turbulence and Isotropic Flame Kernels

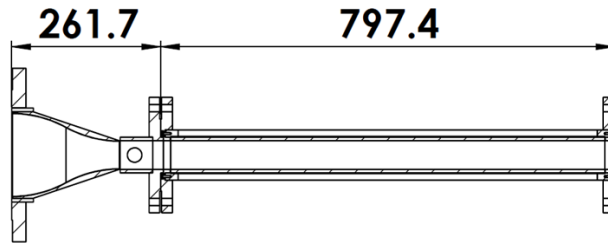
- Turbulence measurements require small spatial scale, i.e. micro PIV
- Flame kernels show expected torus shape at early times
- Plasma kernels experience thermal loss resulting in smaller flame kernels
- Walking motion of flame kernels causes a problem with the interpretation of planar flame kernel measurements (OH PLIF)
- Statistics of freely propagating flame kernels should be conditioned on their location within the laser sheet
- Supersonic flame kernels look very different than their subsonic counterparts
 - May be the result of shock wave-flame interaction
 - Kernels may experience local quenching- due to high intensity turbulence
- Supersonic kernel measurements reasonably match previous OH^* measurements despite kernel motion out of the PLIF sheet
- Supersonic kernels reasonably match classic correlations

3 Experimental Facilities

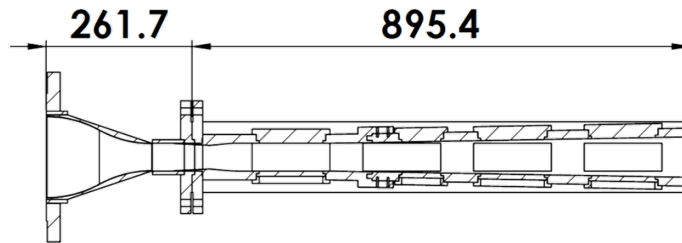
The overall goal of this program is to identify the effects of compressible features (compressed turbulence, heavily strained flows, shocks, etc.) on premixed flames. A series of experimental facilities were needed in order to anchor high speed results to previous, well established studies. An incompressible, low speed tunnel ("Subsonic Incompressible Tunnel") was used to link low speed, flowing kernels to previous flame bomb studies. After the experimental capabilities were demonstrated and data were shown to match previous studies, another tunnel ("Subsonic Compressible Tunnel") expanded the studies to the high subsonic regime ($M < 0.6$). The "Supersonic Reacting Tunnel" expanded the studies into the supersonic realm and opens the capability to study the interaction of flames with common compressible features in supersonic combustors (strong shocks and compressed turbulence).



(a) Subsonic-Incompressible Tunnel $M < 0.1$



(b) Subsonic-Compressible Tunnel $0.1 \leq M \leq 0.6$



(c) Supersonic Fixed Divergence Tunnel $M = 1.5$

Figure 2: Overview of the tunnels used in this research program.

3.1 Subsonic Facility

A schematic of the subsonic combustion facility with associated centerline traverse measurement locations is given in Figure 3. Unheated air is supplied to the facility at 250 psig (1725 kPa) and 20.0 °C, where it is then filtered by a Parker CO2-2362 high-pressure air filter to eliminate particulate contamination with diameters greater than 0.3 μm . Air flow is metered via a gate valve and calibrated orifice plate, monitored by a 0-5 psid (0-34.5 kPa) Omega PX-409 differential pressure transducer with a maximum error of 1% of full-scale (FS). This primary flow meter has been calibrated against a separate Siemens SITRANS F C MASS 2100 DI 3-40 series Coriolis flow meter which has a maximum error of 0.1% of a given flow rate less than 14.4 kg/s. The Siemens flow meter is mounted off of a branch downstream of the primary orifice plate, and meters filtered bleed air flow off of the main line via a globe valve to the blown jet grid system. A description of the fuel supply system, flow conditioning screen array, and associated facility components used in flame kernel studies is given by Grady [44]. All hardware upstream of the turbulence generator location is shared between incompressible duct and subsonic facility configurations.

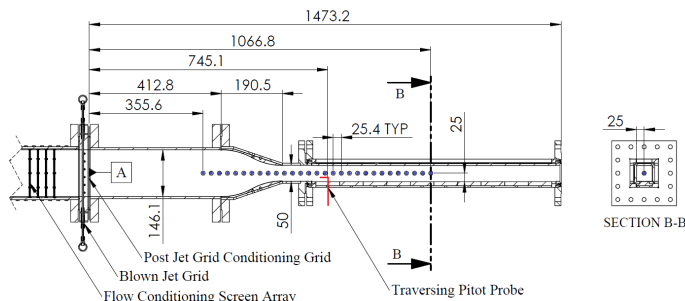


Figure 3: Subsonic facility schematic with centerline traverse locations. All reported x locations are with respect to Datum A, with traverse positions increasing in number in the streamwise direction (Units in mm).

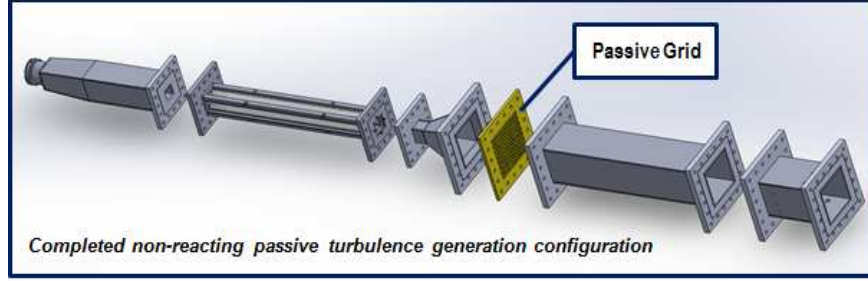
The primary first year focus on the side of Georgia Tech regarding premixed flame structure in compressible flow, was the design, construction and shakedown of a new subsonic wind tunnel capable of Mach numbers in excess of Mach 0.7, with the ability to generate varying turbulence levels and accommodate fuel injection, mixing and ignition. The subsonic facility has been constructed to serve as an initial testing venue for various turbulence generation strategies and their associated impact on flame kernel propagation before evaluating such methods in existing supersonic facilities. Similarly, various non-intrusive measurement techniques such as Laser Doppler Velocimetry (LDV) and Planar Laser-Induced Fluorescence (PLIF) with various tagging species are currently being validated using the subsonic facility before implementation in the supersonic facilities. In addition, design features, subsystems and methodologies developed during the design and construction of the subsonic facility have been or are currently being integrated on the existing supersonic facilities to enable more efficient data collection and processing, as well as to realize cost savings and minimal facility downtime.

3.1.1 Design Concept

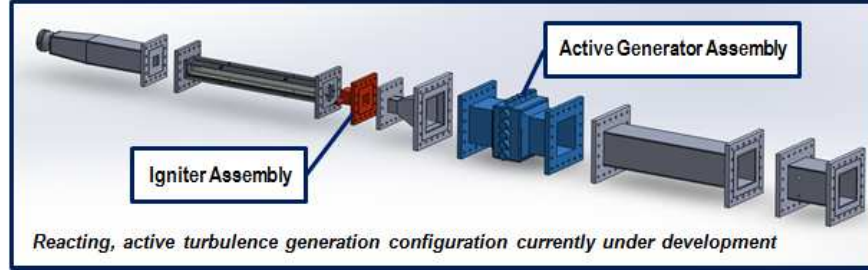
The various requirements of the subsonic facility within the experimental framework of the program call for a facility that is can be rapidly reconfigured to meet a wide range of experimental objectives. A list of required facility capabilities is enumerated below, reflecting major foci of the experimental program.

- *Turbulence Generation:* Accommodate both passive grid-based [45, 46, 47, 48, 49] and active vane-actuated [50, 51, 52, 53] turbulence generation systems, with the ability to rapidly change device parameters (i.e. solidity and geometry for passive grids; vane geometry and driving algorithm for active grids).
- *Turbulence Characterization:* Accommodate intrusive Constant Temperature Anemometer (CTA) systems, as well as non-intrusive LDV and associated particle seeding systems. The CTA (hot wire) system is required for both initial tunnel component turbulence characterization, as well as confirming confidence intervals for integral length scales, as LDV methods cannot take simultaneous data points at two points in the flow.
- *Kernel Generation:* Facilitate ignition using methods that are as non-intrusive as possible while incorporating adequate precautions for test-section survivability in case of an overpressure event, as well as safe integration of high-voltage components
- *Kernel Characterization:* Facilitate varying laser-based data acquisition methods, including UV Raman, Hydroxyl Tagging Velocimetry (HTV), and OH PLIF. The test section windows yield adequate performance for all required laser wavelengths, as well as allow a view of the kernel at all significant points of its evolution.
- *Data Acquisition:* Accommodate varying types of data inputs and outputs, from low-level pressure and thermocouple inputs required for basic facility operation, to higher level signal generation and control required for active turbulence generation schemes. The system must also be able to interface with associated kernel and turbulence characterization data acquisition systems outlined above to allow for synchronized time stamps for all data sets.

As a consequence of the large amount of facility design requirements, a modular concept has been implemented which allows for various assemblies to be installed as needed. This action was made to also expedite construction and minimize risk, as detailed designs for individual components could be made and cleared for production quickly. These components could also be reworked individually if necessary; eliminating the potential of costly redesign of a single integrated facility assembly should difficulties be encountered. Figure 4 illustrates this concept, with both a passive, non-reacting turbulence generation configuration and a reacting active generation configuration.



(a) Passive Grid Configuration



(b) Active Grid Configuration

Figure 4: Modular subsonic facility design concept illustrating (a) passive and (b) active grid configurations.

The details of tunnel components that have been developed and those that are currently under development are described in the following sections of the report.

3.1.2 Detailed Design

Initial component sizing and facility layout was dictated by existing infrastructure available at the Ben T. Zinn Combustion Lab. The preliminary design was first dictated by available run times afforded by the available 250 psi (1.72 MPa) high-pressure air (HPA) system, with a total available storage of capacity of 110,000 SCF (3,115 m³/s) at 2700 psi (18.6 MPa). Various test section cross-sectional areas were evaluated assuming isentropic flow conditions over a span of Mach numbers, ranging from the lowest proposed test condition ($M = 0.3$) to the highest proposed test condition ($M = 0.7$), as well as several supersonic conditions to evaluate the feasibility of running supersonically by adding a modular nozzle assembly. Figure 5 summarizes the key results of this evaluation, with run times in minutes for the associated test conditions. Examination of Figure 5 reveals that despite the additional design challenges of having a small test section cross sectional area of 5 x 5 cm, the run times achieved are significantly larger than other considered geometries Mach numbers in excess of 0.5. This allows for larger time windows to calibrate instruments, as well as more flame kernel ignitions per run.

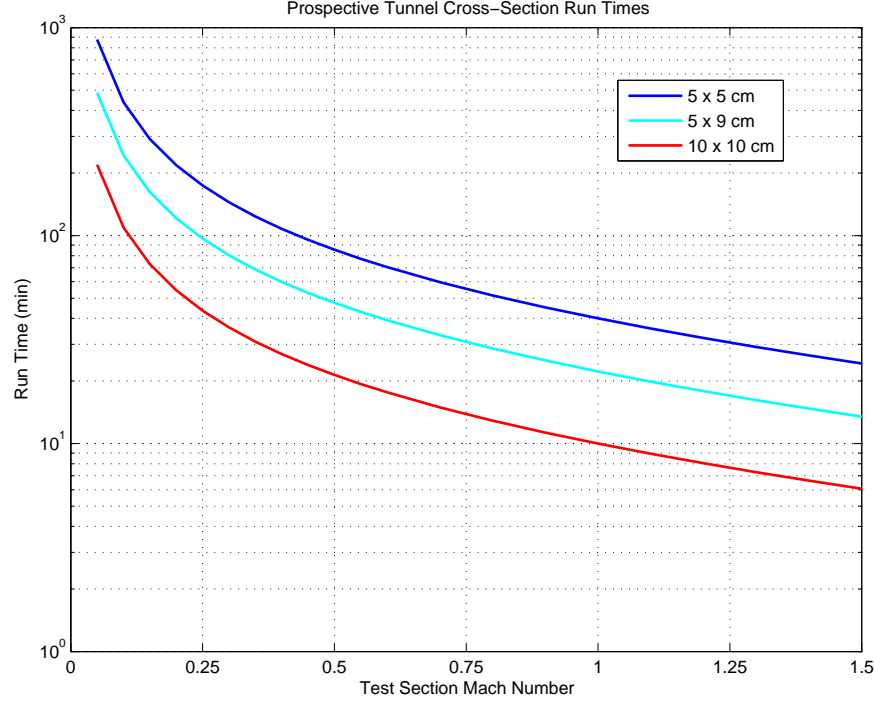


Figure 5: Isentropic test section sizing study run-time evaluation

Additional drivers for test section sizing included requirements for fuel flow (CH_4) afforded by available infrastructure. Preliminary calculations again assumed isentropic flow conditions, and solved for cases assuming a stoichiometric fully mixed out flow before entering the test section. Evaluation of the required volumetric fuel flow rates associated with predefined test conditions to calculate facility run times were used to match a proposed test section size to the capabilities of available fuel delivery systems. The building exhaust system can accommodate 105 SCFM ($0.05 \text{ m}^3/\text{s}$) of CH_4 at atmospheric conditions, with a suggested upper safety limit of 25% of the lower explosive limit (LEL) for CH_4 at those conditions. As shown in Figure 6, utilization of the 5 x 5 cm test section was the only way to accommodate the facility using an available 25 psi line in an unoccupied lab space.

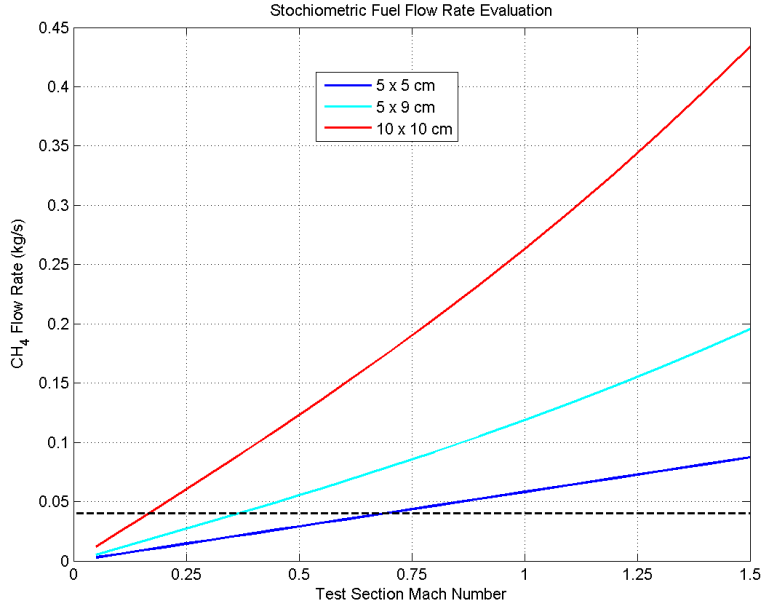


Figure 6: Evaluation of test section with respect to fuel delivery. Note the dotted black line denotes the maximum CH₄ flow rate allowed by building exhaust systems

Preliminary mixing section sizing was driven by a compromise between yielding the largest mixing time possible for a prospective injector design and using manufacturing methods that reduce machining time. A square duct with sides of 6 in. was ultimately selected, with a maximum length of 30 in. as dictated by available floor space within the lab. A 6 in. duct size was the largest possible size allowing all machining and waterjet processes to be completed in-house with lead times of 3 weeks or less. Figure 7 illustrates the dependence of characteristic flow time on duct size and test condition Mach number, as well as highlighting the characteristic flow time trends for the chosen duct size.

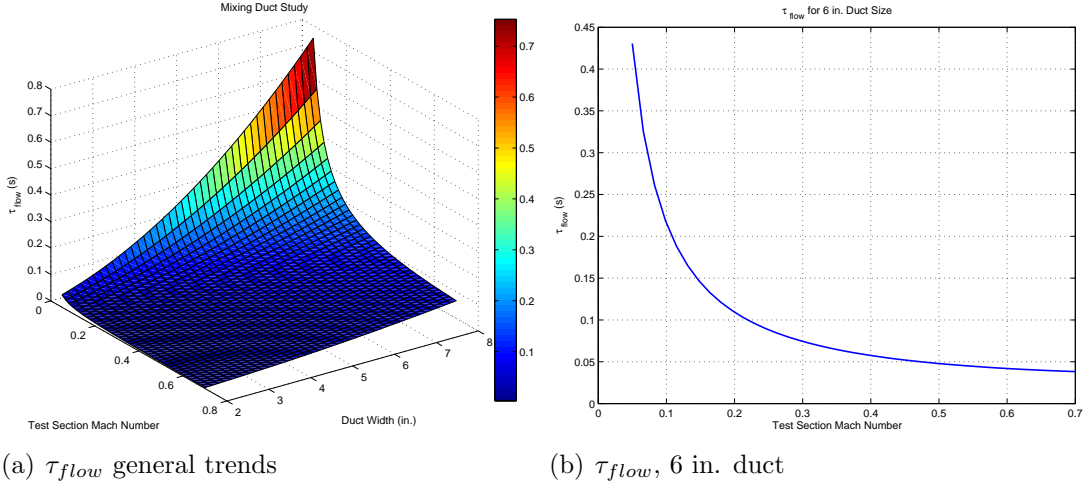


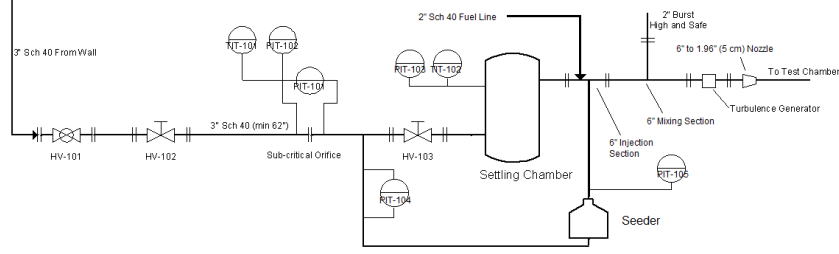
Figure 7: Visual summary of mixing section sizing study, with highlight of 6 in. duct behavior.

Final preliminary evaluation of the facility included compiling a reference data set of local conditions within the facility for a given test condition assuming isentropic flow. Points within the facility included the locations of fuel and seeder injection, test section, and exhaust. The data set served as an initial reference for detailed design of the test section, fuel and seeder injection systems, as well as a reference for facility diagnostics and data acquisition systems. The reference data set is currently in the process of being augmented with measured pressure readings at various downstream stations to gauge pressure loss for more accurate operation of the system with limited basic instrumentation. Table 2 summarizes the outputs of the reference data set for the test section at test condition Mach numbers of 0.3, 0.5 and 0.7.

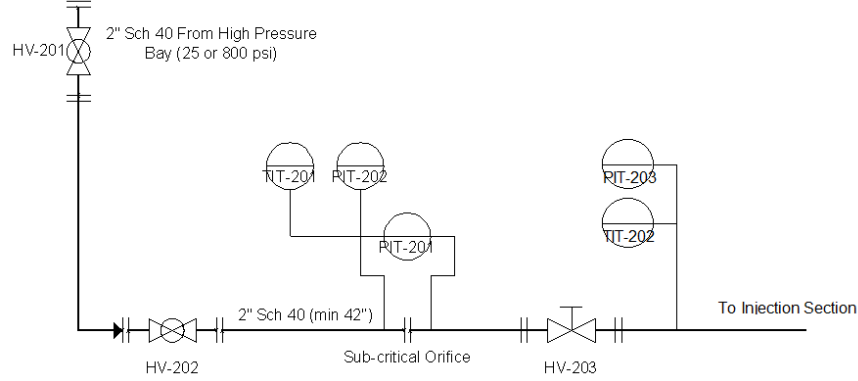
Parameter	Test Condition 1	Test Condition 2	Test Condition 3
Mach Number	0.3	0.5	0.7
Total Pressure (Pa)	102,970	105,300	107,557
Static Pressure (Pa)	96,740	88,730	77,540
Static Temperature (K)	292.70	283.80	271.40
Static Density (kg/m^3)	1.172	1.084	0.968
Speed of Sound (m/s)	343.0	337.7	330.3
Velocity (m/s)	102.9	168.8	231.2
Mass Flow Rate (kg/s)	0.296	0.460	0.575

Table 2: Estimated test section properties at given test conditions

With a general facility layout in place, a piping and basic instrumentation layout was designed to allow for adequate operation of the facility, as well as accommodation of additional control if needed from sensor feedback. Figure 8 below depicts the piping and instrumentation layout for both the air and gas line systems. A summary of basic data points and outputs associated with the piping and sensor layout in Figure 8 is shown in Table 3.



(a) Air line basic facility layout



(b) Fuel line basic facility layout

Figure 8: Air and fuel facility layouts and with basic instrumentation

Instrument	Type	Data Point
PIT - 101	Differential Pressure Transducer	Total air mass flow rate
PIT - 102	Pressure Transducer	Static pressure; air inlet
PIT - 103	Pressure Transducer	Total pressure; stagnation tank
PIT - 104	Differential Pressure Transducer	Seeder air mass flow rate
PIT - 105	Pressure Transducer	Injection manifold pressure; seeder line
TIT - 101	Thermocouple	Static temperature; air inlet
TIT - 102	Thermocouple	Total temperature; stagnation tank
PIT - 201	Differential Pressure Transducer	Total fuel mass flow rate
PIT - 202	Pressure Transducer	Static pressure; fuel inlet
PIT - 203	Pressure Transducer	Injection manifold pressure; fuel line
TIT - 101	Thermocouple	Static temperature; fuel inlet
TIT - 102	Thermocouple	Injection manifold temperature; fuel line

Table 3: Outline of compressible subsonic reacting facility instrumentation

A current as-built CAD representation as of March 20, 2013 of the facility in a configuration without any turbulence generation equipment installed is shown to visually complement Figure 9, with Figure 10 showing the fully assembled tunnel before instrumentation installation. Note that in comparison to the diagram, fuel/seeding media injector rails are not

currently installed in the injector section, the seeding system is not shown as installed off of the air line pipe tee, and the ignition/calibration module is not present. These components as of the time of writing are currently undergoing their final stages of development, or are currently being manufactured.

Elaboration and development up to the current state of the rigs in 2015, is contained in the following sections of this report.

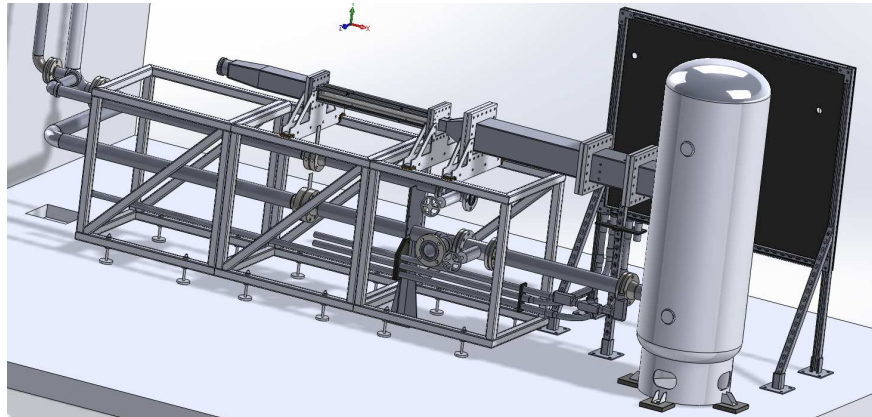


Figure 9: As-built CAD representation of facility as of March 20, 2013

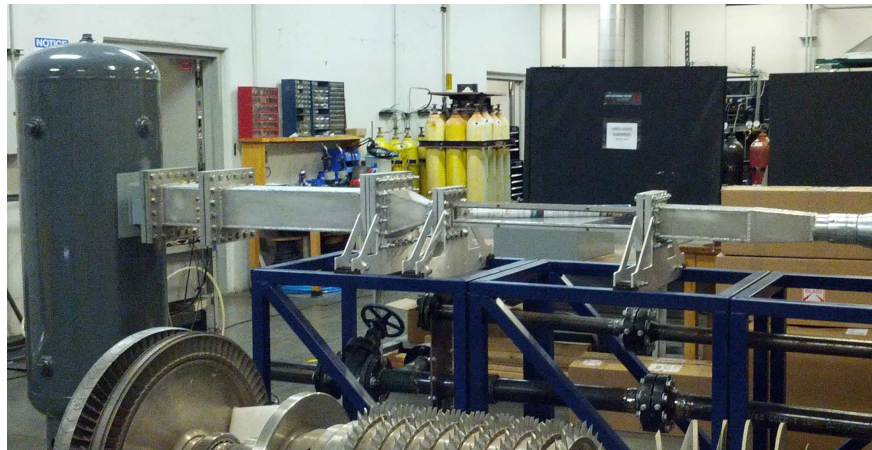


Figure 10: Constructed compressible subsonic reacting facility before DAQ and instrumentation installation.

3.1.2.1 Incompressible Tunnel ($M < 0.1$) A schematic of the divergent duct configuration with associated centerline and transverse traverse measurement locations is shown in Figure 11. The divergent duct facility is set at a given run condition via use of the PC-type Pitot probe used in the subsonic facility that can be fully retracted from the flow at the location shown in Figure 11. Differential pressure measurements between total and static pressure lines were accomplished using a Dwyer Magnahelic 2000-00 0-0.25 in. H_2O (0-62.3

Pa) differential pressure gauge with 4% FS accuracy. After setting the mean velocity of the flow-field, the divergence angle of the lateral tunnel walls were set by equilibrating the static pressure measured at taps indicated in Figure 11 using the Magnahelic gauge at a given grid condition. Centerline traverses were completed with hinge joints and all spanwise traverse ports sealed flush with 3M 425 aluminum tape not exceeding 0.005 in. (0.12 mm) in thickness, with ports only exposed during spanwise traverses at a particular location.

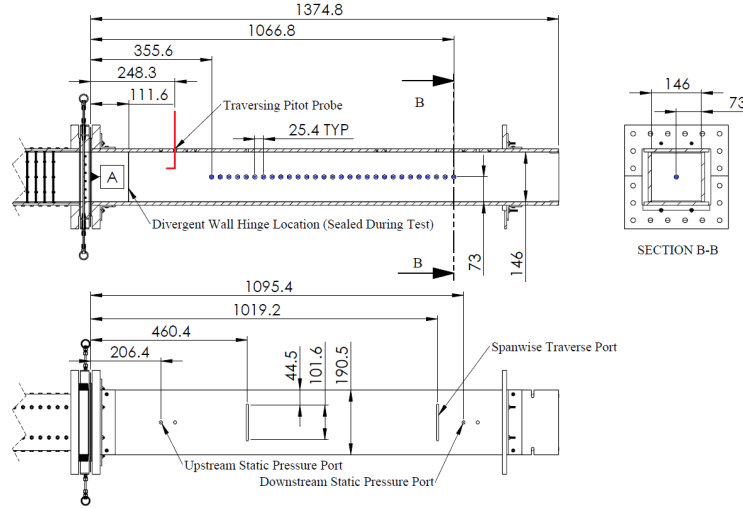


Figure 11: Divergent duct facility schematic with centerline traverse locations and spanwise traverse access ports. Datum A is shared with the subsonic facility shown in Figure 3 (Units in mm).

Quartz windows have been added to three sides of the tunnel to accommodate reacting flows, allowing for usage of optical measurements systems over a length of 635mm and laser ignition, see Fig. 12. Additional slots guarantee more structural stability.

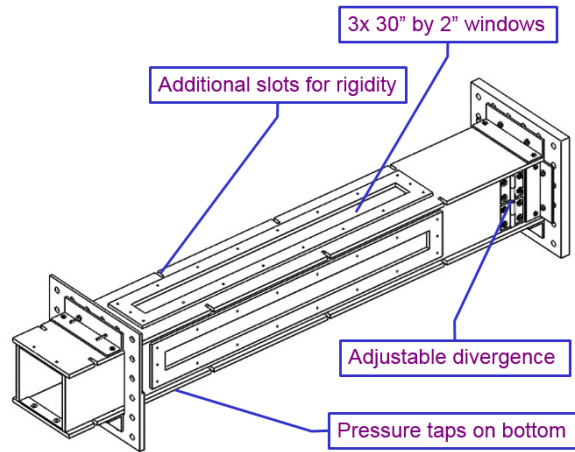


Figure 12: Illustration of the improved divergent duct setup.

3.1.2.2 Compressible Tunnel ($0.1 \leq M \leq 0.6$) Design of a robust test section that could perform well for day-to-day runs as well as survive potential high pressure spikes from an undesirable ignition event was driven by the constraints of the window material. The most economical quartz glass material that would accommodate the 193 nm wavelength ArF laser utilized for HTV measurements was Corning 7980, a synthetic fused quartz that retails on average for around \$1800.00 for 1/4 in. thick machined windows of nominal sizes of 30 x 2 in. The requirement for at least four of these units plus spares for later testing justified more extensive examination of the test section design problem. The relevant material properties of the Corning 7980 material [54] drove a design that considered both limit loading from internal pressure cases and minimizing or eliminating loads at the points of interaction between the panes from thermal expansion.

Extensive use of FEM tools was made to model various window designs, as well as supporting frames constructed out of T6 temper aluminum or stronger. Primary drivers for the frame design included constructing a structure that could support itself and the windows without significant deformation under its own weight, as well as maintain a seal under the expected test section static pressure conditions outlined previously in the Preliminary Design section.

Design and evaluation of frame concepts were first completed by evaluating frame deflection under the weight of the frame and torsional stiffness. The evaluation methodology for bending loads involved imposing a fixed boundary condition on the upstream flange face, and evaluating the assembly with equal deformation boundary conditions at points of interaction of the test section frame assembly. The torsional rigidity evaluations were conducted to see what kind of seal would be adequate, as typical deflections due to torsional loads would have to be sustained by the seals in relation to a non-deforming quartz window. Torsional load cases involved applying moments at the downstream flange about the centerline of the assembly while fixing the upstream flange to determine the amount of force required per degree of assembly deflection.

Limit load cases were constructed utilizing a general pane design featuring a 45° chamfer as a mating surface. Various mounting configurations of the general pane design were evaluated by applying a fixed boundary condition over regions of the window which interacted with the test section frame. Uniform pressure boundary conditions applied on the inside face of the pane represented the pressure differential between test section and ambient atmospheric pressure conditions. Evaluation of limit loads was found by scaling the interior boundary condition until the noted rupture yield condition [54] was reached according to the von Mises yield criterion. Figure 13 shows an isometric view illustrating a sample result obtained during the limit load analysis illustrating boundary condition application and typical deflection patterns for the applied load case. The notations DMX, SMN, and SMX represent maximum displacement, minimum stress and maximum stress, respectively in units of inches and psi.

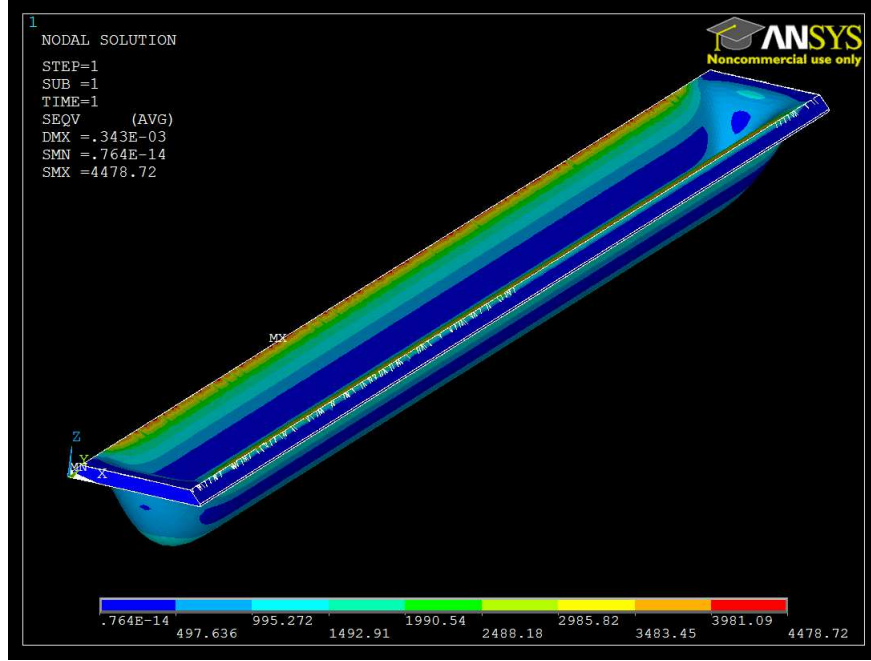


Figure 13: Von-Mises stress plot for window pane at 98 psi internal pressure failure case. Stress represented in psi, displacement in inches.

The final design synthesized the results of the FEM-driven design studies into a cost-effective and easy-to-maintain final assembly. Extra features incorporated in the assembly included using 0.102 in. thick square O-ring stock seal mounted in the corners to aid in locating the individual seals and window panes, as well as RTV silicone gasket seal galleries incorporated into the pane-flange interface. Both of these seals were toleranced according to thermal expansion and ease of assembly considerations. In addition, all glass-on-glass surfaces utilize vacuum grease to make up for tolerances incorporated for ease of assembly and handling. Figure 14 shows an exploded view of the final test section assembly, while Figure 15 shows the real test section after assembly.

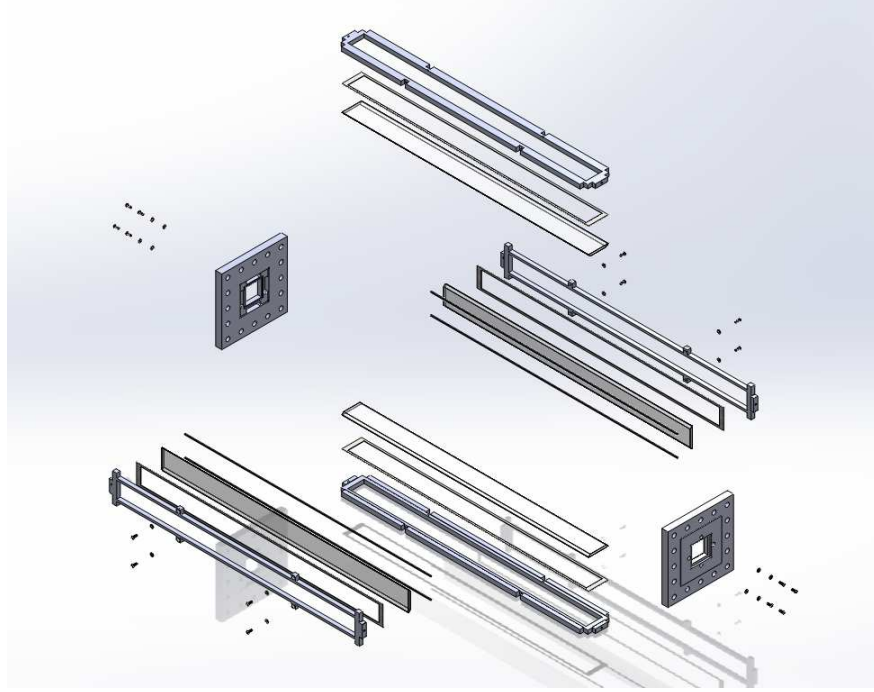


Figure 14: Exploded view of test section assembly.



Figure 15: Completed test section assembly for use with compressible subsonic reacting facility.

The subsonic configuration is as shown in Figure 3. A post-grid duct measuring 45.7 cm long is installed to facilitate homogenization of the turbulent flow-field immediately downstream of the conditioning grid. A square nozzle with contraction ratio $c = 8.5$ based on a scaled design of Sjögren and Johansson [55] with $c = 9$ is followed by an optically accessible test section with a cross-section of 5.00 cm \times 5.00 cm. Test section velocities are

set via a retractable 1.59 mm diameter PC-type Pitot probe constructed by United Sensor Corp. as shown in Figure 3 with total and static pressure lines measured by Omega PX-409 0-30 psia (0-206.8 kPa) pressure transducers accurate to 1% FS.

3.1.2.3 Data Acquisition Systems A single data acquisition system (DAQ) architecture has been designed to be shared amongst the new subsonic facility and both existing supersonic facilities. Each system is based around a National Instruments CompactRIO controller and chassis. The chassis have eight slots which can accept a wide variety of modules, each suited for different tasks. These modules can be installed or removed by hand, aiding in rapid reconfiguration of the system to meet experimental needs. Basic equipment for each individual facility DAQ system includes an analog input module, an analog output module, a digital sourcing module, and a thermocouple module. The analog input module, which can read -10 to 10 volts, -5 to 5 volts and 4-20 mA, is used to receive data from pressure transducers. The digital sourcing module is used to trip relays, which is useful for equipment which must be turned on or off during operation of the facility, such as solenoid valves. The analog output module outputs a 4-20 mA signal, which agrees with industry standards for control valve actuation. The CompactRIO and the various electronics which serve as the interface between the RIO modules and the rig are kept in small electrical enclosures. These enclosures serve to keep the electronics protected from dust and incidental contact, and allow for easy troubleshooting by keeping circuits with different functions separate. Each of the facility DAQ systems consists of three enclosures. The three units consist of relay control box, a master control box consisting of the CompactRIO itself, digital I/O channel outputs and thermocouple inputs, and a pressure transducer control unit which processes and relays incoming signals. These boxes are installed on the facility as shown in Figure 16, with the relay, control and pressure units shown clockwise from top left.

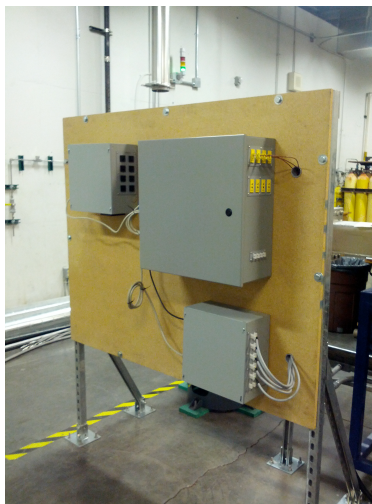


Figure 16: Integration of modular DAQ system with subsonic reacting facility

As illustrated in Figure 16, each box has a number of external plugs which allow for easy reconfiguration of the system. Data is sent between supporting units to the control unit via

standard data cables utilizing DB-type connectors. The use of such pinned connectors and accompanying terminal blocks allows for maintenance concept similar to that of the electronics industry, where faults can quickly be diagnosed via a multimeter by simple continuity tests along individual output channels. An example of the execution of the concept is shown in Figure 17 which shows the internals of the pressure transducer enclosure.

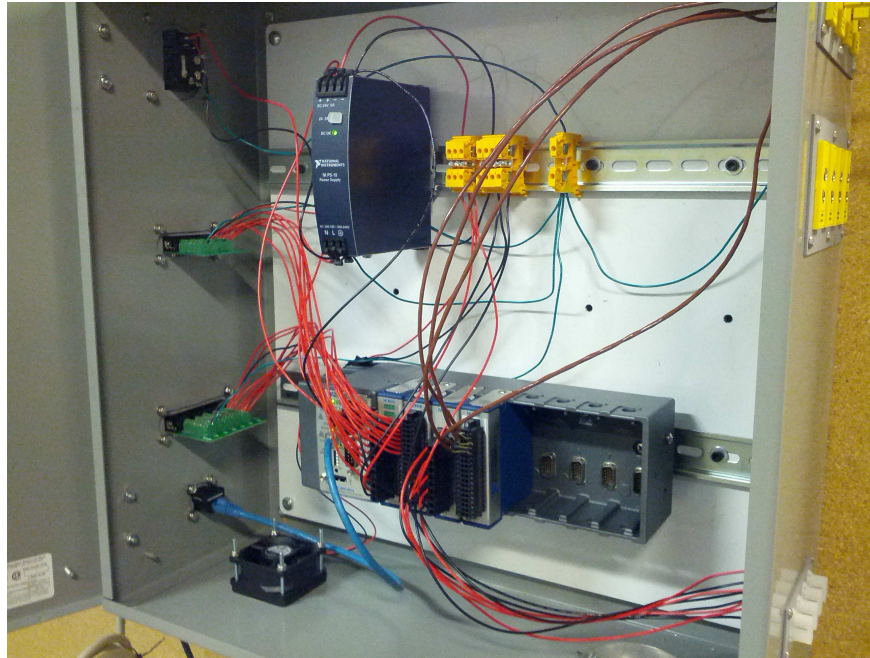


Figure 17: Internals of control module with NI CompactRIO system. Note simplified wiring, with single FPGA channels (center, black modules) corresponding to single terminal block outputs (left of box, green) for instrumentation and data transfer.

The CompactRIO works similarly to the RTOS concept. The unit contains an individual processor coupled with a Field Programmable Gate Array (FPGA) that integrates signal processing and data storage functions on a per-run basis. The FPGA is configured via a separate PC on the local lab network equipped with NIs LabVIEW software connected to the control module via an Ethernet connection. The experiment can be run by any computer in the lab equipped with such software with knowledge of the CompactRIOs Internet Protocol (IP) address, allowing for remote operation of the experiment. Similarly, acquired data can be uploaded to any computer on the network instantaneously, making it significantly easier to build an organized database for the duration of the experimental program.

3.1.3 Facility Improvements

The following improvements have been made to the subsonic facility. These modifications have been primarily driven by a need to better accommodate turbulence measurement techniques, such as Constant Temperature Anemometry (CTA) and Hydroxyl Tagging Velocimetry (HTV). In addition, modifications such as the bleed system have been integrated to

facilitate current active blown grid turbulence generation studies, as well as future seeding systems for use with Laser Doppler Velocimetry (LDV) studies.

3.1.3.1 Particulate Filtration System A high-pressure particulate filtration system was integrated after it was discovered that current air filtration systems at the Ben T. Zinn Combustion Lab were ineffective at filtering rust and oil particles smaller than approximately $100\text{ }\mu\text{m}$. This addition was primarily motivated by the unacceptably high attrition rate of CTA probes. This hindered the ability to take CTA data for extended periods and further refine data acquisition and processing techniques between July and October of 2013. The installation of a Parker CO2-2362 high-pressure air filter capable of filtering out particulate contaminants with diameters greater than $0.3\text{ }\mu\text{m}$ has since resolved this issue and enabled safer CTA measurement.

This modification also helps when using laser diagnostic techniques. During early HTV studies, particulate buildup on the windows made it difficult to quantify signal-to-noise ratios. The buildup of particles over a series of runs, coupled with the difficulty of cleaning and reassembling test section windows resulted in HTV data sets of diminished value. These issues have since been resolved, allowing us to verify that HTV and CTA measurements agree across the $0.1 < Ma < 0.7$ range of the tunnel.

The filtration system will also show benefits when taking LDV data in future experiments. By eliminating particles greater than $0.3\text{ }\mu\text{m}$, the data obtained with $6\text{ }\mu\text{m}$ alumina seeding particles will not be contaminated. The bleed system needed to redirect air off of the main line for use with a fluidized bed seeder is further detailed in a later portion of this section.

Moving the filtration system to a new position behind the flow orifices, also significantly reduced the noise in CTA turbulence measurements.

3.1.3.2 Test Section Access Panels and Probe Array The addition of test section access panels was required to allow accurate span-wise traverses of the tunnel for both mean velocity and CTA measurement. The initial measurements from early passive grid turbulence studies showed that boundary layer displacement thickness growth was non-negligible. Overall, there was a 4% increase in mean velocity over the 20 in (0.50 m) CTA streamwise traverse measurement region, relative to the set point at the test section entrance. This prompted measurement of the mean velocity profiles within the test section to confirm mean centerline CTA measurements, as well as to identify a streamwise corridor outside of the boundary layers. These findings are detailed further within the Results section.

Additionally, experience gained during HTV studies indicated that multiple pitot probe stations are required to accurately set the tunnel to construct a data set that accurately reflected the flow-field of the tunnel. This was primarily due to the fact that the HTV setup takes at least a day to be moved to its next test condition, making it impossible to take a single continuous data set as is possible with the centerline CTA probe traverse. The incorporation of a spanwise traversable pitot probe at the test section entrance, coupled with a second pitot probe that can be installed wherever an HTV grid of interest exists enables direct comparison to CTA data, which was not initially possible.

The traverses shown in Figure 18 were also designed to accommodate CTA probes for evaluation of spanwise turbulent homogeneity and isotropy at a streamwise station of choice.

This capability will be utilized to further evaluate turbulence generated by the blown grid.

3.1.3.3 Centerline Traverse CTA Probe Sting A CTA probe sting was developed to allow for measurement of the streamwise evolution of the turbulent flow field. This was motivated by the fact that the small 5×5 cm cross-section and approximately 0.8 m length of the test section is impossible to access with conventional traverse systems. The sting features a damped ceramic rod with a cruciform to stabilize the probe at test section Mach numbers in excess of 0.3. The probe can also be rotated about its axis, enabling multi-velocity component calibration and measurement using the method of Bruun [56, 57]. The use of the sting also allows for simultaneous CTA and HTV measurement, with the CTA sting stationed at the back of the tunnel when not in use.

3.1.3.4 Hydrogen Torch HTV requires humid air to take velocimetry measurements. The air supplied by the building is very dry, so a method to raise the humidity is required. Furthermore, at compressible Mach numbers, the air in the tunnel is cold enough to condense water vapor. Therefore it is necessary to heat the water to prevent it from condensing. To accomplish this, a hydrogen-air torch was installed in the stagnation tank. The primary product of the reaction is water, and a considerable amount of heat is released as well. The ideal concentration of water vapor in the flow is 1% of the total mass, which corresponds to a hydrogen flow rate of 4.5 g/s at the Mach 0.5 case. The torch system consists of a bottle of hydrogen, tubing, a choked orifice, and an igniter. The choked orifice allows the mass flow rate through the torch to be set by the pressure after the bottle regulator. The igniter consists of an electrode and an ignition transformer. A solenoid on the hydrogen line and the ignition transformer are controlled through LabView.

3.1.3.5 Air Line Bleed System The addition of a precisely controlled bleed line off of the main air line was required to conduct active blown grid turbulence generation studies. The system is installed after the filtration system and before the main tunnel gate valve, as shown in Figure 19. This installation allows for the bleed system feed pressure to be set by the building regulator system. Flow is metered via an FLMG-10100 Omega digital rotometer which currently handles up to 100 SCFM of air at 100 psi and 70 degrees F (0.060 kg/s). The bleed system outlet pressure is monitored and corresponds to the grid injection manifold pressure in the case of an active grid. The system is easily modified for higher flow rates or repurposed for controlled seeder injection at the upstream port location shown in Figure 19.

3.1.3.6 Divergent Test Section The design of a diverging test section was motivated by the need to avoid choking due to heat release from an expanding kernel, and to expand the viewing and measurement domain to the same length as the existing square test section. The design of the divergent test section is detailed in the Supersonic Reacting Facility section. The divergent test section shares the same flange pattern and inlet cross section as the current square test section and can be adapted for subsonic use by swapping out the nozzle section for a square nozzle section with a 5×5 cm cross-section. Re-evaluation of the subsonic kernel studies as detailed in the Subsonic Kernel Studies section using this test section for

Mach numbers in excess of 0.3 will commence following current supersonic kernel studies, as well as more detailed evaluation of the turbulence generated by the blown grid.

A visual overview of the current state of the facility is included in Figures 18 and 19 as to complement the summary of modifications to the facility completed over Year 2. The illustrated setup is the currently being used for turbulence evaluation of the active blown jet grid, as shown in Figure 19. The diverging test section to be shared between subsonic and supersonic reacting test facilities is further detailed within the Supersonic Reacting Facility section.

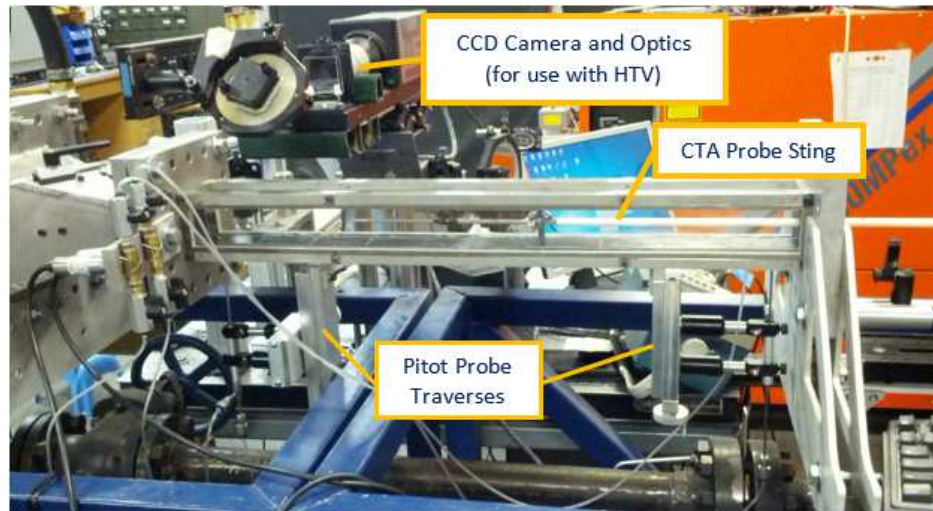


Figure 18: Current status of compressible subsonic facility test section with Year 2 additions

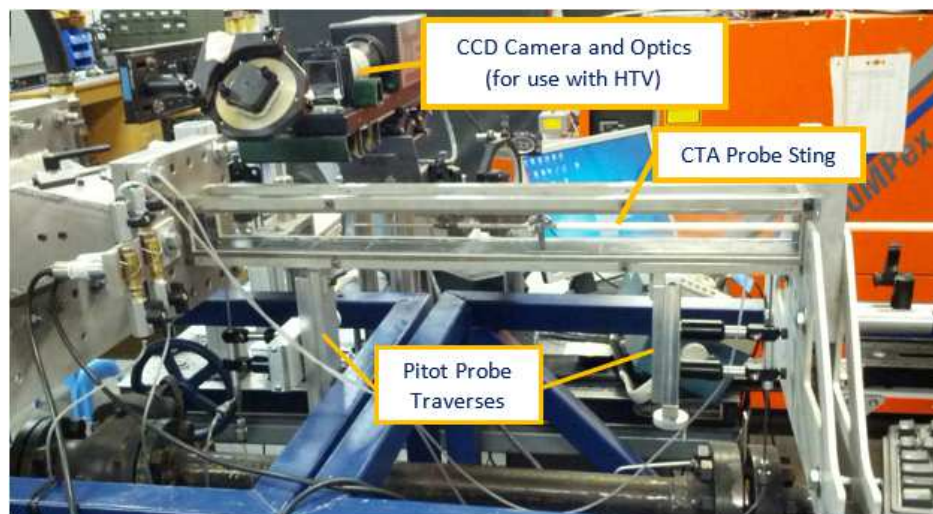


Figure 19: Illustration of bleed system with active blown jet grid installation

3.2 Supersonic Reacting Facility

3.2.1 Introduction

The supersonic reacting facility was initially a preexisting supersonic combustor designed to study premixed flames in a cavity stabilized scramjet. The existing test section was modified by removing the cavity, replacing the existing CD nozzle with a $M = 1.25$ one, and installing electrodes for spark ignition. Initial testing showed that the tunnel was too short, choked prematurely, and that the spark electrodes created flow features that ruined the flame kernels. Subsequent tests were conducted on a new facility based heavily on the Subsonic Compressible Tunnel design. The new tunnel was longer, incorporated a $M = 1.5$ CD nozzle, would utilize laser ignition, had variable divergence to counteract flow deceleration, and was directly comparable to the results in the Subsonic Compressible Tunnel. This tunnel was utilized for initial supersonic studies including CH^*/OH^* chemiluminescence and PIV. It will be shown that this tunnel produced undesirable shock waves at wall-window interfaces. One final modification was made to improve the window-wall interface. This tunnel included a fixed divergence of two degrees; a number chosen to produce near constant mean flow velocity based on previous studies. The facility and various tunnels are discussed below.

3.2.2 Experimental Facility

The experimental facility consists of a fuel and air delivery/measurement system, stagnation chamber, fuel mixing section, a flow straightening section, and the supersonic test section (see Figure 20). The air system has the capability to supply 810 K air at up to 5 MPa. Air metering is accomplished via a calibrated orifice plate meter. The fuel system delivers natural gas (98% CH_4 , 1.5% N_2 , with a balance of CO_2 and higher hydrocarbon) and is metered with a calibrated orifice plate meter. The fuel is delivered through an array of co-flowing jets. The horizontal straightening section was designed to be sufficiently long to produce a homogeneous fuel/air mixture at its exit before entering the turbulence generator (discussed below). After the turbulence generator, a 9.3:1 nozzle contraction was needed to accelerate the flow and to allow sufficient geometric room for the turbulence generator. A converging-diverging nozzle then accelerates the flow to $M=1.5$ in the test section. The test section, shown in Figure 20, is nominally $5 \times 5 \text{ cm}^2$ and 1 meter long. The variable walls were set to one degree divergence to maintain a constant velocity in the test section during kernel growth. The test section is optically accessible on three sides via TSC-4 fused quartz glass.

3.2.3 Supersonic Tunnels

3.2.3.1 $M=1.25$ Tunnel The test section which was used for most of Year 2 in the supersonic tunnel was designed for a Mach 1.25 mean flow, and is shown in Figure 21. The cross-section is $5 \text{ cm} \times 5 \text{ cm}$, matching cross-section as used in the subsonic tunnel. The first attempts at lighting kernels in the tunnel used spark ignition. Two electrodes met at the beginning of the viewable area of the test section, as shown in Figure 22. A gas turbine exciter supplied the electrical energy to produce the spark.

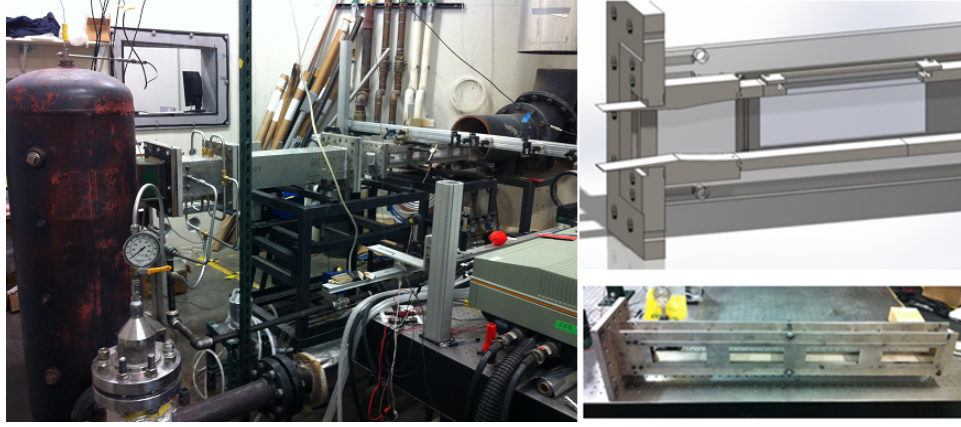


Figure 20: Supersonic reacting facility showing various facility components (left), diverging tunnel section view (top right), and as built diverging tunnel (bottom right).

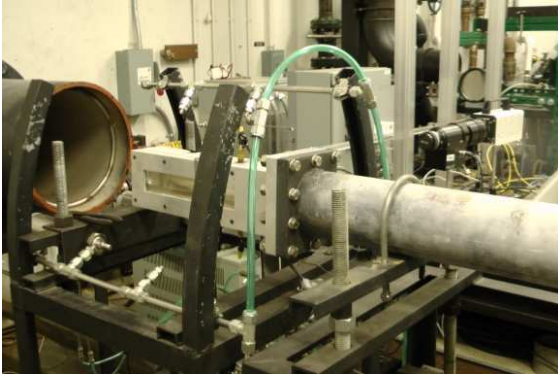


Figure 21: Supersonic reacting facility with $M = 1.25$ nozzle installed.

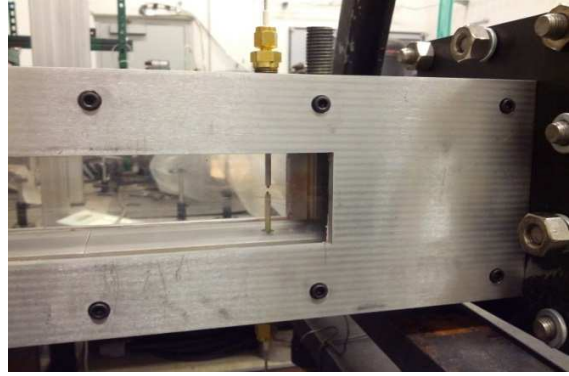


Figure 22: Previous supersonic test section with electrode ignition

3.2.3.2 $M=1.5$ Variable Divergence Tunnel The test section used for flame kernel studies discussed in Section 3.2.1 is rather short, resulting in less than a millisecond of residence time for a flame kernel. A new, longer test section was needed to increase the residence time of the kernels in the tunnel. However, we note that the Fanno effect forces the Mach number in a supersonic channel flow towards unity. It was estimated that for a Mach 1.25 flow, sonic velocity would be obtained in a test section only slightly longer than the existing design. Hence, a new test section was designed with two walls whose angle could be changed to linearly expand the cross-sectional area along the length of the test section. In addition, the Mach number of the test section has been increased to 1.5, which further mitigates the potential to choke the flow due.

A CAD model of the test section is provided in Figure 23, and the installed tunnel is shown in Figure 24. The total length of the test section is 34 inches. The total viewable length is 30 inches, which matches the subsonic-compressible tunnel discussed previously. The test section begins at $5\text{ cm} \times 5\text{ cm}$, as in the subsonic test section, but can expand along its length to $7\text{ cm} \times 5\text{ cm}$ at the exit. This is accomplished by a hinge on each of the two walls that can rotate, which is shown in Figure 25. The hinge is built into the

converging-diverging nozzle. The method of characteristics results for the Mach 1.5 nozzle are shown as a complement to the cross-section shown in Figure 26.

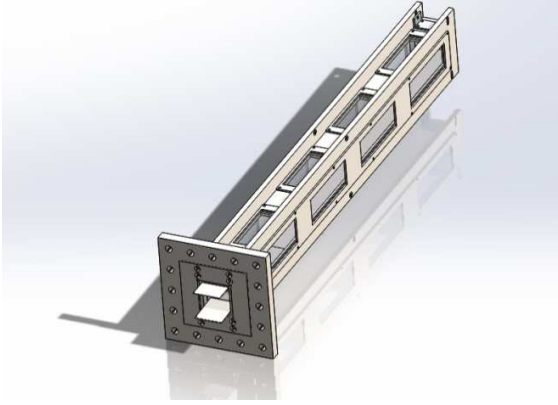


Figure 23: Solid model of redesigned $M = 1.5$ expanding test section.

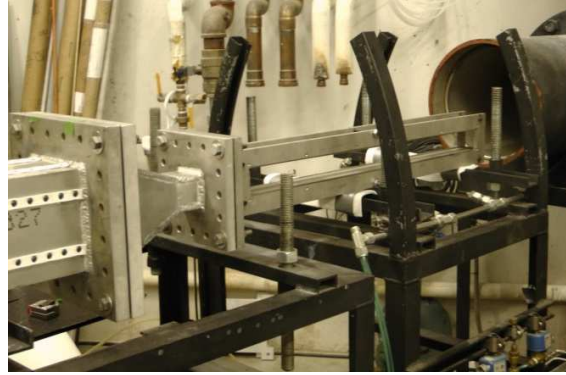


Figure 24: Illustration of installed supersonic test section.

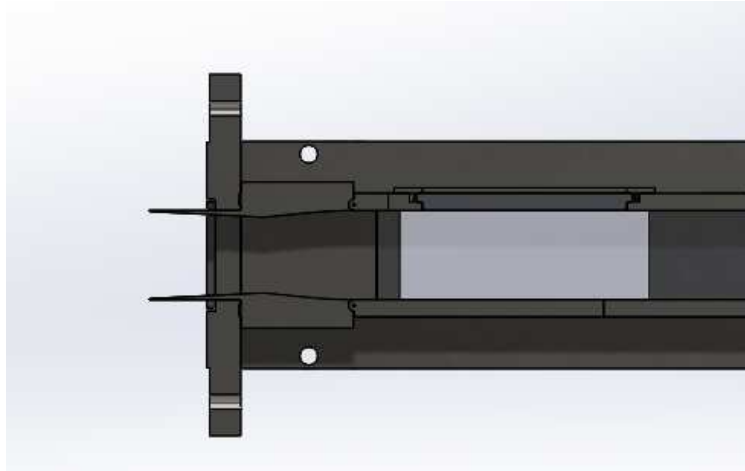


Figure 25: Cross-sectional view of the hinge arrangement of the $M = 1.5$ supersonic tunnel.

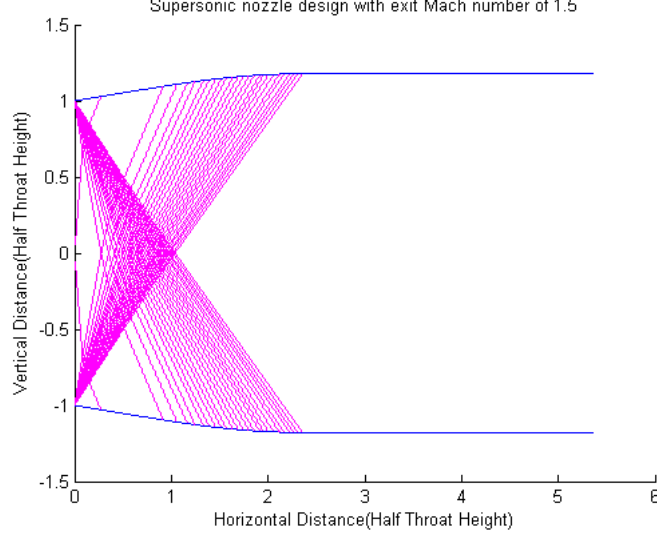


Figure 26: Method of Characteristics representation of $M = 1.5$ nozzle

A simple calculation was used to determine the angle that each wall should be able to rotate through to counteract the Fanno effect. By combining the differential forms of the mass, momentum, and energy conservation equations with the state equation for a calorically perfect gas, and then neglecting heat addition, the following relation in Equation 1 is obtained,

$$\frac{dM^2}{M^2} = \frac{1 + \frac{\gamma-1}{2}M^2}{1 - M^2} \left\{ \gamma M^2 \frac{f dx}{D} - 2 \frac{dA}{A} \right\} \quad (1)$$

where f is the Darcy friction factor, x is the distance along the channel, and A is the cross-sectional area of the tunnel. Because only one pair of walls are expanding outward, the term dA/A can be simplified into dh/h , where h is the length of the dimension that is expanding. The relation can be further simplified by assuming that the expanding walls are at a constant angle, so that $dh = \tan(\theta)dx$. Under the condition that the Mach number should not be changing, Equation 1 takes the form in Equation 2, which can then be simplified to take the form in Equation 3.

$$0 = \frac{1 + \frac{\gamma-1}{2}M^2}{1 - M^2} \left\{ \gamma M^2 \frac{f dx}{h} - 2 \frac{\tan(\theta) dx}{h} \right\} \quad (2)$$

$$\tan(\theta) = \frac{\gamma M^2 f}{2} \quad (3)$$

Using a conservative value for the Darcy friction factor of .015, it is found that the angle that one of the sides should be able to rotate is .675 degrees.

The redesigned test section was fabricated, installed, and tested using schlieren photography as shown in Figure 27 to identify tunnel misalignments which may lead to undesired shock waves in the test section. Several shocks were identified and traced back to the hinge

joint and window seal arrangements. Alternative fabrication and design concepts are being investigated to eliminate these undesired flow features.

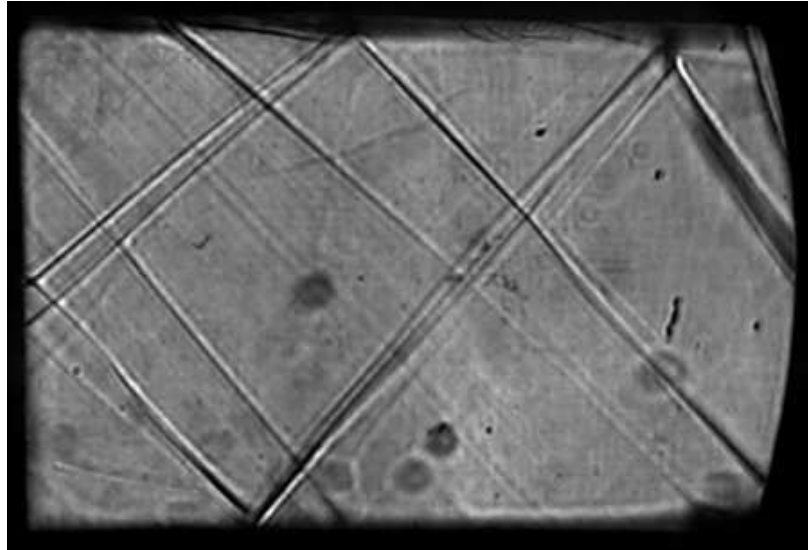


Figure 27: Schlieren photography of shakedown tests in the diverging supersonic tunnel.

3.2.3.3 M=1.5 Fixed Divergence Tunnel The final supersonic tunnel was based on the variable divergence tunnel but had an improved wall-window interface and eliminated the variable divergence joint. Both of these features contributed to several weak oblique shocks within the test section. Their elimination was needed prior to obtaining a baseline set of supersonic kernel measurements; i.e. prior to purposeful exposure to supersonic features such as a well defined shock, jet in crossflow, etc. The new design also incorporated several smaller windows housed in a metal structure for easy access and removal. This design was slightly less flexible in that there was no longer access to the entire tunnel, but proved to be much more robust with little window damage throughout its operation (a problem that plagued the variable divergence tunnel's long windows). The tunnel is shown in Figure 28.

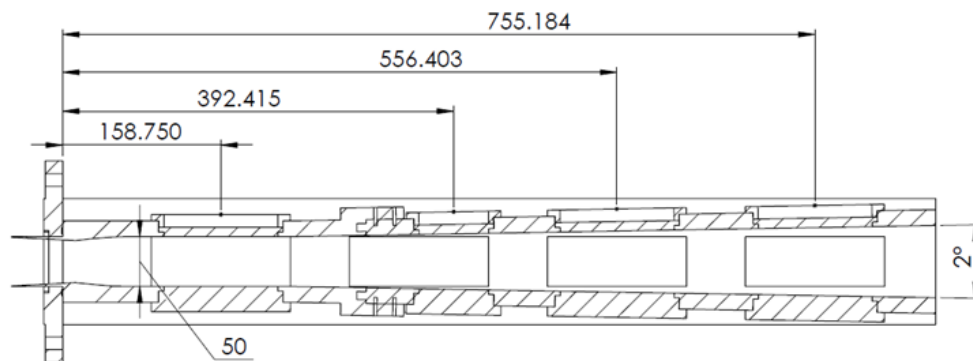


Figure 28: Fixed divergence supersonic tunnel (units in mm).

3.3 Supersonic Turbulence Facility

The supersonic mixing wind tunnel has nozzles for Mach 2.5 and 3.5 flow in the test section. Figure 29 shows an image of the wind tunnel, which has been recommissioned for use through the installation of pressure transducers and thermocouples. Additionally, a fully functional National Instrument CompactRIO DAQ system coupled to a LabView VI been installed. Therefore, characterization of operating flow conditions is now possible. In addition, Figure 30 shows the schematic of the wind tunnel. It is noted that existing components can be added in the test section to facilitate the study of mixing layers and other turbulent phenomena of interest. An example of such a device is the backward-facing step, which is shown in Figure 30.



Figure 29: Recommissioned supersonic mixing wind tunnel with Schlieren system.

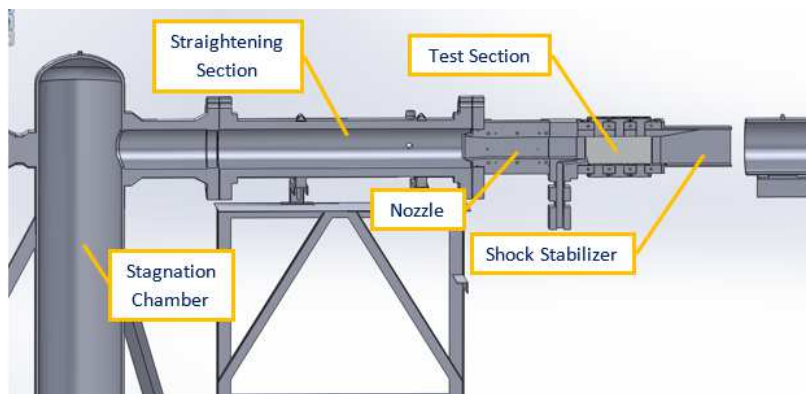


Figure 30: Supersonic mixing wind tunnel schematic.

The Schlieren setup detailed in Section 4.1 has been tested on this facility with and without a backward facing step. These measurements have shown prominent shocks where expected, but also have shown undesired Mach waves throughout the test section. Thus,

a current objectives is to clean the test section of these irrelevant features. Another test performed on this rig is that of an underexpanded jet in a cross flow, for which the Schlieren system has yielded valuable data. The purpose of recommissioning this rig is to provide a robust platform where supersonic phenomena with large pressure and density gradients can be tested. Such conditions cannot be easily tested in the reacting supersonic nozzle. Furthermore, it allows pure turbulence generation to be studied in the realm of compressible flow, allowing examination of fundamental issues of compressible turbulence that are of interest.

3.4 Turbulence Generators

Design and consideration of various passive and active turbulence generation concepts was inspired by past experimental studies. In both cases, prospective configurations were primarily evaluated for the isotropy of the resulting turbulence, resulting intensities, and the magnitudes of resultant Taylor and integral length scales and associated Reynolds numbers for each configuration. As past studies of anisotropic effects of nozzles on turbulence have results that are limited to geometries of specific dimensions [46, 58, 59, 60, 61], and experiments conducted to examine compressible turbulence at a fundamental level are rare [62, 25, 63, 27], such information will have to be ascertained first hand during the characterization of the constructed devices.

Passive grid design was guided by available information of grid turbulence studies traditionally conducted under incompressible conditions at Mach numbers fewer than Mach 0.3. As most studies follow the template set by such workers as Compte-Bellot and Corrsin [46], and Uberoi and Wallace [47] with a primary focus on characterizing turbulence decay using biplane round and square mesh grids of solidities of around 33%, variations of grid geometries that potentially improve on partial anisotropy are limited [49, 64, 65, 66, 67]. For this application, such grids are not as useful for generating high turbulence intensities and large length scales, as this requires an increase in solidity, as well as a comparable increase in anisotropy. Other common geometries include hexagonal grids that produce highly isotropic turbulence at small solidities ($< 30\%$), but produce small Taylor and integral length scales, as well as inhomogeneity when grid solidities are increased to 50% and higher in an attempt to generate higher turbulence intensities [47]. Perforated plates can strike a compromise between rod-based grids and hexagonal grids, as the highly isotropic turbulence generated by hexagonal grids can be merged with the abilities of conventional biplane grids to generate higher turbulence intensities and large length scales. Such grids have been evaluated by Liu [49] successfully, with solidities of 35%, 50% and 60% evaluated to build off of more traditional vane or bar-based grid studies. A general perforated plate design inspired by Liu [49], as well as compressible grid turbulence studies by Zwart [62] is illustrated in Figure 31 for a solidity of 33%. The hole pattern utilized mimics the surfaces of a hexagonal grid, to ensure that isotropy produced by the merging of shear layers coming off of hole surfaces mimics that of a hexagonal grid. The hole size and solidity were also driven by previous studies to ensure spanwise turbulent homogeneity upstream of the contraction [68].

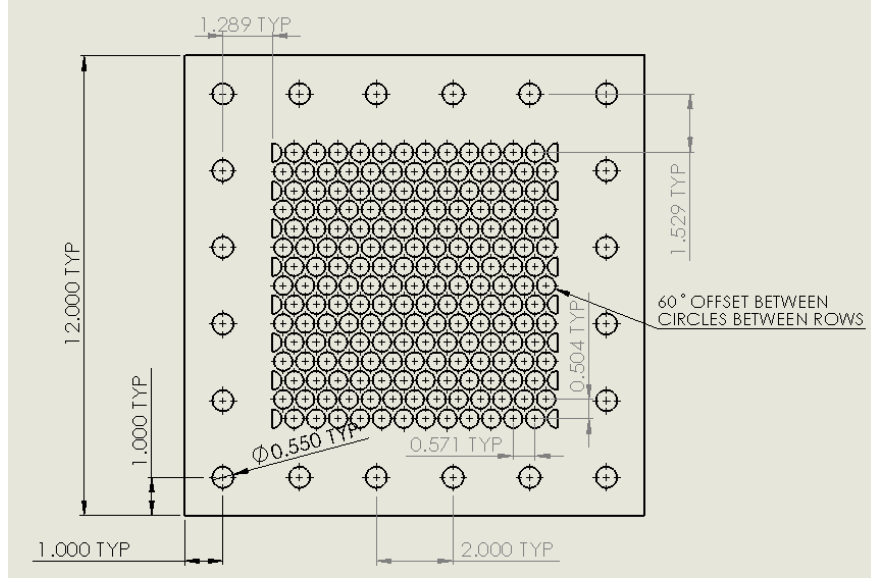


Figure 31: Design of passive grid geometry, with 33% solidity example shown. Units in inches.

Table 4: Properties of the manufactured passive turbulence grids.

Solidity σ	33%	38%	45%
Mesh Size [mm]	5	5	5
	8.9	8.9	8.9
	12.7	12.7	12.7

This general pattern is also easily scalable and can be easily manufactured using a waterjet at varying solidities and plate thicknesses. Characterization of this general geometry at different solidities and plate thicknesses is currently underway to obtain a solution that produces the highest intensities and length scales possible. Figure 32 illustrates an installed perforated plate test article being prepared for hot-wire testing. Note that testing meth-

ods and associated CTA experimental setups are discussed in the Diagnostics Development and Update section of the report. A summary of all manufactured passive grids is given in Tab. 4 and examples are shown in Figures 32 and 38 (a).

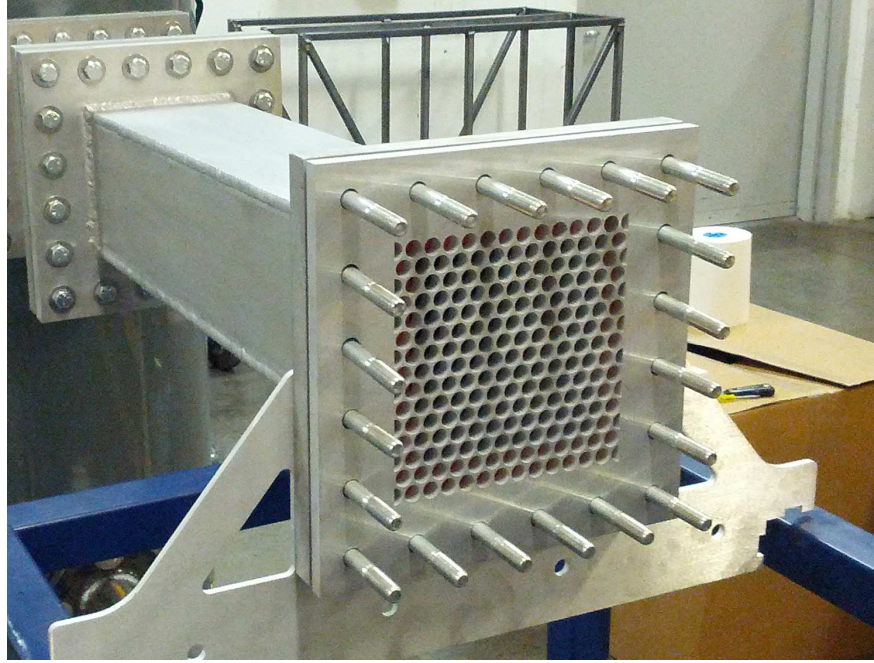


Figure 32: Installed 33% Solidity Passive Grid

The blown-jet grid turbulence generator system used for this study is shown in Figure 33. The design features a bi-plane arrangement of the injector rods of the grid with jet orifices positioned offset of rod crossings to promote generation of closer to isotropic turbulence and homogenization of turbulence closer to the grid [69]. The grid is constructed of 4.76 mm diameter rods that are spaced at a characteristic mesh width M of 24.4 mm. The grid has a geometric solidity of $\sigma = 33\%$ with jet orifices measuring 2.80 mm in diameter. All of the jet orifices face upstream. A second, post-conditioning grid shown in Figure 34 has been installed immediately downstream of the jet grid for bleed cases to break up periodic structures created by the grid under high bleed conditions. The grid is a rectangular perforated plate that halves the characteristic mesh size of the original grid ($M = 12.2$ mm), and has a geometric solidity of 33% with mesh elements that are 2.40 mm wide. The grid system with no bleed and no post-conditioning grid shown in Figure 33 serves as a passive baseline for comparison to a dimensionally similar “RD-35” grid constructed by Lavoie et al. [70], whereas all other data has been collected using the grid configuration shown in Figure 34.

A table outlining the shared inflow conditions and grid settings for both the subsonic and divergent duct configurations is shown in 3.4. Run conditions are reported with respect to grid mesh Reynolds number ($Re_M \equiv \bar{U}_o M / \nu$), where ν is the kinematic viscosity and \bar{U}_o is the mean velocity at the grid. The grid bleed ratio is defined as $\dot{m}_{grid} / \dot{m}_{tot}$. Total mass flow rates are reported for each run in 3.4 for reference.

Table 5: Test matrix of studies conducted with the blown grid. Individual run information is given with the Mach number (Ma) reported at the pitot probe measuring location for a given facility configuration. The grid mesh size M and tunnel stagnation temperature T_o is given as 12.2 mm and 293 K unless specified otherwise.

Config.	Ma	Total \dot{m} (kg/s)	Re_M	No Bleed	10% Bleed	20% Bleed	30% Bleed
Div. Duct	0.0182	0.103	3280	1	2	3	4
Subsonic	0.100	0.103	3280	5	6	7	8
Div. Duct	0.0357	0.206	6580	9	10	11	12
Subsonic	0.200	0.206	6580	13	14	15	16
Div. Duct [†]	0.0285	0.163	10,400	17	—	—	—

[†]Passive grid reference case: $M = 24.4$ mm

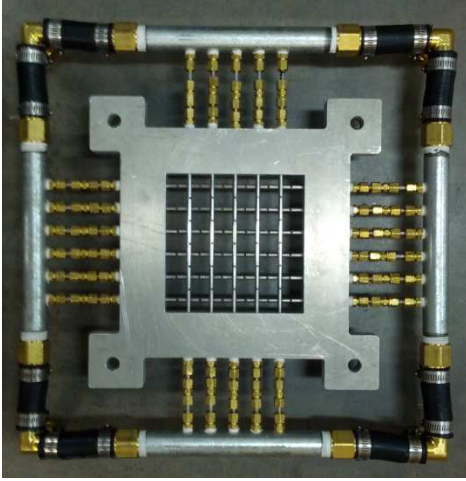


Figure 33: High-bleed active blown jet grid system. The grid with no bleed serves as passive baseline to established data. [70]

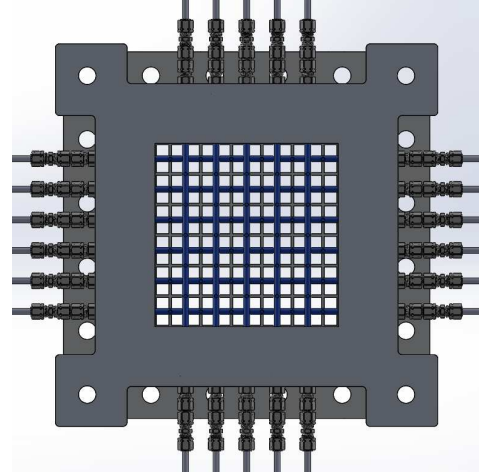
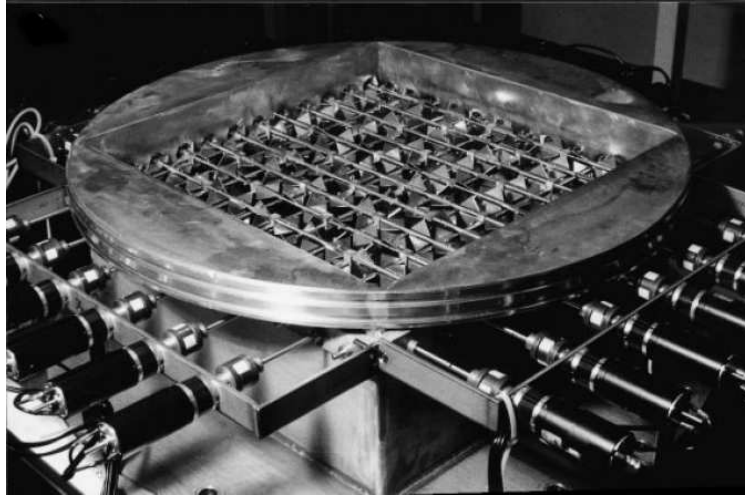


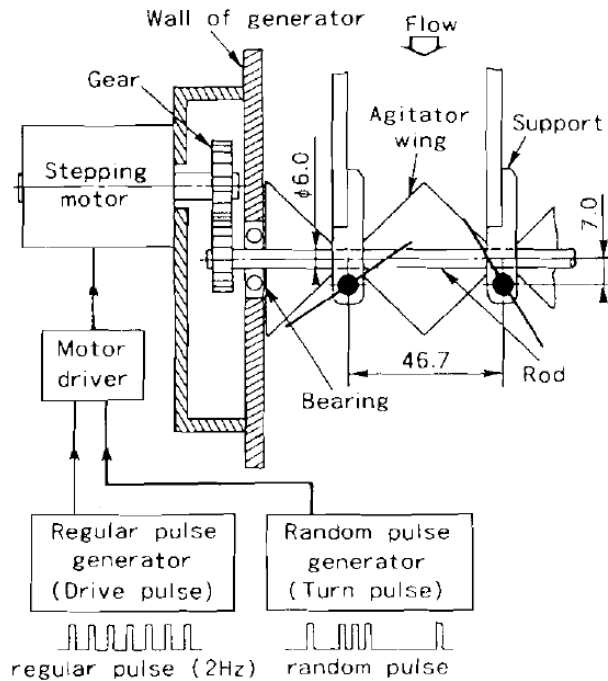
Figure 34: Upstream view of blown jet grid system with post-conditioning grid shown relative to injector rods (blue).

Initial examination of active vane-grid turbulence generation has also been conducted, as development of such systems is required for the generation of turbulence intensities in excess of 15% with Taylor length scale Reynolds numbers ranging from 300-700. As such an assembly will be placed after the straightening section of the wind tunnel where Mach numbers range from Mach 0.03 to 0.06 for test section conditions of Mach 0.3 and Mach 0.7, respectively, past studies such as those conducted by Makita [50], Mydlarski and Warhaft [51] and others [71, 52, 72, 73, 53] are instructive in relating well-understood passive grid scaling laws and resulting turbulence to the initial sizing and design of such vane-stirred grids. From examination of current and past active grid work, an active grid design is currently under development that aims to integrate past successful design elements while attempting to advance the understanding of the technology. Past successful designs all implement triangular winglet elements that are driven by shafts in a grid pattern, which for traditional low-speed applications can be sized accordingly to traditional wind tunnel

grid designs, as discussed previously. These shafts are driven by stepper motors that accept square-wave input signals that either command constant angular velocities over the course of the run, or continuously changing angular velocities according to a randomly generated signal [50]. An example of such a grid is shown in Figure 35 as constructed by Poorte [72], with a schematic representation of how the vanes are driven [50].



(a) Active grid hardware design featuring perforated diamond shaped vanes [72].



(b) Scheme for vane actuation utilizing stepper motors and square-wave control signals [50].

Figure 35: General active grid design and control scheme

The nature of the actively generated turbulence in general exhibits Gaussian-like PDF behavior for u and v fluctuations, and produces 1D energy spectra similar to that of traditional grid turbulence [74]. However, barring some later attempts into understanding how vane driving signal generation algorithms have an affect on the generated turbulence [53, 75], no known significant treatment of the problem associated with connecting the influence of input signals to the generated turbulence has been conducted. In an attempt to further mature active generation technology and to obtain a better understanding of the produced turbulent flow field, a hardware-in-the-loop (HIL) based development track is proposed. The HIL system utilizes MathWorks MATLAB and Simulink software with MathWorks packages that act as board support packages (BSP) that can translate high-level functions in the form of Simulink control layouts into compiled C-code, as well as communicate directly to the hardware under test via a Target PC. The target PC is a machine dedicated to interaction with the hardware under test via installed analog-to-digital (A/D) and digital-to-analog (D/A) drivers. It may also be used to independently simulate additions to the plant model of the hardware under test in real time, due to its independent real-time operating system (RTOS) in the form of MathWorks xPC Target kernel. A schematic layout of the functional relationships of the system is shown in Figure 36 showing how the interdependencies of the proposed HIL system. Additionally, Figure 37 shows a generalized Single Input, Single Output (SISO) representation of the HIL developmental architecture that such a system enables.

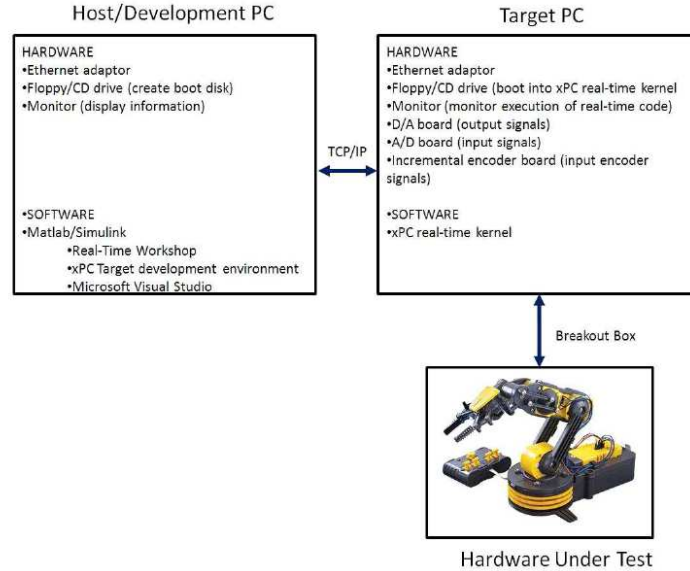


Figure 36: Layout of MathWorks-based HIL development architecture

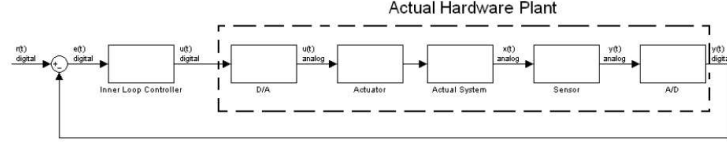


Figure 37: General HIL system architecture in SISO form

In addition to the design of such systems, preliminary calculations relating proposed test conditions to the performance characteristics of the types of strategies presented have been conducted, with certain test conditions highlighted in Tables 6 and 7 for both passive and active generation methods, respectively. As data is limited for in the compressible regime [62], these values give some insight and serve as points of comparison to past studies. Calculations assumed the following turbulence intensity values shown according to typical findings from both passive and active studies, and followed equations derived from turbulent kinetic energy (TKE) equation representations that assume isotropic and homogeneous turbulence [76, 77]. These evaluations are currently in the process of being supplanted by experimental results obtained via CTA methods.

Statistic	M = 0.3	M = 0.5	M = 0.7
u'/U (%)	4.00	4.00	4.00
u' (m/s)	4.09	9.18	17.1
L (mm)	14.5	14.5	14.5
Re_L	4,140	11,437	33,139
Re_λ	166	276	470
λ (mm)	0.713	0.423	0.252
η (μ m)	28.1	13.1	5.9

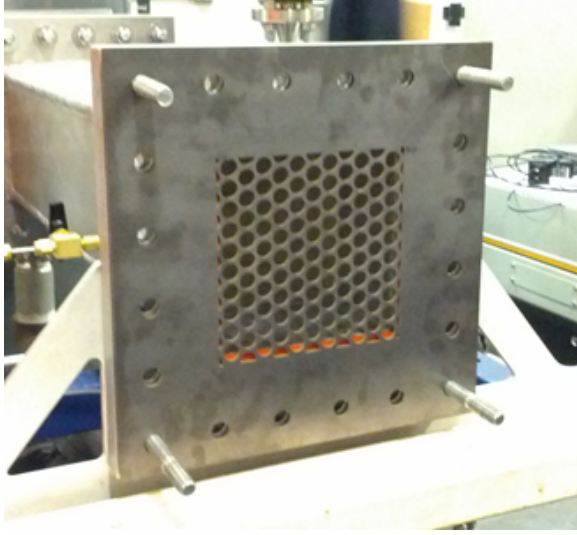
Table 6: Estimated turbulence statistics for proposed passive grid geometry

Statistic	M = 0.3	M = 0.5	M = 0.7
u'/U (%)	15.0	15.0	15.0
u' (m/s)	15.3	34.4	64.2
L (mm)	14.5	14.5	14.5
Re_L	15,526	42,887	124,270
Re_λ	322	535	910
λ (mm)	0.368	0.221	0.130
η (μ m)	10.4	4.87	2.19

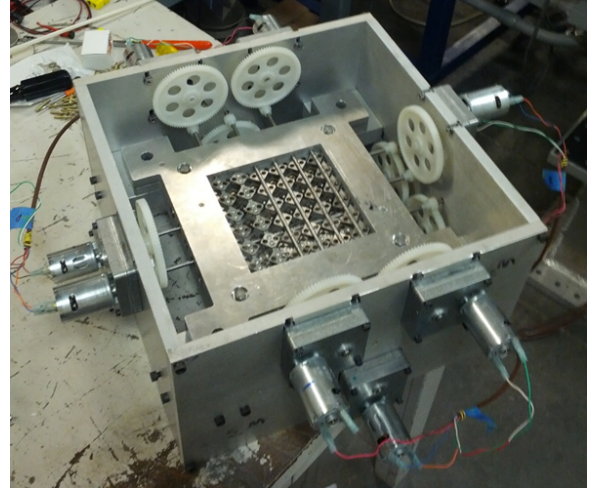
Table 7: Estimated turbulence statistics for proposed active grid geometry

The rotating vane grid consisted of an array of vanes attached to rotating shafts, see Figure 38 (b). The vanes and holes were designed based on results of previous studies with vane grids such as Makita(1991).[78] The shafts were coupled to dc gear motors through a gearbox arrangement. The speed and direction of the motors were controlled through a

LabVIEW interface. In these studies the motors were set to synchronous rotation and the shafts were driven at approximately two rotations per second.



(a) Passive grid



(b) Rotating vane grid

Figure 38: Images of (a) the passive grid turbulence generator and (b) the rotating vane grid turbulence generator.

The active grids generally will result in higher turbulent intensities. The largest turbulent scales depend mostly on the mesh size of the respective grid. In the subsonic flow experiments it was found that high contraction ratios (i.e. 8.5 in this study) after any grid would increase the anisotropy of the resulting turbulence. The small grid in Fig. 39 was designed to fit in the tunnel after the contraction as an attempt to increase isotropy at $0.1 \geq Mach \leq 0.3$. The turbulent intensity measured for this grid is $u'/\bar{U} = 1.5 - 2.5\%$. In contrast, the active vane grid in Fig. 38 (b) was measured to produce $u'/\bar{U} = 10 - 20\%$.

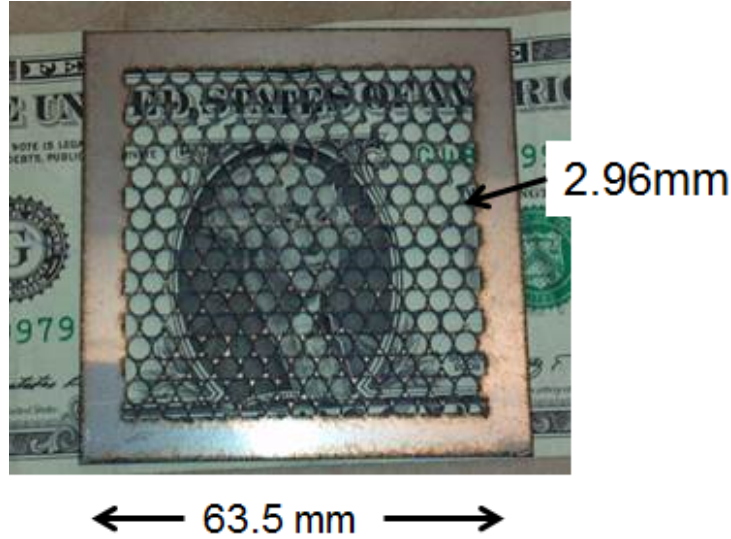


Figure 39: Miniaturized passive grid to be placed after the contraction in the subsonic tunnel.

3.5 Laser-Induced Breakdown Plasma Ignition System

A Woodward gas turbine exciter paired with two electrodes was used to ignite the kernels during the initial flame investigations. The exciter applied a 1 amp current for 50 microseconds. The spark was overly powerful, and had too long of a duration to produce a consistent, round kernel. It created a considerable ball of plasma after the energy was applied. After investigation of other spark ignition systems, it was found that a system which could deliver a spark on the order of 1 microsecond, and that provided enough current to ignite, would be difficult to obtain, or build. Therefore, a non-intrusive laser ignition system was then installed. A Continuum Surelite Nd:YAG laser (195 mJ/pulse at 1064 nm after focusing lens) was used to ignite the flame kernels. The spark laser was focused into the tunnel using a -250 mm lens to expand the original 6 mm beam to ~ 25.4 mm before being focused by a 60 mm lens through a window 50 mm upstream of the test section. These lenses were chosen to prevent damage to the window, which was 2.5 cm from the focal point, to limit the effect of back reflections on the 60 mm lens, and to provide a spot size of $\sim 800 \mu\text{m}$. The entire system was synced with SRS DG645 delay generators and ran at 10 Hz. The produced kernels showed a memory effect based on the ignition power. In particular, a third lobe was seen at high power. This ignition system is shown in Figure 40.

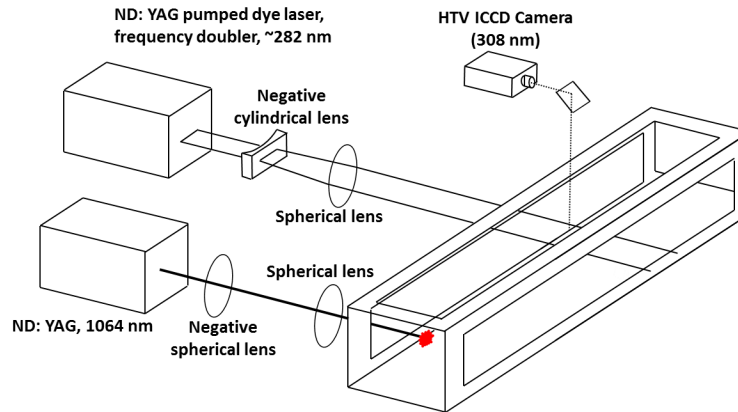


Figure 40: Schematic of OH PLIF and laser ignition system as used on the subsonic facility.

Further improvements to the laser ignition system were made. Next, the Continuum Surelite Nd:YAG laser was frequency doubled (5-30 mJ/pulse at 532 nm after a focusing lens) to ignite the flame kernels. The spark laser was focused into the tunnel using a 40 mm aspheric lens as shown in Figure 41. This ignition system was found to produce reasonably sized flame kernels that behaved as expected.

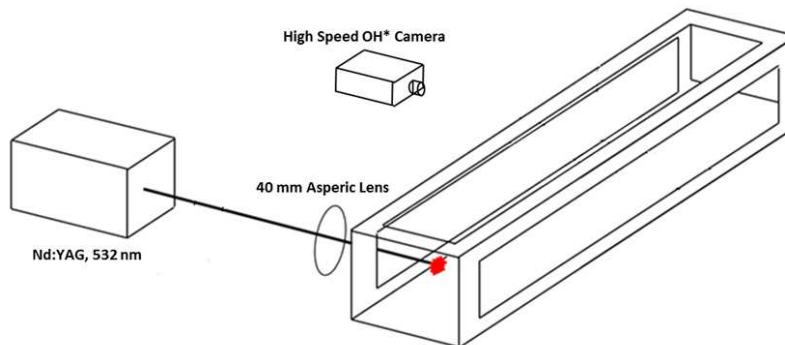


Figure 41: Ignition system for the supersonic reacting facility.

4 Diagnostics

4.1 Constant Temperature Anemometry (CTA)

Direct velocity measurement via hot-wire anemometry is done using a DANTEC StreamLine CTA system, consisting of constant temperature compensation modules for each probe channel, a probe temperature control unit with feedback provided by a thermistor, and a probe calibration unit. A well-characterized jet emitted from the nozzle of the probe calibration unit enables an accurate means of comparing known and measured mean velocities at different points of the flow. The probe calibration unit is also used to construct calibration curves for each probe over a given velocity range, as well as to probe resistance and frequency response properties to ensure accurate temperature compensation and signal processing, respectively. A National Instruments BNC-2090 A/D converter serves as the connection between the measuring equipment and the PC, which is equipped with DANTEC StreamWare software. The StreamWare software enables on-site data reduction to output calibrated velocity data during a given run. Figure 42 shows a labeled representation of the system implemented during the experiment.

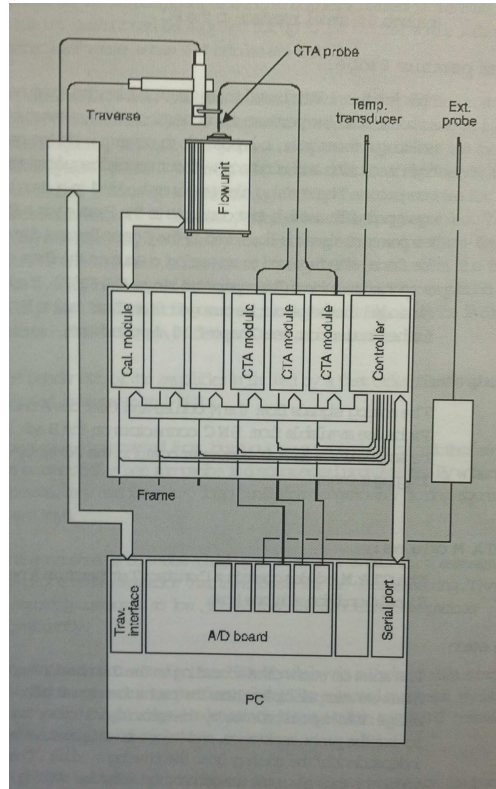
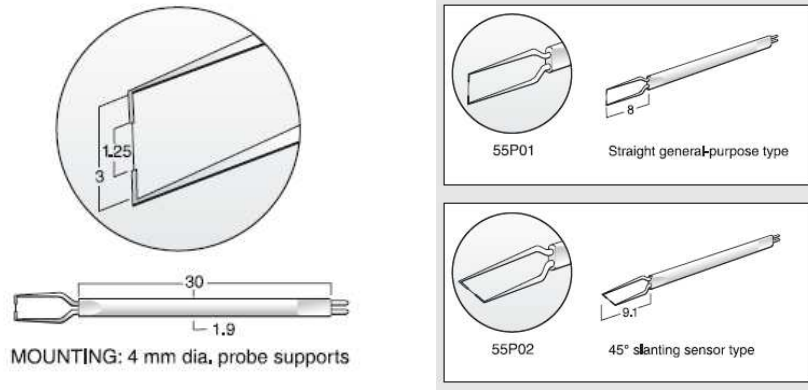


Figure 42: Schematic layout of DANTEC StreamLine CTA system with illustrating functional relationships between various components. Note that the "flow unit" calibration module may also be supplemented by in-situ calibration methods that involve direct velocity measurement in the facility relative to a probe reading [79]

The measurement strategy includes using a combination of conventional Single-Normal (SN) element probes, as well as Single-Yaw (SY) element probes, with the SY filament oriented at 45° from the probe axis. DANTEC 55P01 SN probes and 55P02 SY probes were selected for their robustness in high-speed flows [80] and high measurable bandwidth [81], both are gold plated tungsten wire probes. Both probes with relevant dimensions are illustrated in Figure 43.



(a) General dimensions for Dantec 55P-series gold-plated single channel probes (b) SN 55P01 and SY 55P02 45° gold-plated probes

Figure 43: General dimensions of selected DANTEC hot-wire probes for studies in the compressible regime [82].

A combination of the use of SN and SY probes enables measurement of quantities primarily dependent on fluctuations along the mean flow direction (u), as well as in the v and w directions. Information from a SN probe is sufficient to obtain mean velocity profiles across a test plane, Taylor and integral length scales, one dimensional energy spectra and marginal PDF information for u [83]. This is justified, as the measured velocity magnitude from an SN probe can be assumed to be primarily in the u direction, as the velocity fluctuations are small relative to the mean, even for turbulence intensities as high as 15% [57]. However, an SY probe is necessary to measure velocity fluctuation components not oriented with the mean flow with certainty, as the angled probe configuration shown earlier in Figure 43 enables decomposition of velocity components by virtue of coordinate transformation [80, 57]. Figure 44 illustrates how this is conducted using an SY probe orientation of known angle α_o from the mean flow. The coordinate transformation for decomposition of the measured velocity vector with application of associated probe pitch and roll calibrations is contained in Chapter 5 of Bruun [57].

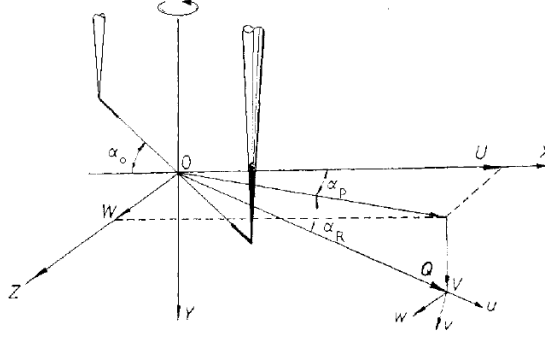


Figure 44: General coordinate system for SY velocity decomposition. Note Q , α_o , α_R , and α_p are the measured velocity vector, wire orientation angle, probe roll angle, and probe pitch angle, respectively, with a positive roll angle defined by the arrow about the Y axis. [84]

From examination of such geometry, it can be seen that common multi-element probes such as X-wire and three-element probes are natural extensions of SY probes, with the convenience of having multiple data points within close proximity of each other at a point in space. The feasibility of using X-probes and three-element probes in a high speed flow was examined. There is only a small amount of successful implementations for this type of flow, as found in a survey of multi element hot-wire methods in compressible and supersonic flows conducted by Smits and Dussauge [85]. Common difficulties encountered included difficult to quantify cross flow effects from wakes emanating from wires, as well as vibrating probe prongs which added an additional velocity component to the hot wire measurements that could not be easily removed during Reynolds decomposition of the raw velocity data [80, 57].

Additional examination of past turbulence measurement concepts yielded a rotating SY probe method that could accurately resolve all three velocity components in a statistically steady flow by rotating through a prescribed set of angular positions [86, 84, 87]. The method also incorporates a variation of the calibration procedure for single angular position SY probe data collection that allows for wire heat transfer model variations to be experienced at different angles. The method has also proven successful in measuring three-dimensional velocity fluctuation quantities such as the full Reynolds stress tensor in non-ideal measurement scenarios where probe access is challenging, such as in the curved duct experiment of De Grande [84]. Such a method yields the highest probability of success, given the combined challenges of limited access and a high-speed flow environment. To achieve accurate hot-wire measurement, a custom traverse system which integrates with the DANTEC StreamLine system and LabVIEW-based modular DAQ system has been designed. This produces synchronized traverse patterns and data collection points that share common time stamps. The traverse system assembly is also modular, and is referenced to tunnel geometry to ensure the capability to obtain a consistent traverse plane zero before each run. Figure 45 illustrates the constructed traverse assembly in action with an installed SN probe and thermistor during facility shakedown.

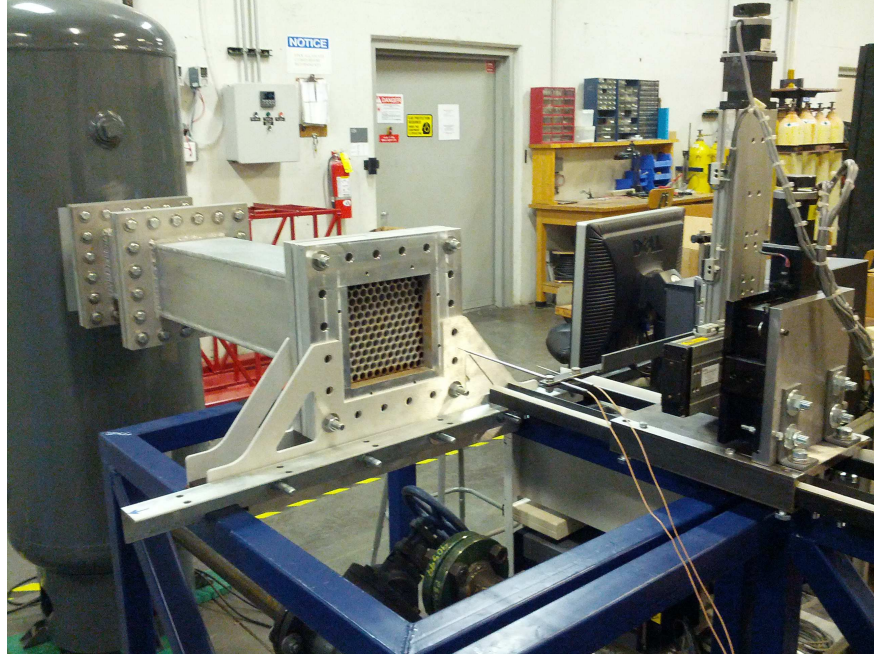


Figure 45: Constructed traverse assembly in use during test run of CTA systems

The general framework established by Compte-Bellot and Corrsin [46] for passive grid characterization has been adopted, extended to the characterization of an evolution of configurations. The configurations are as listed below, with characterization occurring in the following sequence.

- *Passive Grid Characterization:* This configuration consists of only a passive grid, with installed duct extensions to ensure that the centerline mean velocity does not decay with downstream distance, as seen in a jet. Such data from grids of different solidities is to be compared with past studies [49]. A similar configuration has been utilized for initial active grid configuration.
- *Test Section Characterization:* The configuration consists of an installed passive grid, with the square nozzle component and test section installed. This allows for measurements of anisotropy and incorporates compressibility effects that will be experienced by the flame kernel. Such data sets will also provide more insight for detailed design of measures to reduce anisotropy. Measurements are facilitated through use of a modified test section, which replaces top and bottom window panes as seen earlier in Figure 15 with acrylic panes and machined access ports.

As mentioned before, the measurement of the evolution of scales, spectra and Reynolds stresses was accomplished using Constant Temperature Anemometry (CTA) via effective velocity signals from Single-Normal (SN) and Single-Yawed (SY) probe measurements at shared centerline traverse points shown in Figures 3 and 11. The SN-SY technique is a single channel probe method that has been demonstrated in statistically stationary flows

with turbulence intensities as high as 30% [88]. The SN-SY method is described briefly as follows.

The effective velocity V_e is the measured velocity obtained via calibration from how much voltage is required to hold a CTA probe element at constant temperature at a specified orientation described by wire pitch (α), yaw (β) and probe stem roll (γ) angles. The diagram in Figure 46 shows how these angles are defined in relation to the coordinates system of the flow facility [88]. The relation of this voltage to velocity requires the empirical evaluation of wire yaw and pitch response coefficients k and h , respectively across the expected wire orientation and effective velocity ranges of interest. These coefficients are necessary to determine the response of a CTA probe element with respect to the wire coordinate system as shown in Equation 4, where subscripts N , T , and B denote unit vectors that are normal, tangent and bi-normal to the wire, respectively as shown in Figure 46. The effective angle calibration procedure described by Bruun, et al. [89] has been used to evaluate k and h for $0^\circ < \alpha < 85^\circ$, $0^\circ < \beta < 85^\circ$ at $2 \text{ m/s} < V_e < 90 \text{ m/s}$ for both SN and SY probes.

$$V_e^2 = U_N^2 + k^2 U_T^2 + h^2 U_B^2 \quad (4)$$

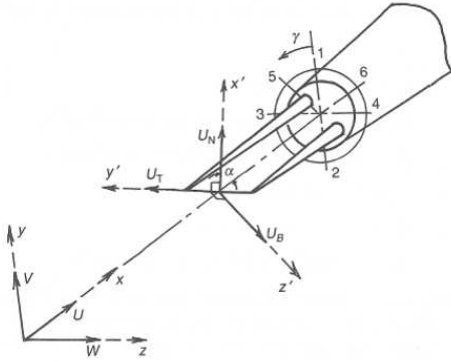


Figure 46: SY Probe wire-fixed coordinate system (x', y', z') in relation to the tunnel coordinate system (x, y, z) [57].

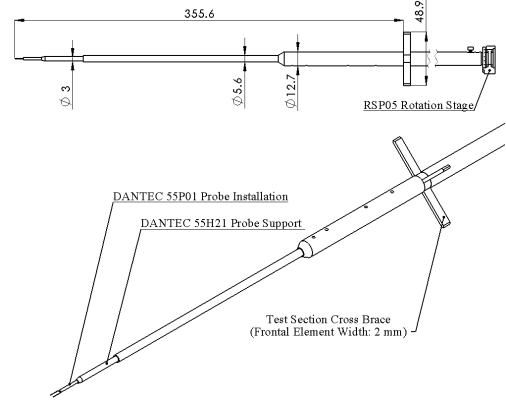


Figure 47: Schematic of rotating CTA probe sting shown in subsonic facility configuration (Units in mm).

The decomposition of the signal content of the effective velocity measurement of a single CTA element is accomplished by use of a coordinate transform of Equation 4 to the probe stem coordinate system at a specified probe orientation [90]. The resultant expression is shown in Equation 10, where the coefficients $A_i = f(\alpha, \beta, \gamma, k, h)$. The SY probe has a fixed yaw angle of $\alpha = 45^\circ$, and is rotated about the probe axis using a rigid ceramic sting shown in Figure 47. A X-shaped cross-brace supports the sting in the center of the test section for both divergent duct and subsonic facility configurations. Precise angular positioning of the SY and SN probes is accomplished using a Thor Labs RSP05 rotation stage at the rear of the sting that is accurate to $\pm 0.5^\circ$.

$$V_e^2 = A_1 U_1^2 + A_2 U_2^2 + A_3 U_3^2 + A_4 U_1 U_2 + A_5 U_1 U_3 + A_6 U_2 U_3 \quad (5)$$

Further decomposition of the effective velocity signal can be accomplished by separating each velocity component into mean and fluctuating components as shown by Buresti and Di Cocco [90], where expressions for the mean and variance of the effective velocity to second order for a probe oriented parallel to the mean flow direction (\overline{U}_1) are shown in Equations 6 and 7, respectively. The coefficients B_i and C_i share the same functional dependence as A_i , and result from the series expansion of the Reynolds decomposition of Equation 5. Numerical subscripts are as they appear in Buresti and Di Cocco for reference.

$$\overline{V}_e = B_1 \overline{U}_1 + B_4 \left(\frac{\overline{u_2^2}}{\overline{U}_1} \right) + B_5 \left(\frac{\overline{u_3^2}}{\overline{U}_1} \right) + B_6 \left(\frac{\overline{u_2 u_3}}{\overline{U}_1} \right) \quad (6)$$

$$\overline{v_e^2} = C_1 \overline{u_1^2} + C_2 \overline{u_2^2} + C_3 \overline{u_3^2} + C_4 \overline{u_1 u_2} + C_5 \overline{u_1 u_3} + C_6 \overline{u_2 u_3} \quad (7)$$

Determination of Reynolds stresses via Equation 7 was accomplished obtaining SY V_e records at six angular locations ($0^\circ, 45^\circ, 90^\circ, 180^\circ, 270^\circ, 315^\circ$), where 0° is denoted by the y-axis of Figure 46. Noting the values of C_i at each position, a signal processing routine is used to decompose the SY records into Reynolds stresses. These Reynolds stresses are then applied to Equation 6 to solve for \overline{U}_1 using the SN measurement record.

All measurements were conducted using a DANTEC StreamLine 90C10 frame with 90M10 constant-temperature bridge modules. DANTEC 55P01 and 55P02 gold-plated tungsten SN and SY probes, respectively were used. Each probe type has an active sensor width of 1.5 mm and diameter of 5 μm . Probes were calibrated using a DANTEC 90H02 automated laminar jet unit and were set at an overheat ratio of 0.8, resulting in a sensor over temperature of 220°C . This ensures that any fluctuations due to temperature for any measurement do not exceed $0.002 \text{ V}/^\circ\text{C}$, or a maximum error 0.1% of the voltage associated with the lowest mean effective velocity measured [91]. Data was sampled at 50 kHz and 250 kHz and low-passed at 30 kHz and 100 kHz for divergent duct and subsonic data points, respectively using an analog 5th order Butterworth low-pass filter incorporated in the StreamLine frame. In response to the inability to fine-tune the low-pass analog filter settings and lack of prior knowledge of the turbulence signal frequency bandwidth for a given grid bleed setting, oversampled raw records were then downsampled to a desired new Nyquist frequency. These downsampled records were then low-pass digital filtered using a zero-phase 20th order IIR-type Butterworth low-pass filter before any further processing [92]. This eliminated inter-record aliasing with signal content identified as being non-turbulent by spectral analysis of the original oversampled SN records. Filtering criteria derived from the SN measurements were then applied to all SY records at a given shared traverse location and test condition.

Data collection and conversion was accomplished using a PC equipped with DANTEC StreamWare software and a NI 6023E 12-bit DAQ board. Records collected for spectral analysis via the SN probe contained 8.3×10^6 samples. This enabled a FFT frequency resolution of 1 and 5 Hz for divergent duct and subsonic data, respectively. At these resolutions and sample lengths, 300 individual independent records could be extracted from the sample and windowed using 50% overlapped processing. Energy spectra were then computed using the Welch algorithm [93] while applying a Hanning window, resulting in a maximum possible error of all spectral-derived quantities of 6%. Use of the Welch method has been validated by confirming that the hypothesis of statistical stationarity is accepted at the 5% significance

level using a reverse arrangement test to evaluate all SN records [92]. Statistical stationarity and the associated lack of any propagating periodic structures could not be initially assumed due to the unknown nature of the high-bleed blown jet grid.

The SN-SY measurement method is well-suited for determining the Reynolds stresses of a highly turbulent, statistically stationary flow. However, in a non-isotropic flow field, only scales and spectra along the mean flow direction can be directly evaluated from SN records with associated error assessment. Nonetheless, known confidence intervals and error estimates can be made by using isotropic or RDT relations in the incompressible and subsonic cases respectively. Sampling criteria must then be selected to ensure that individual raw data records at a particular rotation angle contain the required signal content assuming amplitude domain analysis could be conducted. The sampling of 1.0×10^6 samples per rotation angle at 50 kHz for all SY measurements ensures that all Reynolds stress measurements are statistically accurate to 3% at a confidence level of 98% for turbulence intensities of 20% and lower.

4.2 Hydroxyl Tagging Velocimetry (HTV)

A new velocimetry technique has been developed by the Vanderbilt University element of the of the premixed flame structure in compressible flow portion of the program for use in flows with high backgrounds of OH expected in turbulent premixed combustion. Previously, hydroxyl tagging velocimetry (HTV) has been used to make time-of-flight measurements in a variety of flows [94, 95, 96, 97]. While these approaches have proven successful in moist air and post-flame zones, measurements in reacting regions, such as the kernel flame fronts of interest in this study, has proven difficult due to interference from nascent OH molecules. Therefore, a variant of the HTV method has been developed utilizing two-photon dissociation of water with 2×248 nm photons from a KrF laser which results in vibrationally excited OH molecules [98]. Like previous HTV measurements, an excimer (either KrF or ArF) laser is used to dissociate H_2O to create OH photofragments. In this application, OH is used as a tracer due to its relatively longer lifetime compared to higher vibrational states since the concentration of OH ($\nu = 1$) is only 5-10% of the total OH at flame temperatures.

The lifetime of the OH ($\nu = 1$) tracer and its yield vs. equivalence ratio, ϕ , are shown in Figures 48 and 49 in a H_2 -air flame formed by a 12.5 mm Hencken burner under laminar conditions. As seen in 48, the half-life in lean flames at $\phi = 0.69$ is $8 \mu s$. In rich flames, the half-life at $\phi = 1.23$ the half-life is $6 \mu s$ and decreased to $2 \mu s$ at $\phi = 2.36$. In Figure 49, at both delay times the observed signal peaks around $\phi = 1$ where there is a maximum in temperature and H_2O number density ($[H_2O]$). In lean flames, the OH ($\nu = 1$) signal follows the temperature and $[H_2O]$ dependence vs. ϕ . For rich flames, the signal at $1 \mu s$ delay is significantly less than at 50 ns. The reduction in signal and lifetimes under rich conditions is caused by chemical reactions between the OH tracer and excess H_2 as reported in previous HTV papers [94, 95]. While the tag lifetime of the OH ($\nu = 1$) tracer is less than traditional HTV, it still has sufficient life time to make velocity measurements in fast flows (>100 m/s) where delay times around $2 \mu s$ are typically used [99, 100].

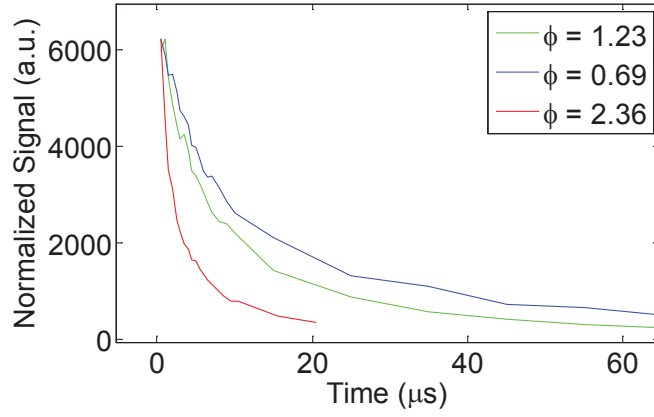


Figure 48: Lifetime of OH ($\nu = 1$) tag at various ϕ in a laminar H_2 -air flame formed by a 12.5 mm dia. Hencken burner ($Re_D = 970$, $x/D = 3.6$).

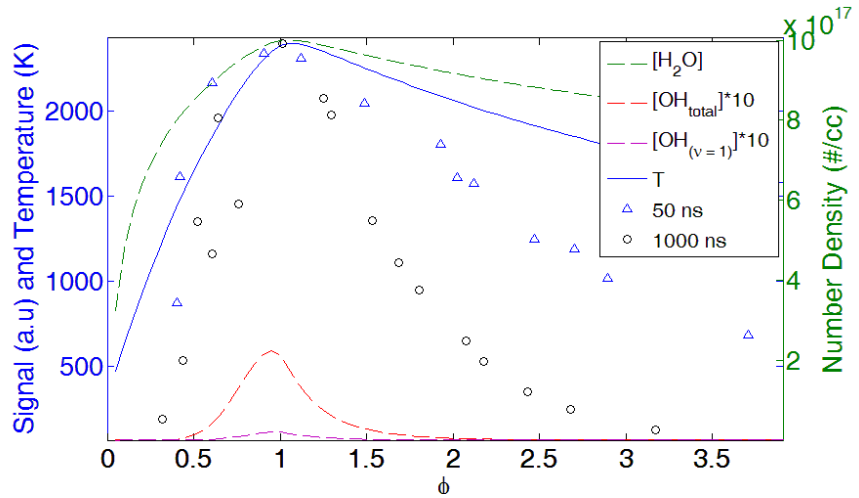


Figure 49: Signal of the OH ($\nu = 1$) tag line vs. ϕ at a time delay of 50 ns and 1 μ s in a laminar H_2 -air flame over a 12.5 mm dia. Hencken burner ($Re_D = 750$ -925, $x/D = 6.25$). Equilibrium values of temperature and number density of H_2O , OH, OH ($\nu = 1$) are shown for comparison.

Velocity measurements were obtained in a turbulent ($Re_D \approx 10,250$) H_2 -air jet flame formed by a 12.5 mm Hencken burner at a high flow rate. A co-annular methane-air pilot flame stabilized the main jet flame at four or five discrete locations at the flame base at this condition. The mean velocity profiles are shown in Figure 50 with a peak velocity of ~ 40 m/s determined from mean undelayed and 10 μ s delayed images by determining the displacement of each pixel column between the two images. The profiles are not symmetric due to the asymmetric turbulent flame anchoring. To obtain these profiles, a mean delayed image (500 single-shots) was used both with and without subtracting an OH ($\nu = 1$) background (i.e.

the KrF laser was not fired); both the raw mean image and the mean image with background subtraction can be found in Figure 51. Overall, there is very good agreement between the two velocity profiles in /refvel indicating that the technique is capable of obtaining velocity data even without background subtraction. With a peak velocity of ~ 40 m/s and a delay of $10 \mu\text{s}$, the maximum displacement is only $\sim 400 \mu\text{m}$ (~ 3.5 camera pixels). The increased jaggedness of the velocity profile towards the edges of the flame is primarily a result of the laser beam expansion which creates a reduced OH ($\nu = 1$) photofragment concentration due to the intensity squared dependence of the two-photon dissociation processes. For comparison, both mean and single-shot images taken in the same flame at $2 \mu\text{s}$ delay are shown in Figures 52 and 53. For the $2 \mu\text{s}$ delay time typically used in high speed flows (>100 m/s), the SNR is higher and single shot measurements can be made especially in regions where there is not significant entrainment of cold and/or dry air or pockets of concentrated unburned fuel such as inside a flame kernel. With this new technique, Vanderbilt can obtain velocity measurements in new conditions without requiring any additional hardware.

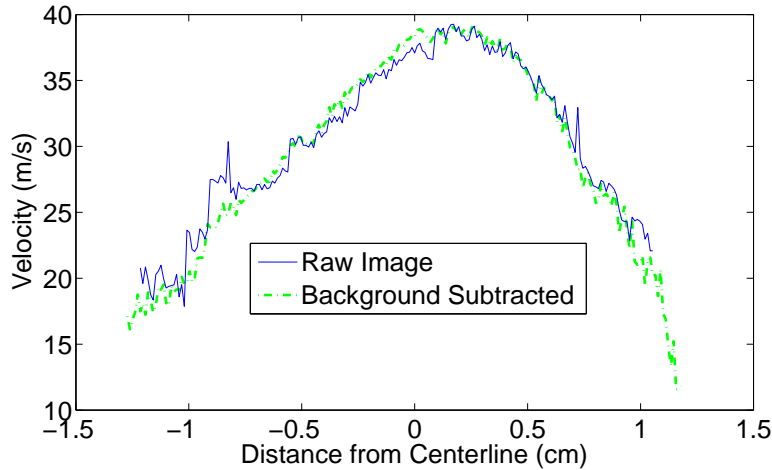


Figure 50: Velocity comparison at $10 \mu\text{s}$ delay both with and without background subtraction in a $\phi = 0.77$ H_2 -air turbulent jet flame produced by a 12.5 mm dia. Hencken burner with a CH_4 -air annular pilot ($Re_D = 10250$, $x/D = 8.25$).

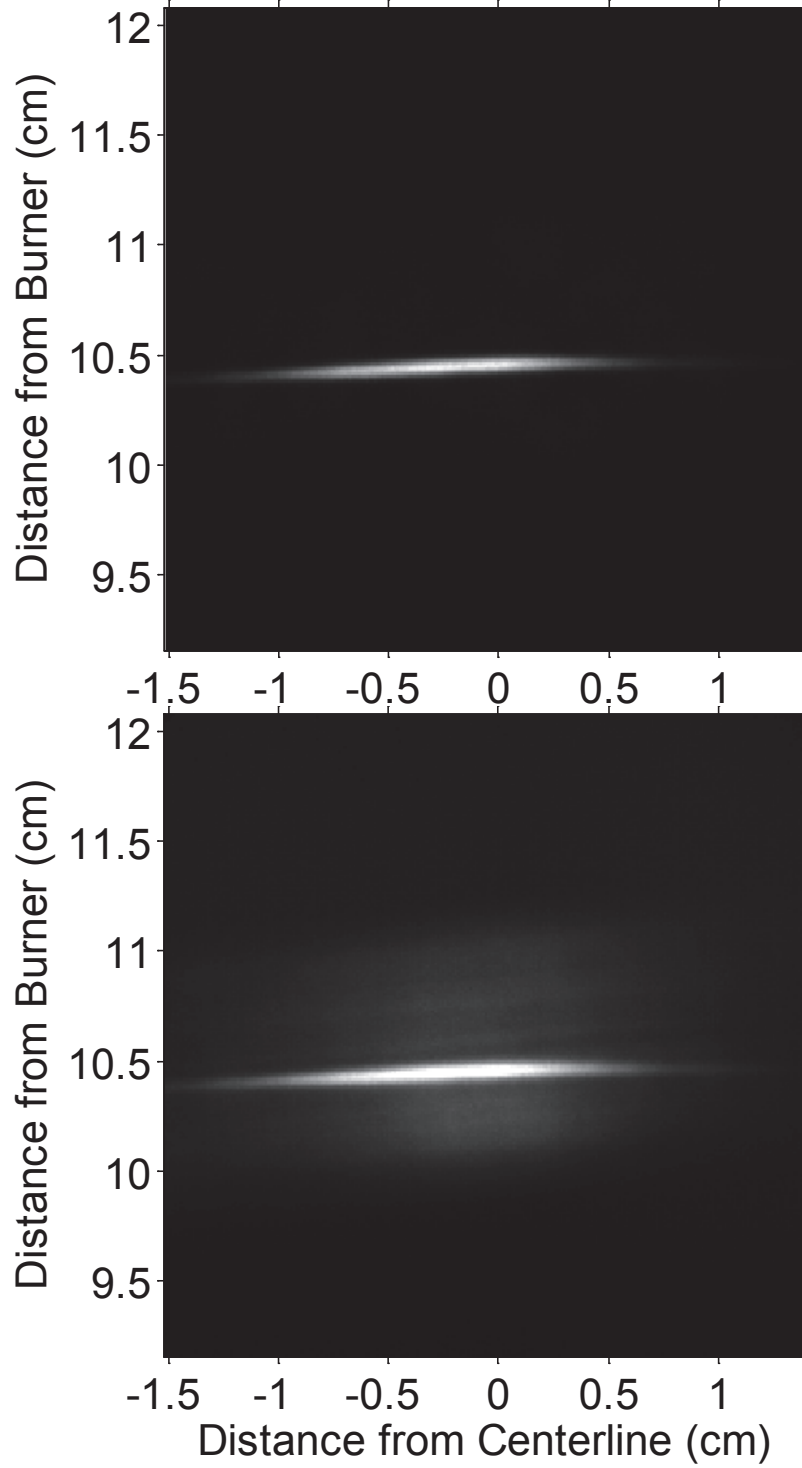


Figure 51: Mean (500 single-shots) OH ($\nu = 1$) image in a $\phi = 0.77$ H_2 -air turbulent jet flame both with (top) and without (bottom) background subtraction with a $10 \mu s$ delay. H_2 -air turbulent jet flame produced by a 12.5 mm dia. Hencken burner with a CH_4 -air annular pilot ($Re_D = 10250$, $x/D = 8.25$). Images used to determine velocity profiles in Figure 50.

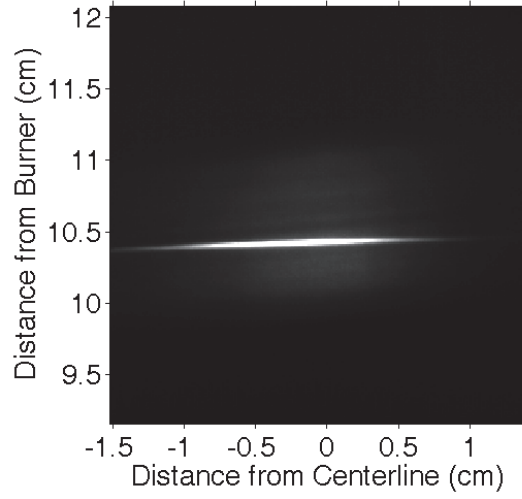


Figure 52: Mean (500 single-shots) OH ($\nu = 1$) image in a $\phi = 0.77$ H₂-air turbulent flame with a $2 \mu\text{s}$ delay. H₂-air turbulent jet flame produced by a 12.5 mm dia. Hencken burner with a CH₄-air annular pilot ($Re_D = 10250$, $x/D = 8.25$).

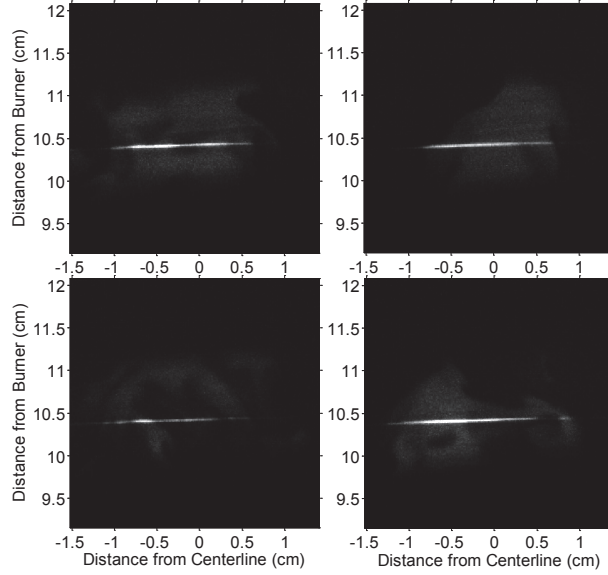


Figure 53: Single-shot OH ($\nu = 1$) images in a $\phi = 0.77$ H₂-air turbulent jet flame with a $2 \mu\text{s}$ delay. H₂-air turbulent jet flame produced by a 12.5 mm dia. Hencken burner with a CH₄-air annular pilot ($Re_D = 10250$, $x/D = 8.25$).

4.3 Particle Image Velocimetry (PIV)

Due to the fragility of the hotwire anemometer in supersonic flows, another method of calculating velocity statistics was needed for these cases. In these cases, a two-dimensional PIV system was used to produce the turbulent statistics. Two frequency doubled Big Sky Nd:YAG lasers (20 hz) provided particle illumination and a Photron SA5 camera operating at 60 frames per second captured image-pairs. See Figure 54 for a cartoon showing an example laser and camera arrangement. One dark image per image-pair was removed in post processing. Mean and rms velocities were calculated from image pairs via Lavision's DaVis software. During this program, PIV was used only for velocity measurements only in the supersonic experiments. For those studies, the time between laser pulses was set to 600 *ns* so that the particles moved approximately 6 pixels (1/4 an interrogation window) on average between images. This value was selected to optimize the measurement by making a trade off between in-plane loss-of-pairs error and pixel resolution error. DaVis's two-image cross correlation with pixel by pixel interpolation has an estimated particle displacement error of 0.1 pixels. For these conditions, this yields an error of approximately 5.8 to 10.8 *m/s* on the instantaneous velocity vectors; however, additional error due to particle drag will be present. The sheet size was 50 *mm* wide by 1 *mm* thick with 50 μm per pixel resolution. Assuming off-axis homogeneity, the resultant out-of-plane rms velocities were small enough for loss-of-pair error due to out of plane motion to be negligible. The sheet entered the test section through the top window and was imaged from the side window. A seeding system mixed a separate air stream with seed particles and injected the mixture upstream of the fuel inlet. A control valve was used to vary the flow rate through the fluidized bed seeder. The seeded air then mixed with the main air via injection through counter-flowing jets which ensured a homogeneous mixture of seeding particles at the end of the horizontal stagnation chamber. The particles used in these studies were 1-2 μm Al_2O_3 which were sufficiently small to resolve motion with spectral content under 4000 Hz.

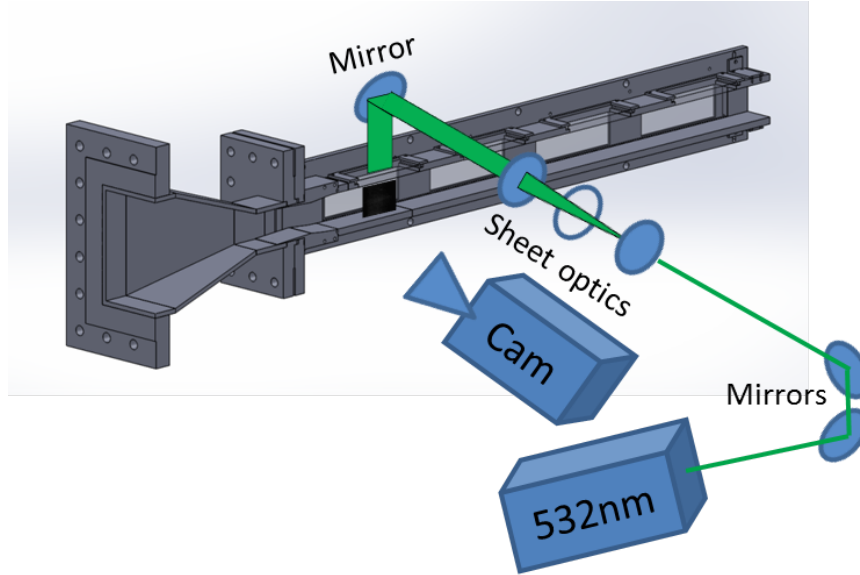


Figure 54: Arrangement of PIV laser and camera installed on the supersonic variable-divergence tunnel.

4.4 Schlieren Photography

The Schlieren technique has been incorporated to assist in characterization of the supersonic facilities. Schlieren is an optical technique based on the difference of the refraction index of the media with different densities. It is particularly useful to determine the existence of shocks, mixing layers, and their behavior. Although quantitative analyses may be performed on Schlieren images, such techniques are not currently employed.

The current Schlieren setup is comprised of a point light source, a converging lens, a pin-hole, a pair of plano-convex lenses, and a razor blade that cuts parts of the light beam off to realize a Schlieren image. Light is then captured with a camera, which is then focused on the wind tunnel test section, as shown in Figure 55. This technique has a disadvantage in that it experiences on-off behavior. When transitioning from shadowgraph (no light cut-off) to Schlieren, there is only a small margin in which the image quality is high. With cut-off out of this margin, the image quickly darkens, absorbing all detail.

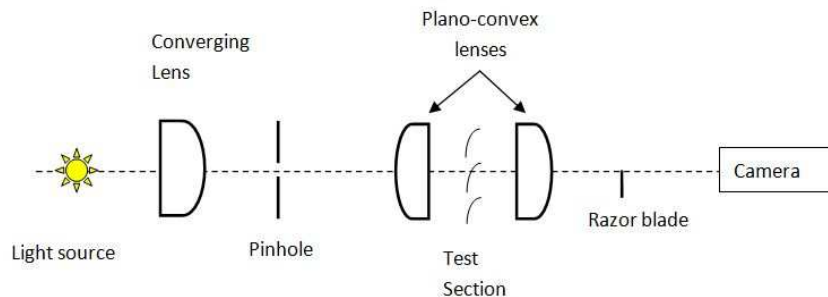


Figure 55: Schematic of point-source lens Schlieren setup.

The schlieren technique has been enhanced throughout the project with the following changes, which focus mainly on the light source:

1. Initial setups featured a 20 Hz arc light source which did not have enough power and did not satisfactorily perform as a point-source.
2. A low power laser light source then provided a directional source with the problem of interferometric structures in the image because of laser-inherent coherence.
3. The pin-hole was changed from a two-dimensional two-closing-blades device on each of the axes to an actual 150 μm pinhole.
4. An automotive halogen headlamp light bulb was used to increase luminosity delivered to the camera CCD. This light source proved to be acceptable, but did not provide the desired resolution.
5. The current implementation utilizes a semi-directional LED.

Later tests utilized an extended light source improvement. Here, the LED was focused on a slit which acts like a continuum of point sources; all of which are projected on the image plane. This avoided the on-off switch behavior of the point source approach.

4.4.1 Schlieren Examples: Backward Facing Step

The supersonic turbulence facility, described above in Section 3.3, with the Mach 2.5 nozzle and a subsonic mixing nozzle was operated at a stagnation pressure of 75 psia. The schlieren arrangement corresponding to the fourth configuration discussed above was used. The recording device was a NAC GX-3 high speed camera with a C-mount telescoping lens. Images were acquired at 4000 frames per second. Two such images are shown in Figure 56. The knife-edge was operated in a high cut-off position to accentuate flow features. The on-off nature of the knife edge can be seen in the background image where the lower left part of the image is black due to the knife. In the schlieren image the expansion fan, subsonic jet, and reattachment shock can all be seen.

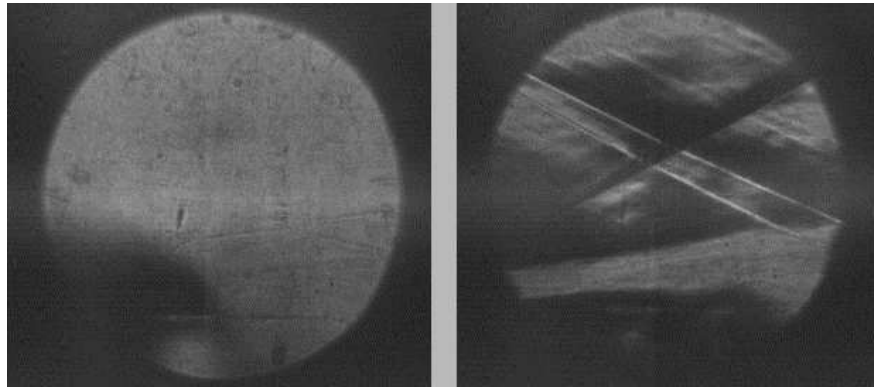


Figure 56: Background image (left) and schlieren of backward facing step with flow entrainment (right).

4.4.2 Schlieren Examples: Sonic Jet in Crossflow

The supersonic turbulence facility described in Section 3.3 with the Mach 2.5 nozzle was operated at a stagnation pressure of 75 psia. The schlieren arrangement corresponding to the fifth configuration discussed above was used. The recording device was a NAC GX-3 high speed camera with an extended 135 mm lens. Images were acquired at 2000 frames per second. Four such images are shown below in Figure 57. The knife-edge was operated in a medium cut-off position to accentuate flow features without affecting the overall image quality. With the tunnel off and the sonic jet on, the top right schlieren image was produced. The underexpanded jet is easily seen with features such as the free jet boundary and triple shock structure appearing clearly. When the jet was turned off and the tunnel started, a number of Mach waves and shock structures were observed, such as those in the image at the bottom right. With the tunnel started and the jet on, a classic supersonic jet in crossflow was observed such as that in the bottom left. The bow shock, lambda shock, windward shock, and leeward shock are all visible in these images.

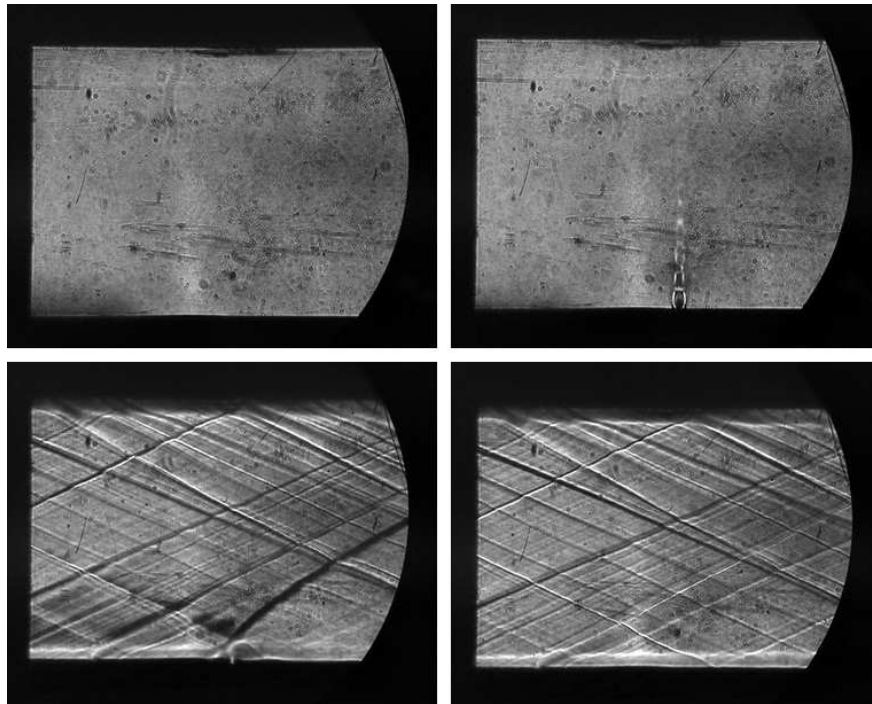


Figure 57: Background (top left) and schlieren of underexpanded jet (top right). Schlieren of jet in $M = 2.5$ crossflow (bottom left) and schlieren of $M = 2.5$ flow (bottom right).

4.5 OH and CH₂O Planar Laser Induced Fluorescence

For these studies, an OH PLIF sheet was produced using a dye laser pumped by a frequency doubled Nd:Yag. Various sheet optics were used to produce a sheet which entered the test section in plane for subsonic tests and orthogonally for supersonic tests. The CH₂O sheet was produced by a frequency tripled Nd:Yag with various sheet optics. For simultaneous tests (subsonic only), the sheets were combined within the test section with OH from the

top and formaldehyde from the bottom. Chemiluminescence measurements were collected orthogonal to the test section when they were used as the primary data (no PLIF). When used as a supplemental measurement, OH* and CH* cameras were placed off axis (22.5%, 45%, 90%, etc.) to the primary PLIF camera. In all studies, timing was accomplished by a digital delay generator (either BNC or Stanford Research brand). All PLIF studies use 10 Hz timing, while some chemiluminescence used up to 50 kHz timing. Figure 58 shows a cartoon depicting an arrangement for simultaneous PIV, OH/CH₂O PLIF, and filtered Rayleigh Scattering with laser ignition.

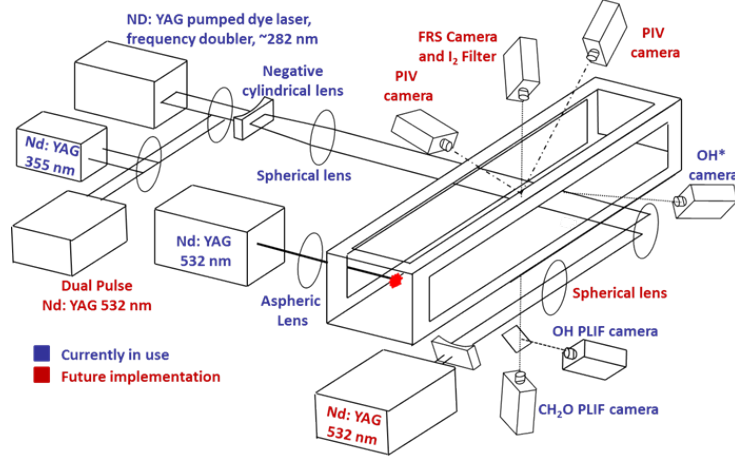


Figure 58: Schematic showing various diagnostics used and proposed future diagnostics.

For the supersonic tests, OH* chemiluminescence was collected at a 22.5° angle to the test section. A Photron SA5 coupled with a HiCATT intensifier at 5 μ s gate and 308 nm filter operated at 272 \times 512 pixels and 50,000 frames per second. The camera was triggered using the ignition TTL signal synced to the Schlieren images. The viewing angle dependence was removed in post processing by dewarping the images using a target grid. Approximately 822 kernels were captured per dataset providing sufficient samples to generate statistics. The kernel was located at each instant in time and the size was calculated by averaging over all kernel realizations. Cross-stream variation was removed by centering each realization prior to averaging. A threshold intensity was used to find the edge of the averaged kernel. The resulting kernel area is equal to the averaged line-of-sight OH* chemiluminescence at each time. The area was converted to an effective diameter and plotted versus time in a similar fashion to the Schlieren images. Following the analysis of Smallbone, [101] the radial growth rate of a freely expanding flame kernel is equal to the global displacement velocity plus the velocity of the expanding burned gas. The global displacement speed is related to the radial growth via Eq. (8).

$$S_n = \frac{\rho_b}{\rho_u} \cdot \frac{dr_{chem}}{dt} \quad (8)$$

5 Results and Discussions

5.1 Turbulence Generation and Evaluation

A significant portion of the experimental effort has been devoted towards the generation of high-intensity turbulence for examination of how the flame kernel behaves in a premixed flow. Past studies of the interaction of a flame kernel with a turbulent flow field have focused on the interaction of the flame kernel with isotropic turbulence to avoid effects from large, non-turbulent vortical structures or large-scale strain [15, 12]. However, there is little experimental data on how flame kernels interact with a highly turbulent, compressible flow and no facility to date has been developed for this purpose. There is little understanding of how to generate high intensity turbulence in this environment, much less turbulence that is also approximately homogeneous and isotropic. The work of Year 2 consisted of a number of experimental forays into this area with the aim of better understanding the properties of the compressible subsonic facility, with detailed evaluation of an active blown jet grid currently underway.

5.1.1 Background

Experimental grid turbulence is typically slightly inhomogeneous in the direction of mean flow, as well as slightly anisotropic. This inhomogeneity is typically seen in the direction of mean flow with anisotropy caused by a bias of $\overline{u_1^2}$ in relation to $\overline{u_2^2}$ and $\overline{u_3^2}$. Typically, the problems of inhomogeneity and anisotropy are dealt with by introducing a duct that diverges to account for acceleration due to boundary layer effects, with a slight contraction with an area ratio of approximately 1.4 or less to remove axial anisotropy [46]. This is illustrated by Figure 59, which shows the setup used for evaluation of incompressible grid turbulence by Lavoie, et. al. [70]. These measures have been shown to produce a better experimental approximation of isotropic turbulence, however slight anisotropies are typically still present.

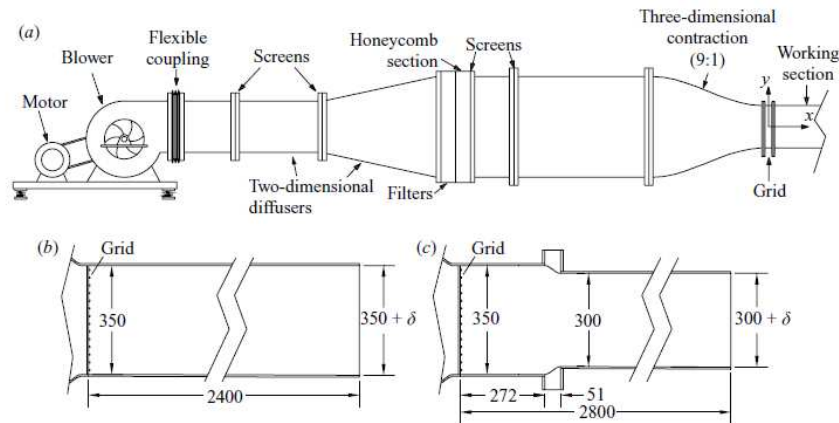


Figure 59: (a) Schematic of wind tunnel and working section as used by Lavoie et. al. [70]. (b) Working section with small divergence δ applied. (c) Working section with slight contraction area ratio of 1.36 with small divergence δ applied.

However, these measures cannot easily be adapted for use in study of grid turbulence in compressible flow. This is primarily due to the fact that the working section would have to be prohibitively large to introduce any sort of meaningful turbulence generation without choking the nozzle and to avoid observing disruptive turbulence amplification effects by shocks. This would result in unacceptably short facility run times with available resources. This was first observed by Zwart [62] and later explained more definitively by Agui [102] by observing turbulence interactions with a propagating shock in a large shock tube. The presence of such a small test section area due to building fuel flow restrictions requires the positioning of the turbulence generator to be upstream of the typical position seen in low-speed studies, as illustrated previously in Figure 59. This is also illustrated in Figure 60 below, which relates choking grid solidity to the test section entrance Mach number, where $\sigma = (1 - A_{open}/A_{total}) \times 100\%$. As seen, any practical solidities of value in the range of $30\% < \sigma < 45\%$ and above for generating homogeneous and approximately isotropic turbulence [47, 103] are not possible across the $0.1 < Ma < 0.7$ range.

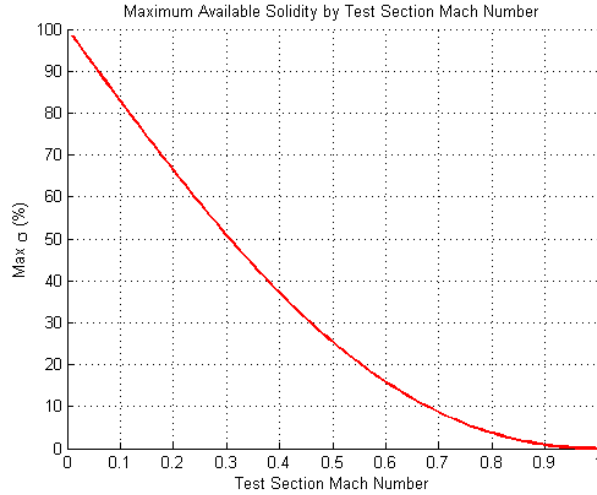


Figure 60: Relationship between maximum grid solidity and test section Mach number for grid placement at test section entrance

A conceptual understanding of the problem can first be created by reverting to the incompressible turbulent kinetic energy (TKE) equation presented in Equation 9. Uppercase quantities are mean values and lower case values are fluctuation values as given by a general Reynolds decomposition of the form $\Psi = \bar{\Psi} + \psi$. The mean strain rate is given as $\bar{S}_{ij} = [d\bar{U}_i/dx_j + d\bar{U}_j/dx_i]/2$; the fluctuating strain rate is formulated equivalently for fluctuating velocities. This equation states that the change of the turbulent kinetic energy per unit mass and of time including the convective transport by mean motion (I) is equivalent to the sum of the work of the total dynamic pressure of the turbulence (II), the work of deformation of the mean motion of turbulent stresses (III), the work of viscous shear stresses of turbulent motion (IV), and of viscous dissipation by turbulent motion (V), all per unit mass and time.

$$\begin{array}{cccccc}
\frac{1}{2} \frac{D}{Dt} (u_i u_i) & = & - \frac{\partial}{\partial x_j} \left(\frac{1}{\rho} \overline{u_j p} + \frac{1}{2} \overline{u_i u_i u_j} \right) & + & 2\nu \frac{\partial}{\partial x_j} (\overline{u_i s_{ij}}) & - \overline{u_i u_j \overline{S_{ij}}} - 2\nu \overline{s_{ij} s_{ij}} \\
\text{I} & & \text{II} & & \text{III} & \text{IV} \quad \text{V}
\end{array} \quad (9)$$

Starting from the full equation, scaling relations and order of magnetude arguments as described by Tennekes and Lumley [76] for a typical grid turbulence case where $U \gg u'$ and $U_1 \gg U_2 \approx U_3$ can be used to simplify the equation to more approximate the problem at hand. This results in the TKE energy balance given in Equation 10, where $k = 1$.

$$U_k \frac{\partial}{\partial x_k} \left(\frac{1}{2} \overline{u_i u_i} \right) = -\overline{u_i u_k} \frac{\partial U_k}{\partial x_k} - 2\nu \overline{s_{ij} s_{ij}} \quad (10)$$

The expression in Equation 10 becomes equivalent to the case of homogeneous turbulence when Taylor's hypothesis is invoked as shown below [104], leaving only a production term and dissipation term. Assuming close to isotropic turbulence, the simplification that $\overline{u_1 u_1} = \overline{u_1 u_2} + \overline{u_1 u_3}$ can be made as well.

$$\begin{array}{rcl}
\frac{\partial}{\partial t} \left(\frac{1}{2} \overline{u_i u_i} \right) & = & -2\overline{u_1^2} \frac{\partial U_1}{\partial x_1} - 2\nu \overline{s_{ij} s_{ij}} \\
\frac{\partial k}{\partial t} & = & \mathcal{P} - \varepsilon
\end{array} \quad (11)$$

As illustrated by Equation 10, the TKE production term in an accelerating flow where off-axis Renolds stresses and mean velocity gradients are negligible acts to decrease TKE. Thus, considering the facility-based challenges relating to grid placement as summarized by Figure 60, it was initially thought that large amount of TKE must be introduced ahead of the converging nozzle needed to accelerate the flow to high subsonic Mach numbers of interest. This required an active generation method upstream of the nozzle to generate high initial turbulence levels in order to achieve reasonable turbulence levels within the test section. A blown jet grid such following the design of Gad-el-Hak [105] was constructed and evaluated for such a task.

Experimental evaluation of the blown grid installed at the location described by Datum A in Figure 61 and numerical analysis of the same geometry has since shown that the assumptions inherent in the above discussion are invalid for a nozzle with a relatively high area contraction ratio of 8.5:1. The abrupt contraction of the nozzle facilitates significant production attributed to vortex stretching effects from negative values of $\overline{S_{22}}$ and $\overline{S_{33}}$, as well as off-diagonal components. This in itself is not surprising, however as shown from experimental and numerical data presented as follows, this is a significant effect for "high contraction ratio" nozzles. Re-examination of Equation 10 with $k = 2$ and $k = 3$ indicates that $\overline{u_1^2}$ and $\overline{u_2^2}$ must increase, while the negative production effects due to accelerating the flow are still apparent for $\overline{u_1^2}$. This produces a highly anisotropic state of turbulence at the exit of the nozzle, prompting a return to isotropy in the test section forward of Datum B in Figure 61.

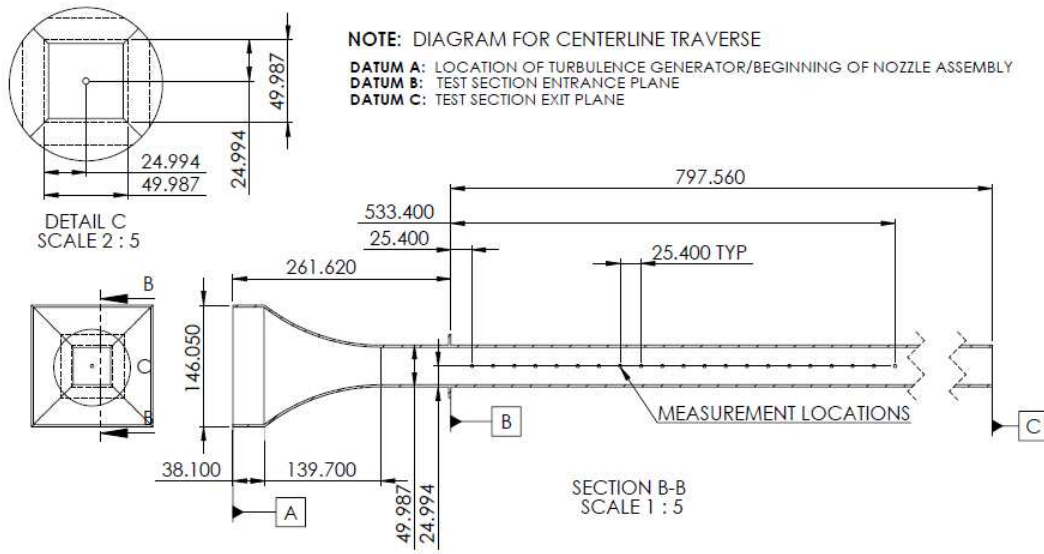


Figure 61: Traverse locations relative to internal geometry of subsonic wind tunnel facility (units in mm; not to scale).

More recent experimental evaluation of the effect of nozzles of various contraction ratios as conducted by Ertunç [106, 107] supports these findings for said “high contraction ratio” nozzles defined as nozzles having a contraction ratio greater than approximately 4:1. It is also observed that contraction ratios below this limit do not show as severe anisotropy due to off-axis strain, facilitating experimental analysis of homogeneous and isotropic turbulence. These findings are key to modifications to the existing nozzle in order to realize high-intensity homogeneous and isotropic turbulence within the test section as discussed in Section 5.1.4.

In light of the anisotropic turbulence present in the test section due to nozzle effects, a diverging box duct for use in low-speed turbulence evaluation similar to that Figure 59(b) was constructed for evaluation of the blown grid. The duct was constructed to serve as a baseline to compare to existing active turbulence generation literature, as well as to tune current and future generation techniques before use in high subsonic and supersonic applications. A schematic of the duct with measurement locations corresponding to the discussion in Section 5.1.4 is shown below in Figure 62.

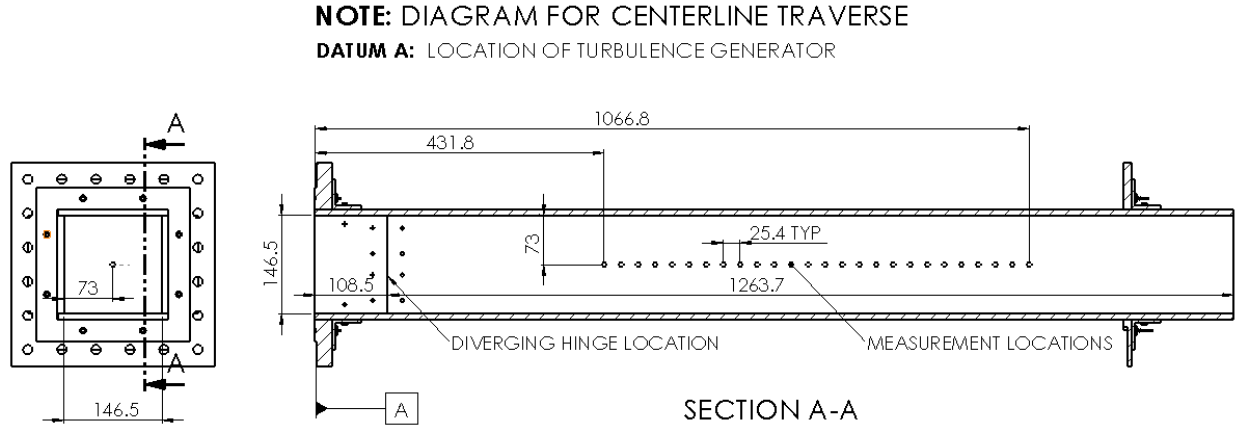


Figure 62: Traverse locations relative to internal geometry of low speed diverging duct (units in mm).

5.1.2 Experimental Investigations of Subsonic, $M < 0.1$ Turbulence

The divergent duct configuration is shown to produce an adequate experimental realization of homogenous turbulence as shown in Figure 63. Transverse mean and RMS velocity profiles (u') are shown to be flat for both passive and 30% bleed cases, with a maximum deviation of $\pm 5\%$ of the centerline value. It is noted that all of these measurements were taken by a single element SN probe and not a rotating SY probe or multi-element X-probe. Hence, higher order velocity corrections in recovering the true mean velocity are not possible without information regarding contributions from $\overline{u_2^2}$, $\overline{u_3^2}$ and $\overline{u_1 u_3}$, as well as triple fluctuating velocity correlations such as $\overline{u_2^3}$ and $\overline{u_3^3}$ in high-intensity turbulence[90]. However, examination of the normalized mean effective velocity $\overline{V_e}$ is an adequate indicator of mean velocity homogeneity, as a homogeneous flow field irrespective of turbulence level should interact with the SN probe element in the same fashion within the homogeneous region.

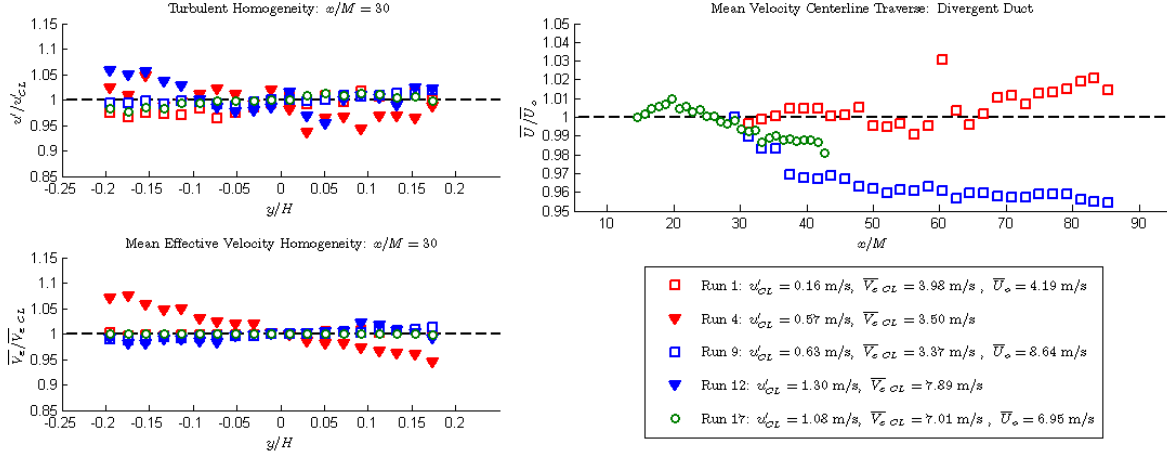


Figure 63: Turbulent and mean effective velocity homogeneity profiles measured by SN probe in divergent duct facility ($H = 0.146$ m). Centerline mean velocity profiles measured by SN probe. (See 3.4 for M Values)

It is shown that both transverse turbulent and mean homogenization is achieved at $x/M = 30$, where $M = 12.2$ mm in this case. This ensures that a homogeneous turbulent flow-field is produced for study in both divergent duct and subsonic facility configurations. This is in agreement with much larger facilities used in traditional grid turbulence studies [46]. However, in the case of Run 17, it is shown that homogenization is achieved considerably sooner at $x/M = 15$ ($M = 24.4$ mm), which is traditionally a region where inhomogeneities are present from merging wake structures [103]. Further investigation is needed to examine if this is indeed a unique property of the small-scale divergent duct.

5.1.2.1 Passive Grid Studies The streamwise centerline traverses for all passive cases are shown in Figure 63 to not deviate by more than 5% of the initially measured value. These relatively large spanwise deviations in comparison to traditional larger facilities that have mean velocities that deviate by 1% or less[70] are challenging to overcome in the case of a diverging duct with small cross-sectional area. In the case of Run 9, the differential static pressure between the first and twenty-eighth traverse points is 3.6 Pa, which is just above the ± 2.5 Pa error range of the differential pressure gauge used to set the diverging angle of the tunnel walls. Additionally, in the case of a highly-turbulent core flow, transient boundary layer interaction has been shown to alter the cross-sectional area of the core flow[69]. Hence, it is demonstrated that a small-scale divergent duct can produce an experimental approximation of homogeneous turbulence.

5.1.2.2 Blown Grid Studies The streamwise evolution of the RMS velocities within the divergent duct for $Ma = 0.0357$ inflow conditions and passive grid reference case is shown in Figure 64. For all bleed settings (Run 10 - 12), the turbulence is shown to be approximately isotropic for all cases, however it is noted that $u' < v'$. The u'/v' ratios are shown in 5.1.2.2 and are approximately 0.95 for all cases, with the exception of the passive grid reference case (Run 17). The anisotropy ratio $u'/v' = 1.25$ at $x/M = 40.6$ for Run

17, which is in agreement with the reference case. However, as grid turbulence is typically classified as approximately axisymmetric anisotropic turbulence with $u' > v' \approx w'$, these results require further analysis.

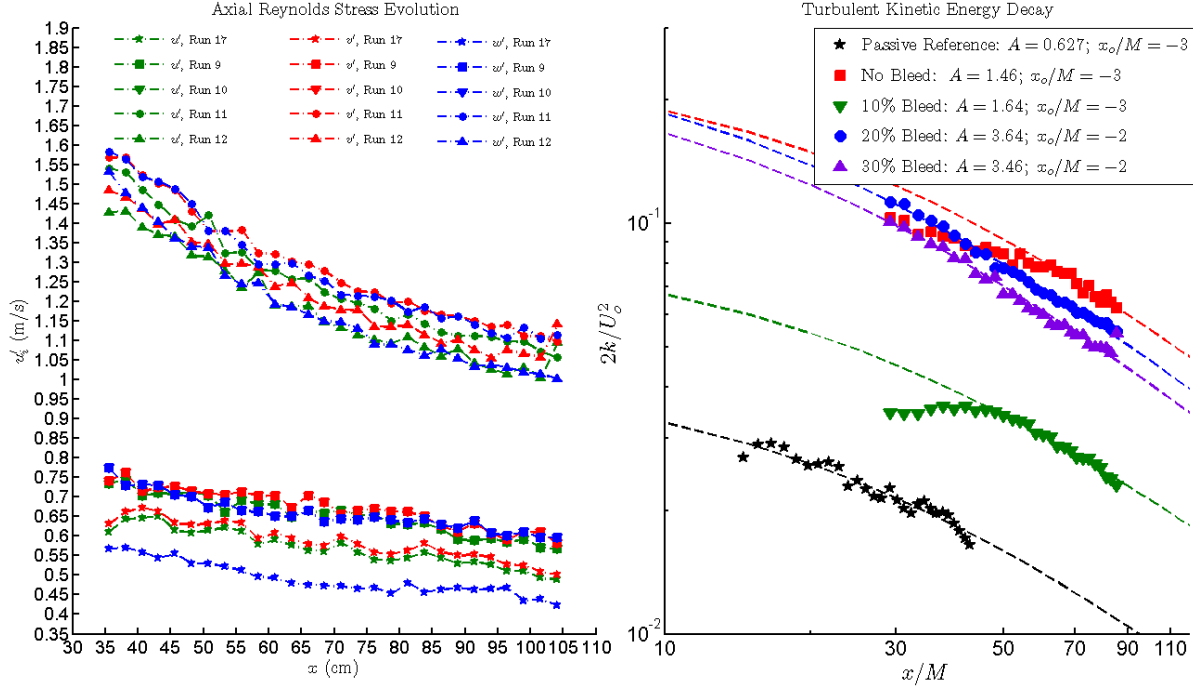


Figure 64: RMS velocity divergent duct centerline traverse and determination of turbulent kinetic energy decay for passive grid baseline case and blown grid settings at $Ma = 0.0357$ inflow conditions. See 5.1.2.2 for n values.

As previously described, a signal processing procedure was used involving the downsampling of raw records to a new Nyquist frequency to facilitate digital low-pass filtering at a desired cutoff frequency. Using Taylor's hypothesis, the resultant energy spectra and associated wavenumber relations shown in Equations 12 and 13 could be used to then filter all records irrespective of frequency bandwidth to a cutoff wavenumber $\kappa_{1, cut}$. This facilitated direct comparison between spectra and associated statistics, regardless if the signal originated in a subsonic case or divergent duct case, with bandwidths on the order of 10^4 Hz and 10^3 Hz, respectively.

$$\kappa_1 = \frac{2\pi f}{\overline{U}_1} \quad (12)$$

$$E_{11}(\kappa_1) = \frac{\overline{U}_1}{2\pi} E_{11}(f) \quad (13)$$

However, while this processing procedure yielded common standards for record processing and mitigation of facility noise, it was found to not be a best practice for the SY processing. This is best illustrated by considering a sample equation for the evaluation of $\overline{u_2^2}$ as shown in Equation 14 from the SY fluctuating effective velocity signal v_e at probe stem rotation angles of 0° and 180° degrees denoted by subscripts and superscripts a and b , respectively. The probe directional response coefficients C_i , as well as equations for the third order correlations $\overline{u_i^2 u_j}$ and remaining second order correlations are given in Appendix 1 of Buresti and Di

Cocco[90].

$$\overline{u_2^2} = \frac{1}{C_2^a} \left[\left(\frac{\overline{v_{e,a}^2} + \overline{v_{e,b}^2}}{2} \right) - C_1^a \overline{u_1^2} - C_7^a \left(\frac{\overline{u_1 u_2^2}}{\overline{U_1}} \right) - C_9^a \left(\frac{\overline{u_1 u_3^2}}{\overline{U_1}} \right) \right] \quad (14)$$

Equation 14 demonstrates that the energy content of $\overline{u_1^2}$, $\overline{u_2^2}$ and $\overline{u_3^2}$ is shared between individual signals from several rotation angles. The use of digital filtering to eliminate facility acoustic noise may force the results to appear “isotropic” or produce results where $u' < v'$. It has been shown experimentally by Ertunç[106] (p. 168) that $E_{22}(\kappa_1)$ has a broader (but less energetic) energy containing range than $E_{11}(\kappa_1)$. If the turbulence intensity is high enough such that an inertial range is present, the filtering of SY records such that $\kappa_{1\text{ cut}}$ is in the inertial range may make $\overline{u_1^2} \approx \overline{u_2^2}$. Filtered energy spectra $E_{11}(\kappa_1)$ are shown and discussed in the following subsection to aid in visualizing this effect. Thus, more accurate results using the rotating SY method requires further mitigation of rig noise, as well as some knowledge of the bandwidth of $E_{11}(\kappa_1)$, $E_{22}(\kappa_1)$ and $E_{33}(\kappa_1)$ to avoid losing valuable high-wavenumber signal content.

While the associated RMS velocities are slightly anisotropic with $u' > v' \approx w'$, the isotropic decay law can still be approximated using Equation 15, where the turbulent kinetic energy is defined as $k = 1/2(u_i^2)$, U_o is the mean velocity at the grid, x_o/M is the virtual origin, and A is a fit coefficient. The decay power coefficient n is typically found to be $-1 < n < -1.7$, with the similarity analysis of Mohamed and LaRue [108] placing the value at $n = -1.3$.

$$\frac{2k}{U_o^2} = A \left[\frac{x}{M} - \frac{x_o}{M} \right]^n \quad (15)$$

Equation 15 is evaluated using the algorithm described by Lavoie[70], where a “Power Law Decay Region” (PLDR) is explicitly identified to avoid arbitrary determination of the virtual origin. As shown in Figure 64, the PLDR is fully developed for the passive grid reference case (Run 17), and progressively develops by bleed setting. Decay is shown to be irrespective of the grid type or bleed setting, with virtual origins that are similar to traditional studies[46]. The decay coefficients are shown to be near $n = -1.0$ as shown in 5.1.2.2.

Table 8: Scale comparison with noted active and passive grid turbulence studies in literature.

Experiment	U_o (m/s)	M (mm)	x/M	Re_M (10^3)	u'/U_o (%)	u'/v'	L_{11} (mm)	λ (mm)	η (mm)	Re_λ	n
Run 2	4.04	12.2	50	3.28	5.0	0.95	22.8	3.0	0.16	90	1.02
Run 3	4.04	12.2	50	3.28	11.2	0.92	36.0	4.1	0.15	182	1.01
Run 4	4.04	12.2	50	3.28	10.9	0.94	36.7	4.2	0.15	190	1.04
Run 10	8.0	12.2	50	6.58	10.0	0.97	24.8	2.4	0.11	137	0.98
Run 11	8.0	12.2	50	6.58	15.9	0.97	34.6	3.1	0.097	270	1.00
Run 12	8.0	12.2	50	6.58	16.0	0.98	30.7	3.5	0.10	298	1.02
Run 17 [†]	6.4	24.4	40.6	10.4	8.70	1.25	17.0	6.2	0.20	65	1.04
Case 1	5.0	46.7	50	15.6	16.4	1.22	197	8.2	0.21	387	1.43
Case 2	4.2	102.0	46	41.8	3.27	1.11	134.7	9.45	0.39	160	0.97
Case 3	10	50.8	42	34.0	2.22	1.0	24	4.9	0.29	72	1.25
Case 4	6.4	24.8	60	10.4	2.2	1.27	11.0	5.5	0.48	33	1.14

[†]Passive grid reference case

All scales and dissipation estimates are calculated from SN records. As previously discussed, the Welch algorithm was used to calculate the one-dimensional energy spectra $E_{11}(f)$, which is then converted to wavenumber space via Equations 12 and 13. The circular autocovariance algorithm enables ensemble averaged estimates of the autocovariance, which is defined as $R_{11}(s) \equiv \overline{u_1(t)u_1(t+s)}$, and s is the record lag time[92]. Determination of the integral length scale is shown in Equation 16, where the temporal autocorrelation is defined as $\rho_{11}(s) \equiv R_{11}(s)/R_{11}(0)$ and τ_{11} is the integral timescale.

$$L_{11} = \overline{U}_1 \tau_{11} = \overline{U}_1 \int_0^\infty \rho_{11}(s) ds \quad (16)$$

The Taylor length scale λ_f and mean dissipation $\bar{\epsilon}$ are estimated via Taylor's hypothesis and assuming local isotropy from velocity derivative statistics as shown in Equation 17 and 18, respectively. The Taylor length scale Reynolds number is defined as $Re_\lambda \equiv u' \lambda / \nu$. Determination of the Kolmogorov length scale follows from Equation 19.

$$\lambda = \left[\overline{U_1^2 u_1'^2} / \overline{(\partial u_1 / \partial t)^2} \right]^{\frac{1}{2}} \quad \bar{\epsilon} = 15(\nu / \overline{U_1^2}) \overline{(\partial u_1 / \partial t)^2} \quad (17) \quad \eta = (\nu^3 / \bar{\epsilon})^{\frac{1}{4}} \quad (18) \quad (19)$$

The use of isotropic relations to estimate $\bar{\epsilon}$ at a given point in anisotropic turbulence in this case is driven by current measurement limitations of the experiment. However, Mydlarski and Warhaft show that for $Re_\lambda > 200$ the assumption of local isotropy for small scales hold[51]. As shown later, this condition is either closely approached or satisfied in this experiment, enabling accurate estimation of λ , Re_λ and η using this assumption.

As shown in 5.1.2.2, the high-bleed blown jet grid is capable of generating high-intensity turbulence with large separation of scales. At $x/M = 50$ and 30% bleed, it is shown that the grid produces a flow field that is similar to that of the active vane grid constructed by Makita[50] at mesh Reynolds numbers Re_M approximately one-fifth of a comparable vane grid case. In comparison to the traditional low bleed ($< 10\%$) blown jet grid of Gad-el-Hak[105], it is shown that turbulence intensities in excess of 16% are realized, with integral length scales that are at least twice the size of the characteristic mesh size of the grid or higher.

The claims of 5.1.2.2 are further supported by sample Kolmogorov-scaled energy spectra and autocorrelation data at $x/M = 50$ shown in Figure 65. As shown, the high-bleed cases show a prominent inertial range characteristic of $Re_\lambda > 160$, over a large normalized wavenumber region $\kappa_1 \eta$ where a $\kappa_1^{-5/3}$ slope is present[45].

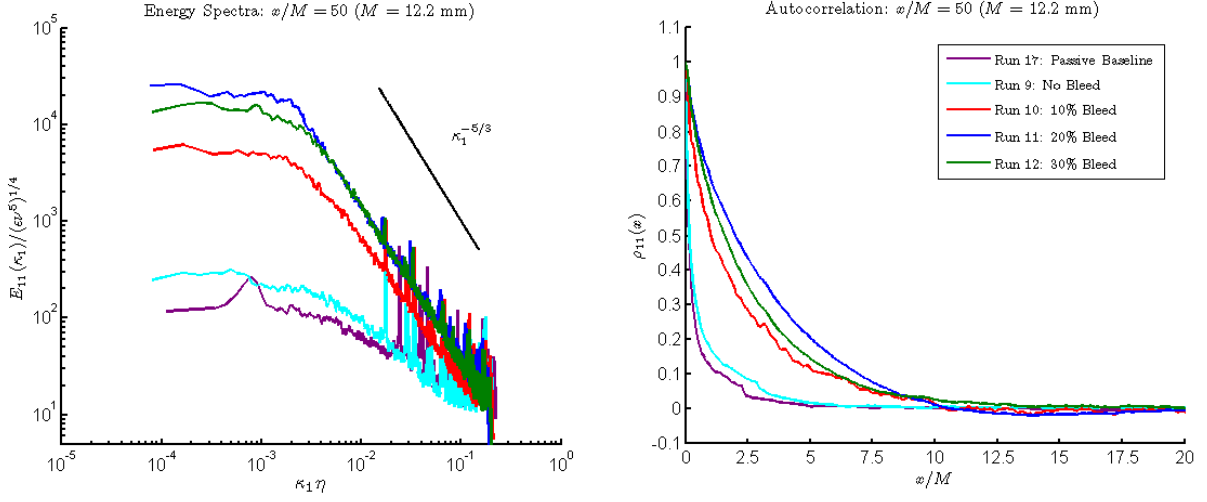


Figure 65: Kolmogorov-scaled energy spectra $E_{11}(\kappa_1)$ and associated autocorrelation $\rho_{11}(x)$ at locations of reported values in 5.1.2.2 for the passive grid baseline case and blown grid settings at $Ma = 0.0357$ inflow conditions. Note that for Run 17 the autocorrelation function is normalized by $M = 12.2$ for comparison.

Further support of the scale estimates of 5.1.2.2 are shown by the sample autocorrelation data in Figure 65. It is shown that $\rho_{11}(x)$ broadens as required for cases with progressively higher turbulence intensities. Additionally, it is illustrated that the integral length scale shown to be larger than the characteristic mesh size of the grid, whereas the blown jet grid configuration with no bleed (passive) produces an integral scale that is a significant fraction of the characteristic mesh size. This is in agreement with past blown-jet and vane grid active generation studies in larger facilities.

As described previously, a downsampling and digital filtering routine was implemented to set uniform wavenumber cutoffs and to minimize signal content attributed to facility noise. As shown in Figure 65, facility noise is still present at lower wavenumbers, and is more prominent in the currently considered passive and 10% bleed cases. Regardless of this effect, the normalized spectra presented in Figure 65 with a cutoff of $\kappa_1 = 2000 \text{ m}^{-1}$ shown at $\kappa_1 \eta \approx 2 \times 10^{-1}$ suggest that information in the dissipation range cannot be resolved, potentially impacting the validity of Taylor length scale estimates calculated with using Equation 17. However, it is shown by Pope (p. 199) that a necessary condition for the application of Equation 17 is smooth autocorrelation function[77], where $d\rho_{11}(0)/dx = 0$ and $\lim_{x \rightarrow \infty} \rho_{11}(x) = 0$. Hence, if the dissipation range is difficult to recover due to acoustic noise contamination as presently experienced, digital record filtering criteria that can produce a smooth autocorrelation and recover turbulent signal content in all of the energy containing range and most of the inertial range can yield accurate estimates of the Taylor length scale λ , mean dissipation $\bar{\epsilon}$ and Kolmogorov scales. Thus, the presented high Re_λ values that have been previously only seen at laboratory scale at higher Re_M using vane grids are valid.

5.1.2.3 Vane-Stirred Grid Studies Following studies by Makita [50] an active vane grid is able to generate high intensity, isotropic turbulence. The design used in this study

is similar but much smaller, thus representing the first attempt to experimentally realize this type of turbulence in a small/medium sized rig. This also allows for the combination of this type of turbulence generation and combustion experiments, which will be discussed in Section 5.2.2. All presented results here were obtained at $\Omega \approx 11/s$, unless otherwise indicated. The exact physical properties of the active vane grid have been described in Section 3.4.

Evaluation of the one-dimensional velocity spectrum in streamwise direction shows that the manufactured vane grid produces an isotropic inertial subrange spanning almost two decades of wave numbers, as shown in Fig. 66. To reduce noise in the spectrum and obtain a smoother estimate of the auto-correlation function (and thus τ_{11}) and dissipation, a moving average filter has been applied to the spectrum. Moreover, the rotation of the vane grid rods introduces non-turbulent energy content at low wavenumbers into the spectrum. Following Mydlarski et al. [51] this content is removed using a least-squares technique. The autocorrelation is then derived using the WienerKhinchin theorem. An example corresponding to the previously shown power density spectrum is plotted in Fig. 70. The streamwise integral length scales estimated from Taylor’s hypothesis and the zero crossing of the autocorrelation function are shown in Fig. 71. Values lie between 2.6 and 2.9cm, i.e. on the order of the openings in the vane grid and larger, as expected. The anisotropy tensor in Fig. 67 is confined to ± 0.075 for all components on the main diagonal, which is a good indicator for isotropy and close to value by other researchers that achieved isotropic flows (compare with Briassulis et al. [109]). Further indicating that the generated turbulence is isotropic. Values for the exponent n in the TKE decay, according to Eq. 15, were determined to be 0.93 and 1.63 for the rotating and the static vane grid, respectively, see Fig. 68. This scatter around $n = 1$ is within expected bounds and has been discussed for example by Lavoie [110]. The increase in n for the static case can be explained with the presence of very large structures (due to the 2.54cm openings in the grid) rapidly breaking up. The main diagonal components of the Reynolds stress tensor are shown in Fig. 69. Moreover the region over which PLIF measurements were taken in this tunnel is indicated, it contains three CTA data points and the variation of $\bar{u'_i u'_i}$ is small. The turbulent intensity is

$$Tu = \frac{u'}{\bar{U}} = 15\% - 13.6\%. \quad (20)$$

The Taylor microscale was computed from both isotropic relations and velocity fluctuations. Values obtained for the Taylor-Reynoldsnumber range from 378 to 490.

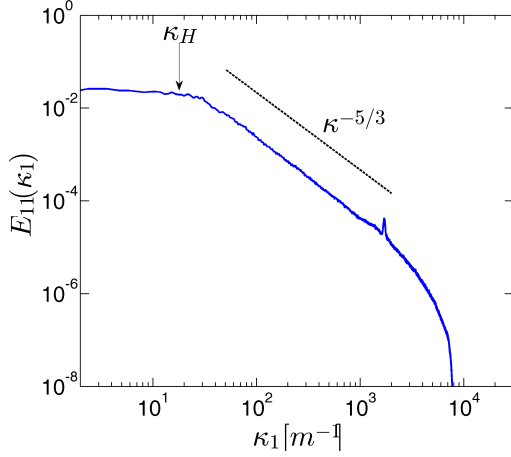


Figure 66: One-dimensional spectrum after removing large scale non-turbulent content and smoothing. The inertial range covers two decades and is isotropic. Part of the dissipation range is resolved.

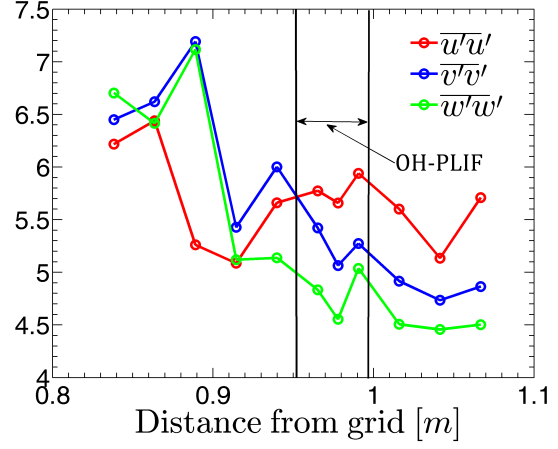


Figure 67: The three main components of the Reynolds stress are shown for the operating vane grid condition.

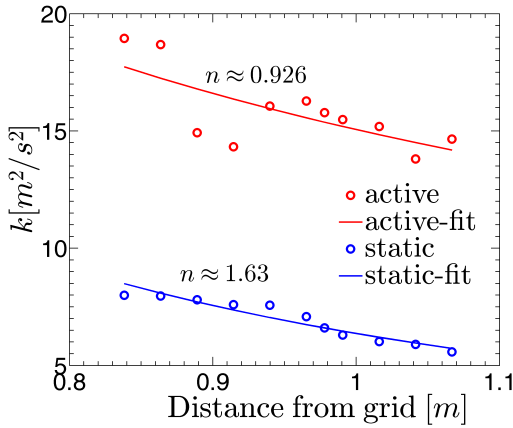


Figure 68: Decay of the turbulent kinetic energy with the respective polynomial fit and power coefficient of decay.

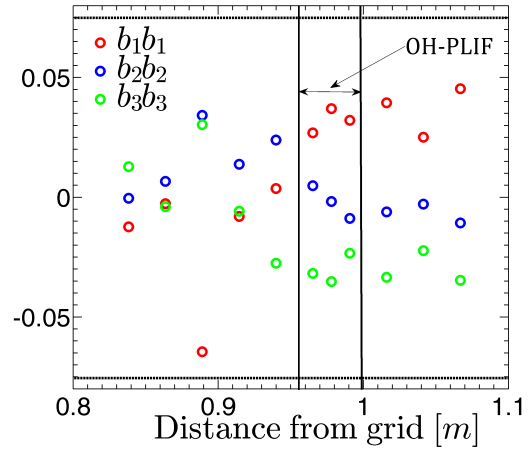


Figure 69: Plot of the anisotropy tensor trace. For all three fluctuating velocity components the values are within ± 0.075 of zero and local isotropy can be assumed.

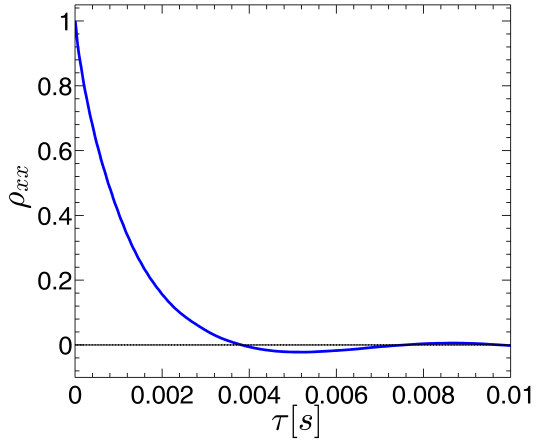


Figure 70: Autocorrelation function corresponding to the spectrum in Fig. 66.

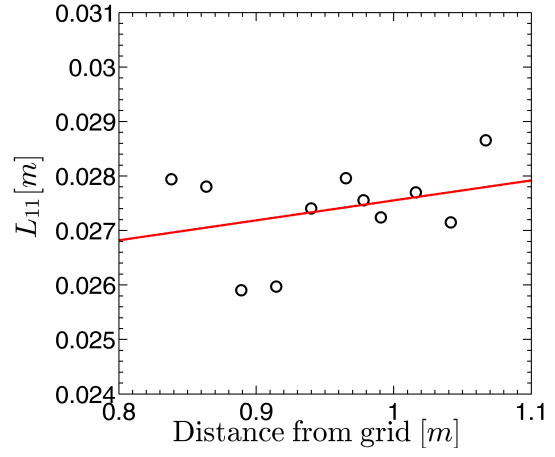


Figure 71: Development of the integral length scale along the duct. An upward trend is indicated by the red linear fit.

of all tested grids The comparison between a sample grid ($\sigma = 33\%$ $M = 8.9$ mm) and no grid installed is shown for both mean and u_{rms} velocities in Figure 73 and local turbulence intensities in Figure 74. The data is presented at distances relative to Datum 2 in Figure 61. Plot symbols and normalization velocities are summarized for both the no grid and grid case in Tables 10 and 11, respectively, where velocities are reflecting the mean and u_{rms} values at the first measurement point. As shown below, the evaluated grid did not provide turbulence intensities much larger than that of the measured background turbulence, with turbulence intensities of less than 1%. These results were typical of all grids tested, with no significant deviations between grids.

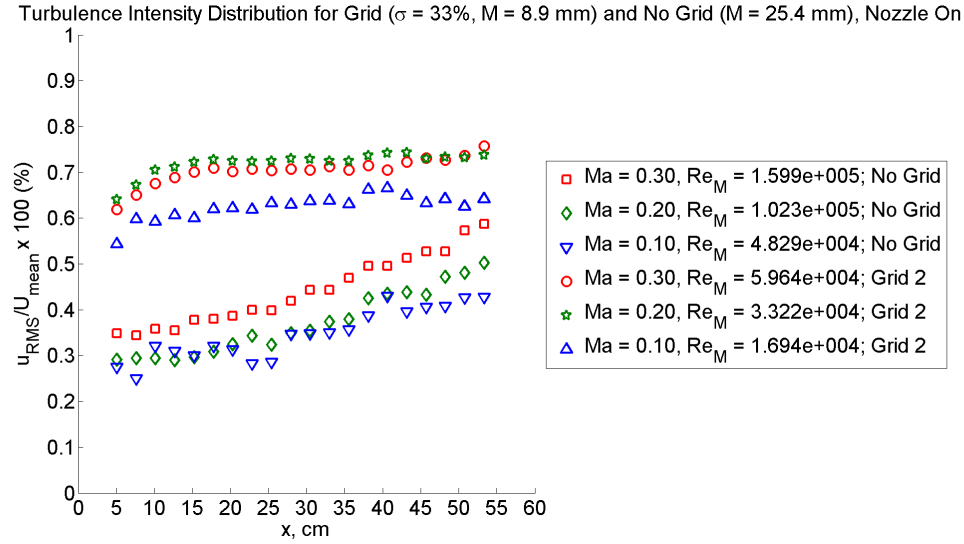


Figure 74: Turbulence intensity comparison between sample grid ($\sigma = 33\%$ $M = 8.9$ mm) and background turbulence (no grid).

Table 10: Grid symbols and normalization velocities for Figure 73: No grid

Mach Number	Grid Symbol	U_o (m/s)	u_o (m/s)
0.1	\square	32.1	0.088
0.2	\diamond	66.8	0.194
0.3	∇	101.3	0.353

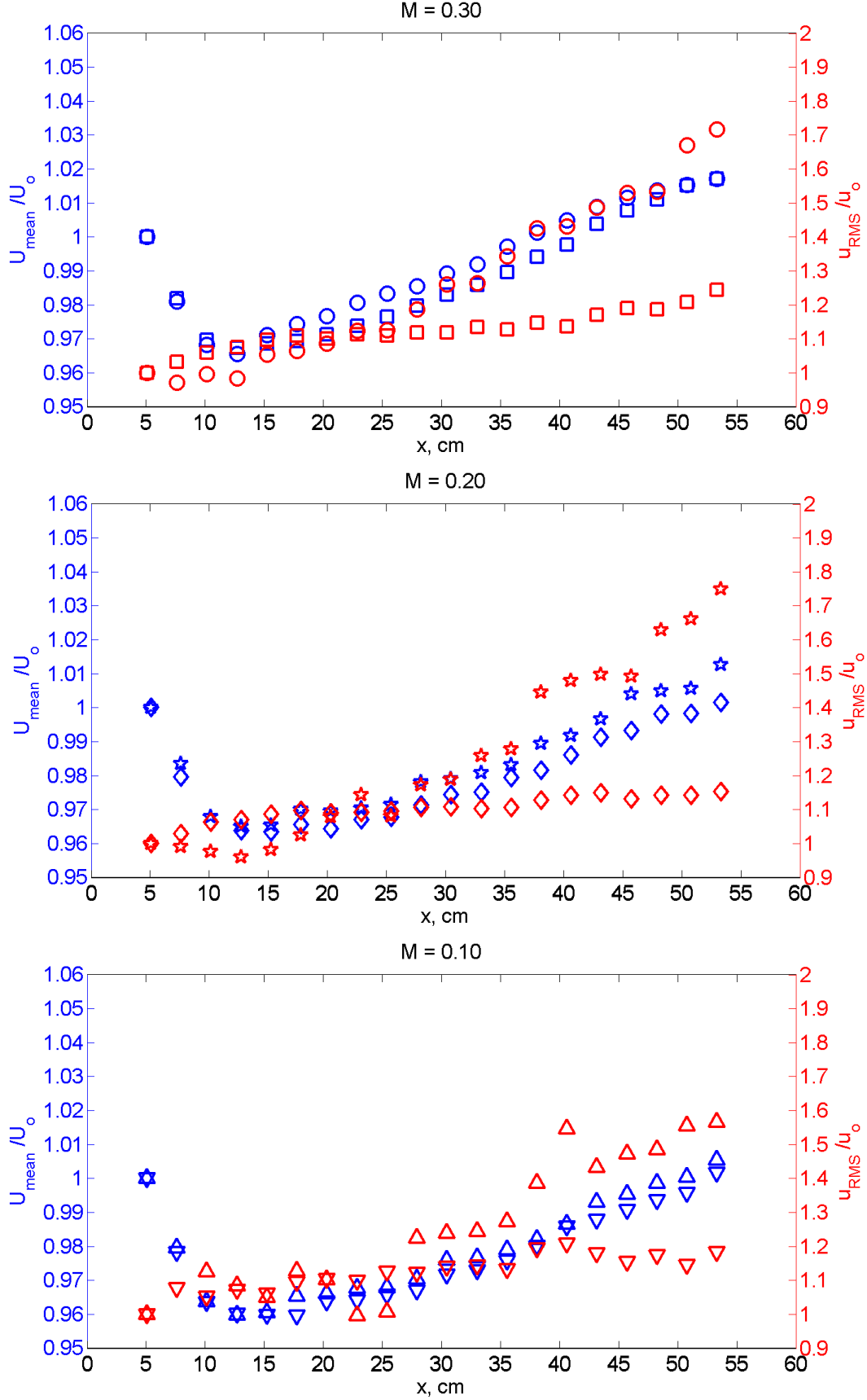


Figure 73: Normalized mean and RMS velocity comparison between sample grid ($\sigma = 33\%$ $M = 8.9$ mm) and background turbulence (no grid).

Table 11: Grid symbols and normalization velocities for Figure 73: Sample Grid ($\sigma = 33\%$ $M = 8.9$ mm)

Mach Number	Grid Symbol	U_o (m/s)	u_o (m/s)
0.1	○	32.2	0.175
0.2	★	62.4	0.400
0.3	△	107.7	0.667

As suggested by Figure 73, the mean flow properties were found to be consistent across all Mach numbers. An initial drop in mean velocity was found to be due to a small area change from the test section flange to the location where the windows were installed. This change is caused by a 0.015 in. (0.38 mm) step across the flange to glass joint near Datum B of Figure 61, as an artifact of the original glass seal design on all interior faces of the test section. This caused a test section cross-section area change from 25.00 cm² to 25.77 cm². However, the additional mean velocity rise past the initial step zone also had to be accounted for.

An analysis of the test section using Head's numerical integral method for turbulent boundary layers [112] for the internal tunnel volume shown in Figure 61 was conducted. The calculation began at the plane of turbulence generation and continued until the end of the test section. The results of these calculations are shown in Figure 76 in comparison to the measured mean velocity profiles gained from the passive grid study. These results confirm that the mean velocity gradient present in the square test section depicted in Figure 75 are indeed due to boundary layer thickness displacement effects, as an approximate 4% increase in velocity over the traverse region is associated with a reduction in effective area from approximately 25.7 cm² to 24.7 cm².

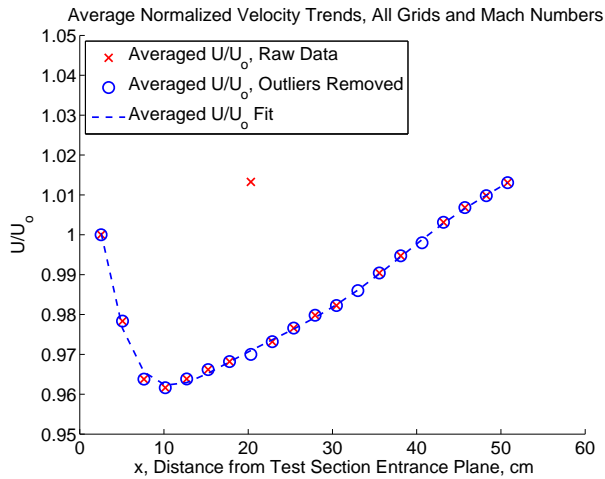


Figure 75: Test section mean velocity profile within traverse region averaged across all grids and Mach numbers; U_o denotes test section inlet mean velocity.

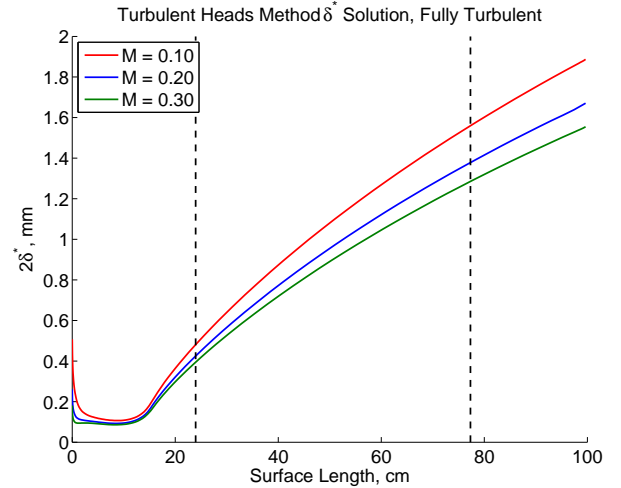


Figure 76: Turbulent boundary layer displacement thickness results for test section entrance Mach numbers. Black lines denote the traverse region shown in Figure 61.

Additional measurement of mean profile evolution complemented the integral method based boundary layer calculations and CTA data. A sample result is shown in Figure 77 for a test section inlet Mach number of $M = 0.3$ with $y = 0$ denoted as the centerline of the tunnel. These profiles agree with earlier mean flow analysis and showed that a 3×3 cm. corridor was present along the length of the test section that was transversely homogeneous in the mean and independent of boundary layer effects. These measurements serve to show that turbulence within this corridor is independent of mean shear, with a small velocity gradient in the streamwise direction.

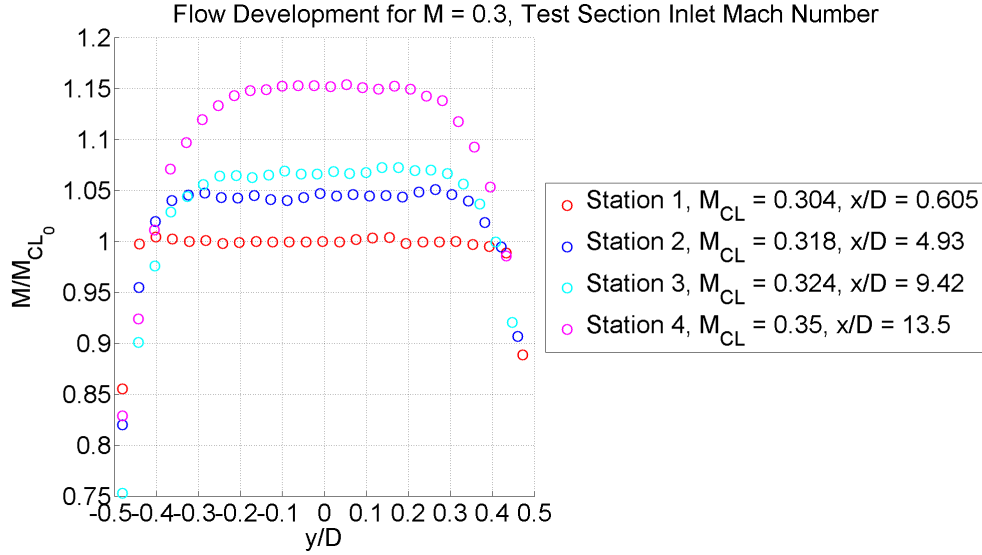


Figure 77: Measured mean profile evolution for inlet test section Mach number of 0.3; $D = 5.0$ cm.

It is also noted that while an apparent increase in u_{rms} was observed as shown in Figure 73, these findings were initially attributed to measurement error due to their apparent counterintuitive nature and larger discrepancies as Mach number decreased. This prompted re-evaluation of the CTA system, from which a new signal conditioning routine was introduced as described by Bruun [57]. However, as discussed in the following sections, this trend proved to be related to the effects of the nozzle on the flowfield.

The usage of passive grids and further analysis of the data set was abandoned due to disappointing performance in generating high turbulence levels for usage in flame kernel studies. However, lessons learned from this study led to several major facility developments as detailed previously in Section 3.1, as well as prompted refinement of CTA and measurement techniques. Additionally, experience was gained on how to best handle the trade-offs between designing a facility that is fully optically accessible and one this able to provide favorable conditions for turbulence and combustion evaluation. These lessons learned have been applied to the design of the supersonic reacting facility as detailed in Section 3.2.2, as well as to current active grid studies.

5.1.3.2 Blown Grid Studies A blown jet grid following the general design of Gad-el-Hak [105] and incorporating the later recommendations of Fransson [69] was designed and constructed in response to the low turbulence intensities observed during the passive grid studies. The grid illustrated in Figure 78 features a solidity of 33% and is constructed of parallel cylindrical rods of diameter 6.35 mm with a mesh width of 16.2 mm. These design characteristics were chosen to emulate single plane round rod grids as used by many investigators to provide a passive baseline [108, 48, 46]. Machined jet orifices with a diameter of 3.86 mm are horizontally spaced at the according mesh width to ensure that the jets merge uniformly and ensure spanwise homogeneous flow in no more than 30 mesh lengths from the grid in a rectangular duct flow [105]. The selection of jet orifice size was chosen to ensure minimal pressure loss between injection ports, as usage of individual jet tuning valves at this scale would be prohibitively expensive. An overview of the bleed system is as shown previously in Figure 19.

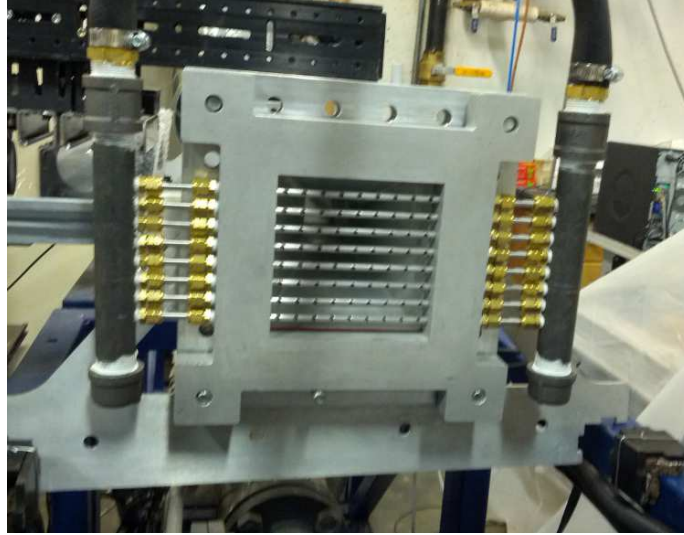


Figure 78: Blown grid installed in counterflow configuration with jets facing upstream

The performance parameters of the grid are given as the bleed mass flow percentage J of a given test section mass flow in Table 12, with individual mean jet velocities shown in Table 13. Test conditions are determined by the test section inlet Mach number.

Table 12: Total bleed mass flow rates (kg/s) for active blown jet grid.

J (%)	10	15	20
$M = 0.1$	0.0099	0.0149	0.0199
$M = 0.2$	0.0200	0.0299	0.0399
$M = 0.3$	0.0301	0.0451	0.0602
$M = 0.5$	0.0509	0.0764	0.1018
$M = 0.7$	0.0729	0.1093	0.1457

Table 13: Average jet velocity (m/s) for active blown jet grid by bleed setting.

J (%)	10	15	20
$M = 0.1$	9.70	14.55	19.40
$M = 0.2$	19.10	28.59	38.12
$M = 0.3$	27.76	41.65	55.53
$M = 0.5$	42.21	63.31	84.42
$M = 0.7$	51.71	77.57	103.42

As detailed by the analysis of Gad-el-Hak [105] using control volume methods and supported by experimental data, higher bleed mass flows correspond to larger pressure drops and turbulence intensities with the jets oriented upstream (counterflow) as opposed to downstream (coflow) for a traditional rectangular duct setup similar to that shown in Figures 59 and 62. As the facility shown in Figure 61 is not similar to anything observed in literature, initial studies have initially focused on measuring RMS velocities and turbulence intensities generated by counterflow conditions. The test matrix of this study is given in Table 14 below.

Table 14: Active blown jet grid test matrix

M	Counterflow J (%)		
0.1	10	15	20
0.2	10	15	20
0.3	10	15	20

A summary of the mean and RMS velocity trends corresponding to the test matrix presented in Table 14 is presented below. Figure 79 shows the differences in RMS velocities between bleed ratios at a glance, while Figures 80 and 81 complement Figure 73 in showing the normalized mean and RMS velocity trends, where U_o and u_o are as defined previously. Figure 82 shows local turbulence intensity relative to axial location within the test section. Axial distance is measured relative to Datum B of Figure 61, similar to the passive grid studies.

It is seen in Figure 79 that increasing the bleed ratio of the blown grid results in increasing the TKE of the flow within the test section. The effect of the blown grid on the mean flow as shown in Figure 81 appears to have the same behavior as discussed previously, however measured downstream acceleration of the flow is not as well defined as the passive grid cases. This effect is more pronounced at higher bleed ratios, suggesting that the boundary layer development along the test section walls is affected by the higher turbulence levels. This in turn influences the local turbulence intensity shown in Figure 82, which resembles that of the flatness shown by the passive case in Figure 74.

The RMS velocity trends of Figure 79 along with the normalized RMS velocity in Figure 80 show that a noticeable increase in u_{rms} is present as injection ratio increases. For $J = 10\%$, this behavior is less pronounced, but does occur further downstream. It can be seen that the normalized u_{rms} first decreases more precipitously for low bleed ratios, while high bleed ratios exhibit this behavior to a lesser extent. This is compared to the passive grid case

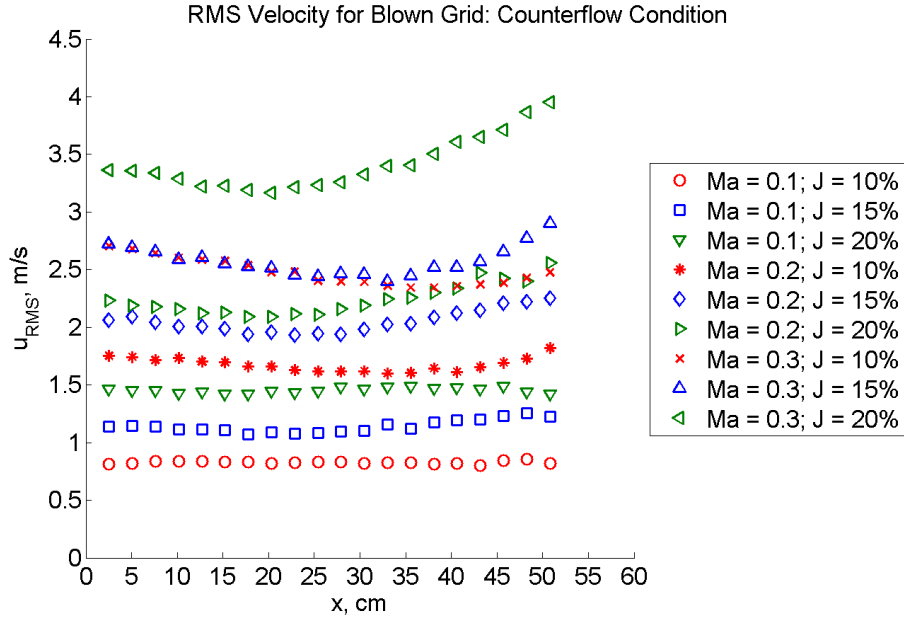


Figure 79: RMS velocity trends corresponding to test matrix in Table 14.

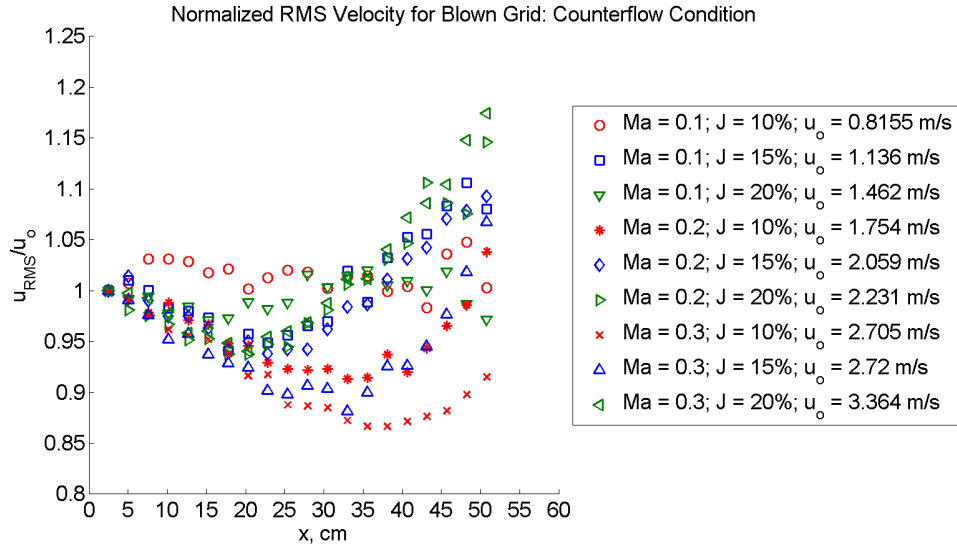


Figure 80: Normalized RMS velocity trends corresponding to test matrix in Table 14.

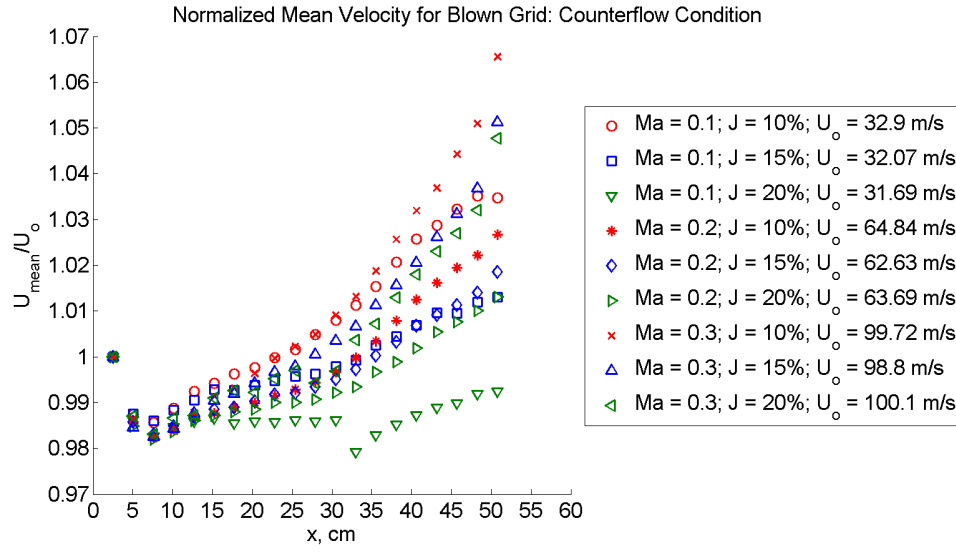


Figure 81: Normalized mean velocity trends corresponding to test matrix in Table 14.

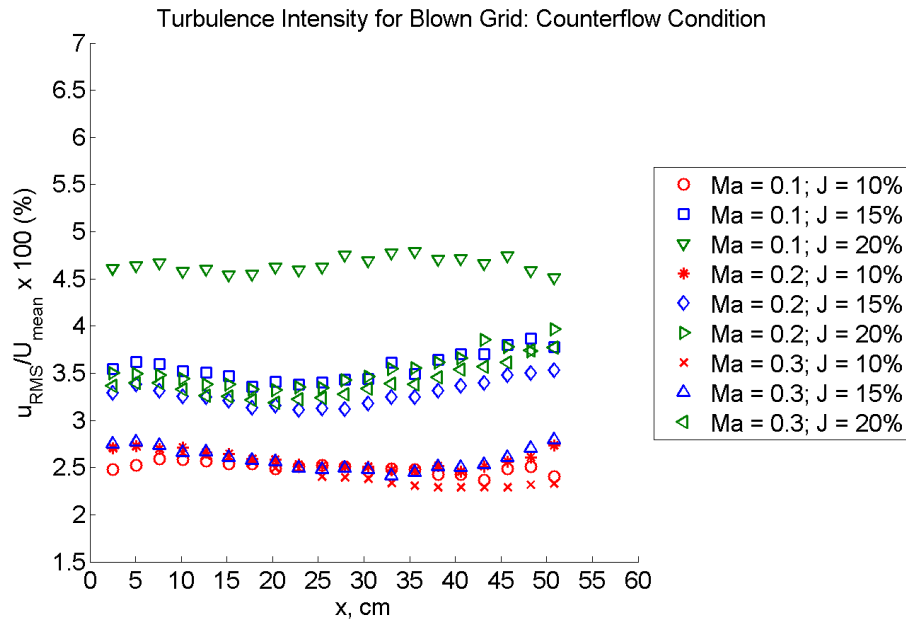


Figure 82: Local turbulence intensity trends corresponding to test matrix in Table 14.

shown in Figure 73, which shows that the normalized u_{rms} is always rising monotonically.

The complex flow physics of having a blown jet grid in addition to the initial observation of an apparent production mechanism in both the active and passive cases required additional analysis before more detailed evaluation of the turbulence. As a result a numerical analysis of the geometry was conducted as described in Section 5.1.4.

In addition, the lack of resemblance to traditional homogeneous and isotropic turbulence prompted the construction of a diverging box duct as shown in Figure 62. The purpose of this facility configuration is to serve as a well-understood baseline and to be able to compare results to literature. A detailed study using the diverging duct has been conducted using a CTA multi-component yaw-probe technique. The results are presented in the following paragraphs and sections.

The normalized streamwise mean velocity and mean velocity derivative profiles for the subsonic facility are shown in Figure 83. Typical experimental results are compared to profiles calculated using isentropic equations ignoring viscous effects such as boundary layer growth. As shown, the facility has a smooth parabolic $d\bar{U}_1/dx_1$ profile within the nozzle, which closely follows that of the isentropic results. Additionally, the small test section exhibits core flow acceleration as attributed to boundary layer growth. However, it is shown that this core acceleration does not result in a significant post-contraction velocity gradient, as $d\bar{U}_1/dx_1 \sim \mathcal{O}(10^0)$ or less. This indicates that the effects of mean strain within the subsonic flow facility are limited to the nozzle, and are negligible in the test section.

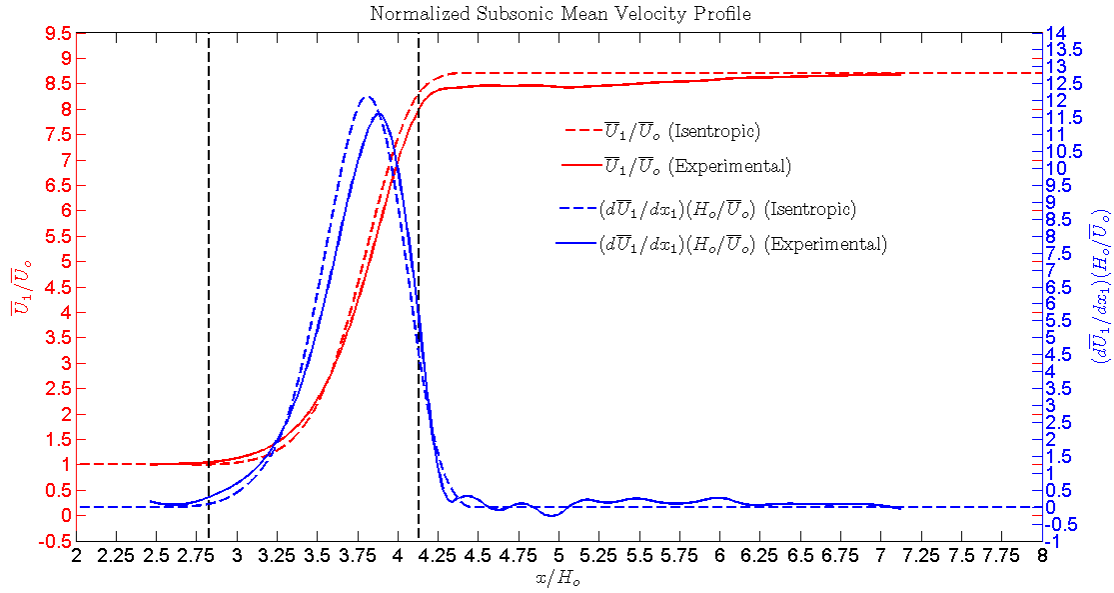


Figure 83: Normalized subsonic facility mean velocity profile and mean velocity derivative. Grid plane mean velocities U_o are given in 3.4 and H_o is the inflow duct height $H_o = 14.6$ cm. The location of the nozzle is shown by the vertical dotted lines.

The streamwise evolution of RMS velocities and turbulent kinetic energy for test section Mach number conditions of $Ma = 0.200$ is shown in Figure 84 for the range of bleed settings considered. Moreover, a passive case with the blown jet grid configured as shown in Figure

34 is presented. In the cases where the bleed ratio is larger than 20%, energy is transferred from the streamwise (u') to the spanwise velocity components (v' and w') and turbulent kinetic energy is produced. Figure 63 illustrates that the inflow turbulence is homogeneous. The effect of the nozzle can be explained by considering Reynolds stress transport in homogeneous turbulence as described by Equation 21, where the density is given as ρ and p' is the fluctuating pressure. The production, pressure-strain and dissipation tensors are defined as \mathcal{P}_{ij} , \mathcal{R}_{ij} , and ϵ_{ij} , respectively.

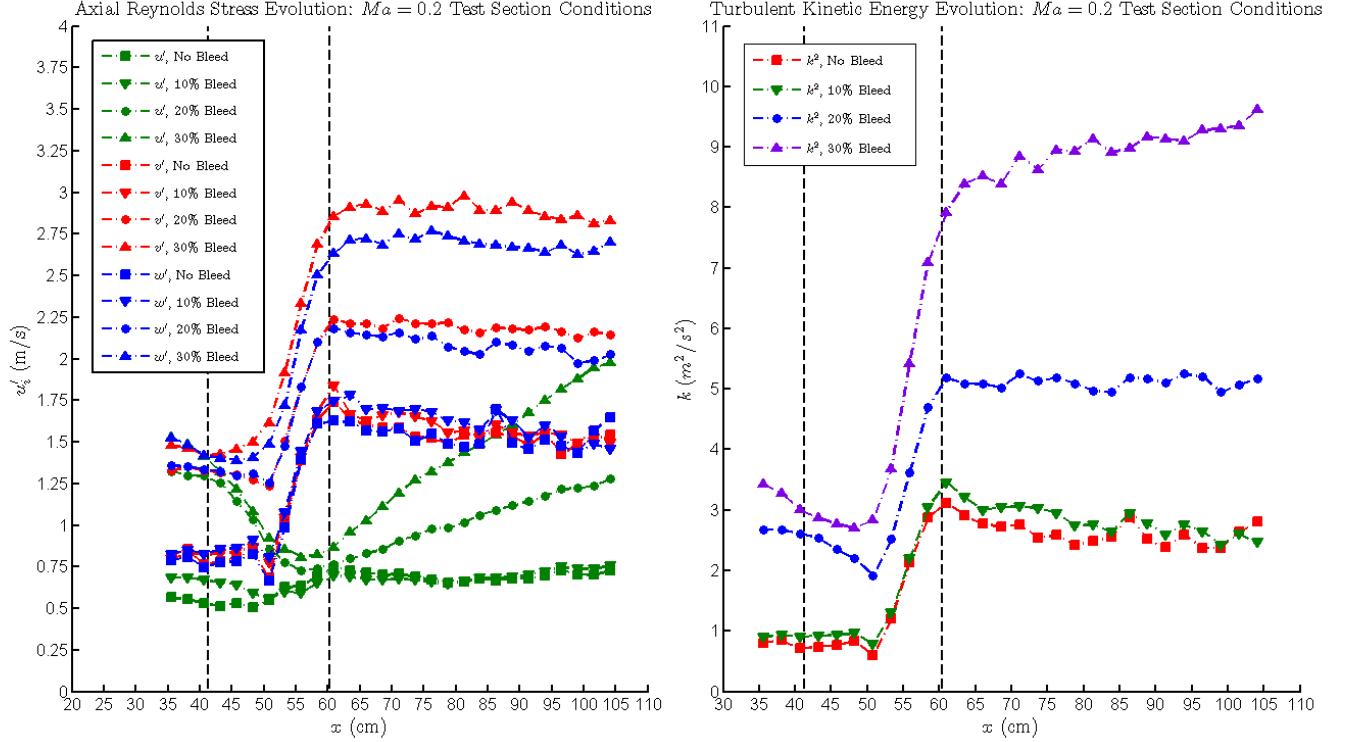


Figure 84: Evolution of RMS velocity and turbulent kinetic energy for blown grid settings associated with test section Mach numbers of $Ma = 0.200$. The location of the nozzle is shown by the vertical dotted lines.

$$\frac{\partial \overline{u_i u_j}}{\partial t} = \underbrace{-\overline{u_j u_k} \frac{\partial \overline{U}_i}{\partial x_k} - \overline{u_i u_k} \frac{\partial \overline{U}_j}{\partial x_k}}_{\mathcal{P}_{ij}} + \underbrace{\frac{1}{\rho} \left(\overline{p' \frac{\partial u_j}{\partial x_i}} + \overline{p' \frac{\partial u_i}{\partial x_j}} \right)}_{\mathcal{R}_{ij}} - \underbrace{2\nu \overline{\frac{\partial u_i}{\partial x_k} \frac{\partial u_j}{\partial x_k}}}_{\epsilon_{ij}} \quad (21)$$

Examination of the production term \mathcal{P}_{ij} reveals that for an accelerating one-dimensional ($d\overline{U}_1/dx_1 > 0$), incompressible ($d\rho = 0$) flow with approximately axisymmetric anisotropic turbulence, the turbulent kinetic energy (TKE) production term \mathcal{P}_k is represented as half the trace of \mathcal{P}_{ij} as shown in Equation 22.

$$\mathcal{P}_k = \left(\overline{u_2^2} - \overline{u_1^2} \right) \frac{d\overline{U}_1}{dx_1} \quad (22)$$

Thus, positive TKE production occurs for $\overline{u_2^2} > \overline{u_1^2}$ as shown experimentally. However, for low bleed cases, u' either decreases slightly halfway through the nozzle, or u' increases through the nozzle. In the latter case, this can partially be explained by acoustic noise that is most prevalent for passive grid cases, see Figure 65 and further discussion in the following paragraphs. However in the former case, further analysis is needed with respect to the Reynolds stress transport budget presented in Equation 21, to identify the relative magnitude of pressure-strain tensor \mathcal{R}_{ij} components in relation to production and dissipation terms.

Insight into \mathcal{R}_{ij} is provided from examining the Poisson equation for fluctuating pressure. It is shown by Pope (p. 391)[77] that fluctuating pressure in an incompressible, homogeneous turbulent flow is described by Equation 23, where $p'_{(r)}$ and $p'_{(s)}$ denote rapid and slow fluctuating pressure contributions, respectively.

$$\frac{1}{\rho} \frac{\partial^2 p'}{\partial^2 x_i} = \underbrace{-2 \frac{\partial \bar{U}_i}{\partial x_j} \frac{\partial u_j}{\partial x_i}}_{\frac{1}{\rho} \frac{\partial^2 p'_{(r)}}{\partial^2 x_i}} - \underbrace{\frac{\partial^2}{\partial x_i \partial x_j} (u_i u_j)}_{\frac{1}{\rho} \frac{\partial^2 p'_{(s)}}{\partial^2 x_i}} \quad (23)$$

In the nozzle, the rapid pressure term dominates and serves as a Reynolds stress “re-distribution” term. While \mathcal{P}_{ij} is in closed form, analysis of \mathcal{R}_{ij} and ϵ_{ij} is needed to fully understand the Reynolds stress budget in the nozzle. It has been shown previously in this paper via analysis of flow fields generated by the blown jet grid in the divergent duct, that high Re_λ inflow turbulence has been generated that satisfies the assumption of local isotropy[51]. This greatly simplifies experimental measurement and analysis of ϵ_{ij} . However, this assumption may or may not hold within and downstream of the nozzle across all components of the energy spectrum tensor E_{ij} . Hence, analysis of energy spectra components $E_{ii}(\kappa_1)$ corresponding to Reynolds stresses $\overline{u_i^2}$ are needed to gain insight into the behavior of ϵ_{ij} at and after the nozzle to complement rapid pressure strain investigations.

5.1.3.3 Vane-Stirred Grid Studies The blown grid was shown to produce favorable turbulence levels for the flame kernel studies. However, a complicated secondary fuel/air mixing system was required to avoid fuel/air discontinuity as a result of the turbulence generator. While some flame studies were conducted using the blown grid with a secondary fuel mixing system, a less complicated solution was desired. An active rotating vane grid was the solution to this problem. RMS velocity trends are shown in Figure 85 for the vane grid set at a synchronous rotation rate of 2 rot/s for Mach numbers up to 0.3. Compared to the blown grid results (see, i.e. Figure 84), the vane grid produced nearly the same turbulence intensities and isotropy levels as the blown grid, without the complexity of a secondary fuel and mixing system. The longitudinal integral length scales for this setup are also shown in Figure 86. These data are used to place flame kernels on regime diagrams and compare them to classical correlations.

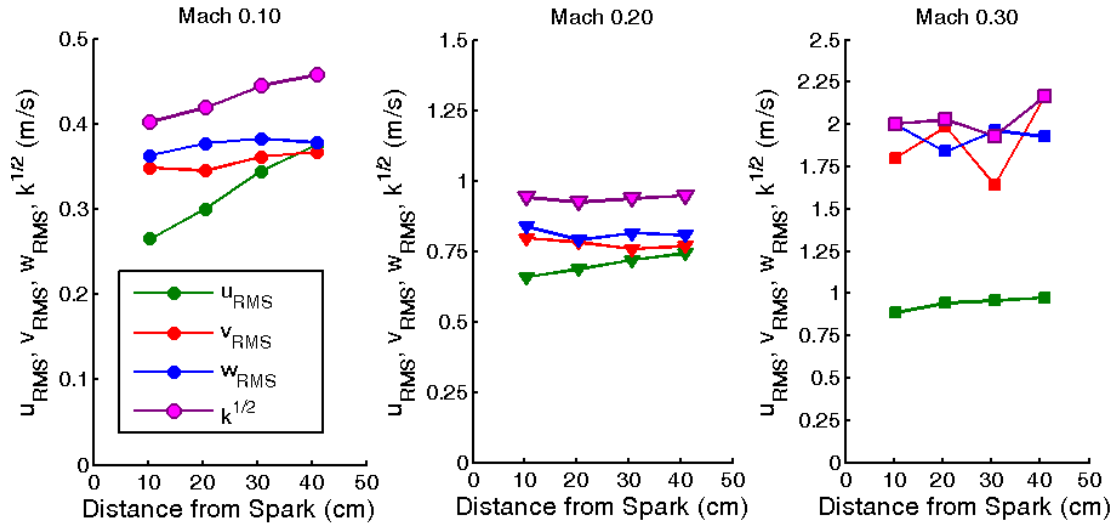


Figure 85: Evolution of RMS velocity for vane grid studies for test section Mach numbers of $M = 0.1 - 0.3$.

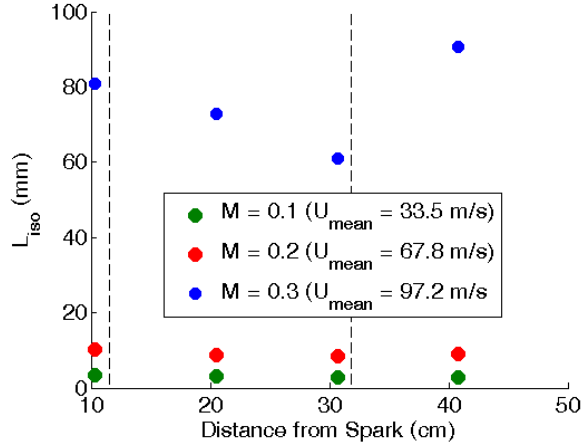


Figure 86: Evolution of the longitudinal integral length scale for vane grid studies in the subsonic compressible rig at Mach numbers $M = 0.1 - 0.3$.

5.1.3.4 Post Contraction Passive Grid In an attempt to increase the isotropy of the turbulence generated at higher Mach numbers, a small grid was placed downstream of the converging nozzle, instead of upstream. The design follows the same guidelines already presented for the other passive grids. As a result, the turbulence levels generated are $\approx 2\%$. The Taylor-Reynoldsnumbers are 43, 86 and 193 for $M = 0.1$, $M = 0.2$ and $M = 0.3$ respectively. An example for the produced velocity power density spectra is shown in Fig. 87. It can be seen that smoothing operations to reduce the noise have been applied to all runs in this section. The aim of increasing isotropy has been achieved for run conditions at $M = 0.1$, see Fig. 90. However, while for the $M = 0.2$ case the condition $\overline{v'v'} = \overline{w'w'}$ holds true, there is a significant deviation to the streamwise $\overline{u'u'}$ component. As $\overline{u'u'} > \overline{v'v'}$ and $\overline{w'w'}$, this significant anisotropy at higher Mach numbers is the opposite trend observed when the turbulence grid is positioned before the contraction, as shown in Fig. 84. Reasons for this effect and the anisotropy could be operation of the passive grid close to choking conditions and suppression of lateral fluid motion due to the grid being positioned after the contraction.

The TKE decay for these experiments is shown in Fig. 89. Scattering of the results for n is within expected boundaries and the values are close to 1, indicating that the behavior of the grid turbulence is normal, even though it is anisotropic at higher Mach numbers.

The integral length scales are shown in Fig. 71. For all four velocity cases the initial size is on the order of the grid spacing. The growth however seems to be influenced by the Mach number. Up to $M = 0.25$ the growth rate increases only to drop back to $M = 1$ levels for $M = 0.3$. This anomalous behavior might be due to the increasing anisotropy but needs to be investigated further.

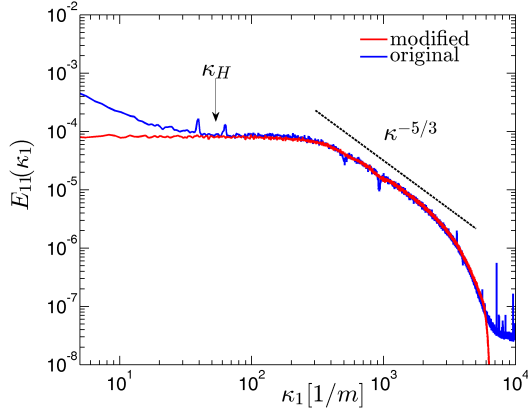


Figure 87: Velocity power density spectrum at $M = 0.1$, before and after operations to remove noise have been applied.

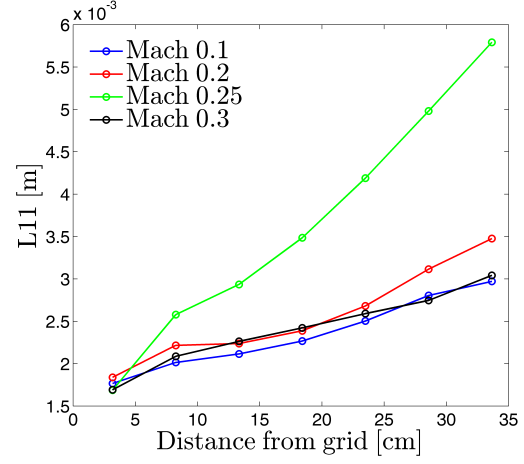


Figure 88: Development of the stream-wise integral length scales along the tunnel.

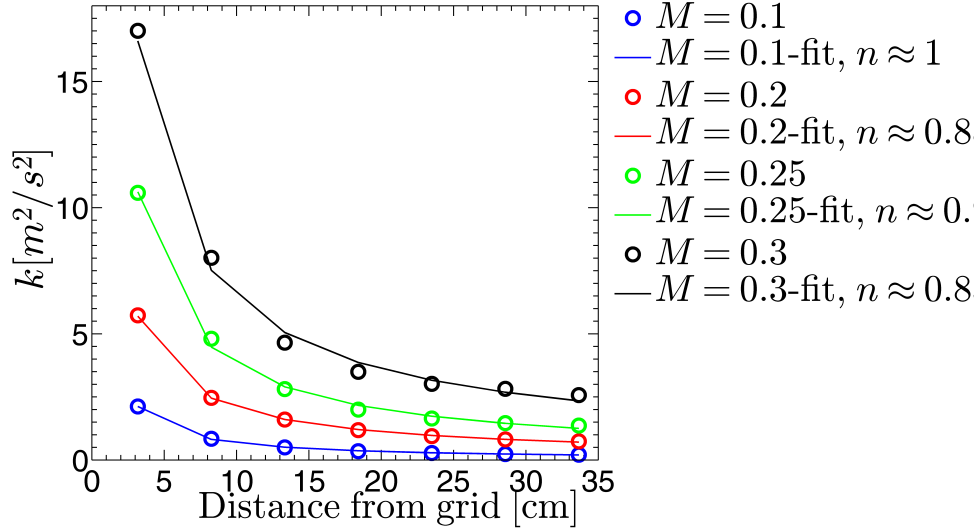


Figure 89: Velocity power density spectrum at $M = 0.1$, before and after operations to remove noise have been applied.

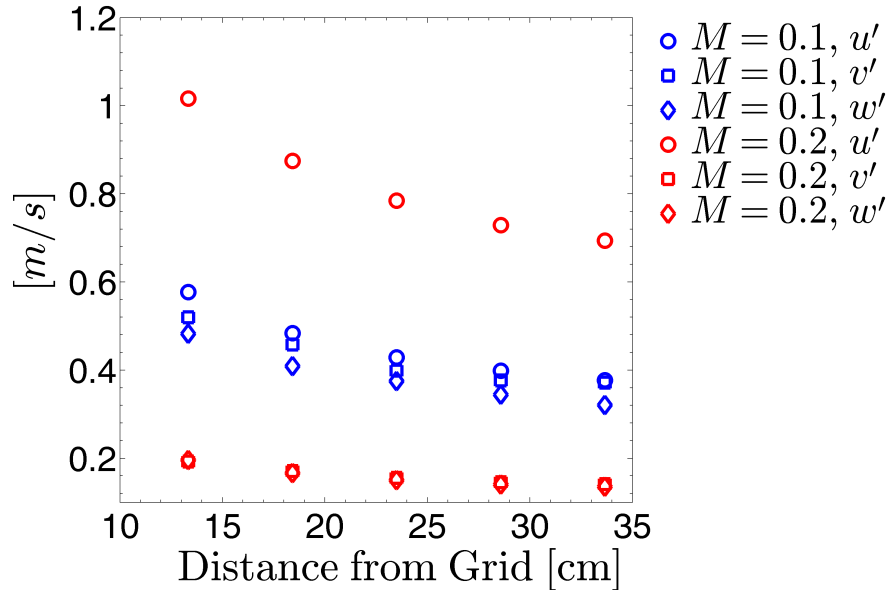


Figure 90: Main Reynolds stress components for two of the investigated Mach numbers. The anisotropy between the streamwise and lateral components at $Mach = 0.2$ case is clearly visible.

5.1.4 Numerical Investigation of Subsonic-Compressible Facility

In this section we perform numerical simulations to investigate the impact of the wind tunnel contraction on the grid-generated turbulence. Previous experiments [58] have shown that severe contraction ratios can lead to anisotropy in the Reynolds stress tensor. Their results, however, are of limited scope to the current experiments because the measurements were terminated shortly after the nozzle. In this experimental investigation, the primary region of interest is the channel section following the nozzle in which flame kernels will be initiated. Hence, a better understanding of the turbulence in the post-contraction section of the channel would aid in interpreting the results from flame kernel experiments. To this end, we perform direct numerical simulations (DNS) to investigate the statistics of turbulence flowing through the same geometrical contraction used in the subsonic experiments.

5.1.4.1 Numerical Methodology The fully-compressible equations for mass, momentum, and energy are solved using the MacCormack second order scheme [113] with a finite volume discretization. Characteristic subsonic inflow and outflow boundary conditions are employed at the entrance and exit of the channel, respectively. Two limitations of the current simulations are that slip-walls are employed for the channel walls, and that Reynolds number of the flow is artificially lowered to make a DNS tractable. We justify the use of slip-wall boundary conditions by noting that the contraction ratio in the channel is severe, and primarily has an inviscid effect on the flow field. Furthermore, the contraction induces a favorable pressure gradient on the flow, which suppresses boundary layer growth and prevents separation. The Reynolds number of the flow is lowered by increasing the fluid viscosity, and we assume that the effect of the severe contraction on the turbulence is largely Reynolds number independent. In other words, the dynamics of vortex stretching, etc. that are expected in this flow field are primarily a function of the contraction ratio, and not of the turbulent Reynolds number.

5.1.4.2 Geometry and Boundary Conditions The geometry used for the simulations is the same from the subsonic experiments, and a rendering is provided in Figure 91. The inflow plane for the numerical simulations is located at the same position as the grids used to generate turbulence in the experiments. A summary of the channel dimensions and grid resolution is provided in Table 15.

Table 15: Summary of relevant geometry and grid information used for channel simulations.

L_x (m)	Inflow $L_y = L_z$ (m)	Outflow $L_y = L_z$ (m)	$n_x \times n_y \times n_z$
1.06	0.146	0.050	$640 \times 128 \times 128$

The mean inflow boundary conditions are realized by specifying a velocity of 20 m/s in the x direction, and a temperature of 300 K. The outflow boundary condition has a specified pressure of 101325.0 Pa.

As can be seen in Figure 91, the location of turbulence generation in the experiments is very close to the start of the nozzle. For numerical simulations, this necessitates that the

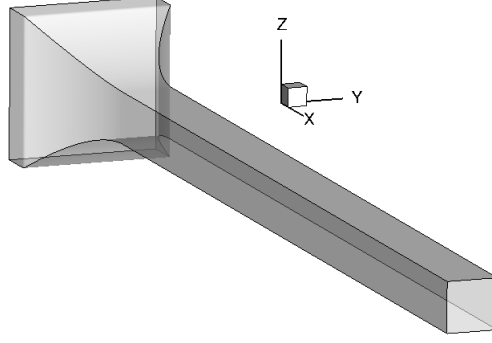


Figure 91: Rendering of the subsonic channel geometry used for the simulations.

inflow turbulence be as physical as possible. To accomplish this, we evolve initially synthetic turbulence to a physical state in a separate simulation, and bring the turbulent fluctuations into the channel with a superimposed mean flow following Taylor’s hypothesis. The initial solenoidal velocity field is constructed following Rogallo [114] with the Kraichnan energy spectrum [115]. The relevant parameters for the generation of the inflow turbulence are given in Table 16.

Table 16: Summary of simulation parameters for inflow turbulence generation. The k_o reported is normalized by the minimum wavenumber upstream of the contraction ($2\pi/0.146 \text{ m}^{-1}$). Re_λ and Re_l are the Reynolds numbers based on the Taylor microscale and integral length scale, respectively.

$L_x \times L_y \times L_z \text{ (m)}$	$n_x \times n_y \times n_z$	k_o	$u_{\text{rms}} \text{ (m/s)}$	$\nu \text{ (m}^2\text{/s)}$	Re_λ	Re_l	$k_{\text{max}}\eta$
$0.438 \times 0.146 \times 0.146$	$384 \times 128 \times 128$	6	7.0	$8.0\text{E-}4$	67.5	84.3	1.32

As seen in Table 16, $k_{\text{max}}\eta = 1.32 > 1$ indicates that the simulation is adequately resolved for the purposes of this investigation. The synthetic turbulence is evolved until it reaches a physical state, during which time it decays because there are no production mechanisms. It is well known [116] that the negative of the velocity gradient skewness takes a limiting value between 0.4 and 0.6 in incompressible isotropic turbulence. This quantity is monitored during the simulation, and was found to be within the acceptable range after approximately 0.5 large-eddy turnover times τ , where $\tau = l/u_{\text{rms}}$. We take the solution at $t/\tau = 1$ as the turbulence for the inflow, which is characterized by $Re_\lambda = 38.3$ and $u_{\text{rms}} = 5.91$.

5.1.4.3 Channel Results

Instantaneous Flow Features

Because the area contraction in this channel is rather large (8.5:1), we expect alteration of the vorticity field through the mechanisms of vortex stretching. To see this effect, we plot an isosurface of the second invariant of the velocity gradient tensor (the Q-criterion) [117] to visualize regions of strong rotation in Figure 92. As can be seen in Figure 92, the vorticity in the x direction is greatly amplified through the contraction. Other results (not shown)

depict a strong reduction in vorticity in the y and z directions, as expected. These qualitative results highlight the impact of the area reduction on the instantaneous flow features.

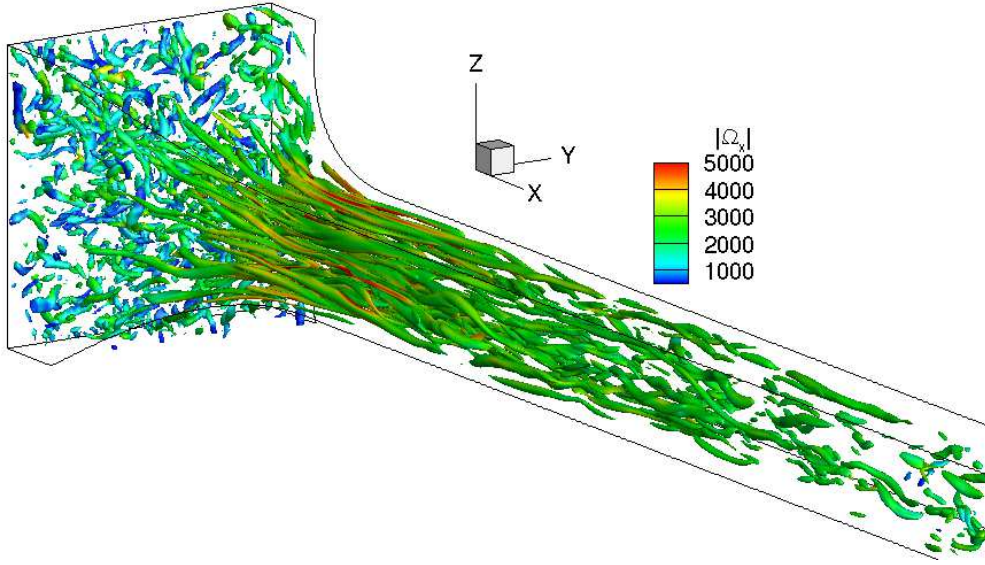


Figure 92: Isosurface of the Q-criterion corresponding to regions of strong rotation. The isosurface is colored by the magnitude of the vorticity vector in the x direction.

Mean Flow Characterization

To evaluate the statistically stationary state of the flow, we employ the Reynolds average, where the mean of a variable f is calculated by

$$\bar{f} = \frac{1}{T} \int_t^{t+T} f dt, \quad (24)$$

where t is the starting time and T is the length of the interval used for averaging. The averaging period T is approximately 20 convective time scales T_f , defined by

$$T_f = \int_0^{L_x} \frac{dx}{\bar{U}(x)}, \quad (25)$$

which is approximately $8.28\text{E-}3$ s. This time interval provided convergence of first- and second-order statistics. The mean flow is expected to agree reasonably well with the results from 1D isentropic flow theory. Figure 93 presents a plot of the mean centerline x -component of velocity, and Figure 94 plots the centerline mean pressure and temperature.

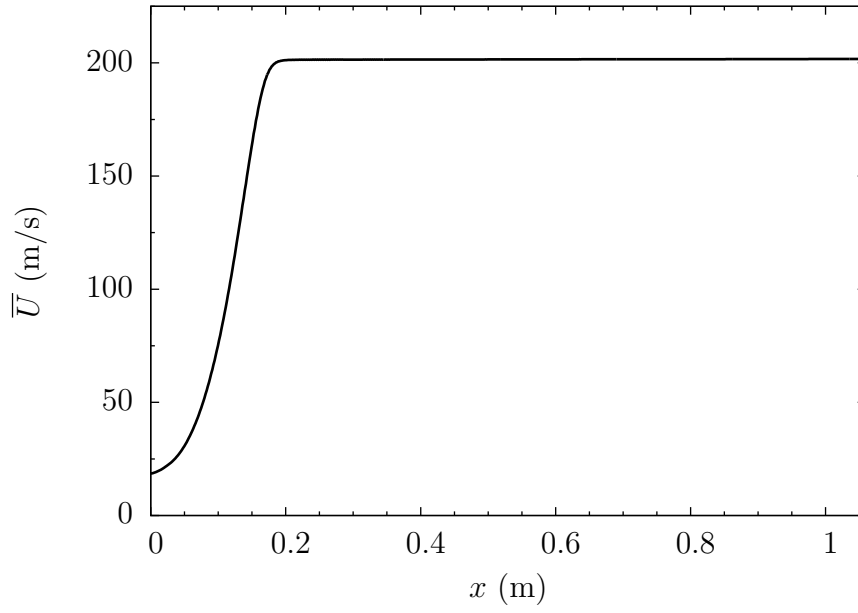


Figure 93: Plot of the mean velocity in the x direction along the centerline of the channel. The symbol at $x = 1.06$ m indicates an estimate of the exit velocity from isentropic flow theory.

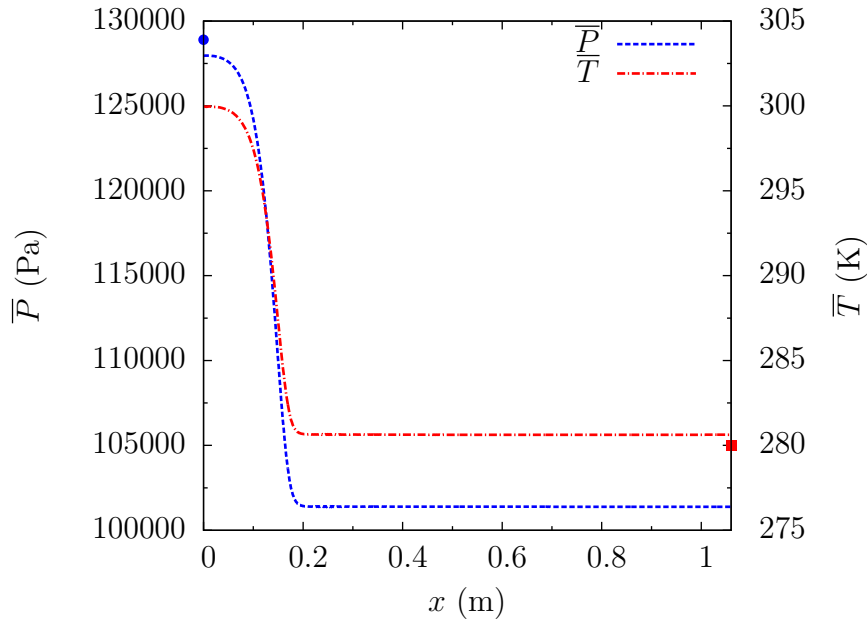


Figure 94: Plot of the mean temperature and pressure along the centerline of the channel. The square symbol at $x = 1.06$ m and the circle at $x = 0$ m indicate the estimated exit temperature and inlet pressure, respectively, from isentropic flow theory.

Turbulence Statistics

In Figure 95 we present profiles of u_{rms} , v_{rms} , w_{rms} , and the turbulent kinetic energy $k = \overline{u_i u_i}/2$ along the centerline of the channel.

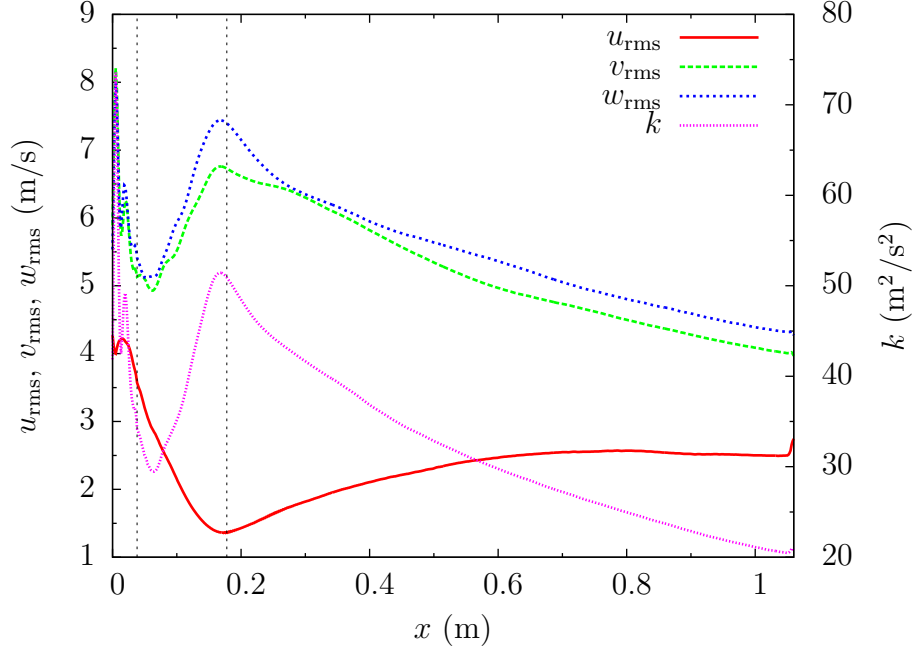


Figure 95: Spatial evolution of rms velocities and turbulent kinetic energy along the centerline of the channel. The beginning and end of the contraction are marked with the vertical dashed lines.

There are many aspects of the results in Figure 95 that should be discussed. First, through the nozzle we see a large anisotropy generated in the Reynolds stress as u_{rms} is suppressed, while v_{rms} and w_{rms} are amplified. Second, isotropy is not regained within the channel, since that would require u_{rms} , v_{rms} , and w_{rms} to be equal. Although it appears that the primary stresses are equilibrating to one another, the channel length is not sufficient for full isotropy to be achieved. Third, paralleling the amplification of v_{rms} and w_{rms} , we see that the turbulent kinetic energy increases through the nozzle.

To better understand the observations, we plot the individual terms of the turbulent production rate $\mathcal{P} = -\overline{S_{ij}u_i u_j}$ along the centerline of the channel in Figure 96. Figure 96 indicates that there is strong production of turbulent kinetic energy through the contraction, which is stemming from the primary stresses in the y and z directions. We see that $-\overline{S_{11}u_1 u_1} < 0$, which is expected because

$$\overline{S_{11}} = \frac{\partial \overline{U}}{\partial x_1} > 0 \quad (26)$$

due to the bulk acceleration through the nozzle. Since the flow is mildly compressible, it is not immediately apparent that $\overline{S_{11}} > 0$ implies that $\overline{S_{22}} < 0$ and $\overline{S_{33}} < 0$. However, inspection of the mean strain rate along the centerline of the channel showed that this is

indeed the case, hence we expect positive contributions to the production rate from $\overline{u_2 u_2}$ and $\overline{u_3 u_3}$, which is confirmed in Figure 96. Finally, we see that the production rate quickly dies off after the contraction is finished, thus allowing dissipation to play a more dominant role, as can be deduced from the decay in turbulent kinetic energy depicted in Figure 95.

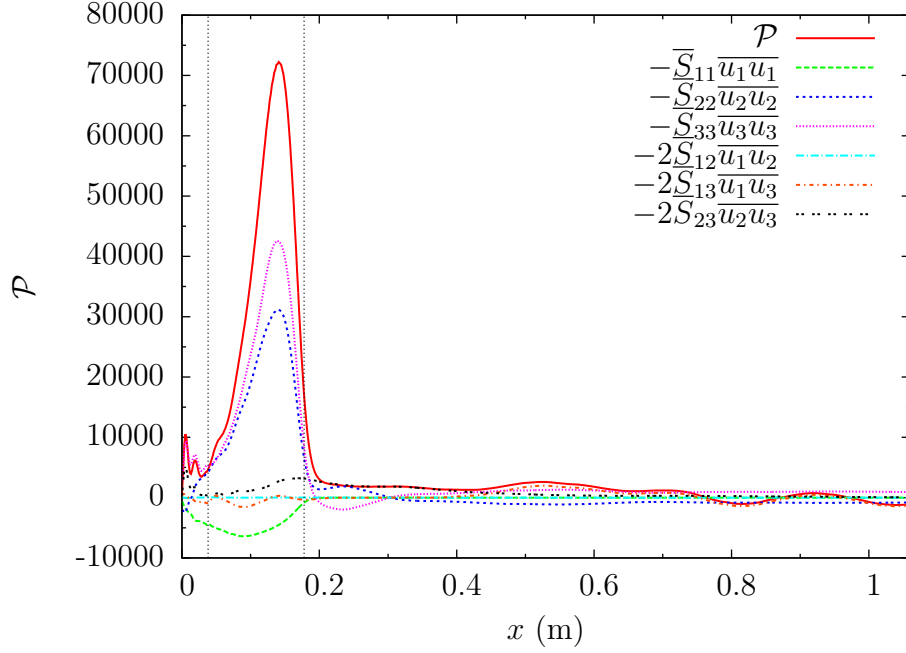


Figure 96: Production rate of turbulent kinetic energy along the centerline of the channel. The beginning and end of the contraction are marked with the vertical dashed lines.

Although the conditions for this numerical study are not identical to the experiment, the results serve to highlight how the contraction alters the incoming turbulence. The overall turbulence intensity is enhanced by the contraction, while isotropy is lost. These results motivate pushing the plane of turbulence generation as far downstream as possible without choking the flow.

5.1.5 Experimental Investigations of Supersonic Turbulence

Several techniques can be used to measure velocities in supersonic flows. These techniques fall roughly into three categories: probe-type, particle tracking and molecular tagging techniques. A supersonic flow may be probed with a Pitot-static or hotwire probe. Interpretation of these data is difficult because both of these probes measure a post shock velocity and therefore a shock correction must be applied. Furthermore, in the case of the Pitot probe, only near zero frequency content can be resolved making it a bad choice if turbulence measurements are desired. Molecular tagging techniques excite either a naturally occurring or seeded molecule and track its motion downstream. The HTV (discussed) above is an example of this technique. This technique is ultimately limited by the accuracy of the optics used and is relatively difficult to install experimentally due to the needed for multiple lasers. Particle tracking techniques include Laser Doppler Velocimetry and Particle Image Velocimetry. In the former, a continuous-wave laser is split and turned on itself to produce a fringe pattern within a probe volume. Particles passing the fringe pattern will be illuminated and a suitable viewing system can measure the speed based on the "bursts" of light. Typically this type of system is used to measure all three components of velocity at a single point using three different laser heads. Joint spatial and temporal statistics are difficult because LDV measures at a single location with a non-uniform time spacing. Formation of the temporal autocorrelation requires very advanced algorithms to convert to uniform time spacing. There have been some attempts to expand the probe volume so as to measure spatial autocorrelations[118], but these techniques require special optical systems typically not included in off-the-shelf LDV systems. PIV is slightly more difficult to set up but offers a two-dimensional measurement of two components of the velocity vector. It can be expanded to three components on a plane using an additional camera (Stereo-PIV) and to three components in a volume with a total of four or more cameras (Tomographic PIV). The spatial resolution can be minimized using special microscopic camera optics; offering spatial resolution down to the Kolmogorov scale for some flows of engineering interest. PIV is clearly a strong choice for initial velocity measurements in this supersonic environment.

5.1.5.1 Flow Field Visualization A brief introduction to the flow field is required prior to discussing detailed PIV results. Three supersonic tunnels were tested throughout the program; each with an improved design on the laser. The Supersonic Fixed Divergence Tunnel was found to produce no shocks (see Figure 97) and is nominally $5 \times 5 \text{ cm}^2$. The channel diverges by 2% after the first viewing window. The CD nozzle is a minimum length nozzle designed to produce Mach 1.5 flow. The divergence will accelerate the flow in cold-flow tests, but will counter Rayleigh flow deceleration during fired (flame kernel) tests. The stagnation temperature was set to approximately $550K$ for the data discussed below. This corresponds to a flow velocity of approximately 550 m/s . At these speeds our PIV particles exit the test section in about 1.8 ms . These conditions require incredibly accurate laser pulse and PIV camera timing.

Table 17: Turbulence generator properties for initial supersonic studies.

Turbulence Generation	Hole Size (mm)	Solidity	u'	v'	k	Re_l^1	Re_λ^2
Baseline (No Grid)	-	-	1.255	1.907	4.424	2,341	187
Passive Grid	8.89	33%	2.759	3.511	16.133	3,601	232
Rotating Vane Grid	5.72	-	5.771	4.393	35.945	5,269	281



Figure 97: Schlieren image of the Fixed Divergence Tunnel. Black streaks are due a seed particle/water mixture accumulating on the windows.

5.1.5.2 PIV Measurements Initially, the pre-combustion flow field was characterized with particle image velocimetry with and without the turbulence grids. Approximately 150 image pairs were processed and smoothed to produce mean and rms velocities for both the streamwise and spanwise velocities. Single point turbulent statistics were produced by selecting a representative center-line value and are shown in Table 17. Clearly, the installation of the passive grid increases both the axial and tangential rms velocities. The estimated turbulent kinetic energy (TKE), which was calculated assuming cross-stream homogeneity, also increases with the installation of the grid. An even larger increase in both axial and tangential rms velocity fluctuations is achieved with the installation of the active grid system. Isotropy is not exactly achieved, however u'/v' is 0.7-1.3, which is close to isotropic. Previous studies in grid-generated turbulence have shown near isotropy downstream of the grid after a short development distance.[119] However, it is well known that contractions modify the turbulence by extracting TKE from axial fluctuations and depositing TKE into off-axis fluctuations.[119] The anisotropy ($u'/v' \simeq 0.7$) in these experiments is well explained by the 9.3:1 contraction prior to the test section. This significant reduction in area was necessary because the upstream turbulence generator required a large area while achieving long runtimes required a small test section area.

Subsequent tests used many more image pairs (approximately 1800), substantially less stringent outlier rejection and no smoothing. These results are more accurate because the previously used strict outlier rejection threw out valid data. Additionally, there were not enough image pairs in the previous analysis for statistical convergence of the results. Figure

¹Integral scale estimated as the channel half-width

²Estimated

98(a), (b), and (c) shows the mean U and V velocities as well as the out of plane vorticity. In the previous analysis, there was no structure to the mean V velocity nor the vorticity further validating that statistical convergence was not achieved. In these images, diagonal structures in the mean tangential velocity and out of plane vorticity suggest that Mach waves are present in the flow. This assumption was already verified in the Schlieren images, Figure 97. The mean U velocity was measured to be $550 \pm 10 \text{ m/s}$.

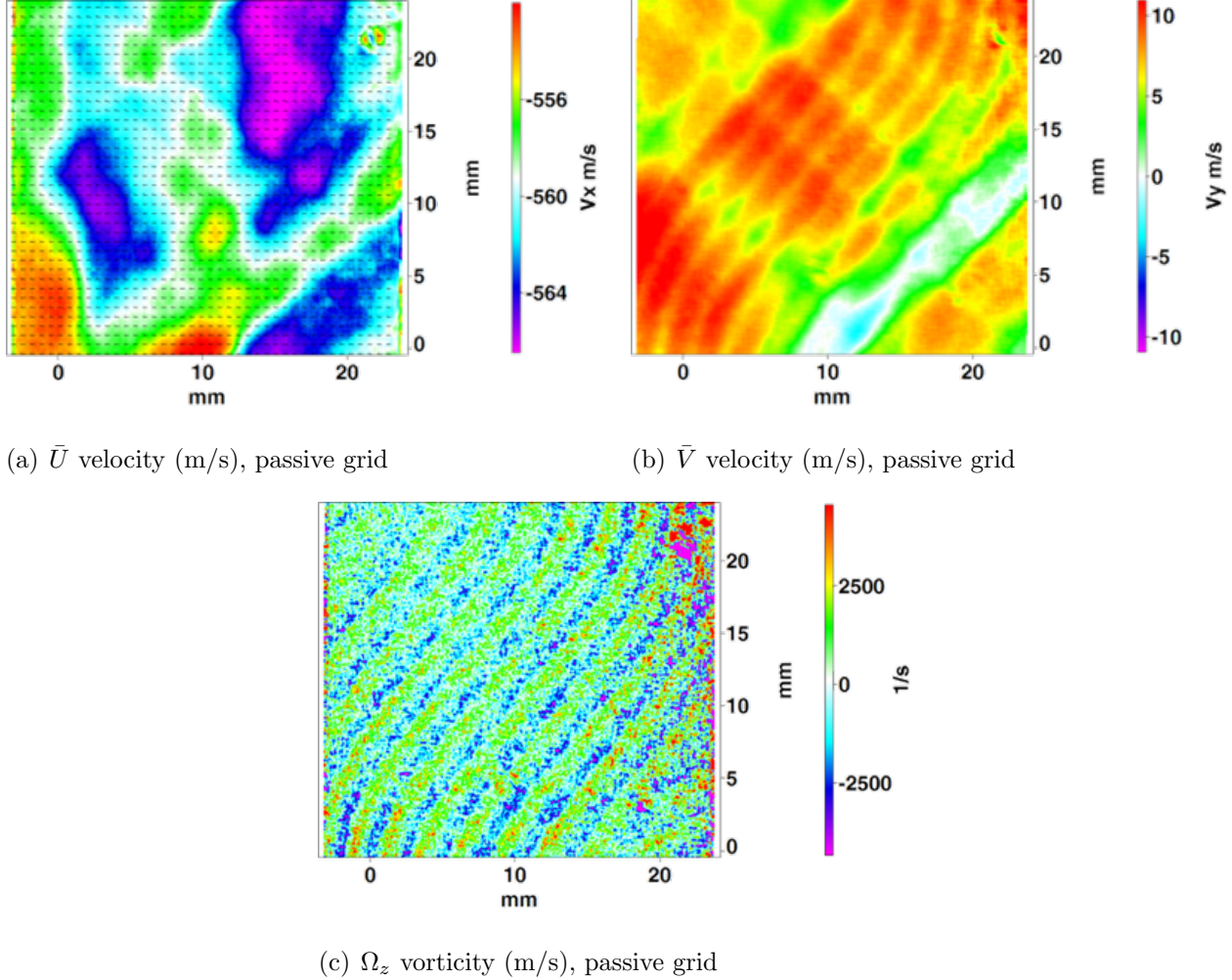


Figure 98: Sample PIV results of (a). mean x-direction velocity, (b). mean y-direction velocity, and (c). mean out of plane vorticity.

Figure 99 shows the mean and rms of the x component velocity. Homogeneity of the mean velocity was achieved while the rms velocity was only homogeneous within the first 12 mm of measurement plane. Noise on the far right side of the image may contribute to some of the inhomogeneity. Statistics formed with this data will be confined to the region $0 \leq x \leq 12 \text{ mm}$.

The u-u spatial autocovariance was formed for both the passive grid and no grid cases over a spatial separation of $0 \leq r \leq 8 \text{ mm}$. The spacing between adjacent points is rather coarse. In fact the plot falls to zero within about 9 data points. This spacing should be

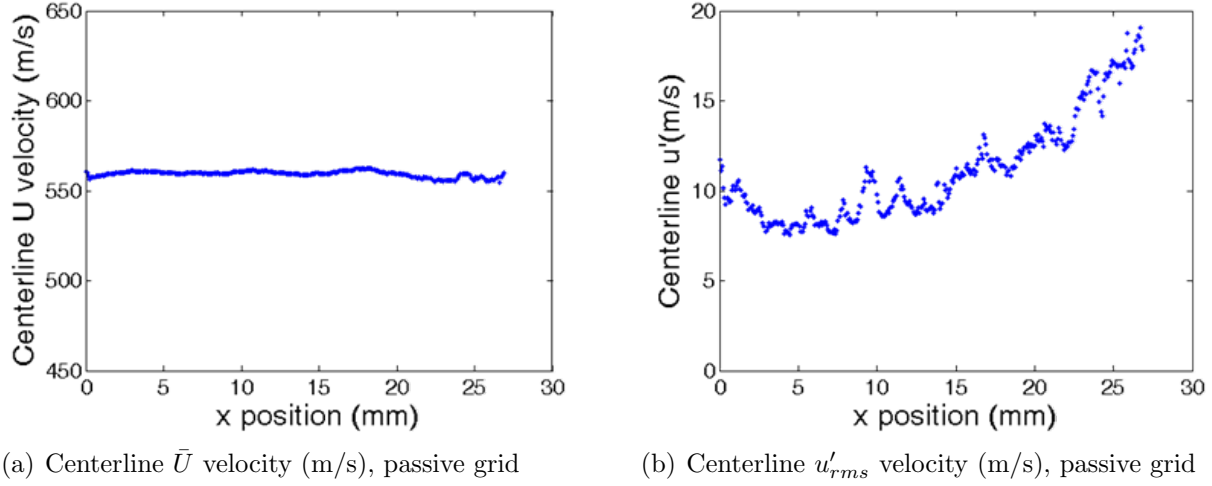


Figure 99: Sample PIV results of (a). Centerline mean x-velocity, (b). Centerline RMS x-velocity.

improved in future studies by using microscopic PIV. The integral length scales (integration of autocovariance from 0 to infinity) were 1 mm and 0.8 mm for the passive and active grids, respectively; however, these numbers should be treated with some caution due to the poor spatial resolution. The autocovariance has the typical shape expected for turbulence but appears to be rather noisy. This is a typical result when using raw spatial velocity data to form the autocorrelation. Another approach would be to first transform into wavenumber space and fit a model equation to the ensemble averaged spectra. The inverse Fourier transform will yield a much smoothed autocovariance. This technique will be used in future supersonic turbulence data analyses.

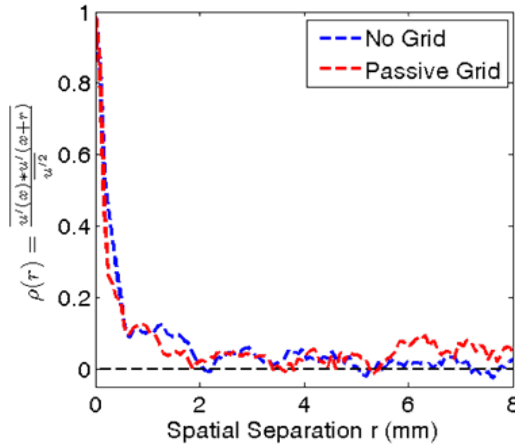


Figure 100: Spatial autocovariance for both no grid and passive grid turbulence generators in $M=1.5$ flow.

5.2 Flame Kernel Analysis

5.2.1 Background and Methodology

Several techniques exist to determine the turbulent global displacement speed. The two used in this project are based on the temporal evolution of the flame kernel radius. The first method to determine the radius identifies the edge of the flame in Schlieren or PLIF images, calculates the number of pixels encompassed by the flame edge and subsequently the flame area and radius, averaged over the number of flame images taken. In the second method, the flame kernel images are averaged first to produce so called c -maps, where c is the progress variable. At $c = 0.5$, it is most likely to have a flame edge and thus, the distance associated to this value is defined as the flame radius. After identifying the flame radius for different points in time, the two methods become identical. The time derivative of the radial growth is found either using finite differences or a curve-fit and the global turbulent consumption/flame speed is then given as

$$S_{T,GC} = \frac{\rho_b}{\rho_u} \frac{dr}{dt}. \quad (27)$$

In theory, the two methods to find the flame radius should give the same final result for regular spherical flames.

Another quantity of interest is the local consumption speed. The definition is more complicated and given by Driscoll [120] (see Eq. 28). PLIF flame images are used to calculate the flame surface density Σ , which is then integrated and combined with a suitable stretch factor I_0 to form the local consumption speed. The local consumption speed will differ from the global displacement speed; the difference can be 30% or higher [121]. One last measure of the turbulent flame speed, the global consumption speed, is not appropriate for this flame configuration because it requires a measurement of the reactant flowrate. In spherical flames, the reactant flowrate depends on the flame speed itself; hence the global consumption speed is ill-defined.

$$S_{T,LC} = S_{L0} I_0 \int_{-\infty}^{\infty} \Sigma d\eta. \quad (28)$$

Furthermore, as mentioned earlier, this project is dealing with turbulent flames. They are different from laminar flames in that the burning velocity is increased and diffusion effects become even more important. A popular theory states that turbulent flames consist of a laminar flamelet structure that has been increased in area or volume by stretching and curvature effects, thus increasing the flux of reactants, i.e. the burning velocity. Part of the flame stretching occurs due to turbulent eddies penetrating and dragging the flame front. This can be described by the Karlovitz number, a dimensionless parameter defined as

$$Ka = \frac{L_{11}}{S_{L0}} \kappa, \quad (29)$$

with the stretch rate $\kappa = 1/A dA/dt$. Other definitions of this factor exist that avoid the usage of the stretch rate. Other stretch effects include curvature and wrinkling. These affect the flame, as they are manifestations of turbulent and thermal diffusion processes.

They can be described through the Lewis ($Le = \alpha/D$) number or the Markstein number ($Mk_L = \delta_M/\delta_L$). Recently however, the Markstein number has gained popularity as it is more general in describing curvature effects [122]. However, measurement of the Markstein length δ_M can be more difficult than determining thermal and mass diffusivity for the Lewis number. Also, several different Markstein numbers with individual meanings can be defined, see Driscoll [120].

In interpreting the results from turbulent flame measurements it is very important to understand how the flame interacts with the energy content of different turbulent scales. According to Abdel-Gayed et al. [123], Bradley et al. [124], Fairweather et al. [125] and Chaudhuri et al. [126] a flame kernel will only interact with a certain range of turbulent scales. On the lower end the scale size is limited by the Gibson scale l_G , on the upper end by the kernel size and the integral length scale. This can be accounted for by computing an effective RMS-velocity representing the energy content of the scales affecting the flame. Non-dimensional spectra have been developed to find the ratio between u'_{eff} and u' . On the other hand, the effective RMS-velocity can also be computed directly from measured energy spectra. This is illustrated in Fig. 101 for a one-dimensional spectra. If the three-dimensional spectra cannot be measured directly, an isotropy assumption has to be made to find an appropriate u'_{eff} with

$$u'_{eff} = \sqrt{\frac{3}{2} \int_{\kappa_G}^{\kappa_R} E_{11}(\kappa) d\kappa}. \quad (30)$$

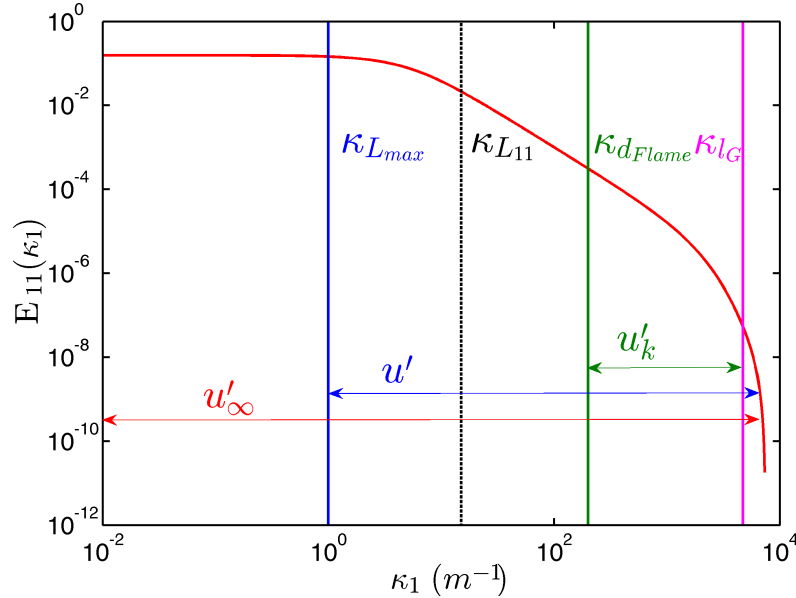


Figure 101: Illustration of different turbulent scales and their wavenumber range in the 1D power density spectrum.

5.2.2 Flame Kernels in Low Speed $M < 0.1$ Turbulent Flow

Under these conditions, flame kernel development should be comparable to results obtained from flame bomb experiments, allowing for validation of measurement and experimental techniques. The OH-PLIF system used here is the same as shown in Fig. 125 and the diverging tunnel used is shown in Fig. 12. The laminar flame speed used for evaluation is determined with the commercial software CHEMKIN. From that, using GASEQ, the thermal diffusivity, the laminar flame thickness and the density ratio across the flame can be determined. As shown in Fig. 102, the current dataset is probing the kernel at a very early stage of its development during which the radial growth is not linear and the kernel is not regarded as fully developed [125]. Based on the Borghi-Diagram classification, the kernels under investigation are in the Thin Reaction Zone, with $L_{11}/\delta_L \approx 10$ and $u'/S_{L,0} \approx 10$.

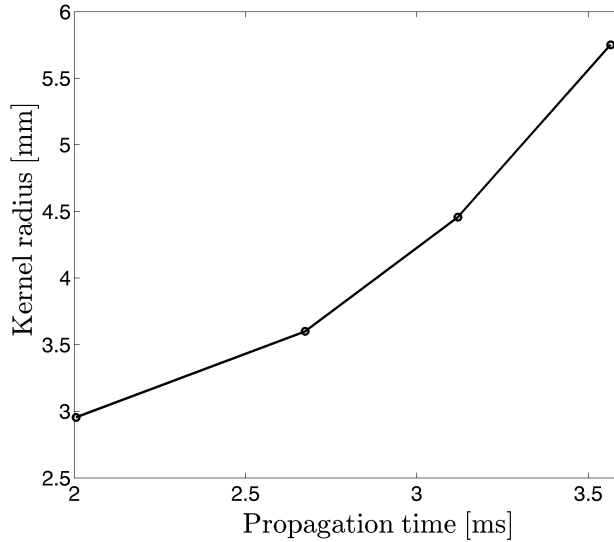


Figure 102: Radial growth of the kernels investigated in the $M < 0.1$ case.

At each of the four measurement positions, 1000 PLIF images are recorded. A greyscale threshold is chosen and the pictures binarized to evaluate the kernel size. Images showing no kernels and kernel sizes below the 15th quartile are sorted out, resulting in ≥ 700 images per data point for evaluation of desired quantities. At a 90% confidence level this resulted in a confidence interval of $\pm 0.34\text{mm}$ or $\approx 6\%$ deviation in the mean flame radius.

A flame kernel will only interact with a certain range of turbulent scales. This is accounted for by calculating an effective RMS-velocity directly from the one-dimensional spectra measured with CTA. Correcting only for this effect the turbulent flame speeds do not correlate well with results by other researchers or expressions given by Bradley and Damköhler, as seen in Fig. 103.

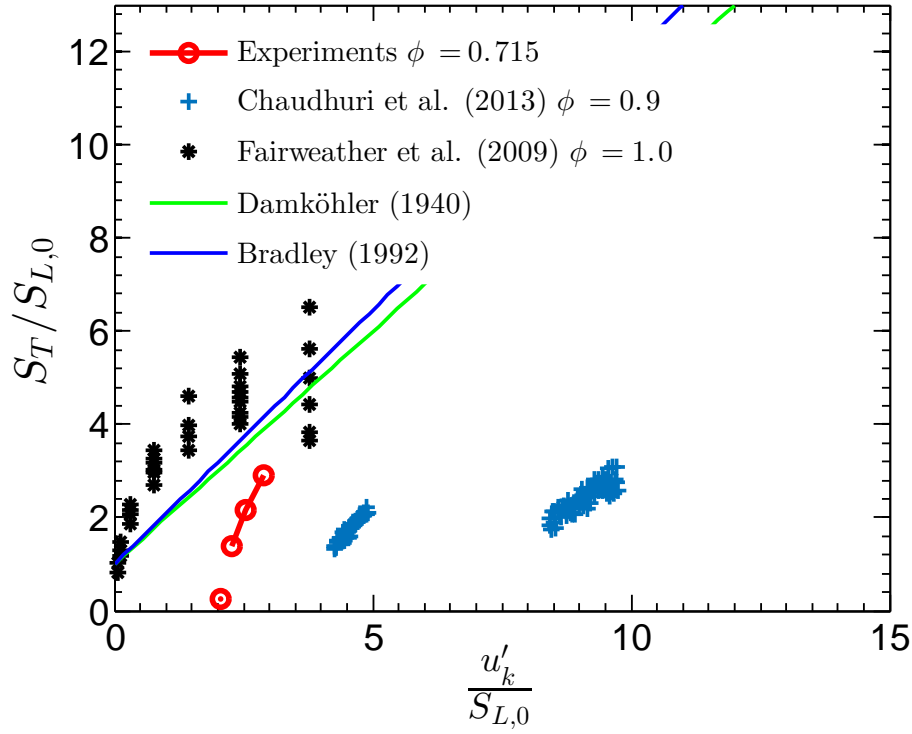


Figure 103: Comparison of turbulent flame speed data only correcting for the effective RMS-velocity.

Following the work of Chaudhuri et al. [126] and including effects of Markstein diffusivity, the agreement can be improved. Since direct measurement was not possible, the Markstein length for the desired correction is found using a correlation given by Driscoll [2] for the Markstein number of methane-air mixtures,

$$Mk_L = 3.3\phi - 2.3, \quad 0.5 < \phi < 1.4. \quad (31)$$

This correlation is sensitive around the point of neutral diffusivity ($\phi \approx 0.7$ for which $Mk = 0$) and Chaudhuri's correction has been developed specifically for positive Markstein lengths. The result of applying this correction is shown in Fig. 104 and collapses the data much better. Thus, it can be concluded that the facility produces results comparable to previously established measurements and the instrumentation is correct.

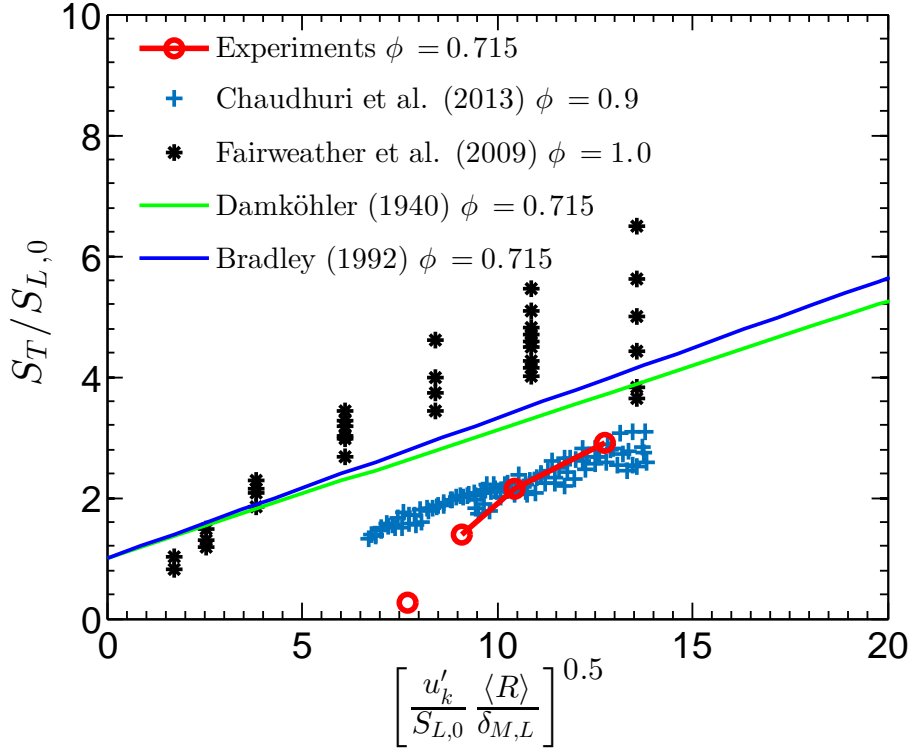


Figure 104: Accounting for curvature effects on the flame speed in addition to an effective RMS-velocity, the data collapses well with previous work by other researchers.

The results suggest that future inclusion of Karlovitz number effects and/or more precise values for the Markstein length will collapse the data even better. Moreover, the flame kernel should be observed at a later stage when it is closer to being fully developed to obtain more of a steady state.

5.2.3 Flame Kernels in Medium Speed $0.1 \leq M \leq 0.3$ Turbulent Flow

5.2.3.1 Isotropic Turbulence

Flame studies of $0.1 \leq M \leq 0.3$ kernels contain the bulk of the data collected. Experimental campaigns are organized roughly by the turbulence generator used and include: passive grids, blown-grid, vane-grid, and the post contraction passive grid. Only the post contraction grid experiments yielded isotropic turbulence but, chronologically, these studies occurred after the others. However, isotropic turbulence is more simple and will appear first in this document.

The same lasers and cameras used in the vane grid experiments were used in the PCPG experiments with the following changes: 1) the binning of the cameras was reduced by a factor of 2 (2x2 binning for the CH_2O camera and full frame for the OH camera), and 2) the SpectraPhysics spark laser was operated at full power with only a small portion of the beam being sent to the test section as shown in Figure 105. The reduced binning provided for increased spatial resolution at the cost of repetition rate now being 5Hz resulting in every

other kernel going unrecorded by the cameras. The later change was to improve laser beam quality and reduce the required energy for successful kernel ignition. It was found that at low power the beam quality was significantly reduced which resulted in the need for higher spark power in the vane grid experiments. By running the laser at full power, kernels could be sparked at approximately 4.5 mJ/pulse for low turbulence cases, but at higher turbulence this was insufficient to initiate a chemical reaction due to heat convection as described by previous authors [127], but still resulted in hot gases as indicated by the CH_2O signal shown in Figure 106 (n.b. there was no OH signal for any of these kernels indicated the reaction never initiated). Further testing demonstrated approximately 7 mJ/pulse was required for reliable kernel ignition for the high turbulence cases. To reduce systemic variations between experiments, 7 mJ/pulse was used for all cases.

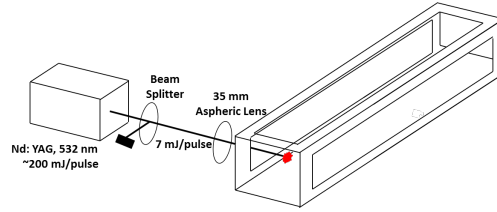


Figure 105: Schematic of revised spark laser system for PNPG experiments.

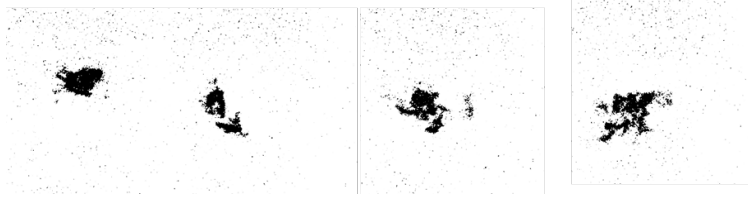


Figure 106: Sample raw CH_2O created by plasma kernels which failed to initiate a flame kernel at $M = 0.3/\phi = 1$ for the PNPG turbulence.

The turbulence intensity, length scales, and regime diagram locations for PCPG kernel tests are shown in Figure 107. The turbulence produced by the passive grid is isotropic, thereby enabling a proper comparison with classical flame bomb correlations. Furthermore, since the length scale is appreciably smaller than the anisotropic turbulence, the PCPG kernels are mostly in the TRZ; however, the turbulence levels are still too low to have any significant local extinction.

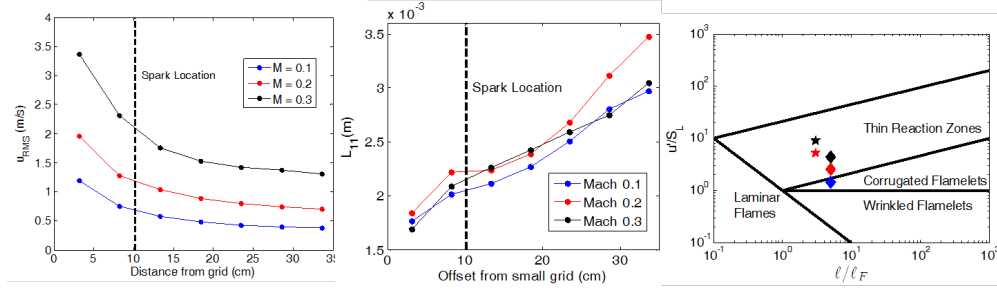


Figure 107: Turbulence values for PNPG kernel experiments (left) with regime diagram (right) with $L_{11} = 3mm$ (i.e. the mesh size of the PNPG). The spark location is indicated by the dash line.

As noted in Figure 107, the spark location is approximately 10 cm downstream of the grid which resulted in optical access at time delays closer to ignition. Furthermore to increase temporal resolution and range of kernel propagation, the probe locations were spaced 2.54 cm apart over a total range of approximately 30.5 cm (approximately 1 ms to 4.5 ms propagation time). The c-maps for all conditions are shown in Figures 108 and 109 with respect to both space and time.

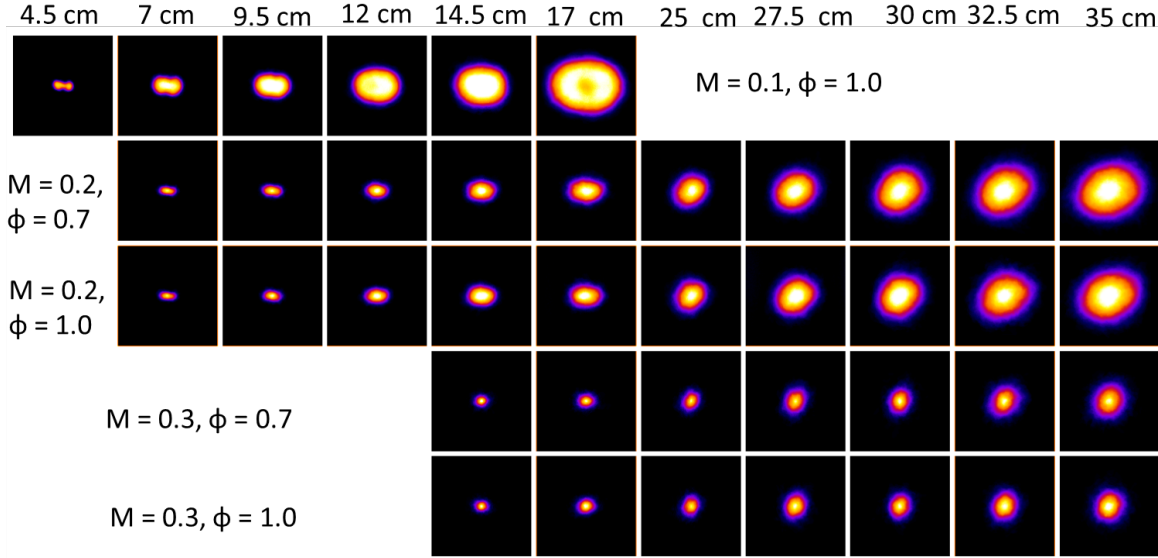


Figure 108: Evolution of centered kernel c-maps. The columns are the nominal positions of the kernels (i.e. position of the camera) with distances given relative to spark location.

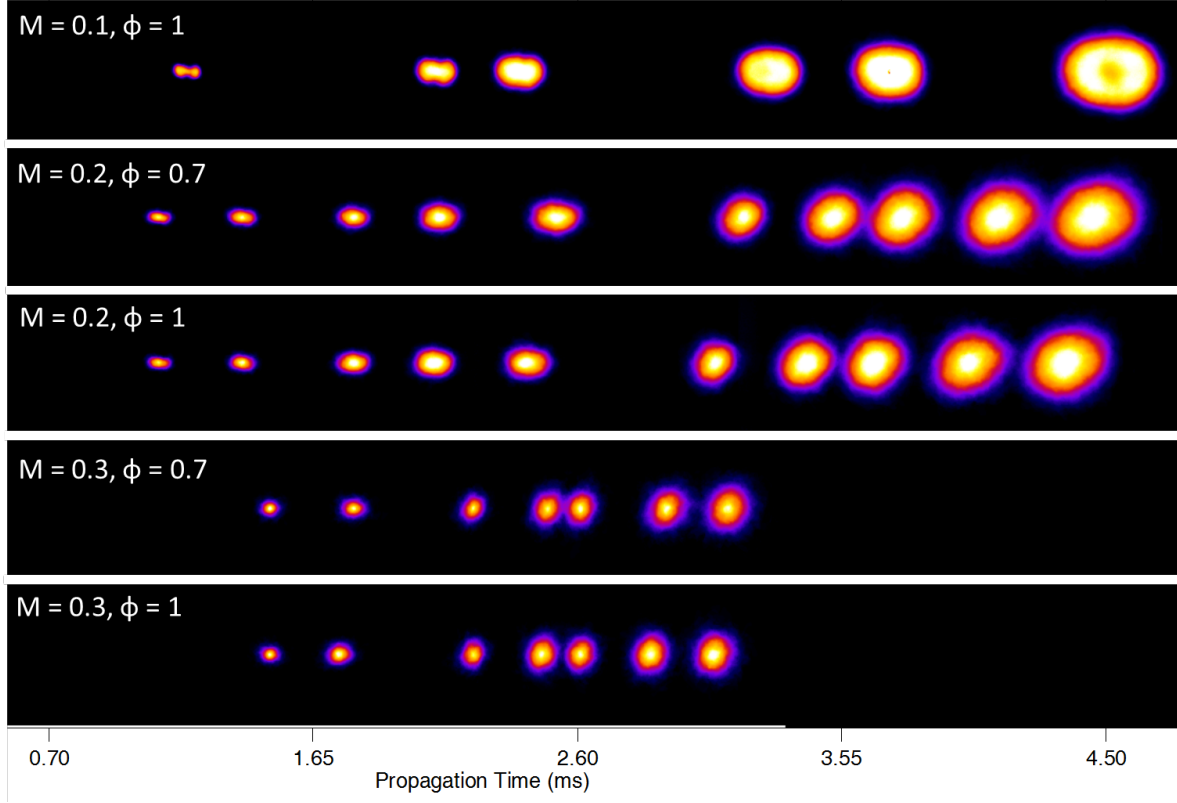


Figure 109: Temporal evolutions of kernel c-maps. Times are relative to the laser spark.

The radius and growth rates of the kernels is shown in Figure 110. As can be seen in the Figure 110, dR/dt is a function of both R and t . Therefore, variations in initial flame kernel radius affect dR/dt and need to be accounted for when comparing the flame speeds of different data sets.

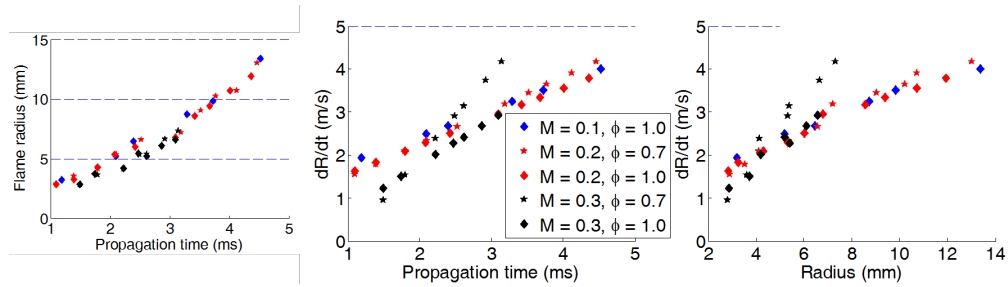


Figure 110: Flame radius and growth rates.

Finally, the measured flame speeds are compared to flame bomb correlations to determine if there are any affects of compressibility on flame kernel propagation. The correlations, shown in Figure 111 are compared to flame bomb correlations done by Chaudhuri et al. [128, 129, 126, 130]. In addition to the dependence on ReT,R , they found that propagation

speed are inversely proportional with Markstein number (i.e. the $\phi = 0.7$ kernels should propagate faster than the $\phi = 1$ kernels). Before initial conditions are considered, the current flame speeds exceed their correlated values at similar Ma (i.e. comparing the current $\phi = 1$ data to their $\phi = 0.9$ data), but the $\phi = 0.7$ kernels due propagate faster as expected. However, when non-zero initial kernel size is accounted for and the data initialized, the flame speeds agree reasonably well with the flame bomb correlations. Additionally, if stretch effects on flame speed are considered by recalculating the laminar flame speed by Eq. 32. The data for $\phi = 1$ collapse reasonably well across all turbulence levels.

$$S_L = \frac{S_{L,0}}{1 + MaKa} \quad (32)$$

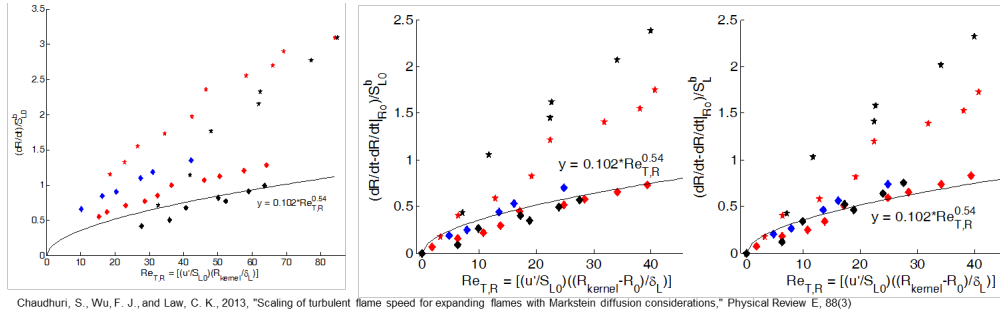


Figure 111: Flame speed correlations of uncorrected data (left), initialized data (center), and stretch corrected laminar flame speed data (right). The solid line is from Chaudhuri et al. [5] for CH_4 air mixture at $\phi = 0.9$.

5.2.3.2 Anisotropic Turbulence Here we discuss only experiments conducted with the blown grid and vane grid turbulence generators. However, passive grid studies (low turbulence) were conducted and are included in Grady et al. 2014[131] included in Appendix B. This section contains a discussion of $0.1 \leq M \leq 0.3$ kernels with the blown grid followed by similar kernels with the vane grid.

The first round of tests generated turbulence with a passive grid consisting of a 2.29 mm thick perforated plate with 12.7 mm holes. The grid featured a plate solidity of 33 percent (percentage of blocked area) with holes arranged in a hexagonal pattern. A Continuum Surelite Nd:YAG laser (195 mJ/pulse at 1064 nm after focusing lens) was used to ignite the flame kernels. The spark laser was focused into the tunnel using a -250 mm lens to expand the original 6 mm beam to 25.4 mm before being focused by a 60 mm lens through a window 50 mm upstream of the test section. These lenses were chosen to prevent damage to the window which was 2.5 cm from the focal point and limit the effect of back reflections on the 60 mm lens, and provided a spot size of $800 \mu m$.

Data was taken at 3 streamwise locations (12.7 cm, 16.5 cm, and 20 cm) from the spark laser. Example raw single-shot images for $\phi = 1$ are shown in Figure 112 and mean and RMS images of the binarized images also for $\phi = 1$ are shown in Figures 113 and 114. The binarized images were corrected for the unevenness of the laser sheet. The flow direction is

from left-to-right, and the top of the images is towards the spark laser. The third lobe found in the images is an artifact of the laser ignition similar to the results of Mansour et al. [132].

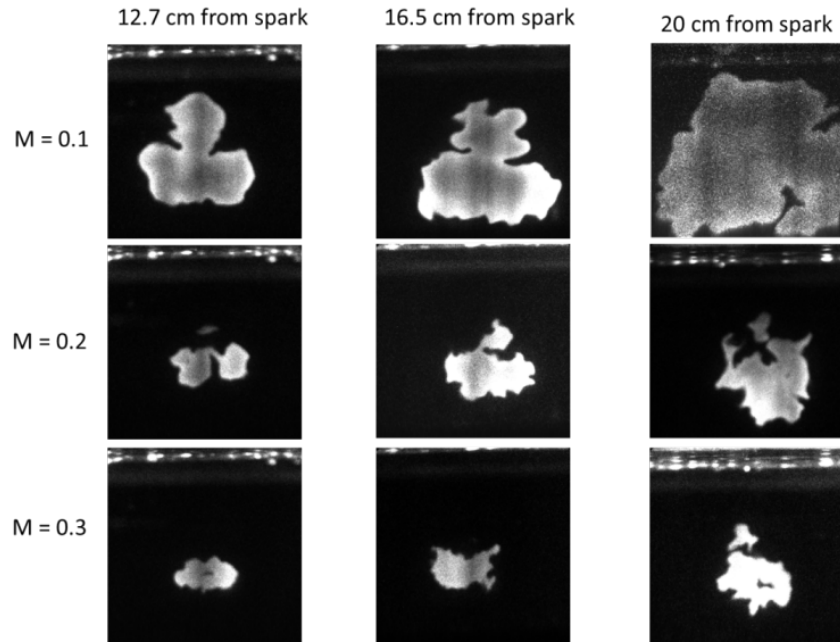


Figure 112: Raw single-shot OH PLIF images of flame kernels at $\phi = 1$ with 195 mJ/pulse ignition.

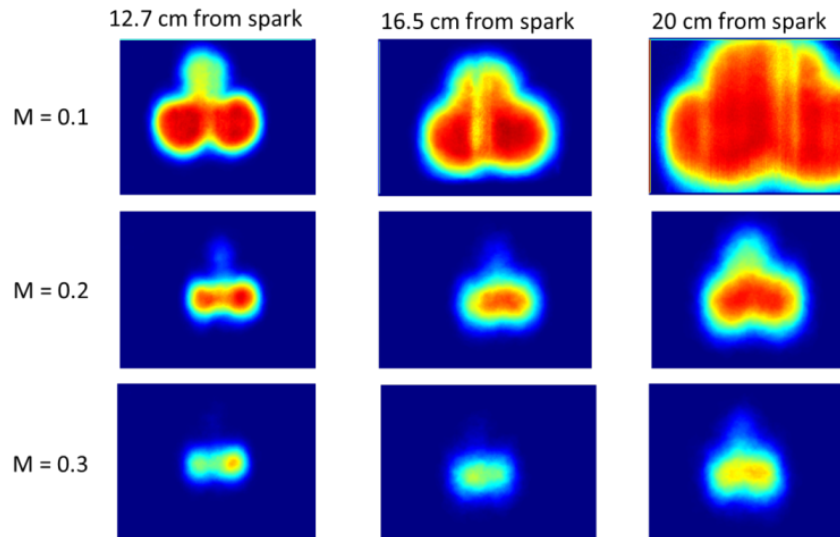


Figure 113: Mean of binarized images (i.e. c-map) of flame kernels at $\phi = 1$ with 195 mJ/pulse ignition.

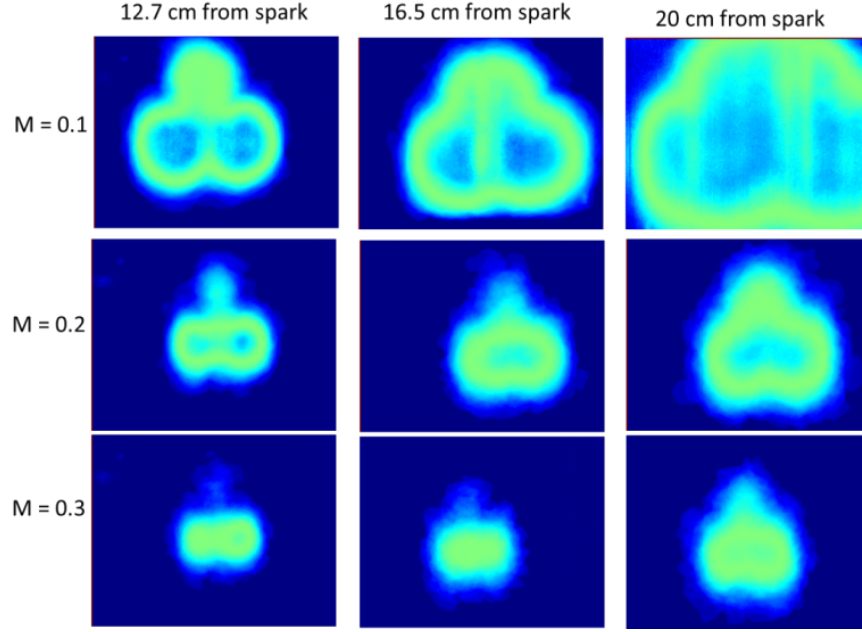


Figure 114: Standard deviation of the binarized images of flame kernels at $\phi = 1$ with 195 mJ/pulse ignition.

From Figure 114, it can be seen that the primary fluctuations in progress variable are towards the edges of the flame kernels and the third laser artifact lobe demonstrating an overall very repeatable ignition process. Additionally, there are also higher fluctuations between the two primary lobes seen in younger, upstream kernels indicating that these two lobes grow towards each other similar to the peanut like structure observed by Mansour et al. [132].

The mean images are used to calculate an equivalent radius for the kernels, and are plotted verse propagation time in Figure 115 for $\phi = 1$. Both the $M = 0.2$ and $M = 0.3$ curves are nearly collinear and the two upstream $M = 0.1$ data points also lie on these lines (the third has made contact with the wall and was excluded). This trend is similar to that observed by Mansour et al. [132] where changes in the mean flow velocity did not result in an appreciable change kernel growth rate. This demonstrates that tunnel can: 1) maintain a constant equivalence ratio across a wide range of mean flows and 2) the laser ignition process is fast enough to prevent causing an elongated ignition region possible from slower ignition coils.

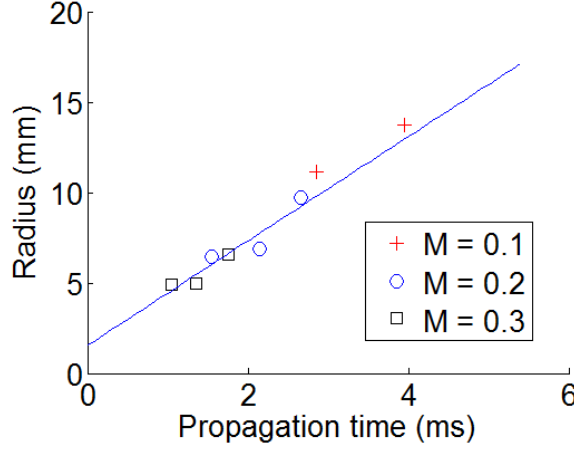


Figure 115: Characteristic radius verse time for $\phi = 1$ for the passive grid.

Flame thickness is determined from Equation 33 using the inverse gradients from the c-maps along the $\bar{c} = 0.5$ contour. Flame thickness is plotted vs time for all Mach numbers with trend line (solid black line) shown in Figure 116. Normalized flame thicknesses are also shown in the figure using a laminar flame thickness of 0.6 mm approximated using $S_L = 40\text{cm/s}$ and $\alpha_{mix,1200K} = 2.38\text{cm}^2/\text{s}$.

$$\delta_T = \frac{1}{(\partial \bar{c} / \partial x)_{max}}^{-1} \quad (33)$$

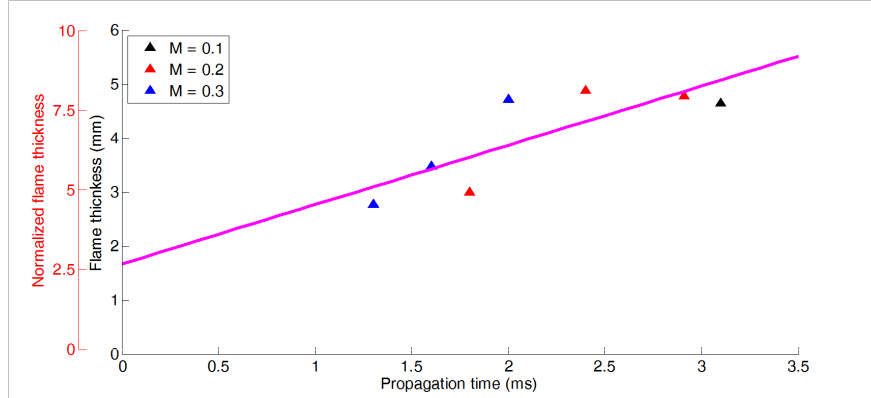


Figure 116: Flame brush thickness and normalized flame thickness verse time with trend lines for the passive grid.

The second round of testing including the following experimental improvements: 1) new spark system, and 2) new turbulence generator. To eliminate the previous lobed kernel structure, a 35 mm aspheric lens replace the previous optics and a second harmonic crystal was added to existing spark laser to double the 1064 nm laser to 532 nm laser. These two

changes allowed for 7.5 mJ/pulse spark energy used across all of the cases studied. The new turbulence generator was the blown grid system described previously. The higher turbulence levels achieved in this second study were sufficient to cause significant walking of the flame kernels. In order to obtain proper statistics, an additional orthogonal camera was used to monitor the locations of the PLIF sheet and the OH* chemiluminescence of the kernel. Using this additional camera, only flame kernels which are centered on the PLIF sheet were used in the statistics of flame growth/speed. The revised experimental schematic and data analysis process are shown in Figures 117 and 118 respectively. The formation of the c-map also required recentering each flame kernel realization to the center of the image.

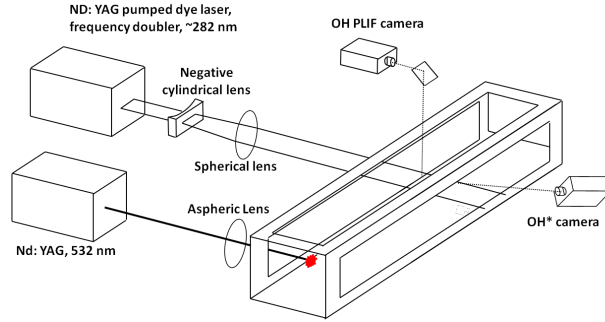


Figure 117: Experimental configuration with OH* included.

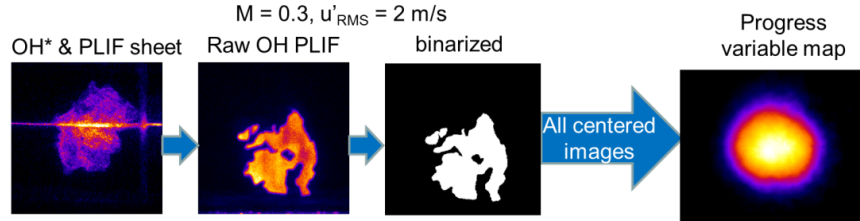


Figure 118: Data processing including the PLIF sheet/OH* conditioning.

The u' values stated in the second set of tests are given for the fluctuations in the streamwise direction. Due to vortex stretching within the nozzle, the turbulence is highly anisotropic with the fluctuations in the streamwise direction being suppressed while the other two components are significantly higher. Additionally, the degree of anisotropy is a strong function of the Mach number with higher mean flow rates creating more anisotropy as shown in Figures 119 and 120. Since there is higher turbulence in the transverse directions at higher M , then there should be changes in $R(t)$ as a function of M . The effects of this anisotropy can be seen in Figure 121, where c-map of the kernels starts in ellipse with the major axis in the streamwise direction and with time becomes an ellipse in the transverse direction. The original ellipse shape is most likely an artifact of the laser ignition as explained previously which overtime becomes spherical then an ellipse in the transverse direction due to the higher turbulence fluctuations in that direction. Eventually, the expansion wave reaches the

wall and flame propagation is inhibited in the transverse directions. This is most likely the reason why there is no apparent change in the $R(t)$ plots shown in Figures 115 and 122 for the turbulence intensities studied.

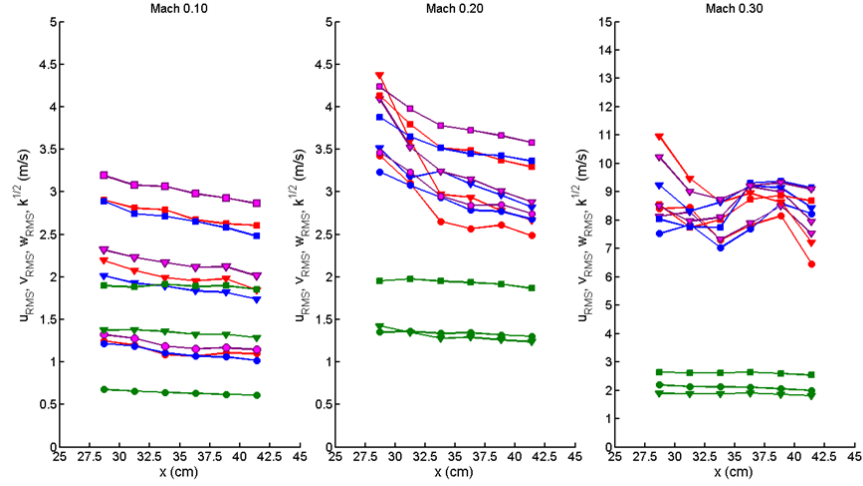


Figure 119: Hot wire anemometry data showing the correlation between Mach number and anisotropy for the blown grid turbulence generator on both intensity (top) and length scale (bottom).

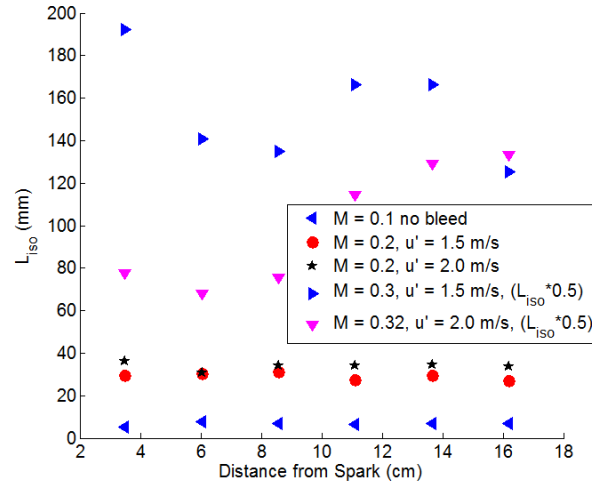


Figure 120: Hot wire anemometry data showing the correlation between Mach number and anisotropy for the blown grid turbulence generator on both intensity (top) and length scale (bottom).

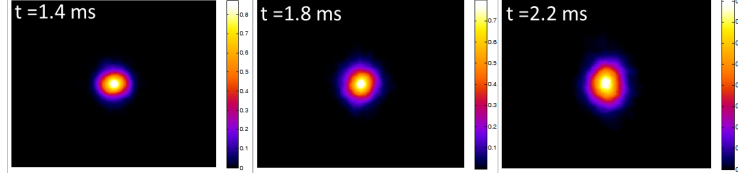


Figure 121: C-maps for $M = 0.5$ and $u' = 2m/s$ for the blown grid generator with 7.5 mJ/pulse ignition.

For the second series of tests mean Mach number range was increased up to $M = 0.6$. The flame growth rates were similar to the previous attempt, and no significant changes with respect to Mach number were observed as shown in Figure 122.

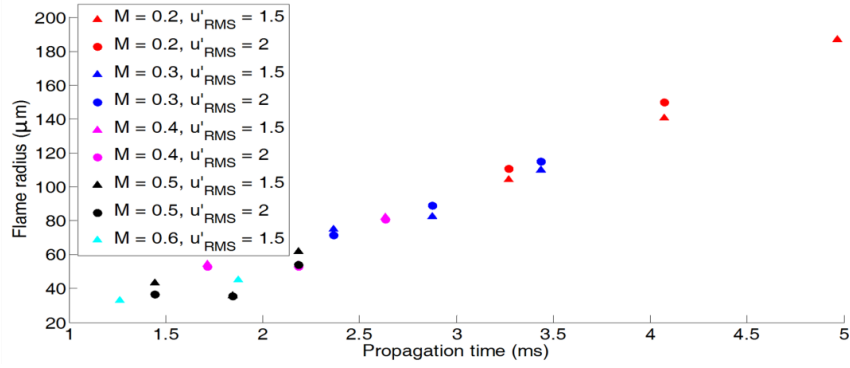


Figure 122: Flame radius verse time for blown grid studies.

Additionally, analysis of flame surface density was conducted and peak values were observed to decrease with time as shown in Figure 123. The u' values quoted in the figure label are for the fluctuations in the streamwise direction. The other two components are significantly larger, and the discrepancy between these two is caused by vortex stretching in the nozzle. Finally, instantaneous statistics were obtained as well, and an examples of these are shown in Figure 124. Higher turbulence levels resulted in higher values for both curvature and flame length. The curvature values shown in Figure 124 are determined first finding the all curvature values on a given frame (with zero curvature being the most common), then averaging all positive and negative values independently. However, there were no significant differences between flame thickness for the two cases, and the thicknesses themselves were much larger than the laminar values. The primary reason for the large flame thicknesses is due noise, pixelization, and the filtering process used to account for these two. To mitigate these effects, spatial resolution was increased in future experiments.

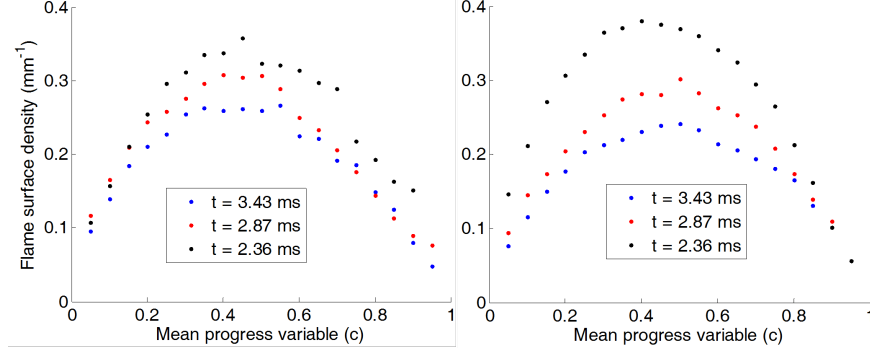


Figure 123: Flame surface density for $M = 0.3$ at $u' = 1.5m/s$ (left) and $2m/s$ (right) for the blown grid.

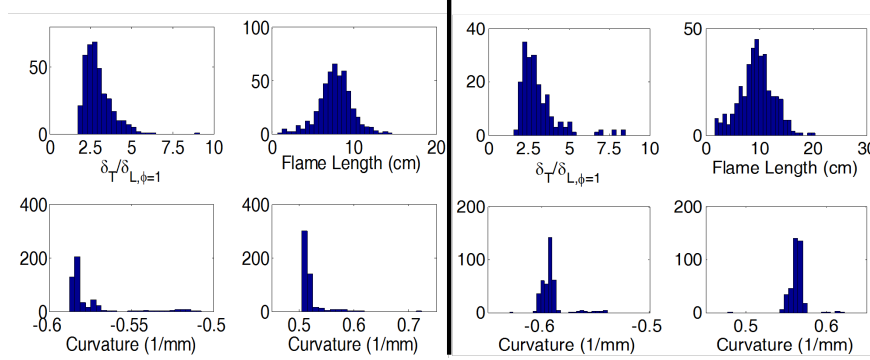


Figure 124: Single shot statistics for $M = 0.3$ at $u' = 1.5m/s$ (left) and $2m/s$ (right) taken at $t = 3.43ms$ for the blown grid. Curvature values are determined by averaging the positive and negative curvatures values of each frame independently.

Further research was done using the vane grid turbulence generator and combined CH_2O/OH PLIF. In order to obtain the requisite 355 nm light for CH_2O PLIF, the Continuum Surelite previously used to make the spark was repurposed by adding a third harmonic crystal. A Spectra Physics Nd:YAG laser (10-12 mJ/pulse at 532 nm after focusing lens) was used to ignite the flame kernels. It should be noted that this is a 30 percent increase in laser energy used due to differences in laser beam quality. The CH_2O fluorescence was imaged on a PI-MAX 2 ICCD camera with approximately 100 ns second gating. To ensure consistent triggering between the two cameras, the output of the OH PLIF camera was used to trigger the CH_2O camera. This triggering scheme resulted in a 100 ns delay between the two cameras. The raw OH/CH_2O images are then dewarped to account for any perspective distortion and translated to ensure that each pixel has the same physical size ($72.5 \mu m$ x $72.5 \mu m$ square) and location. A schematic of the revised experimental configuration is shown in Figure 125.

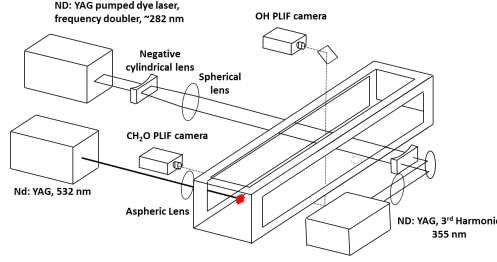


Figure 125: Schematic of CH_2O/OH PLIF and laser ignition system.

Turbulence data was taken using hot wire anemometry (HTA), and the results for the three Mach numbers used are shown in Figure 126. Due to vortex stretching in the nozzle, the turbulence is highly anisotropic in the test section with the streamwise component, u'_{RMS} , being approximately 25 percent of the other components in the $M = 0.3$ case and approximately 40 percent at $M = 0.1$. The streamwise component increases slowly in the streamwise direction due to the tendency of the turbulence to return to isotropy. The square root of the turbulent kinetic energy, k , is also shown in Figure 126: and shows a slow decay of the overall turbulence. The values for $k^{1/2}$ were 0.67, 1.5, and 3.8 m/s ($u'/S_L = 1.68$, 3.75, and 9.5 respectively for $S_L = 40$ cm/s) for the $M = 0.1$, 0.2 and 0.3 cases respectively.

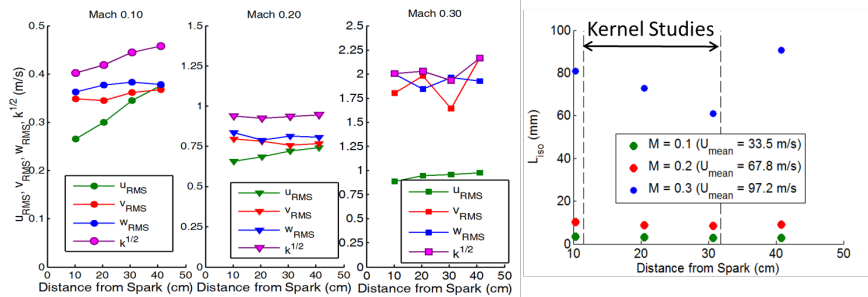


Figure 126: Turbulence levels for $M = 0.1$ (left), 0.2 (center left), 0.3 (center right), and length scales (right) as determined via hot wire anemometry for the vane turbulence generator.

Stoichiometric kernels were observed at three different $M = 0.2$, and 0.3 at 5 streamwise locations and $M = 0.1$ at two different locations to achieve similar kernel propagation times for the three different mean flows. Only two locations are shown at $M = 0.1$ since the kernel takes approximately 3.5 ms to enter the cameras field of view at upstream location and begins to have significant wall interactions after approximately 4.5 ms. Raw images for the two PLIF systems are shown in Figures 127 and 128. The CH_2O image in Figure 128 shows a possible break, but the overlap still shows a continuous section. In general there was a continuous CH_2O layer around the OH indicating that local extinctions were rare events. Broadened regions of CH_2O were generally between folds in the kernel although there were regions where preheat zone broadening was apparent such as the rightmost CH_2O image in Figure 127. Given the measured turbulence levels and since there is little evidence of

local extinction, local extinction was assumed negligible and preliminary results presented in this paper focus on data from the OH PLIF images only. Future work will reexamine the CH_2O/OH PLIF images to evaluate the validity of these assumptions.

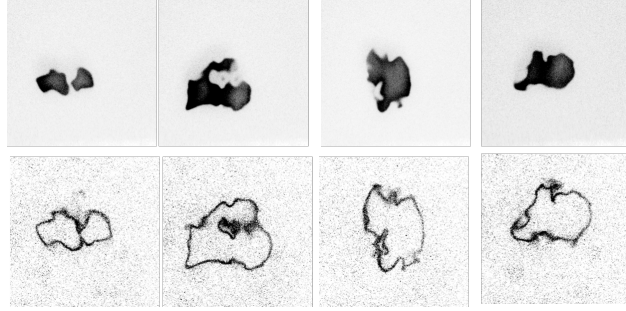


Figure 127: Raw images of OH PLIF (top) and CH_2O PLIF (bottom) taken at $M = 0.3$ and $t = 2.892ms$.

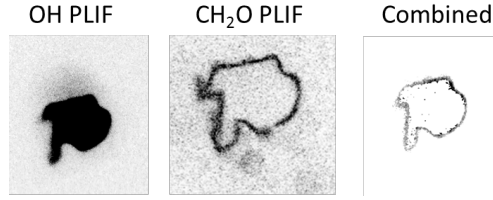


Figure 128: Example raw images of OH and CH_2O PLIF, and the combined image of the two taken at $M = 0.3$ at $t = 1.992ms$.

Example c-maps for $M = 0.2$ and 0.3 are shown in Figure 129 as determined from the OH images. The peanut like structure in the earlier stages of kernel growth is an artifact from beam quality produced by the new spark laser (this will be discussed further in the next section). From these images, kernel growth was inferred as shown in Figure 130. As shown, the growth rates are higher for both $M = 0.2$ and 0.3 than for $M = 0.1$ due to the higher levels of turbulence produced with the $M = 0.3$ profiles growing slightly faster than $M = 0.2$.

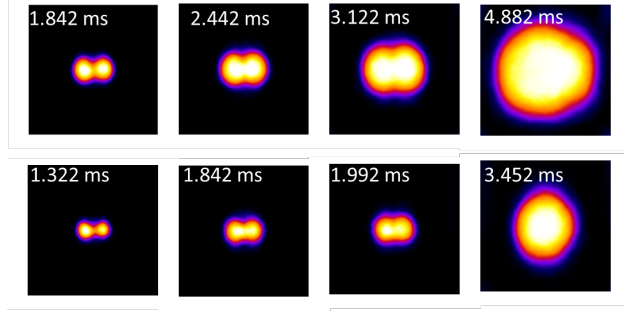


Figure 129: C-maps for $M = 0.2$ (top) and $M = 0.3$ (bottom) at 11.5cm (left), 15.2cm , 19.0cm , and 31.8cm (right) with $10\text{-}12\text{ mJ/}$ ignition for the vane grid.

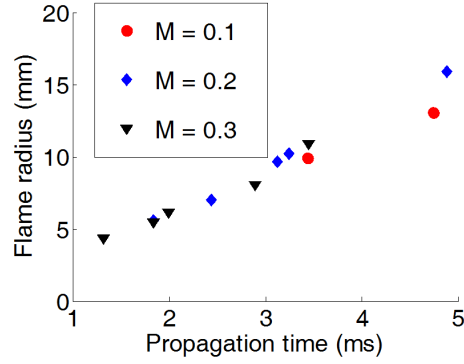


Figure 130: Radius verse time for the vane grid.

To further examine the changes in burning rates due to increased turbulence achieved at higher Mach numbers, FSD was calculated as can be seen in Figure 131 showing the FSD as a function of time for both $M = 0.2$ and 0.3 . In both Mach numbers, the FSD decreases with time due to the decaying turbulence in the tunnel as shown in Figure 131. Comparing the maximum FSD values at $t = 1.842\text{ ms}$ between the two Mach numbers shows a slightly higher value for $M = 0.2$ than for 0.3 .

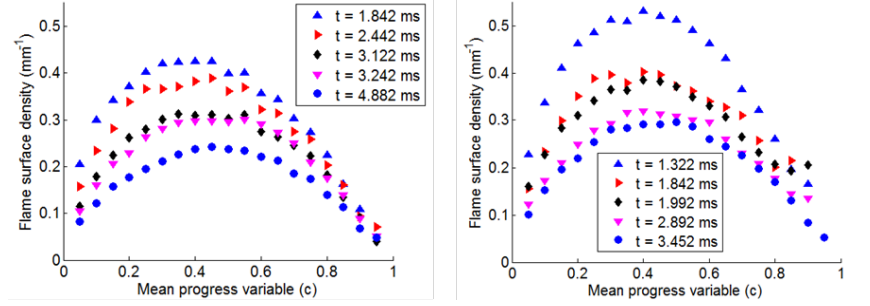


Figure 131: Flame surface density (FSD) vs time for $M = 0.2$ (left) and $M = 0.3$ (right) for the vane grid.

This can also be seen in Figure 132 where FSDmax is higher for the lower turbulence levels. However, it can be seen that the FSD times the brush thickness is higher for $M = 0.3$ than for 0.2 indicating a faster consumption rate as shown in Figure 132. While in general the consumption rate increases with time, the final points for both $M = 0.1$ and 0.2 are slowing perhaps due to the interaction between the tunnel walls and the expansion waves created by the kernels. Additionally, the current results compare well with the results by Renou et al. [133] showing the same trends with respect to both FSD and brush thickness, although the values for both of these are higher in the current experiment as expected from the higher turbulence levels.

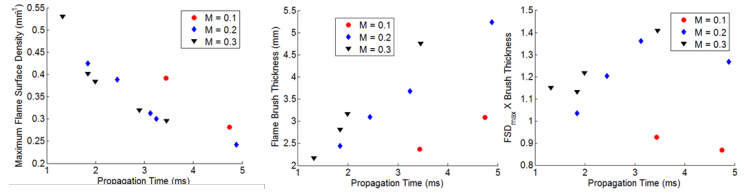


Figure 132: Maximum FSD (left), flame brush thickness (center), and the product the maximum FSD and brush thickness (right).

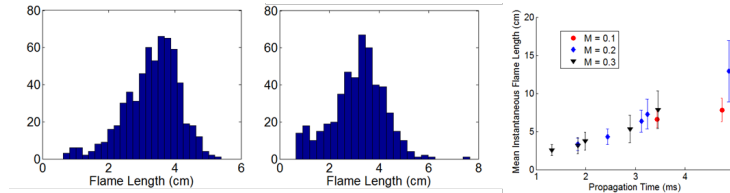


Figure 133: Instantaneous flame length histograms for $t = 1.842ms$ for $M = 0.2$ (left) and $M = 0.3$ (center). Mean flame length verse time is also shown (right) with error bars for standard deviations.

Figure 133 shows the instantaneous flame length at $t = 1.842ms$ for $M = 0.2$ and 0.3 as well as the average instantaneous flame length (error bars represent standard deviation) for

all Mach numbers and propagation times. Instantaneous flame lengths are determined by finding the total length of the flame edge in a given frame of a single shot image. Longer flame lengths indicate more wrinkling than shorter flame lengths. The trend observed for flame radius was also observed for the mean flame length where the values for $M = 0.1$ were noticeably smaller than for the other two cases. While the mean values at $t = 1.842ms$ were similar between $M = 0.2$ and 0.3 , the distribution was slightly broader for the $M = 0.3$ case than for the $M = 0.2$ case ($\sigma = 1.05cm$ and $0.8cm$ respectively). Additionally, the $M = 0.2$ distribution is skewed towards smaller overall flame lengths. These two things are consistent across all propagation times indicating more highly wrinkled flame kernels at the higher turbulence levels. Therefore, the increase in consumption rates is most likely due to the increase in flame area.

Finally, the flame speed data was compared with flame bomb correlations done by Chaudhuri who found that spherical flame growth can be correlated using a turbulent Reynolds number based off of the flame radius via Re_T , $R = (u' * R)/(S_L * \delta_L)$. Raw flame speed data was found to be below their correlated values, and when initial kernel size and speed are accounted for (the reason why this is done will be explained in the next section) the values compare even less favorably to the correlation. This dependency is most likely due to the large scale anisotropic turbulence. Flame kernels can only be wrinkled by scales which can fit inside of the kernels, and all scales larger than the kernels are ineffective at wrinkling the flame kernels and therefore do not increase flame speed. Therefore, in order to conduct a proper comparison with flame bomb measurements and determine if mean flow compressibility effects kernel propagation, small-scale isotropic turbulence studies need to be conducted.

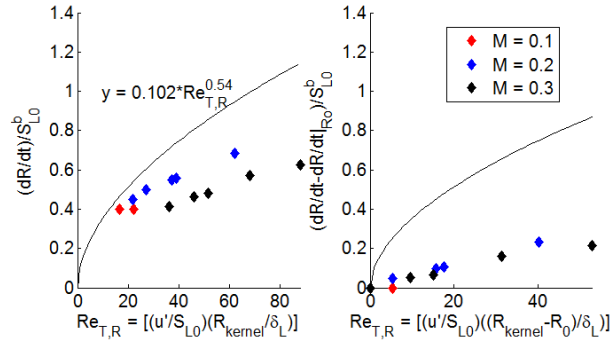


Figure 134: Flame speed correlations of uncorrected data (left) and initialized data (right). The solid line is from Chaudhuri et al. [50] for CH₄ air mixture at $\phi = 0.9$.

5.2.4 Flame Kernels in Supersonic $M = 1.5$ Turbulent Flow

Several investigations of flame kernels in supersonic flow were conducted. Initially, an electrode spark system was used with a modified scramjet combustor. While chemiluminescence was collected, there was some question as to whether a self-propagating flame was formed. The test section was elongated and the spark system was replaced with a laser spark system similar to those discussed in the subsonic kernel studies. The diagnostics were improved to

include high speed OH* and Schlieren. With these improvements, it was shown that the kernels were indeed growing. However, advanced diagnostics would be needed to measure more interesting flame properties such as the curvature or flame surface density. In addition, RMS velocity and longitudinal integral scale measurements were needed to compare our kernels with previous studies. Finally, small changes were made to the test section and PLIF/PIV were used. These tests appear as a demonstration of the capability at the time of this writing.

5.2.4.1 Initial Studies Flame kernels were evaluated in the supersonic reacting facility using the old, non-diverging test section. Initially, an intrusive spark electrode was used to ignite the $M = 1.25$ natural gas/air mixture. Later a non-intrusive laser ignition system was used. In all cases chemiluminescence was used to capture the ignition kernel.

CH Chemiluminescence with Electrode Ignition*

A NAC GX-3 high speed camera operating at 4000 frames per second coupled to a Video Scope intensifier was used to capture luminescence from the spark-initiated kernel. A 55 mm lens and 430 nm (± 20 nm HWFM) filter focused on the CH* chemiluminescence. The ignition system is discussed above in Section 3.2.3. A schematic of the test section is shown in Section 3.2.1. The converging-diverging nozzle was sized to achieve a $M = 1.25$ free stream velocity. Natural gas is injected through counter-flowing sonic jets sufficiently far upstream to achieve a fully mixed flow in the test section.

The tunnel was operated at a stoichiometric equivalence ratio. A series of ignition events is shown below in Figure 135. It is clear that the ignition kernel is highly variable and influenced heavily by the unstable flow field induced by the presence of the electrodes. These data proved the need for a laser ignition system. No further analysis was conducted on these data.

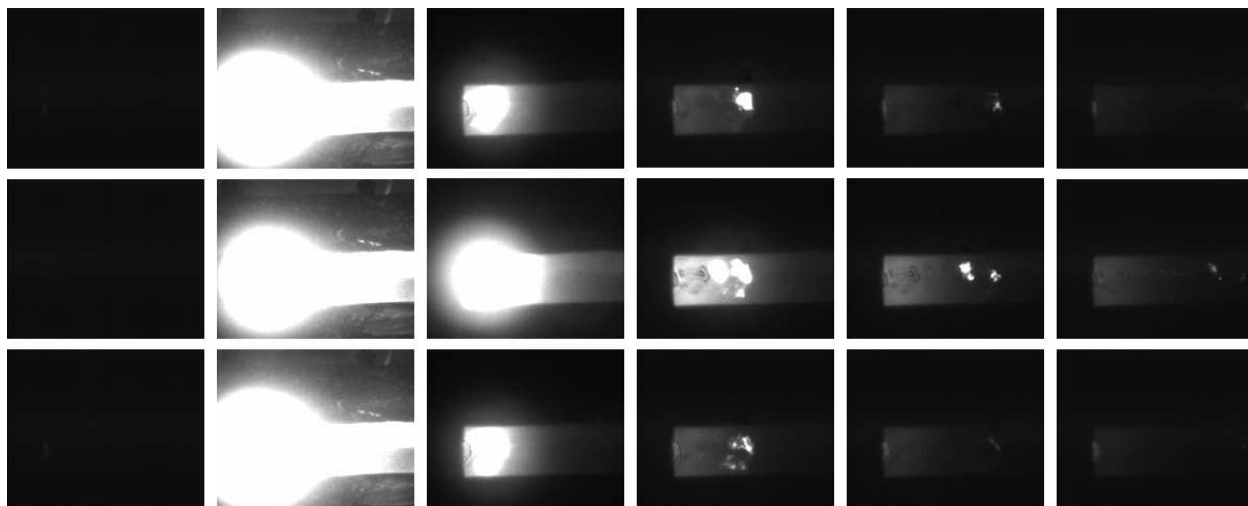


Figure 135: Three series of CH* chemiluminescence images of an electrode-spark initiated kernel in $M = 1.25$ flow.

OH Chemiluminescence with Laser Ignition: Non-Diverging Test Section*

A Photron SA-5 high speed camera operating at 50,000 frames per second coupled to a Highcat intensifier was used to capture luminescence from the spark-initiated kernel. A 55 mm lens and 308 nm filter focused on the OH* chemiluminescence. The ignition system is discussed above in Section 3.2.3. A schematic of the test section is shown in Section 3.2.1. The converging-diverging nozzle was sized to achieve a $M = 1.25$ free stream velocity. Natural gas is injected through counter-flowing sonic jets sufficiently far upstream to achieve a fully mixed flow in the test section.

The tunnel was operated as $\phi = 0.9/1.0$ and ignited with laser energy of 10/30 mJ/pulse. A series of ignition events is shown in Figure 136. Approximately 33 images were captured for each kernel and a total of 8 kernels were captured for each run condition. For each condition the 8 kernels were averaged to produce a series of images of the average kernel size. Kernels that did not grow were removed from the analysis. Three kernels were removed from Case 2 and four kernels were removed from Case 3 (see Table 18). Each averaged image was background subtracted and binarized. The remaining pixels were added and converted to a physical kernel area through the conversion $1^2 \text{ pixel}^2 = 0.58142 \text{ mm}^2$. The kernel area was converted to an effective diameter by assuming a circular cross section. The effective diameter versus time is shown below in Figure 137. For each case, the averaged kernel diameter first decreases before increasing. The kernel images start approximately 100 microseconds after the laser is fired. This suggests that there are remaining startup effects from the laser ignition pulse. These effects appear to linger for another 200-300 microseconds before the kernels appear fully developed and begin to grow linearly. This effect was not seen in the subsonic kernel measurements because there was a much longer time delay between ignition and the start of the images. Further analysis of the kernel startup process is necessary to validate these claims.

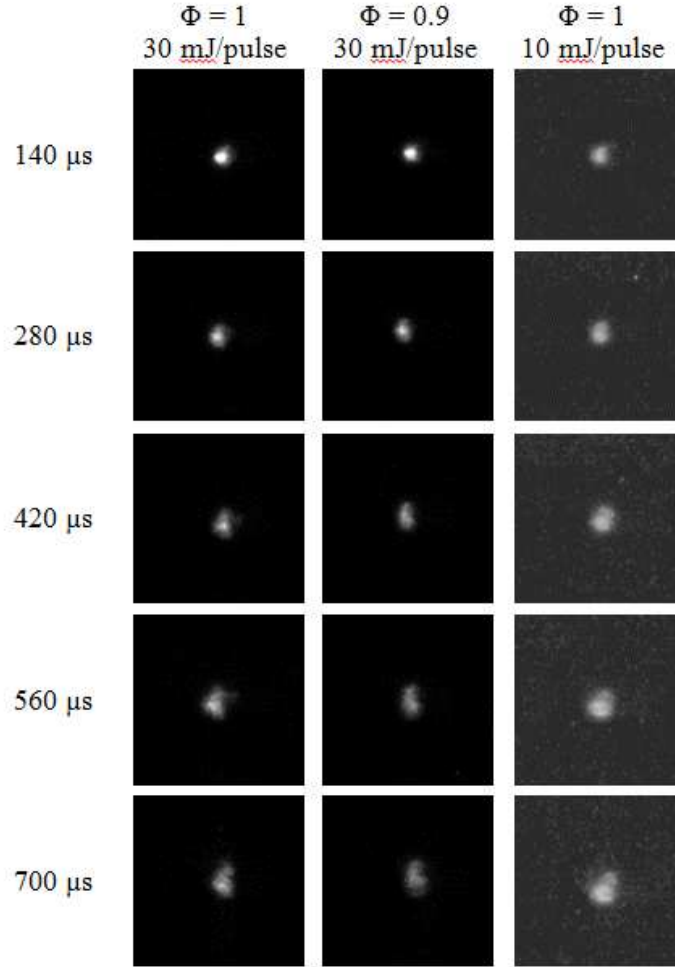


Figure 136: Series of OH* chemiluminescence images of a laser-sparked methane/air mixture at $M = 1.25$ free-stream velocity for varying equivalence ratio and ignition energy.

A linear fit was added to the diameter versus time data by ignoring the images prior to kernel development. These curve fits are included in the data in Figure 137. Following the analysis of Smallbone et. al. [134] an average stretched turbulent burning velocity can be calculated using Equation 34,

$$u_n = \frac{\rho_b}{\rho_u} \frac{dr_{chem}}{dt} \quad (34)$$

where the ratio of burned to unburned density is approximated by the adiabatic equilibrium flame temperature and r_{chem} is assumed equivalent to one half the measured averaged diameter with the derivative equal to one half the slope of the linear curve fit for each case. The results of this analysis are shown in Table 18.

These results show that the measured turbulent burning velocity decreases between the stoichiometric and $\phi = 0.9$ cases and decreases with decreased spark energy. The second

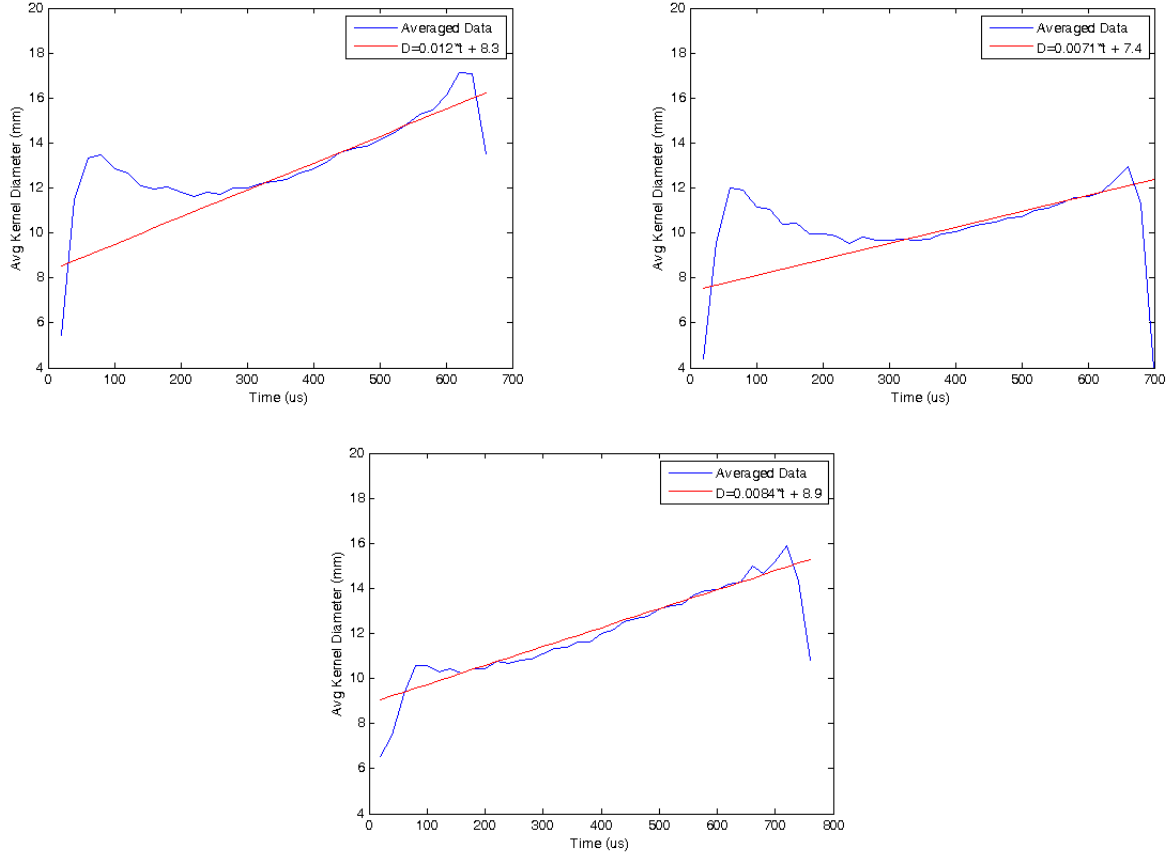


Figure 137: Averaged flame kernel diameter vs. time for $\phi = 1$ and 30 mJ/pulse ignition energy (top left), $\phi = 0.9$ and 30 mJ/pulse ignition energy (top right), $\phi = 1$ and 10 mJ/pulse ignition energy (bottom)

Table 18: Averaged stretched turbulent burning velocity calculated from OH* chemiluminescence images.

	ϕ	Ignition Energy (mJ/pulse)	ρ_b/ρ_u	dr_{sch}/dt (m/s)	u_n (m/s)
Case 1	1.0	30	0.135	6	0.81
Case 2	0.9	30	0.141	3.55	0.501
Case 3	1.0	10	0.135	4.2	0.567

result is counter-intuitive as the turbulent burning velocity should rely on the chemical and turbulent properties of the flow which were unchanged between Case 1 and 3. This extra dependence on laser ignition energy suggests that the burning velocity may yet be influenced by the kernel development several hundred milliseconds after ignition. This further necessitates a more thorough investigation of the kernel initiation in these high speed flows. In addition, the turbulence properties, out of plane kernel development, and bulk features of the test section all need to be investigated prior to drawing any conclusions.

OH Chemiluminescence with Laser Ignition: Diverging Test Section*

A Photron SA-5 high speed camera operating at 50,000 frames per second coupled to a Highcat intensifier was used to capture luminescence from the spark-initiated kernel. A 55 mm lens and 308 nm filter focused on the OH* chemiluminescence. The ignition system is discussed above in Section 3.2.3. A schematic of the test section is shown in Section 3.2.2. The converging-diverging nozzle was sized to achieve a $M = 1.5$ free stream velocity. Natural gas is injected through counter-flowing sonic jets sufficiently far upstream to achieve a fully mixed flow in the test section. The tunnel was operated at $\phi = 1.0$ and ignited with laser energy of 30 mJ/pulse.

The camera was operated in burst mode (30 images) and triggered by a ttl signal from the master timing box which also controlled the spark laser. The camera was focused on the test sections first window and was installed at a 45 degree angle to allow simultaneous single-shot schlieren imaging. A series of superimposed images was produced for each kernel. An example series of images is shown in Figure 138. The kernel clearly grows but travels vertically which is undesirable for PLIF imaging and higher order analysis. A defect on the window is responsible for the reduced luminescence on the sixth kernel image. Analysis is ongoing at the time this report was written.



Figure 138: Sample OH* chemiluminescence images of kernel propagating at $M = 1.5$ free-stream velocity in diverging test section.

Schlieren Photography

The redesigned diverging supersonic test section described in Section 3.2.2 was used to investigate the nature of the flow field inside the supersonic-diverging test section. Initially, a NAC GX-3 high speed camera was used with the schlieren arrangement discussed in Section 4.1. The schlieren system was setup to look through the second window where the kernel should have had sufficient time to develop and be large enough to find easily. A 10 μ s internal

camera gate was necessary to provide adequate light to the CMOS sensor. A sample image is shown in Figure 139. The schlieren images do provide sufficient data to produce kernel growth rates as a comparison to future high speed chemiluminescence and PLIF imaging, however the light source needed improvement because the long gate allowed the kernel to move approximately 3 mm during exposure. A set of time-locked schlieren images show that the kernel walks as much as 12 mm up or down from the average vertical position. Orthogonal chemiluminescence shows similar behavior in the orthogonal direction. It is postulated that the shocks are responsible for the observed walking.

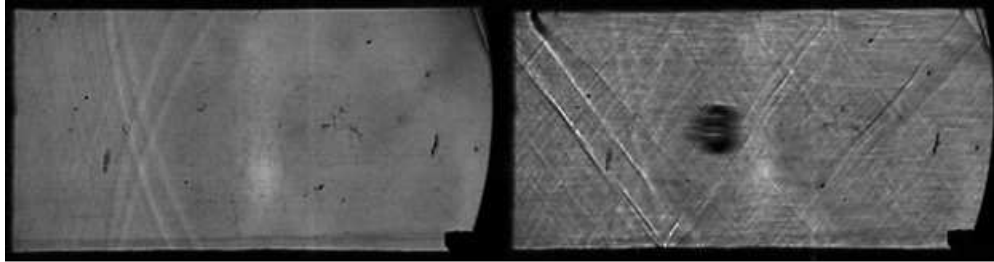


Figure 139: High-speed schlieren photography of a no flow condition (left) and an ignition kernel in a $M = 1.5$ free stream flow (right).

In order to test this hypothesis, additional schlieren images were taken near the ignition location. For these tests, a Photron SA5 high speed camera was used with a $5 \mu s$ gate at 50 kHz. The overall light intensity was low so additional post-processing was performed to improve the image and enhance the kernel features. For each set of kernel images (30 images) the series of images are background subtracted, brightness corrected, then contrast corrected. A sample pre and post processed image is shown in Figure 140.

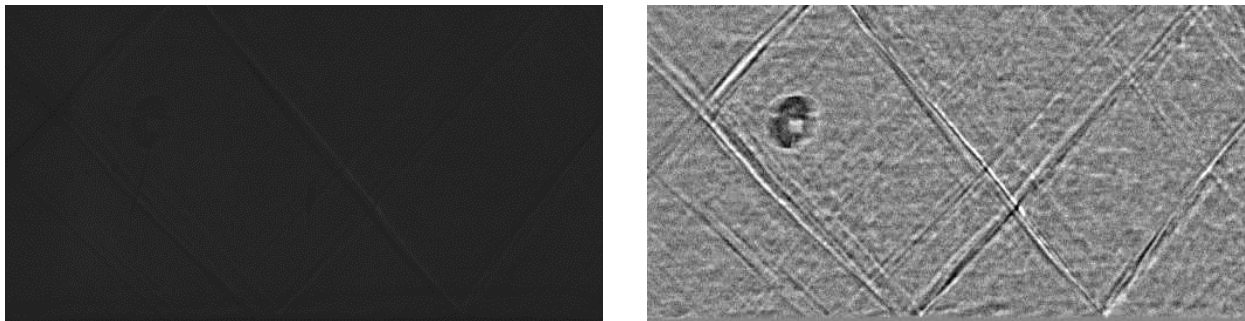


Figure 140: Sample kernel propagation image post-processing. Raw image shown at left, with resultant image shown at right

A series of processed images were superimposed onto a single image to better track the motion of a single kernel. Two examples are shown in Figure 141. For these images, the kernel has only propagated 100 mm but has already walked approximately 6 mm. The shock locations vary in time and it appears that the instantaneous location of upstream shocks at the time when the kernel passes through has an important role on the propagation and

development of the flame kernel. These observations are still being investigated at the time this report was written.

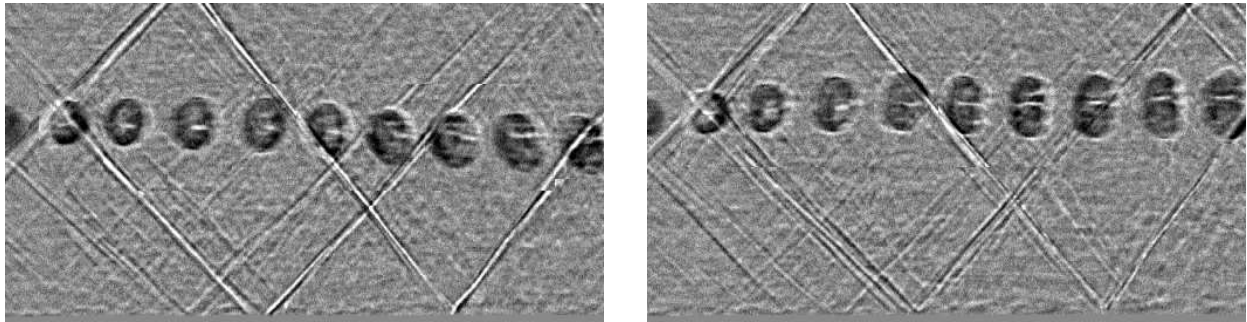


Figure 141: Superimposed kernel propagation images showing the kernel walking down (left) and walking up (right).

5.2.4.2 Detailed Measurements Chemiluminescence and Schlieren measurements were collected at two axial locations corresponding to the tunnel’s first and second windows. From these data, global displacement speeds were calculated using Eq. (8). Table 19 summarizes the test conditions and results of this analysis. Six cases are identified: two turbulence settings (baseline and passive grid) and three equivalence ratios. The turbulent statistics for the baseline and passive grid cases are summarized in Table 17. For all cases the stagnation pressure was $P_0 = 320.5 \pm 5 \text{ kPa}$ and the stagnation temperature was $T_0 = 550 \pm 20 \text{ K}$. Methane-air laminar flame speeds were taken from the bomb data of Andrews and Bradley.[135] An example output of the averaging process is shown in Figure 142 for Case 5 at the upstream axial position.

Figure 142(a) shows the OH^* chemiluminescence of the averaged kernel at each propagation time overlaid onto one image. The intensity clearly decreases as the kernel propagates downstream. This is due to the high energy input of the ignition laser and the resulting large luminescence of the initial kernel. The laser energy was set at 30 mJ/pulse to minimize shot to shot variation. The result was an ignition kernel that necessarily over exposes the camera during early propagation times. This phenomena causes an error in the initial size of the kernels measured with the OH^* technique. By the third image (approximately $73.3 \mu\text{s}$ after ignition) this error appears to be gone. Self propagating and growing kernels were achieved with ignition energies as low as 6 mJ/pulse, however a significant portion of these kernels did not grow. Ignition energy may contribute a memory effect to the growth of kernels but the energy was not included as a variable in this study. In fact, ignition in supersonic flows is a relatively unexplored topic that deserves its own study. Brieschenk[136] successfully used laser ignition in a scramjet environment but to the authors’ knowledge this is the first attempt at ignition of supersonic, freely propagating kernels using laser induced plasma ignition.

Figure 142(b) shows the Schlieren photography of the averaged kernel at each propagation time overlaid onto one image. Unlike the chemiluminescence images, kernels measured with

³Laminar flame speeds from Andrews and Bradley.[135]

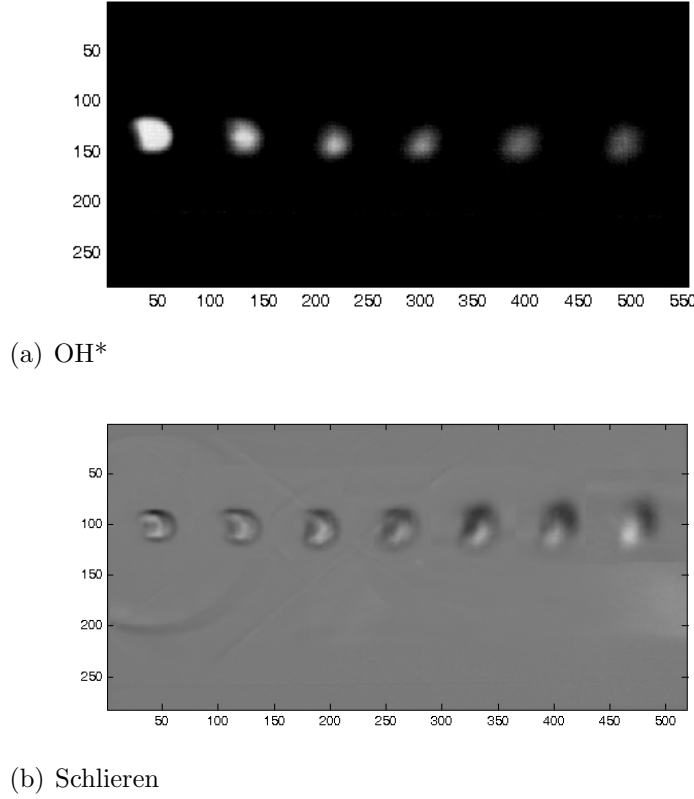


Figure 142: Sample high speed OH* chemiluminescence and Schlieren images overlaid onto a single image. (a) ~ 7.45 pixels/mm, (b) ~ 5.82 pixels/mm. Images are averaged over 822 independent kernel realizations.

the Schlieren technique have a positive growth rate starting, presumably, at the ignition location (outside the field of view). The kernel is at the smallest effective diameter at the first frame. There is also some structure to the kernel which is an artifact of the ignition process. This structure persists downstream and may influence the global growth rate of the flame kernel. Also visible in Figure 142(b) is a spherical shock wave propagating away from the flame kernel. This is the spherical shock resulting from the ignition process. This shock reflects off the side walls of the tunnel and passes through the kernel by the fourth frame (not shown). The ignition laser focusing lens was slightly off-center which caused the reflected shocks to return to the kernel at different times. The effect of this spherical shock on kernel growth is still being explored. There are also two weak oblique shocks in Figure 142(b) that are a result of the variable hinge construction in the tunnel. A slight deviation in the average kernel trajectory can be seen in both the chemiluminescence and Schlieren images due to the location of these shocks and possibly the interaction with the spherical ignition shock.

Figure 143 shows a summary of the measured kernel diameter versus propagation time for both the Schlieren and OH* chemiluminescence techniques. Also shown are linear regression curve fits of the kernel diameter from the first to second window. For both techniques, there is a clear increase in the kernel diameter with propagation time, i.e. the kernels are growing

Table 19: Summary of test conditions and global displacement velocities.³

Case	Turbulence Grid	ϕ	$\frac{u'}{S_L}$	$\frac{dr_{chem}}{dt}$	$u_{n_{chem}}$	$\frac{dr_{sch}}{dt}$	$u_{n_{sch}}$
1	No Grid	1.2	2.08	-	-	4.12	0.687
2	No Grid	1.1	1.91	6.86	1.13	2.59	0.427
3	No Grid	1.0	1.98	8.72	1.45	2.54	0.422
4	Passive Grid	1.2	4.58	11.92	1.99	15.3	2.56
5	Passive Grid	1.1	4.21	12.52	2.06	15.8	2.60
6	Passive Grid	1.0	4.36	11.83	1.97	18.5	3.08

as expected. There is also a clear difference in the growth rate between the baseline and turbulence grid cases. Kernels growing in the flow field with the turbulence grid have a higher final kernel diameter. This is because the increase in turbulence level (u'/S_L) leads to an increase in flame surface density which leads to a larger global displacement velocity and finally a kernel of increased size.

Comparing Schlieren and OH* chemiluminescence, there appears to be a discrepancy in the kernel diameter measured by each technique. The Schlieren technique produces larger kernels than OH* with the turbulence grid but smaller kernels without the turbulence grid. The first of these comments may be explained by the fact that the Schlieren edge is expected to be in the preheat zone of the flame and hence be larger than the OH* edge which is expected to lie in the reaction zone. The second issue, that Schlieren produces much lower kernel diameters downstream than OH* without the grid, may be explained by heat losses. The flame kernels may quench downstream due to radiative heat loss or large rates of scalar dissipation encountered when passing through Mach waves or weak shock waves. Flames growing in higher turbulence may survive these losses better. Luminescence due to chemical excitation of OH has a relatively long lifetime and may survive downstream (despite quenching), explaining the difference between the two measurements. Perhaps a more likely explanation is that the Schlieren technique, as implemented here, suffers from a low signal to noise ratio due to the low irradiance of the chosen light source and relatively long exposure times. These issues were especially problematic when imaging kernels further downstream. The low signal to noise makes edge detection more difficult and resulted in edges that were 15-20% smaller than those of the corresponding OH* measurement at the downstream location.

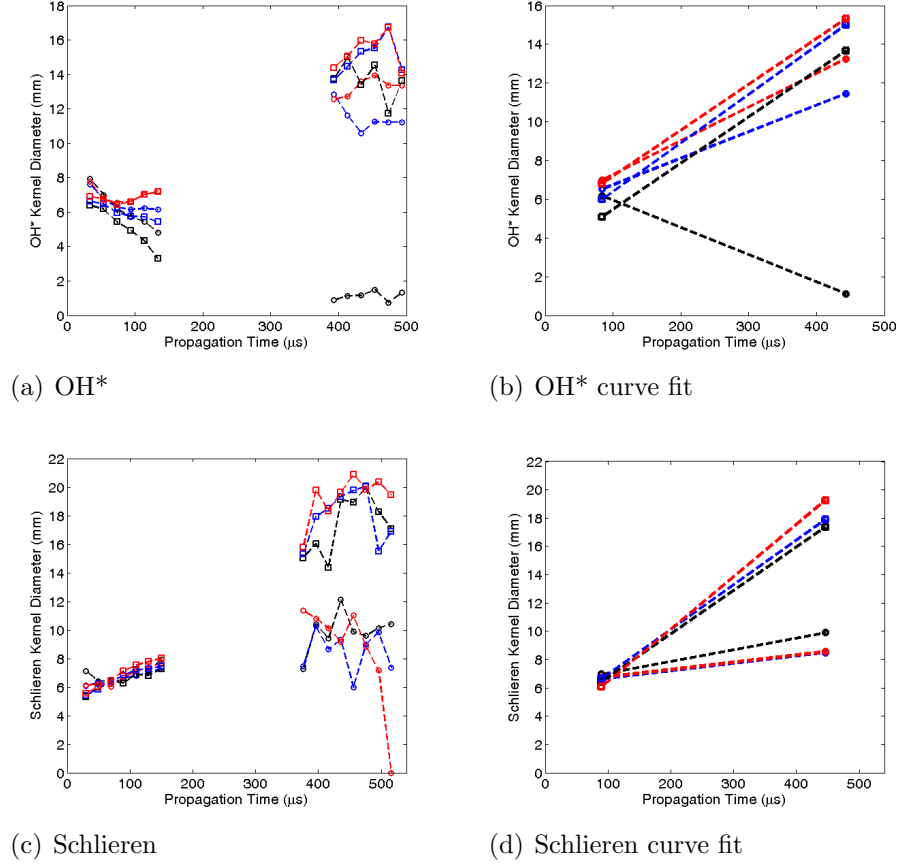


Figure 143: Kernel diameter versus time at $M=1.5$ comparing OH* chemiluminescence and Schlieren methods. Case 1: black circles, Case 2: blue circles, Case 3: red circles, Case 4: black squares, Case 5: blue squares, Case 6: red squares. Case descriptions are in Table 19.

Measured global displacement velocities, $S_{T,gd}$ were normalized by the laminar flame speed, S_L and plotted versus u'/S_L as shown in Figure 144. Also shown are the classical turbulent flame speed correlations of Damköhler[137] (see Eq. 35), and Bradley[138] (see Eq. 36). Damköhler's correlation is derived by assuming the flame area is increased proportionally to the turbulent velocity resulting in Eq. (35). Bradley's correlation is more complicated in that an attempt is made to correct for thermo-diffusive effects and variations due to the turbulent length scale. Equation 35 is based on a consumption velocity derivation while Eq. (36) combines displacement and consumption velocity data into a single empirical relationship. It should be expected that Eq. (36) more faithfully represents the physics in this study but may fall short of matching these data due to the wide variety of source data used to produce the correlation. In producing these graphs the integral scale l was estimated to be 8.9 mm (which is less than the channel half-width and matches the turbulent grid hole size) and the Lewis number was assumed unity for all cases. Based on these estimates, all of the flames investigated in this study were in the thin reaction zone.

$$\frac{S_T}{S_L} = 1 + \frac{u'}{S_L} \quad (35)$$

$$\frac{S_T}{S_L} = 1 + 0.95Le^{-1} \left(\frac{u'}{S_L} \frac{l}{\delta_L} \right)^{0.5} \quad (36)$$

The same generally upward trend is seen in the experimental data and correlations (Figure 144), however, there is a fairly significant absolute deviation in the data of this study from the correlations. For the baseline tunnel (no grid), $S_{T,gd}/S_L$ is approximately 60% the value of the Damköhler correlation and 40% the value of the Bradley correlation. With the turbulence grid installed, $S_{T,gd}/S_L$ is approximately 60% of both correlations. A linear fit between the two turbulence levels results in a more gradual slope than the Damköhler correlation. Reasons for these discrepancies fall broadly into two categories: measurement errors and physical phenomena. Based on the PIV error analysis above, there is a relatively small error band on u'/S_L . The measured displacement speeds have a larger error band for reasons discussed above. However, the kernels would need to be 66% larger than measured to explain the difference. This is unlikely to be the case because two different measurement techniques yielded very similar results. Additionally, no single kernel realization came close to the flame speed required to match the correlations. Measurement error alone cannot explain these differences. Heat losses in the form of radiation to the tunnel walls may account for some of the difference between measurement and theory. Heat losses would drive down the laminar flame speed and reduce the burned gas density resulting in a reduced growth rate of the flame kernel. Interaction of the flame kernel with the tunnel walls may also have an effect on kernel growth. The free expansion of the outward propagating gas in front of the flame has the tunnel walls as a physical limit. The expanding gas will have to slow and turn in direction after a certain critical kernel size. This will limit the growth of the kernel and may appear as a kink in the diameter versus propagation time plot. A third possibility is that interaction of the kernel with Mach waves, weak oblique shocks, and the ignition shock may impact its growth, i.e. the classical correlations presented here may do a poor job of predicting turbulent flame speeds in compressible flows. Mean-flow compressibility has a known retarding effect on turbulent phenomena such as mixing in shear layers,[139] but whether or not mean compressibility has an effect on kernels propagating in this shear-free environment is unclear. Further studies with various levels of mean-flow compressibility are needed to elucidate any effects of compressibility on the turbulent flame speed. Finally, the Bradley correlation presented is relatively general in that a variety of experimental configurations and conditions were used to fit the correlation constants and it is not expected to exactly match the data of this study.

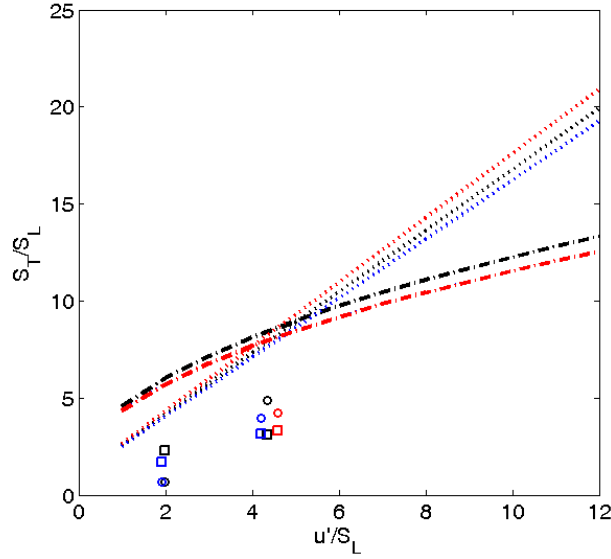


Figure 144: Global displacement velocity versus u'/S_L . Black: $\phi = 1.0$. Blue: $\phi = 1.1$. Red: $\phi = 1.2$. Symbols: data from this study (circles: Schlieren method, squares: OH* chemiluminescence method). Dotted line: correlation of Damköhler[137], Dash-dotted line: correlation of Bradley.[138]

5.2.5 Summary of Freely Flowing Flame Kernel Data Collected to Date

Applying the correlation procedure by Chaudhuri et al. [126] to the incompressible, the isotropic subsonic and the supersonic kernel measurements gives the result shown in Fig. 145. The effective turbulent intensity for the $Mach \geq 0.1$ cases has been estimated using non-dimensional expressions by Bradley [124], the respective Markstein length by using the aforementioned correlation in Driscoll's review paper [2].

The data collapses consistently across flow conditions and equivalence ratios. This increases confidence in the earlier conclusion, that the built facilities are capable of producing meaningful results and that the instrumentation works correctly. However, the question remains why the $\phi = 1$ cases seem to deviate from the lean mixture results, not only for the experiments in this study but also for other researchers. Future efforts should investigate this as well as extend the extracted information to usage in modeling efforts of turbulent flames at high flow velocities.

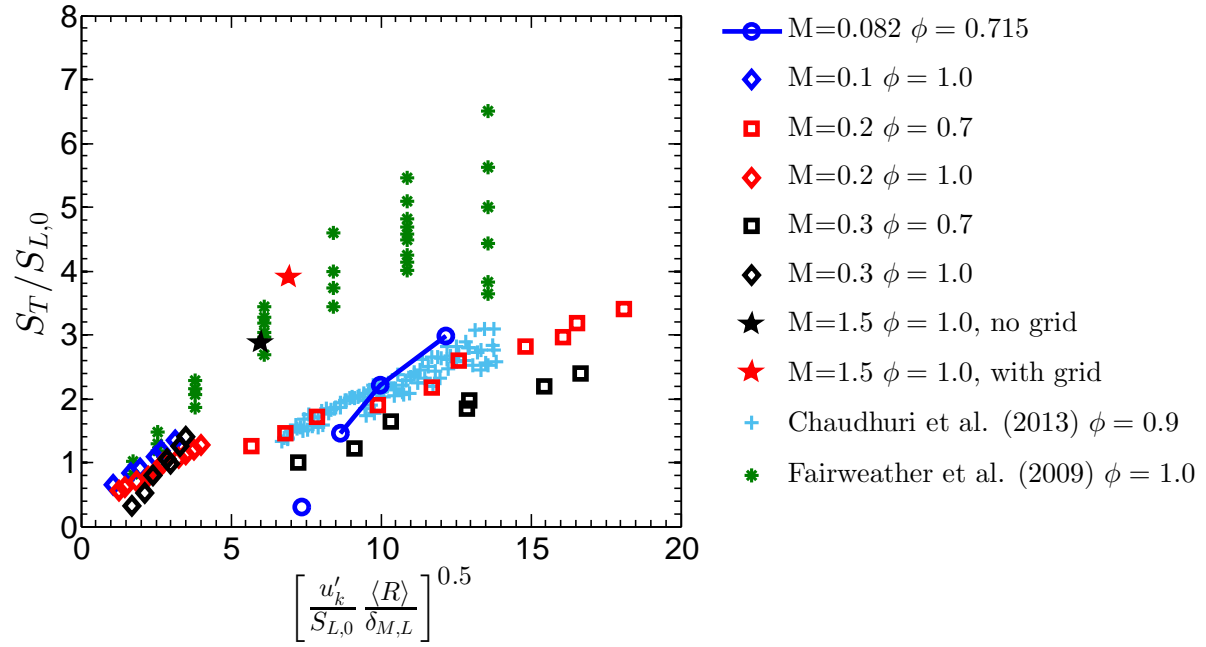


Figure 145: Summary of freely propagating flame kernels, correlated using Chaudhuri's [126] approach. Results from this study as well as from other researchers and two empirical correlations are shown.

6 Conclusions and Future Work

This report summarizes the efforts of a three year program to study flames in high speed flows, such as supersonic combustors. In these scenarios, state of the art numerical schemes are often completely unvalidated and/or fail to capture even the most simple of flow features. The ultimate goal of this research program is to advance our understanding of flames in supersonic flows and, in doing, improve the design capabilities of high speed combustors through validation and enhancement of predictive models. This goal requires an extensive set of experimental data be collected at a number of conditions. We have chosen to break the problem into a set of experimental scenarios of gradually increasing complexity. These are summarized below:

1. First, an incompressible subsonic experiment was built to study low speed flame kernels and directly compare the results to previously established flame bomb studies.
2. Next, with an anchor to the well established studies, complexity was added by increasing the Mach number. A new subsonic tunnel was built allowing mean flow Mach numbers up to 0.6. Those results were then compared to our low speed kernels.
3. Finally a supersonic tunnel was built for extension up to Mach 1.5.

In this way, the premixed supersonic flames were compared to flame bombs through a step-up method that was well validated. This report concludes with a complete archived set of turbulence and flame measurements for $M < 0.3$, a partial set at $M < 0.6$, and a set of demonstration data for $M = 1.5$. The following summarize the major accomplishments of this research program:

Developmental Accomplishments

- Built a new incompressible subsonic reacting facility for comparison to flame bomb studies
- Built a new compressible subsonic tunnel for examination of turbulence generation methods, flame kernel propagation, and diagnostic validation
- Built a new supersonic facility to study flames in supersonic flows
- Developed hot-wire Constant Temperature Anemometry (CTA) and particle image velocimetry (PIV) methods for use in turbulence characterization
- Built and characterized passive, blown and vane grid turbulence generation systems
- Developed a reliable and consistent laser ignition system to initiate flame kernels

Experimental Accomplishments

- Completed turbulence generation studies in subsonic flows (passive and active grids)

- Obtained an archival quality set of data for kernels flowing in $M, 0.3$ flow for both isotropic and anisotropic turbulence
- Showed that low speed kernels match previous flame bomb studies
- Obtained some measurements of flame kernels in $M < 0.6$ anisotropic turbulence
- Conducted exploratory studies of flame kernels in supersonic flows, including Schlieren, CH^* , OH^* , OH PLIF and PIV.
- Showed that supersonic kernels match previous correlations but require special treatment
- Demonstrated that compressible features such as Mach waves and shock waves will have an effect on flame kernels that numerical models will likely not capture directly

Future Plans

These studies will be expanded to include a complete set of flame kernel studies for high compressible ($M < 0.6$) kernels and supersonic kernels. In addition, new complexity will be added to approach more realistic engineering conditions. The effect of shocks and high turbulence levels will be studied by developing/installing new shock and turbulence generators. Also, the homogeneous flow studied up to this point will be made more complex by imparting a constant shear rate along the entire channel. This homogeneous shear flow approaches more realistic conditions because combustors rarely experience a constant unidirectional flow. Most importantly, all of these results (past and present) will be analyzed for direct comparison to numerical model results. Compressible models will be analyzed and if necessary modified to improve agreement.

7 Supported Students and Personnel

Doctoral Students

- Bradley Ochs- Current student
- Dan Fries- Current student
- Nathan Grady- Graduating Summer 2015

Master's Students

- Thomas Slais- Graduating Summer 2015
- John Berlette- Graduated Spring 2014
- Tyler Hannan- Graduated Fall 2013

A Measurements of Leading Point Conditioned Statistics of High Hydrogen Content Fuels

Contents

1. Introduction.....	2
2. Experimental measurements	6
2.1. Experimental Facility	6
2.2. Optical Diagnostics	7
2.3. Chemical Kinetic Calculations.....	7
2.4. Flame Front Topology.....	8
2.5. Global (Unconditioned) and Leading points Curvature Statistics	9
3. Numerical simulations	13
3.1 Numerical methods	13
3.2 Definitions.....	14
3.3 Results	16
4. Conclusions.....	21
5. Publications.....	22
6. References.....	23

1. Introduction

Fuel/Oxidizer composition influences the turbulent burning rates of premixed flames at both low and high turbulence intensities [1]. The turbulent flame speed is commonly correlated using:

$$S_T = s_{L0} f\left(\frac{u'}{s_{L0}}\right) \quad (1)$$

where s_{L0} is the unstretched laminar flame speed and u' is the turbulence intensity [1, 2]. S_T is also affected by turbulent length scales [3], bulk flow velocity [4], experimental configuration [5, 6], and fuel composition [1, 7-9]. This report investigates the effect of fuel composition, which has been well-documented in the literature [1]. For example, our group has reported measurements of H₂: CO blends showing factor of three variations in S_T across fuel blends with identical s_{L0} values, even at turbulence intensities u'_{rms}/s_{L0} up to 40. Similar observations were made by Wu *et al.* [10], Bradley *et al.* [11], Kido *et al.* [7, 12], Brutscher *et al.* [13] and others, and summarized in the review of Lipatnikov and Chomiak [1].

The sensitivity of S_T to fuel composition is associated with the stretch sensitivity of the reactant mixture. This leads to variations in the local consumption speed along the turbulent flame front that can arise from both non-unity Lewis number and preferential diffusion effects [14]. In particular, the high mass diffusivity of H₂ makes H₂-bearing mixtures highly stretch sensitive, such as shown in the illustrative calculations in Figure 1.

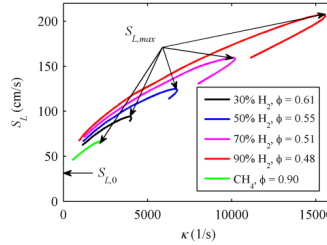


Figure 1: Stretch sensitivity calculations of H_2 :CO fuel blends and CH_4 [15].

A typical justification for this increase of turbulent burning rates by turbulent velocity fluctuations is given on "global" arguments relating to flame area [16] - i.e., in constant burning velocity flames, the turbulent burning velocity increase is directly proportional to the increase in flame surface area. Some authors have attempted to generalize these ideas to stretch-sensitive flames by also accounting for variations in local burning rate along the flame [1]. The interactions between burning area and flame area, as well as the fact that zones of intense burning are often accompanied by zones of extinction in high stretch sensitivity flames complicates this approach.

"Leading points" concept provides an alternate approach to understand this augmentation of burning rates. This concept was originally proposed by Zeldovich [17], who described the "leading/pilot" points as the most forward-lying points of the flame front in the direction of the reactants. In a turbulent premixed flame, the largest velocity fluctuations in the direction of propagation create convex bulges with respect to the reactants which generate flame surface area behind them and determine the average combustion velocity [18]. Thus, leading points are the positively curved points on the turbulent flame front that propagate out furthest into the reactants in spatial regions where turbulent eddies induce low approach flow velocities. The importance of the leading edge of the turbulent flame brush was suggested based on application of the KPP (Kolmogorov-Petrovskii-Piskunov) theorem [19], which shows that, under certain assumptions [2], a one dimensional statistically stationary turbulent flame behaves as a "pulled front", for which the turbulent flame speed is controlled by the average reactant consumption rate at the leading edge of the turbulent flame brush, i.e., the points where averaged progress variable

This concept has been used to correlate experimental turbulent flame speed data or to develop closure models for RANS/LES turbulent combustion equations. Some of these studies have further argued that the flame front at the turbulent flame brush leading edge consists of "critically" stretched laminar flames, such as stationary curved flame balls [20, 21], expanding spherical flames of small radius [22, 23] and planar, counterflow twin flames near extinction [3, 9, 15, 24]. Other studies have modelled leading points burning rates using empirical formulae based on some "effective" Lewis number of the mixture [25-27].

Calculations of laminar flame stretch sensitivities show that the positively curved leading point flame speed can substantially exceed s_{L0} , as shown in Figure 1 [14]. Assuming that S_T is controlled by the leading point characteristics, the ensemble averaged laminar burning rate of this leading points turns out to be a very significant turbulent flame property. Venkateswaran *et al.* [15, 28] developed a scaling law for the turbulent flame speed of negative Markstein length flames, using the maximum stretched laminar flame speed, $s_{L,max}$, as the normalizing parameter, as opposed to the traditional approach of using the unstretched laminar flame speed, s_{L0} . The form of this scaling law is given by:

$$\frac{S_T}{s_{L,max}} \leq 1 + \frac{u'_{LP}}{s_{L,max}} \quad (2)$$

where u'_{LP} is the turbulence intensity at the leading point of the flame. The idea that $s_{L,max}$, and not s_{L0} , is the suitable velocity scale for correlating S_T was suggested by [29] and has found justification in data from Venkateswaran *et al.* [15], as shown in Figure 2, which plots data obtained with a range of $H_2:CO$ mixtures normalized by s_{L0} (Figure 2a) and $s_{L,max}$ (Figure 2b). Note the strong fuel effects manifested in the s_{L0} scaled data, but the good collapse of the data using the $s_{L,max}$ scaling.

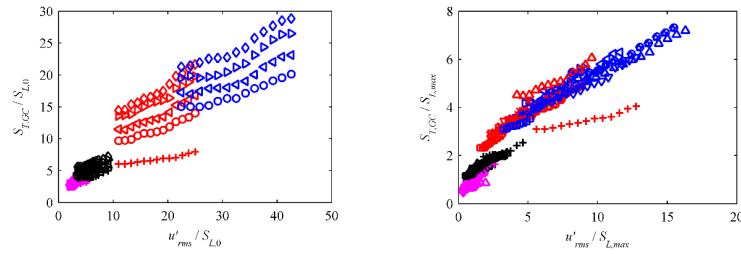


Figure 2: (a) Measured dependence of the turbulent flame speed, $S_{T,GC}$, upon turbulence intensity, u'_{rms} , normalized by s_{L0} at various conditions for several $H_2:CO$ ratios and pure CH_4 . **(b)** $S_{T,GC}$ data from (a) normalized by $s_{L,max}$. See Venkateswaran *et al.* [15] for details on experimental conditions.

This report summarizes some of the key work under this program. We have not attempted to exhaustively detail the work, but provide a summary of several key outcomes. Further work and analysis is described in the key journal publications which have stemmed from this work:

1. Marshall, A., Lundrigan, J., Venkateswaran, P., Seitzman, J., Lieuwen, T., “Fuel Effects on Leading Point Curvature Statistics of High Hydrogen Content Fuels,” *Proceedings of the Combustion Institute*, 2014
2. Amato, A., Day, M., Bell, J., Lieuwen, T., “Leading Edge Statistics of Turbulent, Lean, H₂-Air Flames”, *Proceedings of the Combustion Institute*, 2014.
3. Venkateswaran, P., Marshall, A., Seitzman, J., Lieuwen, T., “Scaling Turbulent Flame Speeds of Negative Markstein Length Fuel Blends Using Leading Points Concepts”, *Combustion and Flame*, 2014
4. Venkateswaran, P., Marshall, A., Seitzman, J.M., Lieuwen, T., “Turbulent Consumption Speeds of High Hydrogen Content Fuels from 1-20 atm,” *Journal of Engineering for Gas Turbines and Power*, 2014
5. Amato, A., Lieuwen, T., “Analysis of Flamelet Leading Point Dynamics in an Inhomogeneous Flow,” *Combustion and Flame*, 2013
6. Amato, A., Day, M., Cheng, R. K., Bell, J., Lieuwen, T., “Topology and Burning Rates of Turbulent, Lean, H₂/Air Flames,” Submitted to *Combustion and Flame*, 2014
7. Marshall, A., Lieuwen T., “Curvature and Strain Characteristics of Turbulent, Stretch Sensitive fuel mixtures”, in preparation for submission to *Combustion and Flame*, 2015.
8. Lyra, S., Wilde, B., Seitzman, J., Lieuwen, T., Chen, J., “Structure and Stabilization of Hydrogen-Rich Transverse Jets in a Vitiated Crossflow”, *Combustion and Flame*, Vol. 162, 2015, pp. 1234-1248.

Section 2 describes the experimental facilities and measurements for several H₂-containing blends. H₂ is an important fuel to consider for air-force platforms as all engines utilize staged combustion concepts that burn a rich aviation fuel, followed by secondary air injection and combustion of H₂/CO blends. Flame leading edge characteristics are compared across these fuels. The objective of the measurements is to evaluate the validity of the physical arguments leading to equation (2)

Section 3 describes the leading edge conditioned and statistics obtained from DNS originally presented by Aspden et al. [30]. The leading edge characteristics are compared to model laminar flame calculations, and the burning velocities and flame curvatures to $s_{L,max}$ and curvature values obtained from “critically” stretched laminar flames. The topology of the

flames are also analysed. In contrast to the experimental measurements, these DNS consider a single fuel/oxidizer composition (H_2/Air at an equivalence ratio of $\phi=0.31$), but span a larger range of turbulent intensities.

2. Experimental measurements

The low swirl burner (LSB) is a useful geometry for local measurements of turbulent flame characteristics, and has been recommended as a canonical geometry for turbulent displacement speed measurements [31]. The LSB was developed by Cheng *et al.* [32] as a method of generating a freely propagating flame that does not rely on flow recirculation for flame stabilization; the flame stabilizes where the flame speed matches the axial velocity. The flame brush in the central region is flat, providing a close approximation to a statistically 1-D planar turbulent flame [33]. The experiments in this work were performed for H_2/CH_4 mixtures over a wide range of conditions outlined in Table 1.

Table 1: Experimental parameters and conditions for the datasets acquired using PIV.

Experiments:	H_2/CH_4
Swirl number, S	0.57-0.60
Mean flow velocity, U_0 (m/s)	20, 30, 40
Fuel Composition (% H_2)	0-75
$S_{L,0}$ (cm/s)	34

2.1. Experimental Facility

The LSB nozzle used in this research is shown in Figure 3a. Turbulence is generated with the variable turbulence generator detailed in Marshall *et al.* [34]. Thus, the turbulence intensity can be varied on-the-fly, without changing the bulk flow velocity or replacing blockage plates. The swirler, shown in Figure 3b, is similar to Cheng’s [35] except the central channel blockage plate was removed. Air flow rates through each channel are adjusted by independent valves. This adds the benefit of being able to vary the swirl number S on-the-fly. S is defined as the ratio of angular to axial flow momentum nondimensionalized by the burner radius R_b [36] and has a value of approximately 0.58. Mean flow velocities quoted in

this paper are defined as $U_0 = \dot{m}/\rho A$, where $\dot{m} = \dot{m}_c + \dot{m}_s$ is the total mass flow rate, ρ is the reactant density, and A is the area of the exit tube.

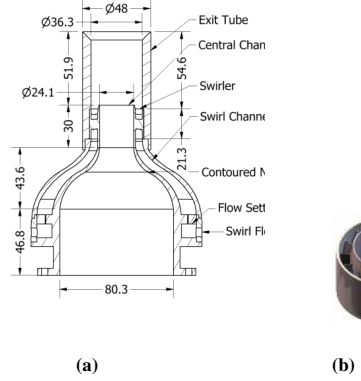


Figure 3: Detail view of the (a) LSB nozzle and (b) swirler. Dimensions in mm

2.2. Optical Diagnostics

Velocity characterizations were obtained using particle image velocimetry (PIV). A Litron Lasers Ltd. LDY303He Nd:YLF twin head frequency doubled laser with a wavelength of 527 nm is used. The camera is a Photron FASTCAM SA1.1 high-speed camera with a full resolution of 1024 x 1024 pixels at repetition rates up to 5 kHz. Velocity calculations were performed using DaVis 7.2 software from LaVision. The interrogation window size used in the calculations was 32 x 32 pixels with an overlap of 50%, giving a spatial resolution of approximately 2 mm between adjacent vectors. See Marshall *et al.* [37] for more details on the PIV setup.

2.3. Chemical Kinetic Calculations

This section describes the calculation approaches used for relating S_T values to detailed kinetic properties of the mixture. Estimates of the unstretched laminar flame speed, $s_{L,0}$, and thickness, $\delta_{f,0}$, were determined using the PREMIX module [38] in CHEMKIN with the Davis mechanism [39]. The flame thickness is calculated using:

$$\delta_{f,0} = \frac{T_b - T_u}{(dT/dx)_{\max}} \quad (3)$$

where T_b and T_u are the burned and unburned temperatures, respectively. To determine the response of the mixtures to stretch, planar counterflow premixed flame simulations were performed using the OPPDIF module with an arc-length continuation approach [40] in CHEMKIN. Typical calculation results are shown in Figure 1.

2.4. Flame Front Topology

Mie scattering from the PIV experiments is used to estimate the instantaneous flame front positions [41]. Figure 4 demonstrates the procedure used for analysing these images. The raw image, shown in Figure 4a, is median-filtered using a 5 x 5 filter to obtain Figure 4b. Once filtered, the image is binarized with the threshold intensity selected using Otsu's method [42], as shown in Figure 4c, to separate reactants from products and find the flame edge. Figure 4c shows the resulting instantaneous progress variable c field, which is defined to be 0 in the reactants and 1 in the products [43]. The flame edge, shown in green in Figure 4d, is quantified by the arc length s , which is calculated from the x - and y -coordinates of the flame edge found from binarization of the image. The details can be found in Marshall *et al.* [44]

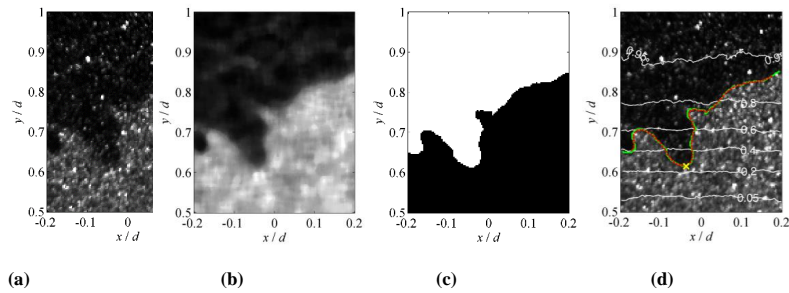


Figure 4: Post-processing procedure used to identify the flame edge from Mie scattering. (a) raw image, (b) median-filtered image, (c) threshold image used to identify reactants and products and find the flame edge, and (d) leading flame edge (green), fitted spline curve (red), instantaneous leading point

(yellow x) and average progress variable, $\langle c \rangle$, (white) overlaid onto raw image (75:25 $\text{H}_2\text{:CH}_4$ fuel mixture, $U_0 = 40$ m/s, $\phi = 0.63$).

2.5. Global (Unconditioned) and Leading points Curvature Statistics

To provide global baselines, Figure 5 plots curvature PDFs over the entire extracted surface (i.e., $0 \leq \langle c \rangle \leq 1$) for two fuel compositions. While the effect of fuel composition on the curvature PDFs is weak, turbulence intensity has a much stronger effect, as shown in Figure 6.

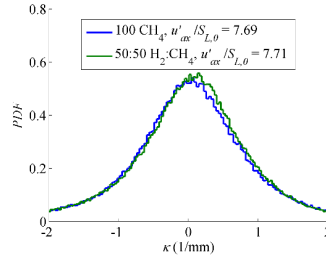


Figure 5: Unconditioned curvature PDFs ($0 \leq \langle c \rangle \leq 1$) for two fuel compositions at $U_0 = 30$ m/s.

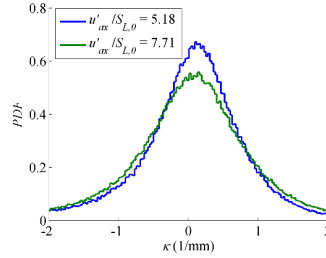


Figure 6: Unconditioned curvature PDFs ($0 \leq \langle c \rangle \leq 1$) at low and high turbulence intensities for a 30 m/s, 50:50 $\text{H}_2\text{:CH}_4$ mixture.

Figure 7 shows instantaneous leading point characterizations for two fuel compositions. These plots show that the resolved curvature at the instantaneous leading point

of the flame is weakly influenced by fuel composition. Similarly, Figure 8 presents curvature PDFs conditioned on the flame brush leading point for two different fuel compositions. These results again show only mild changes in the PDFs with changing fuel composition.

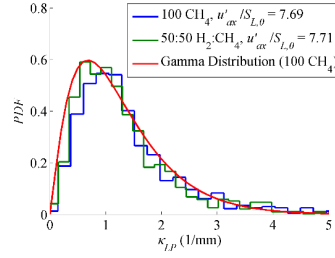


Figure 7: Instantaneous leading point curvature PDFs for two fuel compositions at $U_0 = 30$ m/s.

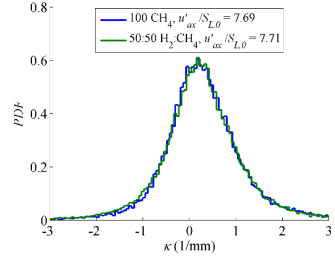


Figure 8: Flame brush leading point ($0 \leq \langle c \rangle \leq 0.1$) curvature PDFs for two fuel compositions at $U_0 = 30$ m/s.

We also include sensitivities of leading point curvature to turbulence intensity for reference. Figure 9 plots the PDFs of instantaneous leading point curvatures at low and high turbulence levels. The results show that as the turbulence increases, the PDF broadens in the direction of short length leading edge flame wrinkles. Thus, these results do show that statistically significant differences in leading point curvature do occur.

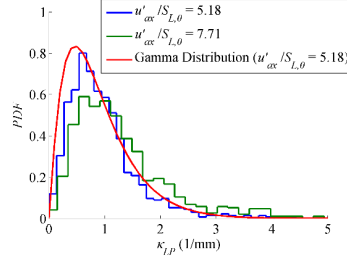


Figure 9: Instantaneous leading point curvature PDFs at low and high turbulence intensities for a 50:50 H₂:CH₄ mixture.

A detailed discussion of these results is presented in Marshall *et al.* [44].

To investigate flame stretch effects, we calculated curvatures and tangential strain rates along the flame front, which represent two components of the overall flame stretch rate.

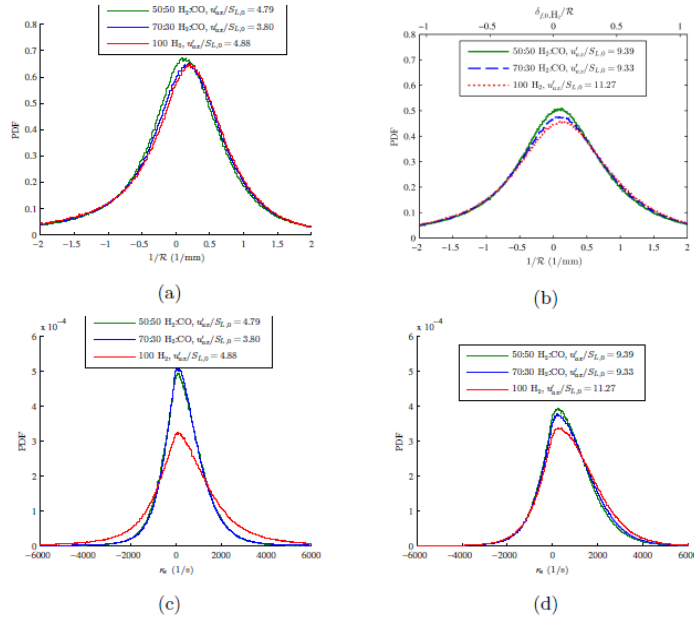


Figure 10. Unconditioned ($0 \leq c \leq 1$) (a, b) curvature and (c, d) tangential strain rate PDFs for varying fuel compositions at (a, c) $U_0 = 30$ m/s and (b, d) $U_0 = 50$ m/s. The secondary top-axis in (b) shows the curvature normalized by the unstretched flame thickness for the 100% H₂ case.

While the effect of fuel composition on the curvature PDFs is weak, turbulence intensity has a much stronger effect, as shown in Figure 10 (top) for two different fuel compositions over a wide range of turbulence intensities.

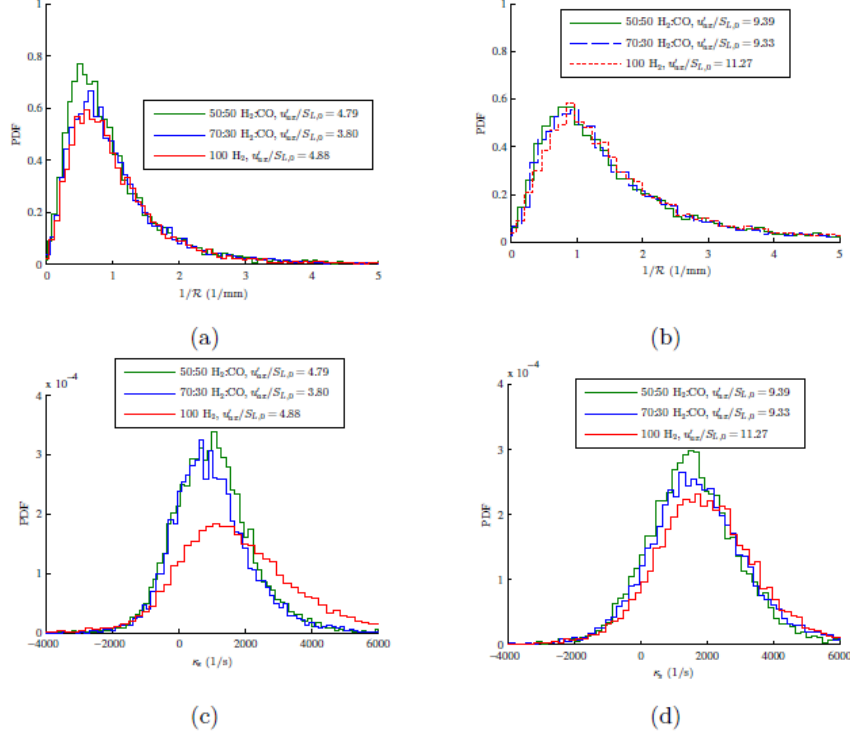


Figure 11: Instantaneous leading point (a, b) curvature and (c, d) tangential strain rate PDFs for (a, c) $U_0=30$ m/s and (b, d) $U_0=50$ m/s.

These plots show that the curvature at the leading points of the flame is only weakly influenced by fuel composition. For example, the mean curvature increases by only 7% from the lowest to highest H2 content for the 50 m/s case. On the contrary, for the tangential strain rate there appears to be a stronger fuel composition effect. From the least stretch sensitive mixture (50% H2) to the most stretch sensitive (100% H2), the time-averaged tangential strain rate increases by 84% for the low turbulence cases (Figure 11a,c) and 26% for the high turbulence cases (Figure 11b,d). These increases are much closer to the observed 84% and

49% increases in the turbulent flame speed for the low and high turbulence cases, respectively.

Marshall *et al.* [45] discusses these effects extensively with the support of other PDFs and JPDFs.

3. Numerical simulations

The objective of this section is to summarize the results obtained numerically (1) for conditional leading edge flame characteristics and comparison with model laminar flame calculations, (2) compare these burning velocities and flame curvatures to $s_{L,max}$ and curvature values obtained from “critically” stretched laminar flames and (3) for topology and burning rates. To achieve these objective, this section analyses leading edge characteristics using DNS results originally presented by Aspden *et al.* [30]. In order to interpret the statistical information obtained by these simulations, we calculate reference, one dimensional computations of stretched premixed flames in several geometrical configurations shown in Figure 10: a planar counterflow twin flame (PCF), a tubular counterflow flame [46] (TCF) and an expanding cylindrical flame (ECF) ignited from a pocket of burnt gases. These different geometries allow for a comparison of the flames response to stretch rates that are imposed through both hydrodynamic strain and flame curvature.

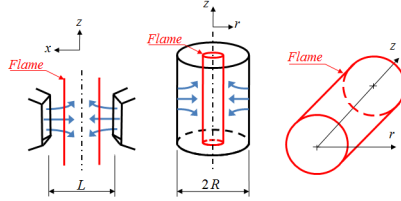


Figure 10. Premixed flame geometrical configurations utilized in this study as model problems to investigate strongly stretched flames: planar counterflow twin flame (left), tubular counterflow flame (center), expanding cylindrical flame (right).

3.1 Numerical methods

All the numerical simulations considered in this paper utilize the transport coefficients, thermodynamics properties and chemical kinetics of the H_2/O_2 system of GRI 2.11 mechanism [47] and a mixture averaged formulation [48] to model molecular diffusion.

We consider an H₂/Air flame at an equivalence ratio of $\phi = 0.31$ and with an initial reactants temperature $T'' = 298K$ and at pressure $p = 1atm$. The computational details for the configurations shown in Figure 12 can be found in Amato *et al.* [49].

The DNS considered in this paper were performed in a computational domain consisting of a high-aspect-ratio ($5\delta_{T0} : 5\delta_{T0} : 40\delta_{T0}$) parallelepiped volume. The flow was initialized with fresh H₂/Air mixture beneath the hot combustion products, resulting in a downward-propagating flame. Periodic lateral boundary conditions were specified, along with an insulating free-slip fixed wall at the bottom of the domain and outflow at the top. A density-weighted forcing term in the momentum equations was used to maintain the turbulent background, characterized by an integral length scale $\ell_t/\delta_{T0} = 0.5$ and turbulent intensities $u'/s_{L0} = 3.69$ (Case A31), $u'/s_{L0} = 17.1$ (Case B31), $u'/s_{L0} = 32.9$ (Case C31) and $u'/s_{L0} = 106.8$ (Case D31). Further details of the DNS database are described in Ref. [30].

3.2 Definitions

Burning velocities and mean curvatures were calculated using the same procedure described in Day *et al.* [50]. For the three-dimensional flame obtained by the DNS, this procedure starts with the tessellation of a temperature isosurface T_{ref} , and the construction of normal vectors by extending along integral curves s_j of temperature gradient. A prism, Ω , can then be built as shown in Figure 11. The consumption speed s_c is then calculated by integrating the hydrogen mass consumption rate $\dot{\omega}_{H_2}$ over the Ω volume and normalizing by the area A_{ref} intersection between Ω and the flame surface, multiplied by the initial hydrogen density contained in the reactants $(\rho Y_{H_2})_{reac}$

$$s_c = \frac{\int_{\Omega} \dot{\omega}_{H_2} d\Omega}{(\rho Y_{H_2})_{reac} A_{ref}} \quad (4)$$

The mean curvature is computed at the flame surface using the identity $K_c = -\nabla \cdot \vec{n}$, where \vec{n} is a unit vector locally aligned with the temperature gradient.

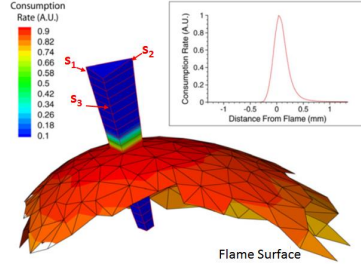


Figure 11. Prism shaped volume, Ω , constructed using curves s_j locally normal to the temperature isotherms; the inset plot shows a typical variation of $\dot{\omega}_{H_2}$ along s_j [50].

To determine the local flame thickness, temperature and H_2 consumption rate fields were interpolated along the integral curves s_j of Figure 11. From these profiles, a flame thickness based on maximum temperature gradient, δ_T , and full width at half maximum of H_2 consumption rate profile, δ_{H_2} , were defined for each of the triangular elements dividing the flame surface as

$$\begin{aligned}\delta_T &= \frac{1}{3} \sum_{j=1}^3 \frac{T^{b,0} - T^u}{\left(dT_j / ds_j \right)_{\max}} \\ \delta_{H_2} &= \frac{1}{3} \sum_{j=1}^3 \text{FWHM}(\dot{\omega}_{H_2,j}(s_j))\end{aligned}\tag{5}$$

where the summation is taken over the three s_j corresponding to a single triangular element. The lengths δ_T and δ_{H_2} are intended to provide an estimate of the local thickness of preheat-zone and H_2 consumption layer, respectively

Statistical data for the DNS were gathered at multiple time instants on temporal intervals in which the turbulent flame can be considered statistically stationary (see Figure 7a in Ref. [30]). To identify the leading edge of the turbulent flame brush, the H_2 consumption rate field was averaged spatially at each time instant in the direction perpendicular to the

mean direction of flame propagation, obtaining a one dimensional average consumption rate profile. Based on this profile, the leading edge of the flame brush was then defined as the portion of space comprised between the most forward lying flame position towards the reactants and the position at which the cumulative average H_2 consumption rate reaches 1/20 of the total. This particular value was chosen for practical reasons as a compromise between collecting values sufficiently close to the edge of the flame brush and having enough realizations across different snapshots in time to build meaningful statistics. This procedure is similar to defining a progress variable $\langle c \rangle$ at each time instant based on the instantaneous consumption rate of H_2 . We note also that implicit within the approach described above is an ansatz that the flame is statistically flat.

3.3 Results

In interpreting the results, it is important to recognize that the sensitivity of premixed flames to large stretch values is not unique, but a function of the stretch profile through the flame and, therefore, the configuration in which the calculation is performed e.g., the maximum burning rate $s_{L,max}$ is not a unique quantity but varies with geometrical configuration. In order to illustrate this sensitivity, Figure 12 presents consumption speed s_c values plotted against flame stretch, κ , for the geometries shown in Figure 10. The stretch rate, κ , is evaluated at the T_{ref} isotherm.

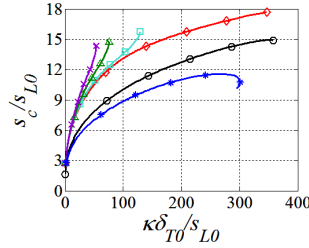


Figure 12. Consumption rate s_c dependence on stretch rate κ for PCF “*”, TCF “○”, ECF with different initial ignition radius ($R_i/\delta_{T0} = 0.25$ “◇”, $R_i/\delta_{T0} = 0.5$ “□”, $R_i/\delta_{T0} = 0.75$ “△”, $R_i/\delta_{T0} = 1$ “x”).

Plots for the variations of s_c , δ_T and δ_{H_2} with stretch and curvature can be seen in Amato *et al.* [49].

We next analyse statistical data collected at the leading edge of the turbulent flame brush. Figure 13 presents area weighted probability density functions of the consumption rate s_c , mean curvature K_C and inverse of flame thickness δ_T and δ_{H_2} . These data show that the flame front tends to burn more intensely and in thinner layers as the turbulent intensity is increased from case A31 to D31; values of mean curvature at the leading edge tend to be positive (by geometric necessity), but at higher turbulent intensity more finely wrinkled flames accommodate a wider range of features in the leading edge interrogation zone (e.g., see Fig. 5 in [30]).

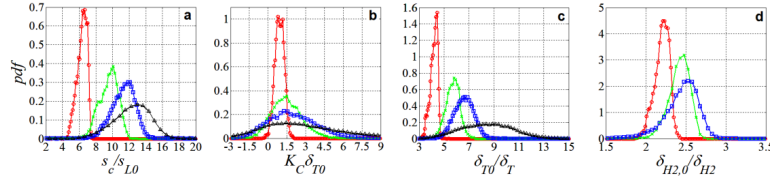


Figure 13. Probability density functions at the leading edge (weighted by area) of consumption rate s_c (a), mean curvature K_C , (b) inverse of flame thickness δ_T (c) and δ_{H_2} (d). Symbols refers to different DNS cases (A31 “○”, B31 “×”, C31 “□” and D31 “△”).

Error! Reference source not found. 16 plots JDF’s, weighted by local fuel consumption, of the principal curvatures k_1 and k_2 of the $T_{ref} = 1088K$ isosurface for case A31 to D31. The figure shows that at low turbulent intensity (i.e. Case A31), most of the fuel is consumed by flame elements with a cylindrical/spherical shape convex toward the reactants. At higher turbulent intensities, the flame becomes more tightly wrinkled and exhibits a wider variety of local geometries, including saddle-point and cylindrical shapes. Figure 16 also shows that the most highly curved elements tend to be cylindrical [51], rather than spherical.

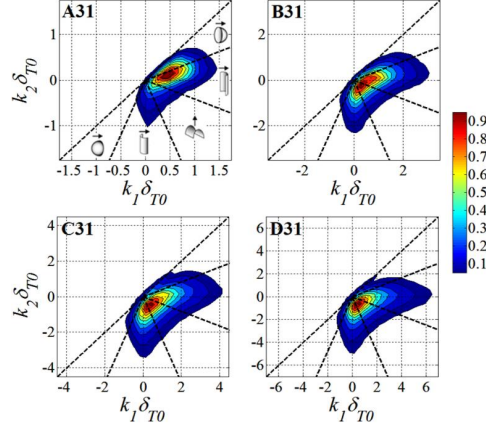


Figure 16. Fuel consumption-weighted JDFs of principal curvatures k_1 and k_2 ($K_C = k_1 + k_2$, $k_2 < k_1$) of the $T_{ref} = 1088K$ isosurface for case A31, B31, C31 and D31.

Figure 14 shows the JDFs of strain rate K_S and curvature K_C , weighted by fuel consumption, for cases A31 to D31. Mean strain rate values are positive and increase with consumption, for cases A31 to D31. Mean strain rate values are positive and increase with increasing turbulent intensity, consistent with prior studies [52,53]. For each case, the correlation of K_S and K_C is negative, similar to past DNS studies which considered lower turbulent intensities [54-58].

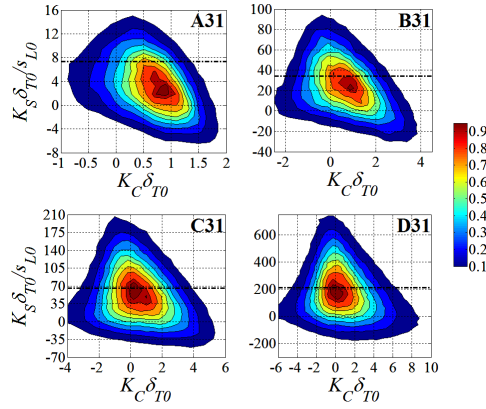


Figure 14. JDFs of curvature K_C and strain rate K_S , weighted by fuel consumption, based on the $T_{ref} = 1088K$ isosurface for case A31, B31, C31 and D31. The height of the dot dashed lines is equal to u'/l_t .

Many such JPDFs have been analysed in Amato *et al.* [49].

To compare statistics collected at the leading edge of the flame brush with the laminar simulations, the pdf's shown in Figure 13 are presented in Figure 15 in terms of mean μ and standard deviations σ weighted by flame area

$$\begin{aligned}\mu &= \left(\sum_i A_{ref,i} x_i \right) / \left(\sum_i A_{ref,i} \right) \\ \sigma &= \sqrt{\left(\sum_i A_{ref,i} (x_i - \mu)^2 \right) / \left(\sum_i A_{ref,i} \right)}\end{aligned}\tag{6}$$

where $A_{ref,i}$ denotes the area of the triangular element associated with the i -th value x_i which either represents mean curvature K_C , consumption speed s_c or flame thickness δ_{H_2} and δ_T . Figure 15a shows that the 1D laminar simulations computed at the average value of mean curvature reasonably follow the enhancement in consumption speed with increasing turbulent intensity and that case D31 seems to approach the highest values of consumption speed and curvature calculated by the model geometry. This result might be a manifestation of the insensitivity of curvature-induced flame speed modifications to frequency, as opposed to its strong sensitivity to nonsteadiness in hydrodynamic stretch [59]. This conclusion seems also justified by the data of Figure 15c which show that the decreasing trend in the average thickness of the H_2 consumption layer with increasing turbulence levels follows the 1D laminar simulations. Figure 15b, however, shows that the structure of the thermal layer as measured by δ_T is captured by the 1D simulations up to case B31, while cases C31 and D31 seem to progressively diverge from this solution. This effect is presumably due to non-quasi-steady effects as the divergence seems to occur for curvature values at which the ECF also exhibits these types of effects due to ignition transients, and also to the growing influence of mean strain rates at higher turbulent intensities [60].

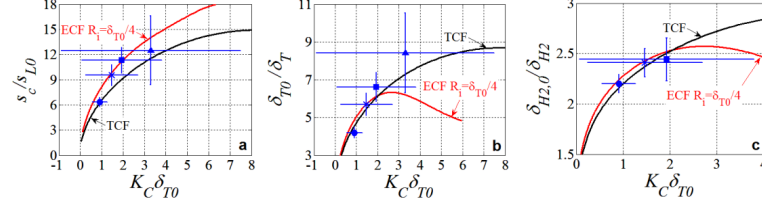


Figure 15. Leading edge mean consumption rate s_c (a), mean of the inverse of flame thickness δ_T (b) and δ_{H2} (c) plotted against leading edge average mean curvature K_C . Symbols refers to different DNS cases (A31 “•”, B31 “x”, C31 “■” and D31 “▲”). The total length of the error bars is equal to σ on each side. Thicker lines refer to ECF with $R_i = \delta_{T0}/4$ and TCF computations.

These plots allow some assessment of theories of the structure of the flame leading points, discussed in the introduction. Given the ambiguities and configuration-specific nature of $s_{L,max}$ noted above, it is difficult to make a precise assessment, but in terms of orders of magnitude, it is clear that the burning velocities and curvature values are of similar magnitude as would be expected of “critically stretched flamelets”. In other words, the computed values are not much less than, nor much greater than, values that are deduced from model laminar geometries. More quantitatively, these comparisons show that curvatures and burning velocities can be a factor of two or three below those of “critically” stretched laminar flames for the lower turbulence intensity cases. The highest turbulent intensity case burning rate does appear to approach the computed range of $s_{L,max}$ values.

4. Conclusions

A key contribution of this work was the demonstration of very strong fuel effects on turbulent burning velocities for fuels and conditions of interest for air force platforms. We noted that current models could be off by factors of over 3 in turbulent burning velocity using standard closures. We also developed physics-based approaches to understand and model these fuel sensitivities using leading points analysis. We show that measured displacement and consumption-based turbulent flame speeds can be correlated very well using detailed kinetic models of the high stretch sensitivity of these mixtures. We also show the results of local studies, using experiments and DNS, to evaluate the assumptions of these models at a local level. The leading edges show sensitivities to the turbulence intensities. Experimentally weak sensitivity to fuel composition was observed in spite of the increase in S_T and $s_{L,max}$. Only minor effects of fuel composition on curvature statistics at the flame leading points are observed. Rather, curvature statistics are dominated by the turbulence intensity. However, there does appear to be a stronger effect of fuel composition on the tangential strain rate statistics. Changes in the time-averaged values at the leading points were similar to the changes observed in the turbulent flame speeds. However, these values of the time-averaged tangential strain rate are still well below those for critically stretched conditions. The numerical data is compared with model geometries for stretched flames. Many factors need to be accounted for when comparing local turbulent flame structure and model laminar flame computations, including unsteadiness in the flame response, non-flamelet behaviors, and correlations between flame front curvature and local strain rate. At the leading edge of the turbulent flame brush, where strongly positive curved flamelet geometries dominate the topology of the flame front, the average structure of the flame front is represented reasonably well by quasi-steady laminar calculations even at very high turbulent intensities. The main difference is the relation between curvature and strain rate; in the turbulent flame, curvature and strain rate are negatively correlated while the model laminar flames are positively correlated. This different relation between curvature and strain rate makes a direct comparison between the model laminar flame and the turbulent flame difficult for the cases with higher turbulent intensities (case B31, C31 and D31), for which mean strain rates have higher values. This work highlights merits and limitations of model laminar flame computations in reproducing the structure of turbulent flames and seems to suggest that at low turbulent intensities “critically” stretched flamelets are not a good model for leading

points burning rates, at least for the low Reynolds number and Damköhler number of the direct numerical simulations utilized in this study.

5. Publications

Journals

1. Marshall, A., Lundrigan, J., Venkateswaran, P., Seitzman, J., Lieuwen, T., “Fuel Effects on Leading Point Curvature Statistics of High Hydrogen Content Fuels,” *Proceedings of the Combustion Institute*, 2014
2. Amato, A., Day, M., Bell, J., Lieuwen, T., “Leading Edge Statistics of Turbulent, Lean, H₂-Air Flames”, *Proceedings of the Combustion Institute*, 2014.
3. Venkateswaran, P., Marshall, A., Seitzman, J., Lieuwen, T., “Scaling Turbulent Flame Speeds of Negative Markstein Length Fuel Blends Using Leading Points Concepts”, *Combustion and Flame*, 2014
4. Venkateswaran, P., Marshall, A., Seitzman, J.M., Lieuwen, T., “Turbulent Consumption Speeds of High Hydrogen Content Fuels from 1-20 atm,” *Journal of Engineering for Gas Turbines and Power*, 2014
5. Amato, A., Lieuwen, T., “Analysis of Flamelet Leading Point Dynamics in an Inhomogeneous Flow,” *Combustion and Flame*, 2013
6. Amato, A., Day, M., Cheng, R. K., Bell, J., Lieuwen, T., “Topology and Burning Rates of Turbulent, Lean, H₂/Air Flames,” Submitted to *Combustion and Flame*, 2014.
7. Marshall, A., Lieuwen T., “Curvature and Strain Characteristics of Turbulent, Stretch Sensitive fuel mixtures”, in preparation for submission to *Combustion and Flame*, 2015.
8. Lyra, S., Wilde, B., Seitzman, J., Lieuwen, T., Chen, J., “Structure and Stabilization of Hydrogen-Rich Transverse Jets in a Vitiated Crossflow”, *Combustion and Flame*, Vol. 162, 2015, pp. 1234-1248.

Conferences

1. Marshall, A., Lundrigan, J., Venkateswaran, P., Seitzman, J., Lieuwen, T., "Measurements of Stretch Statistics at Flame Leading Points for High Hydrogen Content Fuels," GT2014-26420, *ASME Turbo Expo 2014*, Dusseldorf, Germany, June 16-20, 2014
2. Marshall, A., Venkateswaran, P., Seitzman, J., Lieuwen, T., "Flame Leading Point Stretch Statistics of Negative Markstein Length Fuels," *Eastern States Fall Technical Meeting*, Clemson, South Carolina, October 13-16, 2013
3. Marshall, A., Venkateswaran, P., Seitzman, J., Lieuwen, T., "Measurements of Leading Point Conditioned Statistics of High Hydrogen Content Fuels," *8th U.S. National Combustion Meeting*, Park City, Utah, May 19-22, 2013
4. Amato, A., Lieuwen, T., "Analysis of flamelet leading point dynamics in an inhomogeneous flow," *8th U.S. National Combustion Meeting*, Park City, Utah, May 19-22, 2013
5. Amato, A., Day, M., Cheng, R.K., Bell, J., Lieuwen, T., "Leading Point Statistics of a Turbulent, Lean, H₂-Air Flame," *Spring Technical Meeting of the Central States Section of the Combustion Institute*, Dayton, OH, April 22-24, 2012

6. References

- [1] A. Lipatnikov, J. Chomiak, *Progress in Energy and Combustion Science*, 31 (2005) 1-73.
- [2] A. Lipatnikov, J. Chomiak, *Progress in Energy and Combustion Science*, 28 (2002) 1-74.
- [3] V.R. Kuznetsov, V.A. Sabel'nikov, *Turbulence and combustion*, Hemisphere Publishing, New York, 1990.
- [4] S.A. Filatyev, J.F. Driscoll, C.D. Carter, J.M. Donbar, *Combustion and Flame*, 141 (2005) 1-21.
- [5] J.F. Driscoll, *Progress in Energy and Combustion Science*, 34 (2008) 91-134.
- [6] R.K. Cheng, *Turbulent Combustion Properties of Premixed Syngas*, in: T.C. Lieuwen, V. Yang, R.A. Yetter (Eds.) *Synthesis Gas Combustion: Fundamentals and Applications*, CRC Press, 2009, pp. 129-168.
- [7] M. Nakahara, H. Kido, *AIAA journal*, 46 (2008) 1569-1575.
- [8] H. Kido, M. Nakahara, J. Hashimoto, D. Barat, *JSME International Journal Series B Fluids and Thermal Engineering*, 45 (2002) 355-362.
- [9] P. Venkateswaran, A. Marshall, J. Seitzman, T. Lieuwen, *Proceedings of the Combustion Institute*, 34 (2013) 1527-1535.
- [10] M. Wu, S. Kwon, J. Driscoll, G. Faeth, *Combustion science and technology*, 73 (1990) 327-350.
- [11] D. Bradley, P. Gaskell, A. Sedaghat, X. Gu, *Combustion and flame*, 135 (2003) 503-523.

- [12] H. Kido, M. Nakahara, K. Nakashima, J. Hashimoto, Proceedings of the Combustion Institute, 29 (2002) 1855-1861.
- [13] T. Brutscher, N. Zarzalis, H. Bockhorn, Proceedings of the Combustion Institute, 29 (2002) 1825-1832, [http://dx.doi.org/10.1016/S1540-7489\(02\)80221-8](http://dx.doi.org/10.1016/S1540-7489(02)80221-8).
- [14] C.K. Law, Combustion Physics, Cambridge University Press, New York, 2006.
- [15] P. Venkateswaran, A. Marshall, D.H. Shin, D. Noble, J. Seitzman, T. Liewen, Combustion and Flame, 158 (2011) 1602-1614.
- [16] G. Damköhler, Zeitschrift für Elektrochemie und angewandte physikalische Chemie, 46 (1940) 601-626.
- [17] I. Zeldovich, G.I. Barenblatt, V. Librovich, G. Makhviladze, Mathematical Theory of Combustion and Explosions, Consultants Bureau (Plenum Publishing Corporation), New York, 1985.
- [18] A. Amato, T.C. Liewen, Combustion and Flame, 161 (2014) 1337-1347.
- [19] U. Ebert, W. van Saarloos, Physica D: Nonlinear Phenomena, 146 (2000) 1-99.
- [20] V.P. Karpov, A.N. Lipatnikov, V.L. Zimont, Flame curvature as a determinant of preferential diffusion effects in premixed turbulent combustion, in: W.A. Sirignano, A.G. Merzhanov, L. De Luca (Eds.) Advances in combustion science: in honor of YA. B. Zel'dovich, AIAA, 1997.
- [21] N.K. Aluri, S.P.R. Muppala, F. Dinkelacker, Combustion and Flame, 145 (2006) 663-674.
- [22] V. Karpov, A. Lipatnikov, V. Zimont, Symposium (International) on Combustion, 26 (1996) 249-257.
- [23] A. Lipatnikov, J. Chomiak, Combustion Science and Technology, 137 (1998) 277-298.
- [24] P. Venkateswaran, A. Marshall, J. Seitzman, T. Liewen, Journal of Engineering for Gas Turbines and Power, 136 (2014) 011504-011501.
- [25] S.P.R. Muppala, M. Nakahara, N.K. Aluri, H. Kido, J.X. Wen, M.V. Papalexandris, International Journal of Hydrogen Energy, 34 (2009) 9258-9265.
- [26] F. Dinkelacker, B. Manickam, S. Muppala, Combustion and Flame, 158 (2011) 1742-1749.
- [27] F.T. Yuen, Ö.L. Gülder, Proceedings of the Combustion Institute, 34 (2012) 1393-1400.
- [28] P. Venkateswaran, A. Marshall, J. Seitzman, T. Liewen, Proceedings of the Combustion Institute, 34 (2013) 1527-1535, <http://dx.doi.org/10.1016/j.proci.2012.06.077>.
- [29] V.R. Kuznetsov, V.A. Sabel'nikov, Turbulent Combustion of a Homogenous Mixture, in: P.A. Libby (Ed.) Turbulence and Combustion, Hemisphere Publishing Corporation, New York, Washington, Philadelphia, London, 1990, pp. 235-251.
- [30] A. Aspden, M. Day, J. Bell, Journal of Fluid Mechanics, 1 (2011) 1-34.
- [31] F. Gouldin, R.K. Cheng, International Workshop on Premixed Turbulent Flames, <http://energy.lbl.gov/aet/combustion/workshop/workshop.html>.

- [32] C.K. Chan, K.S. Lau, W.K. Chin, R.K. Cheng, Symposium (International) on Combustion, 24 (1992) 511-518.
- [33] R.K. Cheng, Combustion and Flame, 101 (1995) 1-14.
- [34] A. Marshall, P. Venkateswaran, D. Noble, J. Seitzman, T. Lieuwen, Experiments in Fluids, 51 (2011) 611-620.
- [35] R.K. Cheng, D. Littlejohn, W.A. Nazeer, K.O. Smith, Journal of Engineering for Gas Turbines and Power, 130 (2008) 021501.
- [36] R.K. Cheng, D.T. Yegian, M.M. Miyasato, G.S. Samuelsen, C.E. Benson, R. Pellizzari, P. Loftus, Proceedings of the Combustion Institute, 28 (2000) 1305-1313.
- [37] A. Marshall, P. Venkateswaran, J. Seitzman, T. Lieuwen, in: 8th U.S. National Combustion Meeting, Park City, Utah, 2013, pp. 15.
- [38] R.J. Kee, J.F. Grcar, M. Smooke, J. Miller, Sandia National Laboratories Report SAND85-8240, Sandia National Laboratories, Livermore, (1983).
- [39] S.G. Davis, A.V. Joshi, H. Wang, F. Egolfopoulos, Proceedings of the Combustion Institute, 30 (2005) 1283-1292.
- [40] R.J. Kee, J.A. Miller, G.H. Evans, G. Dixon-Lewis, Proceedings of the Combustion Institute, 22 (1989) 1479-1494.
- [41] S. Pfadler, F. Beyrau, A. Leipertz, Opt. Express, 15 (2007) 15444-15456.
- [42] N. Otsu, IEEE Transactions On Systems, Man, And Cybernetics, 9 (1979) 62-66.
- [43] T. Poinso, D. Veynante, Theoretical and Numerical Combustion, RT Edwards, Inc., Philadelphia, 2005.
- [44] A. Marshall, J. Lundrigan, P. Venkateswaran, J. Seitzman, T. Lieuwen, Proceedings of the Combustion Institute, 2014
- [45] A. Marshall, J. Lundrigan, P. Venkateswaran, J. Seitzman, T. Lieuwen, Due for submission in Combustion and Flame.
- [46] D.M. Mosbacher, J.A. Wehrmeyer, R.W. Pitz, C.J. Sung, J.L. Byrd, Proceedings of the Combustion Institute, 29 (2002) 1479-1486.
- [47] C.T. Bowman, R.K. Hanson, D.F. Davidson, W.C.J. Gardiner, V. Lissianski, G.P. Smith, D.M. Golden, M. Frenklach, M. Goldenberg, GRI-Mech 2.11, http://www.me.berkeley.edu/gri_mech/.
- [48] R. Kee, J. Warnatz, J. Miller, Sandia report SAND83-8209, (1983).
- [49] A. Amato, M. Day, R.K. Cheng, J. Bell, T. Lieuwen, Submitted to Combustion and Flame, 2014
- [50] M. Day, J. Bell, P.T. Bremer, V. Pascucci, V. Beckner, M. Lijewski, Combustion and Flame, 156 (2009) 1035-1045
- [51] Rutland, C. and A. Trouvé, Combustion and Flame, 1993. **94**(1-2): p. 41-57.
- [52] Katragadda, M., S.P. Malkeson, and N. Chakraborty, Proceedings of the Combustion Institute, 2011. **33**(1): p. 1429-1437.

- [53] Meneveau, C. and T. Poinso, Combustion and Flame, 1991. **86**(4): p. 311-332.
- [54] Haworth, D.C. and T. Poinso, Journal of Fluid Mechanics, 1992. **244**(1): p. 405-436.
- [55] N. Chakraborty, and R.S. Cant, Physics of Fluids, 2005. **17**: p. 065108.
- [56] N. Chakraborty, and R.S. Cant, Combustion and Flame, 2004. **137**(1-2): p. 129-147.
- [57] N. Chakraborty, and R.S. Cant, Physics of Fluids, 2005. **17**: p. 105105.
- [58] N. Chakraborty, and R.S. Cant, International Journal of Heat and Mass Transfer, 2006. **49**(13-14): p. 2158-2172.
- [59] H.G. Im, J.H. Chen, Proceedings of the Combustion Institute, 28 (2000) 1833-1840.
- [60] A. Amato, PhD thesis, Georgia Institute of Technology, 2014.

B OH PLIF Laser Diagnostics of Turbulent, Premixed, Freely Propagating Flame Kernels

AIAA SciTech
13-17 January 2014, National Harbor, Maryland
52nd Aerospace Sciences Meeting

52nd Aerospace Sciences Meeting
National Harbor, MD, 13 - 17 Jan 2014

DOI: 10.2514/6.2014-0315

OH PLIF Laser Diagnostics of Turbulent, Premixed, Freely Propagating Flame Kernels

Nathan R. Grady, Robert W. Pitz

Mechanical Engineering Department, Vanderbilt University, Nashville, TN 37235

Tom A. Slais, John Berlette, Brad Ochs, Suresh Menon, David Scarborough

School of Aerospace Engineering, Georgia Institute of Technology, Atlanta, GA 30332

Abstract

A subsonic wind tunnel facility has been built to study the effects of compressibility on turbulent premixed combustion up to Mach number (M) = 0.7 although the current study focusses on M = 0.1-0.3. Flame kernels are ignited in a stoichiometric premixed methane/air flow with a single pulse of an infrared (1.06 μm) YAG laser. The flame kernels are allowed to freely propagate downstream inside a wind tunnel and imaged at fixed downstream locations with planar laser-induced fluorescence (PLIF). The laser ignition resulted in two distinct streamwise lobes and third lobe that was attributed to the residual effects of laser ignition. The three lobes eventually merged into one lobe at downstream locations. The mean flow was varied from M = 0.1 to M = 0.3, and kernel growth rate was not affected by the increase in mean flow velocity. The flame surface density of the flame kernels was found to vary as a function of time due to the laser ignition and the resultant three lobes. However, once they merged, typical flame surface distributions were observed. Both flame thickness and maximum flame surface density were found to decay with respect with time indicative of either a developing preheat zone or attenuation of tunnel turbulence. In future tests, the laser ignition energy will be reduced by using the double Nd:YAG wavelength (532 nm) and flame kernels will be studied at compressible flow conditions (M = 0.3 to 0.7).

Introduction

Premixed combustion has various advantages over non-premixed combustion: no mixing time, less pollutants, and improved fuel economy. Lean premixed turbulent combustion could lead to smaller/lighter combustors with increased thrust-to-weight ratios in propulsion systems. Additionally, even in non-premixed gas turbine combustors there are regions of either partially premixed or fully premixed combustion [1]. However, premixed combustion is subject to flashbacks and instabilities (both of which can destroy the combustor), and extinction [2]. Furthermore, the occurrence and severity of these instabilities changes with the turbulence level. Therefore, the study of turbulent premixed combustion is relevant to all practical combustion/propulsion devices.

While premixed turbulence combustion has been studied extensively at low speeds and for relatively low levels of turbulence [3-6], there are few experiments or numerical simulations dedicated to either high turbulence or high speeds/compressibility effects. However, most propulsion devices have compressible flow regions either induced by turbine blades or from high mean flows (e.g.

52nd Aerospace Sciences Meeting
National Harbor, MD, 13 - 17 Jan 2014

ram/scramjets), and also have regions of high turbulence. Therefore, in order to correctly model and/or design combustors with premixing, facilities need to be designed/fabricated so that studies can be conducted for turbulent premixed combustion under high levels of turbulence in the compressible regime. Additionally, it has been found that flame propagation has a “memory” [3] of large scale structures such as those created by shear layers, recirculation zones, or the geometry of a particular burner and this “memory” affects the propagation of turbulent premixed combustion. Therefore, the turbulent premixed experiment needs to be free of such memory effects and only dependent on the flow turbulence itself.

In order to obtain a sound understanding of turbulent premixed combustion from which a reliable and robust numerical simulation can be based, turbulent flame propagation needs to be rigorously studied. Aside from flame speed measurements and temperature profiles, experiments and simulations have shown that statistical representations of flame surface and thickness also need to be obtained to ensure that a model is accurately predicting all phenomena. These quantities will be obtained by planar laser-induced fluorescence (PLIF) measurements of radical species representative of the reaction zone.

In order to achieve the turbulence and mean flow conditions necessary to study the aforementioned effects, a new wind tunnel device has been developed and is briefly described below. A kernel will be ignited in the flow away from any shear layers, and will be freely convected downstream. This tunnel has optical access to allow for the non-intrusive diagnostics needed to properly study the propagation of the flame kernels and properties of the flame surface as function of time (which for this system is equitable to the distance traveled by the kernel).

However, before compressible kernel measurements can be reliably interpreted in this new system, flame kernels in relatively low speeds need to be studied and compared with previous results. This paper will examine OH PLIF images of laser ignited kernels at $M = 0.1$ - 0.3 with turbulence generated via passive grids to demonstrate that this facility is providing reliable flame kernels. Previous studies of incompressible kernel formation [7-9] have found increased wrinkling and surface area as a function of both turbulence and equivalence ratio. This paper will primarily explore the reliability and repeatability of flame kernels across a range of Mach numbers under low turbulence at a constant equivalence ratio.

Experimental System

A schematic of the wind tunnel facility is shown in [Figure 1](#). Unheated air is supplied to the facility at 1825 kPa and 25°C with controlled stagnation pressures and flow rates ranging from 203 kPa and 208 kPa to 0.09 kg/s and 0.270 kg/s for test section Mach numbers of 0.1 and 0.30, respectively, as shown in [Table 1](#). The incoming air is filtered using a Parker CO2-2362 high-pressure air filter to eliminate particulate contamination with diameters greater than 0.3 μm from building supply lines.

Natural gas is supplied at 170 kPa to a pair of injector manifolds. The average composition of the natural gas mixture includes 98% CH_4 , 1.5% N_2 , with the remaining 0.5% consisting of CO_2 and heavy hydrocarbons. Flow metering is achieved via a calibrated orifice plate and injector manifold pressure. Fuel is injected via three linear spray bars with an outer and an inner diameter of 13.7 mm and 9.25 mm,

respectfully. Each spray bar features an array of 10 equidistant 3.18 mm diameter orifices arranged linearly facing downstream. The mixing section has square cross-section of the same length of the spray bar and extends 71.1 cm from the plane of injection to the location of the first flow conditioning screens. Shakedown testing using a Foxboro MIRAN 1BX gas analyzer unit verified that this system produced desired homogeneity and stoichiometry in the test section volume.

The turbulence generated by the upstream fuel injector array used to facilitate mixing is then damped by an array of flow conditioning screens. The array features an upstream perforated plate with 3.96 mm holes oriented in a hexagonal pattern that initiates the break-up of large scale structures shed off of the fuel injection rods. This grid is then followed 10.2 cm downstream by an array of three fine woven square mesh grids with holes 1.04 mm wide. The fine mesh grids are spaced 2.54 cm from each other. The spacing of the grids as shown in [Figure 1](#) ensures that the following grid is positioned well after the conclusion of the grid turbulence decay region of the previous grid. A passive turbulence grid consisting of a 2.29 mm thick perforated plate with 12.7 mm holes is installed downstream of the flow conditioning array. The grid featured a plate solidity of 33% (percentage of blocked area) with holes arranged in a hexagonal pattern. Hydroxyl tagging velocimetry (HTV) measurements [10, 11] were conducted in this tunnel and typical turbulence values were at least 2% of the mean flow, and an example of the mean flow velocity at $M = 0.1$ is shown in [Figure 2](#) demonstrating the overall homogeneity of the core flow.

The nozzle section features a fused silica glass access window for laser ignition mounted flush with the interior wall. The access port is 5.08 cm upstream from the entrance of the test section. The test section itself features a square cross section of $5 \times 5 \text{ cm}^2$ and is 19.1 cm long and is optically accessible on three sides through Corning 7980 fused silica quartz with a $5 \times 35 \text{ cm}^2$ viewable area. Setting the facility at a particular test condition is accomplished by using a 1.59 mm diameter PC-type Pitot probe constructed by United Sensor Corp. installed in the aft end of the test section.

A schematic of the laser ignition and OH PLIF system is shown in [Figure 3](#). A Continuum Surelite Nd:YAG laser (195 mJ/pulse at 1064 nm after focusing lens) was used to ignite the flame kernels. The spark laser was focused into the tunnel using a -250 mm lens to expand the original 6 mm beam to ~ 25.4 mm before being focused by a 60 mm lens through a window 50 mm upstream of the test section. These lenses were chosen to prevent damage to the window which was 2.5 cm from the focal point and limit the effect of back reflections on the 60 mm lens, and provided a spot size of $\sim 800 \mu\text{m}$. A frequency doubled Continuum Powerlite Nd:YAG laser pumping a Continuum ND6000 dye laser with a Continuum UVX frequency doubler to provide ~ 282 nm (10 mJ/pulse) to probe the $\text{OH } A^2\Sigma^+(v'=1) \leftarrow X^2\Pi (v''=0)$ band. The 282 nm pulse was formed into a sheet by a -150 mm cylindrical lens and a 1 m spherical lens. OH fluorescence was imaged on a PI-MAX 4 ICCD camera with ~ 10 ns gating. The entire system was synced with SRS DG645 delay generators and ran at 10 Hz.

The OH images are used to acquire single shot and averaged images of the flame edge for comparison with previous studies of flame kernels. The flame edge was determined using a *smallest univalue segment assimilating nucleus* (SUSAN) method [12]. Additionally, measurements of flame surface density and flame thickness will also be acquired from binarized single shot images averaged together to form c-maps similar to previous authors [13-18]. Once this flame edge has been found, each image is

“binarized” with the value of either 0 or 1 being given to the unburned or burned side respectively. Then each of these binarized images are averaged together thus producing a “c-map” with equidistant bins. From this c-map both flame surface density (FSD) and flame thickness can be derived.

A 2D dimensional representation of FSD, FSD' , can be obtained using the c-map as mentioned in Shepherd and Cheng [14] :

$$FSD'(\bar{c}) = \frac{1}{n_f} \frac{L(\bar{c})}{A(\bar{c})} \quad (1)$$

The terms in Equation 1 are shown pictographically in Figure 4. For a given progress variable bin, the area is determined from the number of pixels in that bin. $L(\bar{c})$ represents the total flame length from all single-shot images that lie within a given bin; this is determined frame-by-frame as shown in Figure 4 by overlaying the flame edge and the current bin, adding all the segments across all frames. Finally, $L(\bar{c})$ is normalized by the number of frames used (i.e. n_f). Typically, profiles of FSD vs \bar{c} form an inverted parabola or bell-shape centered around $\bar{c} = 0.5$ [14, 16, 18].

The flame zone thickness can be calculated by finding the maximum gradient in the c-map by:

$$\delta_T = \frac{1}{(dc/dn)_{max}}$$

Results

(2)

Data was taken at 3 streamwise locations (12.7 cm, 16.5 cm, and 20 cm) from the spark laser. Example raw single-shot images for $\phi = 1$ are shown in Figure 5 and mean and RMS images of the binarized images also for $\phi = 1$ are shown in Figures 6 and 7. The binarized images were corrected for the unevenness of the laser sheet. The flow direction is from left to right, and the top of the images is towards the spark laser. The third lobe found in the images is an artifact of the laser ignition similar to the results of Mansour et al. [7].

From Figure 7, it can be seen that the primary fluctuations in progress variable are towards the edges of the flame kernels and the third laser artifact lobe demonstrating an overall very repeatable ignition process. Additionally, there are also higher fluctuations between the two primary lobes seen in younger, upstream kernels indicating that these two lobes grow towards each other similar to the “peanut” like structure observed by Mansour et al. [7].

The mean images are used to calculate an equivalent radius for the kernels, and are plotted versus propagation time in Figure 8 for 1. Both the $M = 0.2$ and $M = 0.3$ curves are nearly collinear and the two upstream $M = 0.1$ data points also lie on these lines (the third has made contact with the wall and was excluded). This trend is similar to that observed by Mansour et al. [7] where changes in the mean flow velocity did not result in an appreciable change kernel growth rate. This demonstrates that tunnel can: 1) maintain a constant equivalence ratio across a wide range of mean flows and 2) the laser ignition

process is fast enough to prevent causing an elongated ignition region possible from slower ignition coils.

An example plot of flame surface density (FSD') for $M = 0.1, 0.2$, and 0.3 are shown in **Figures 9-11**. Due to the laser ignition and the resultant three lobes which propagate towards each other, FSD' is initially a strong function of time delay as seen in **Figures 9-11**. For $M = 0.3$ seen in **Figure 11** there is a sudden decrease in FSD'_{max} to roughly a two-thirds of its previous value (see change in scales between the first and second locations), and then FSD'_{max} has partially recovered at the third location. This sudden dip corresponds to when the three lobes converge resulting a loss of $\sim 1/3$ surface length without a corresponding loss in area. It should be noted that above $\bar{c} = 0.6$ there is no significant values of FSD' indicating that flame is highly intermittent with no consistent zone which is always reacted.

Due to similar reasons, FSD'_{max} occurs at significantly different values of \bar{c} for different propagation times for the same Mach number. While the mean values of c may be high, the three lobes surfaces fluctuate as seen in the high RMS values shown in **Figure 7** resulting in high values of $L(\bar{c})$ with relatively low values of $A(\bar{c})$ compared to other flames. This can be seen in **Figure 9 a and b** at $M = 0.1$ where there is a strong peak at $\bar{c} = 0.8$ representative of merging lobes, and a secondary peak around $\bar{c} = 0.4$ which is closer to the exterior of the lobes. At longer propagation times (i.e. **Figure 9b**) $FSD'_{max} = 0.6$ closer to the typical value of 0.5 and the typical curve shape (inverted parabola centered at $c = 0.5$) [14, 16, 18]. A similar trend can also be found in the $M = 0.2$ case in **Figure 10** where at the last location the curve has formed into the expected inverted parabola even though the overall propagation time is less than in either of the $M = 0.1$ cases. The failure of the $M = 0.1$ cases to reach typical behavior may be due to their greater size and an adverse effect of their closer proximity to the wall. As the kernels grow larger, the area/length in the streamwise direction becomes larger than in the transverse direction. If the wall was in fact affecting flame propagation, the preferential increase in the streamwise direction would obtain a higher statistical weight and explain why the FSD' vs \bar{c} trends began to approach typical behavior.

Finally, flame thickness is determined from Equation 2 using the inverse gradients from the c -maps along the $\bar{c} = 0.5$ contour. Flame thickness is plotted vs time for all Mach numbers with trend line (solid black line) shown in **Figure 12**. Normalized flame thicknesses are also shown in the figure using a laminar flame thickness of 0.6 mm approximated using $S_L = 40$ cm/s and $\alpha_{mix, 1200K} = 2.38$ cm²/s. The FSD'_{max} values determined from **Figure 9-11** are also shown in **Figure 12** as well with a trend line (dot-dashed black line). In general, flame thickness and FSD'_{max} decays with respect to time and is fairly consistent across all Mach numbers studied. While previous authors have observed a reduction in FSD'_{max} with respect to kernel growth time [9], previous experiments on spherically expanding flames have found that flame thickness increases with time [4, 9, 19] contrary to the results shown here. This attenuation with time may be a result of the three flame-lobe interaction, or indicative that the heat release from the kernel is decaying the global turbulence in the entire wind tunnel test. Further study is required to determine if the flame kernels are in fact attenuating the global turbulence. If there is global turbulence attenuation some means of compensating for this needs to be installed (e.g. gradual expansion or scaled up wind tunnel).

52nd Aerospace Sciences Meeting
National Harbor, MD, 13 - 17 Jan 2014

For future experiments using this tunnel, the laser ignition source will be refined and the amount of laser energy and spot size will be reduced to lessen the effect of the laser ignition on the kernel propagation (i.e. three converging lobes). The authors have already inserted a positive 250 mm f.l. lens between the -250 mm f.l. lens and the 60 mm lens to improve focusing. The spot size was thereby reduced to $\sim 450 \mu\text{m}$ (down from $\sim 800 \mu\text{m}$), and the laser energy could be reduced to 55 mJ/pulse (down from 195 mJ/pulse) thus largely eliminating the third lobe as shown in Figure 13. Further refinements will be made to spark system to provide a more spherical kernel which will simplify data analysis (and will also make the kernel easier to model). These refinements include switching to a 532 nm Nd:YAG laser where pulse energies as low as 2.5 mJ/pulse have been used [20]. Additionally, experiments measuring the effect of kernel heat release on the global turbulence will be conducted to determine if the tunnel size/geometry needs to be changed to provide a more consistent turbulent flow field. Once these changes have been made, experiments over wider a Mach number (up to $M = 0.7$) and equivalence ratio range will be conducted.

Conclusions

Flame kernels were laser ignited in a premixed stoichiometric CH_4/air wind tunnel, and the mean flow was varied from $M = 0.1$ to 0.3 . The laser ignition resulted in two streamwise lobes and a third transverse lobe in the direction of the laser ignition; this lobe was caused by the residual effects of laser ignition. Kernel growth rate was not significantly affected by increasing the mean flow of the tunnel demonstrating that: a) the tunnel can reliably and repeatedly provide a consistent equivalence ratio across a wide range of mean flows, and b) the laser ignition process is fast enough to prevent causing an elongated ignition region. Due to the three laser induced lobes, flame surface density was found to be a strong function of time until after all three lobes had merged. Before the lobes had fully merged FSD'_{max} occurred at a progress variable well above the expected value of 0.5 due to fluctuations between the lobes. When the lobes were small FSD'_{max} occurred at a progress variable well below the expected value of 0.5 . In both cases the FSD'_{max} versus \bar{c} curve did not have a typical inverted parabolic profile. Additionally, the plots of flame surface density indicated that kernels for the $M = 0.1$ case were potentially affected by their proximity to the wall. Finally, the flame thickness was determined and was found to slowly decrease as a function of propagation time either due to an increased heat release and stronger preheat zone, or that the global turbulence is decaying.

Acknowledgements

This research was supported by the Air Force Office of Scientific Research Energy Combustion and Sciences Program (Dr. Chiping Li Manager, under Contract No. FA9550-12-1-0107/RC657). The authors also thank technician S. Hutchins and research engineer C. Ballance at Georgia Tech for their assistance.

References

- [1] Dhanuka, S. K., Temme, J. E., and Driscoll, J. E., 2011, "Unsteady aspects of lean premixed prevaporized gas turbine combustors: flame-flame interactions," *Journal of Propulsion and Power*, 27(3), pp. 631-641.

52nd Aerospace Sciences Meeting
National Harbor, MD, 13 - 17 Jan 2014

- [2] Swaminathan, N., and Bray, K. N. C., 2011, *Turbulent Premixed Flames*, Cambridge University Press, Cambridge, UK.
- [3] Driscoll, J. F., 2008, "Turbulent premixed combustion: Flamelet structure and its effect on turbulent burning velocities," *Progress in Energy and Combustion Science*, 34(1), pp. 91-134.
- [4] Lipatnikov, A. N., and Chomiak, J., 2002, "Turbulent flame speed and thickness: phenomenology, evaluation, and application in multi-dimensional simulations," *Progress in Energy and Combustion Science*, 28(1), pp. 1-74.
- [5] Peters, N., 1999, "The turbulent burning velocity for large-scale and small-scale turbulence," *Journal of Fluid Mechanics*, 384, pp. 107-132.
- [6] Peters, N., 2000, *Turbulent combustion*, Cambridge Press, Cambridge.
- [7] Mansour, M., Peters, N., and Schrader, L.-U., 2008, "Experimental study of turbulent flame kernel propagation," *Experimental Thermal and Fluid Science*, 32(7), pp. 1396-1404.
- [8] Kaminski, C. F., Hult, J., Alden, M., Lindenmaier, S., Dreizler, A., Maas, U., and Baum, M., 2000, "Spark ignition of turbulent methane/air mixtures revealed by time-resolved planar laser-induced fluorescence and direct numerical simulations," *Proceedings of the Combustion Institute*, 28, pp. 399-405.
- [9] Renou, B., Mura, A., Samson, E., and Boukhalfa, A., 2002, "Characterization of the local flame structure and the flame surface density for freely propagating premixed flames at various Lewis numbers," *Combustion Science and Technology*, 174(4), pp. 143-179.
- [10] Grady, N. R., Pitz, R. W., Carter, C. D., Hsu, K.-Y., Ghodke, C., and Menon, S., 2011, "Supersonic flow over a ramped-wall cavity flameholder with an upstream strut," *Journal of Propulsion and Power*, 28(5), pp. 982-990.
- [11] Ribarov, L. A., Wehrmeyer, J. A., Pitz, R. W., and Yetter, R. A., 2002, "Hydroxyl tagging velocimetry (HTV) in experimental air flows," *Applied Physics B-Lasers and Optics*, 74(2), pp. 175-183.
- [12] Smith, S. M., and Brady, J. M., 1997, "SUSAN - A new approach to low level image processing," *International Journal of Computer Vision*, 23(1), pp. 45-78.
- [13] Cheng, R. K., Shepherd, I. G., Bedat, B., and Talbot, L., 2002, "Premixed turbulent flame structures in moderate and intense isotropic turbulence," *Combustion Science and Technology*, 174(1), pp. 29-59.
- [14] Shepherd, I. G., and Cheng, R. K., 2001, "The burning rate of premixed flames in moderate and intense turbulence," *Combustion and Flame*, 127(3), pp. 2066-2075.
- [15] Sweeney, M. S., Hochgreb, S., and Barlow, R. S., 2011, "The structure of premixed and stratified low turbulence flames," *Combustion and Flame*, 158(5), pp. 935-948.
- [16] Lawn, C. J., and Schefer, R. W., 2006, "Scaling of premixed turbulent flames in the corrugated regime," *Combustion and Flame*, 146(1-2), pp. 180-199.
- [17] Sweeney, M., and Hochgreb, S., 2009, "Autonomous extraction of optimal flame fronts in OH planar laser-induced fluorescence images," *Applied Optics*, 48(19), pp. 3866-3877.
- [18] Shepherd, I. G., 1996, "Flame surface density and burning rate in premixed turbulent flames," *Proceedings of the Combustion Institute*, 26, pp. 373-379.
- [19] Abdelgayed, R. G., Bradley, D., and Lawes, M., 1987, "Turbulent burning velocities - a general correlation in terms of straining rates," *Proceedings of the Royal Society of London Series a-Mathematical Physical and Engineering Sciences*, 414(1847), pp. 389-413.
- [20] Bak, M. S., Im, S.-K., and Cappelli, M. A., 2013, "Successive laser-induced breakdowns in atmospheric pressure air and premixed ethane-air mixtures," *Combustion and Flame*, 10.1016/j.combustflame.2013.12.029.

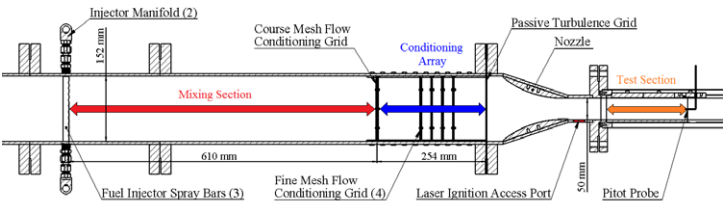


Figure 1: Schematic of wind tunnel facility.

Table 1: Tunnel flow conditions

Mach Number	\dot{m} (kg/s)	P_0 (kPa)
0.1	0.09	203
0.2	0.18	205
0.3	0.27	208

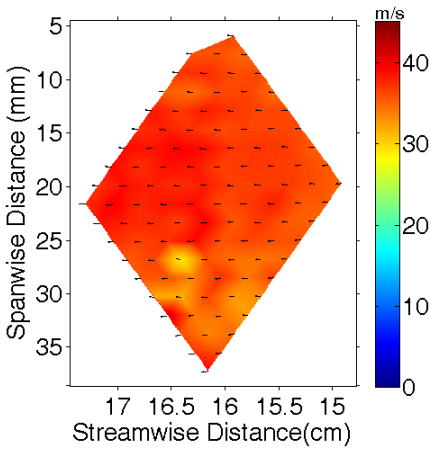


Figure 2: Hydroxyl tagging velocimetry data of the mean flow velocity on the tunnel mid-plane at $M = 0.1$. Streamwise distance is relative to spark, and the delay is 10 μ s.

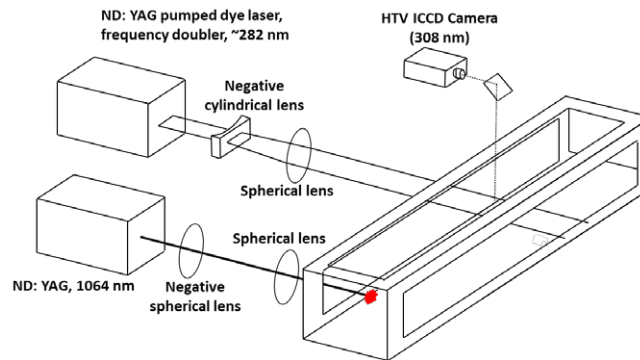


Figure 3: Schematic of OH PLIF and laser ignition system.

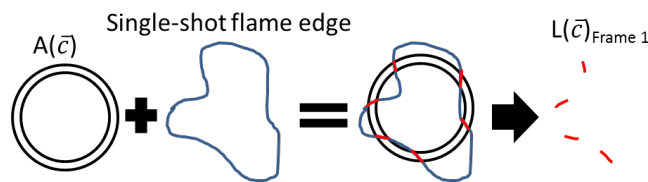


Figure 4: Schematic of FSD' determination from \bar{c} -maps for a given progress variable bin.

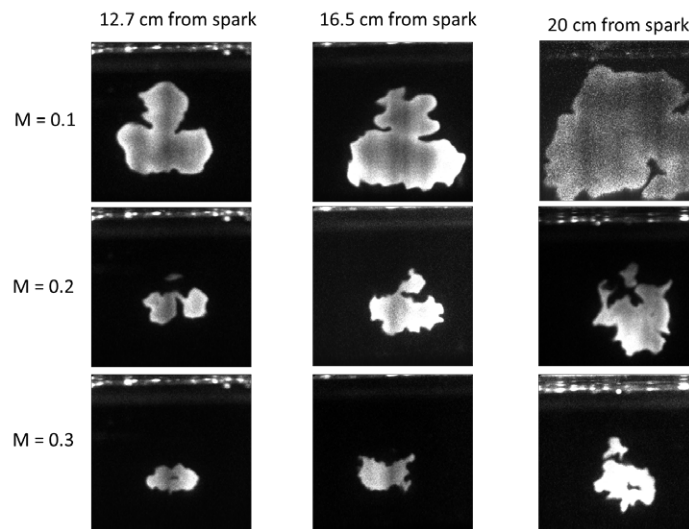


Figure 5: Raw single-shot OH PLIF images of flame kernels at $\phi = 1$.

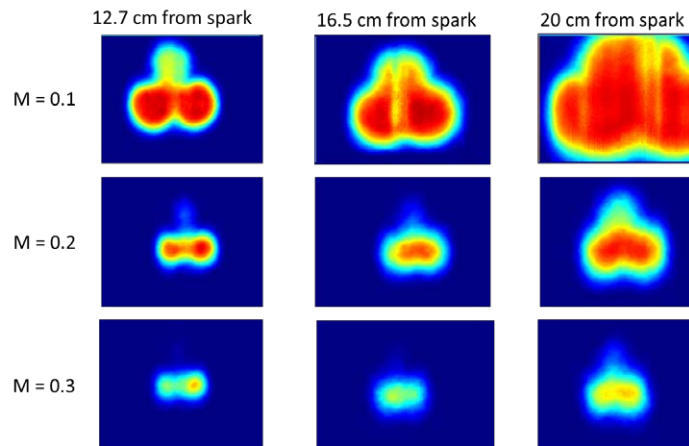


Figure 6: Mean of binarized images (i.e., c-map) of flame kernels at $\phi = 1$.

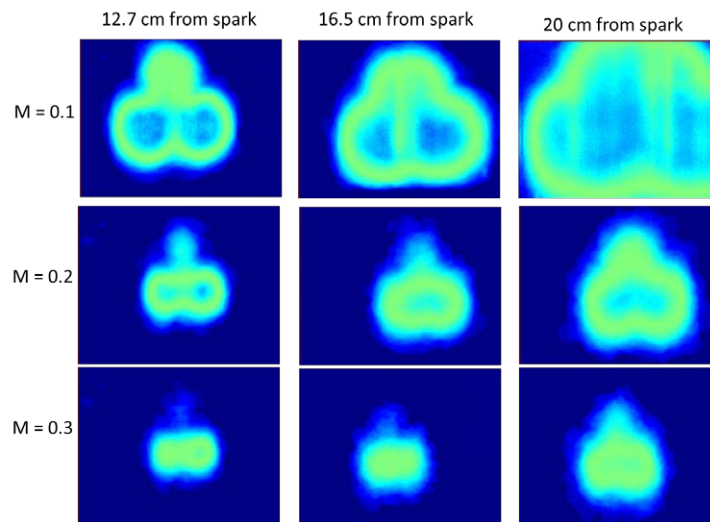


Figure 7: Standard deviation of the binarized images of flame kernels at $\phi = 1$.

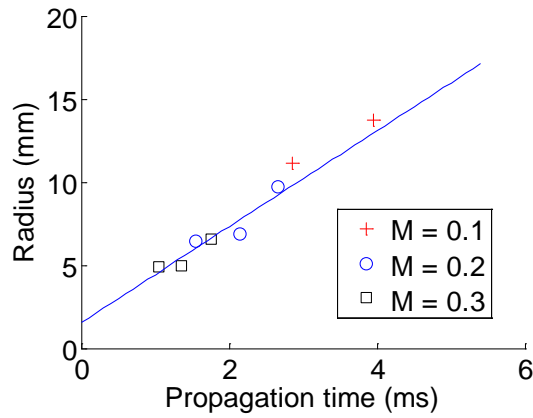


Figure 8: Characteristic radius versus time for $\phi = 1$.

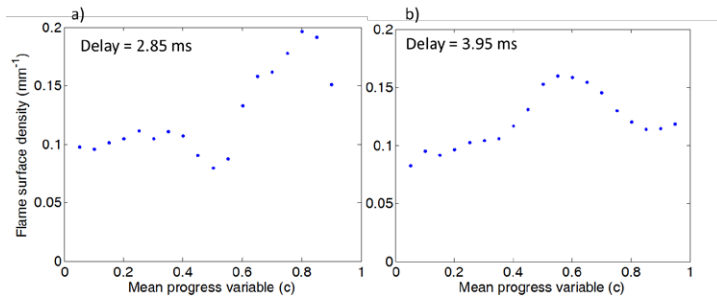


Figure 9: Flame surface density (FSD') vs. progress variable (c) for $M = 0.1$

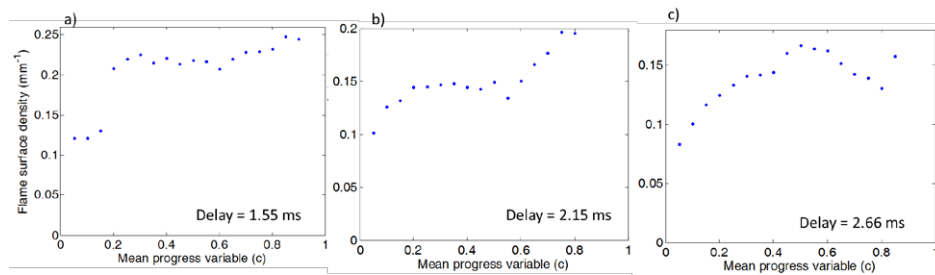


Figure 10: Flame surface density (FSD') vs. progress variable (c) for $M = 0.2$

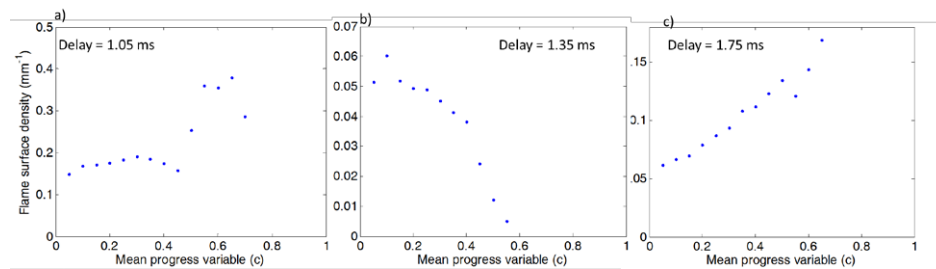


Figure 11: Flame surface density (FSD') vs. progress variable (c) for $M = 0.3$

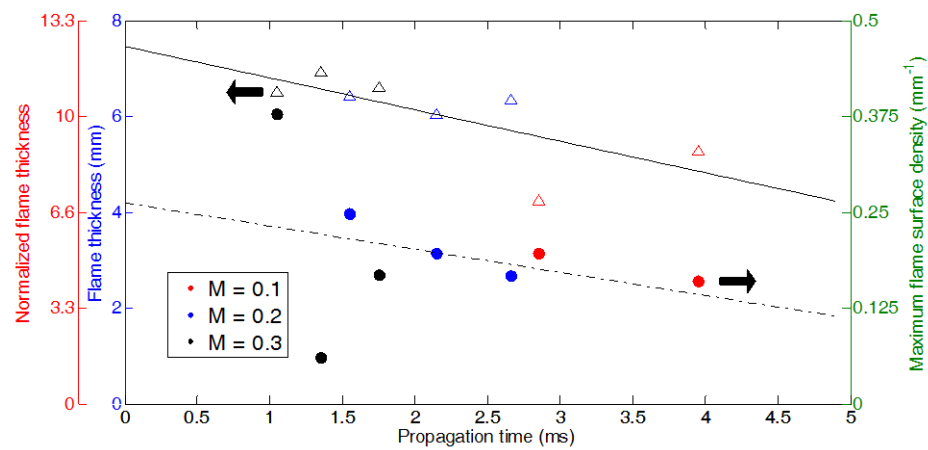


Figure 12: Flame thickness and normalized flame thickness (triangles, left axis) and maximum flame surface density (FSD'_{max} , solid circles, right axis) versus time with trend lines.

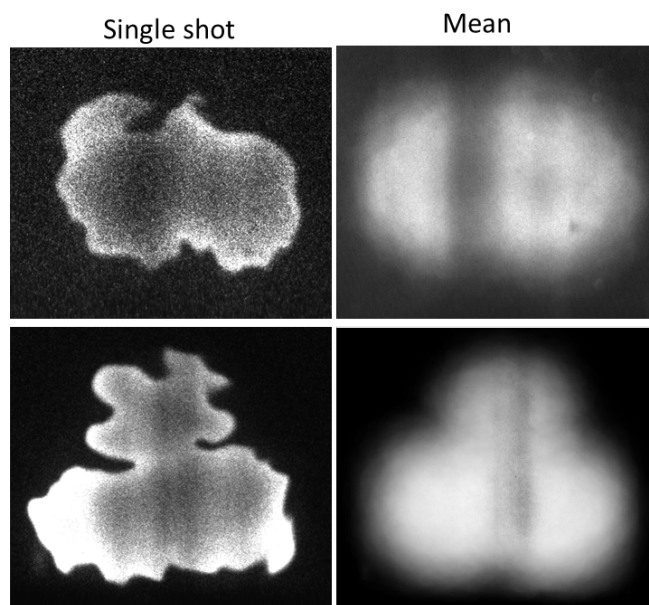


Figure 13: Comparison between 55 mJ/pulse kernels (top row) and 195 mJ/pulse kernels (bottom row).

C An Experimental Study of Homogeneous Anisotropic Turbulence in Channel Flow

AIAA SciTech
5-9 January 2015, Kissimmee, Florida
53rd AIAA Aerospace Sciences Meeting

AIAA 2015-1275

An Experimental Study of Homogeneous Anisotropic Turbulence in Channel Flow

Thomas Slais*, Bradley Ochs†, David Scarborough‡ and Suresh Menon§

School of Aerospace Engineering, Georgia Institute of Technology, Atlanta, GA, 30332-0150

Nathan Grady¶ and Robert Pitz||

Vanderbilt University Department of Mechanical Engineering, Nashville, TN, 37235-1826

A novel high bleed blown jet grid turbulence generator has been developed and tested in both a small-scale divergent duct and subsonic wind tunnel facility developed for flame kernel studies. The small-scale divergent duct is shown to produce an experimental realization of homogeneous turbulence that is comparable to traditional larger turbulence facilities. The high-bleed blown jet grid is shown to produce high Re_λ turbulence, with $90 < Re_\lambda < 298$ for tunnel total mass flow bleed ratios ranging from 10% to 30%. The resultant turbulence is comparable to that achieved by active vane grids, however the blown jet grid produces such results at grid mesh Reynolds number $Re_M \leq 6580$, which is less than half of what is observed for similar turbulence generated by active vane grids. Turbulence generated under shared inflow conditions as the divergent duct study are evaluated in the subsonic facility configuration. The “High Contraction Ratio” anomaly is identified and analyzed, enabling measures for its removal from future turbulence studies in the subsonic facility.

I. Introduction

THE study of homogeneous and isotropic turbulence (HIT) is a fundamental flow in the study and development of turbulence theory and models. This idealization affords considerable simplification in both the governing equations and in the amount of statistical quantities that are required to describe such a flow.¹ It is for this reason that HIT is typically seen as an ideal framework within which to further refine and probe turbulence theory in regimes that are currently not well understood. Of current interest to the field is the structure and behavior of turbulence at ever-higher intensities with large separation of scales in both the incompressible and compressible regimes.²⁻⁴ Such flow fields are also of interest to processes that are highly dependent on turbulence, such as combustion. A fundamental question of interest in combustion is how flame interacts with high-intensity turbulence under premixed conditions in both incompressible and compressible flows. Thus, achieving an experimental realization of a premixed, high-intensity HIT flow field across a large flow regime of interest is highly desirable.

Satisfying both requirements to generate a high-intensity HIT flow-field that can be evaluated under both incompressible and compressible conditions lends itself to a configuration that resembles a subsonic wind tunnel. In lieu of stationary, non-decaying turbulence where the development of the kernel is examined in time as in the case of traditional fan-stirred cruciform burner studies,^{5,6} the kernel must be examined using ensemble-averaging techniques of over many realizations at a particular point in space. This is dictated in part by the sampling frequency bandwidth limitations common to various forms of current non-intrusive, laser based techniques such as Particle Image Velocimetry (PIV), Planar Laser Induced Fluorescence (PLIF), and Hydroxyl Tagging Velocimetry (HTV) in relation to the residence times of interest.⁷ This approach to

*MS Student, Georgia Institute of Technology, AIAA Student Member

†PhD Student and Research Engineer, Georgia Institute of Technology, AIAA Member

‡Research Scientist, Georgia Institute of Technology, AIAA Member

§Professor, Georgia Institute of Technology, AIAA Senior Member

¶PhD Student, Vanderbilt University, AIAA Student Member

||Professor, Vanderbilt University, AIAA Senior Member

studying turbulence-flame interaction has been successfully demonstrated at Georgia Tech⁸ and is under continuous development.

Grid-generated turbulence is well-established as a means to generate approximately HIT, with typical “passive” grid geometries ranging from bi-plane arrays of rods forming grids with square elements,^{9–11} to perforated plates of various patterns.¹² Much effort has been spent on the design and study of passive grids alone in better experimentally approximating and understanding HIT.¹³ However, the vast majority of these studies have been carried out under low-speed conditions at the incompressible limit ($\bar{U}_1 < 10$ m/s) in slightly diverging, zero pressure gradient ducts in large facilities with test section cross-sectional areas on the order of 1 m² or larger. It is noted hereafter that the overline denotes time averaging, with subscripts 1, 2 and 3 denoting velocity components or correlations in the x , y and z directions, respectively. Typically available fuel flow rates and safety concerns relating to mitigating flashback and deflagration-to-detonation (DDT) make such facilities cost-prohibitive to construct at the laboratory scale. Thus, non-traditional small-scale zero-pressure gradient facilities must be developed and examined in relation to their larger counterparts for flame kernel studies.

The challenges of supporting flame kernel studies at flow rates associated with subsonic flows at this scale also require the use even smaller test sections with cross sections on the order of 10^{-3} m², which bring with them unique challenges. The addition of small contractions with area contraction ratios $c \leq 1.4$ are commonly used in traditional passive grid turbulence studies to correct out anisotropy that is an artifact of the turbulence generator.¹⁴ Passive grids typically have anisotropy ratios with respect to the turbulent RMS velocities of $1.2 < u'/v' < 1.5$ where $v' \approx w'$ and $u' = \sqrt{u_1^2}$ due to the nature of merging wake structures at convective timescales where the turbulence has homogenized.¹⁵ However, in support of subsonic flame kernel studies, a nozzle or series of several smaller nozzles with an overall large contraction ratio must be implemented. This nozzle system must ideally accelerate the flow while correcting any resultant anisotropy from the turbulence generator. For large contraction ratio nozzles of $c > 4$, it is known that analytical methods such as vortex-stretching and Rapid Distortion Theory (RDT) are not adequate due to the more biased effect of mean strain on the large scales.^{16,17} More elaborate Reynolds stress models are still being developed for RANS-CFD for applications where large mean strain rates are applied to flow fields of high turbulent Reynolds number (Re_T),^{16,18} leaving only more computationally expensive techniques such as LES to currently confront this issue.

The requirement for the generation of high-intensity turbulence for combustion studies brings with it its own challenges. The aforementioned traditional small contraction ratio nozzle anisotropy correction methods require experimental data as priori to provide initial inflow conditions to guide a nozzle design. The behavior of active generation techniques such as blown jet grids and vane grids is typically unique to the construction and application of a given grid, as there exists much variability between systems.^{19–22} Hence, it is impossible to design a facility that produces a subsonic, high-intensity HIT flow-field without first experimentally determining the resultant anisotropy of a given turbulence generation technique, and investigating the effects of mean strain in correcting or producing anisotropy on the associated flow-field.

This paper presents an examination of the scalability of traditional decaying HIT grid turbulence studies using a small-scale divergent duct facility, as well as the effects of mean strain on the flow-field present in the subsonic combustion facility configuration. A new active blown jet grid similar to that presented by Gad-el-Hak²¹ has been developed that is capable of high tunnel mass flow rate bleed ratios not seen previously in literature. This grid has also been configured to represent a traditional passive round-rod biplane grid for comparison to established passive grid studies.¹³ The blown jet grid is then examined in both zero-pressure gradient duct and subsonic converging nozzle facility configurations for a set of shared inflow conditions.

II. Experimental Setup

A. Facility Overview

A schematic of the subsonic combustion facility with associated centerline traverse measurement locations is given in Figure 1. Unheated air is supplied to the facility at 250 psig (1725 kPa) and 20.0 °C, where it is then filtered by a Parker CO2-2362 high-pressure air filter to eliminate particulate contamination with diameters greater than 0.3 μ m. Air flow is metered via a gate valve and calibrated orifice plate, monitored by a 0-5 psid (0-34.5 kPa) Omega PX-409 differential pressure transducer with a maximum error of 1% of full-scale (FS). This primary flow meter has been calibrated against a separate Siemens SITRANS F C MASS 2100 DI

3-40 series Coriolis flow meter which has a maximum error of 0.1% of a given flow rate less than 14.4 kg/s. The Siemens flow meter is mounted off of a branch downstream of the primary orifice plate, and meters filtered bleed air flow off of the main line via a globe valve to the blown jet grid system. A description of the fuel supply system, flow conditioning screen array, and associated facility components used in flame kernel studies is given by Grady.⁸ All hardware upstream of the turbulence generator location is shared between divergent duct and subsonic facility configurations.

The blown-jet grid turbulence generator system used for this study is shown in Figure 2. The design features a bi-plane arrangement of the injector rods of the grid with jet orifices positioned offset of rod crossings to promote generation of closer to isotropic turbulence and homogenization of turbulence closer to the grid.²³ The grid is constructed of 4.76 mm diameter rods that are spaced at a characteristic mesh width M of 24.4 mm. The grid has a geometric solidity of $\sigma = 33\%$ with jet orifices measuring 2.80 mm in diameter. All of the jet orifices face upstream. A second, post-conditioning grid shown in Figure 3 has been installed immediately downstream of the jet grid for bleed cases to break up periodic structures created by the grid under high bleed conditions. The grid is a rectangular perforated plate that halves the characteristic mesh size of the original grid ($M = 12.2$ mm), and has a geometric solidity of 33% with mesh elements that are 2.40 mm wide. The grid system with no bleed and no post-conditioning grid shown in Figure 2 serves as a passive baseline for comparison to a dimensionally similar “RD-35” grid constructed by Lavoie et al.,¹³ whereas all other data has been collected using the grid configuration shown in Figure 3.

A table outlining the shared inflow conditions and grid settings for both the subsonic and divergent duct configurations is outlined in Table 1. Run conditions are reported with respect to grid mesh Reynolds number ($Re_M \equiv \bar{U}_o M / \nu$), where ν is the kinematic viscosity and \bar{U}_o is the mean velocity at the grid. The grid bleed ratio is defined as $\dot{m}_{grid} / \dot{m}_{tot}$. Total mass flow rates are reported for each run in Table 1 for reference.

The subsonic configuration is as shown in Figure 1. A post-grid duct measuring 45.7 cm long is installed to facilitate homogenization of the turbulent flow-field immediately downstream of the conditioning grid. A square nozzle with contraction ratio $c = 8.5$ based on a scaled design of Sjögren and Johansson¹⁸ with $c = 9$ is followed by an optically accessible test section with a cross-section of 5.00 cm \times 5.00 cm. Test section velocities are set via a retractable 1.59 mm diameter PC-type Pitot probe constructed by United Sensor Corp. as shown in Figure 1 with total and static pressure lines measured by Omega PX-409 0-30 psia (0-206.8 kPa) pressure transducers accurate to 1% FS.

A schematic of the divergent duct configuration with associated centerline and transverse traverse measurement locations is shown in Figure 4. The divergent duct facility is set at a given run condition via use of the PC-type pitot probe used in the subsonic facility that can be fully retracted from the flow at the location shown in Figure 4. Differential pressure measurements between total and static pressure lines were accomplished using a Dwyer Magnahelic 2000-00 0-0.25 in. H_2O (0-62.3 Pa) differential pressure gauge with 4% FS accuracy. After setting the mean velocity of the flow-field, the divergence angle of the lateral tunnel walls were set by equilibrating the static pressure measured at taps indicated in Figure 4 using the Magnahelic gauge at a given grid condition. Centerline traverses were completed with hinge joints and all spanwise traverse ports sealed flush with 3M 425 aluminum tape not exceeding 0.005 in. (0.12 mm) in thickness, with ports only exposed during spanwise traverses at a particular location.

B. Measurement

The measurement of the evolution of scales, spectra and Reynolds stresses was accomplished using Constant Temperature Anemometry (CTA) via effective velocity signals from Single-Normal (SN) and Single-Yawed (SY) probe measurements at shared centerline traverse points shown in Figures 1 and 4. The SN-SY technique is a single channel probe method that has been demonstrated in statistically stationary flows with turbulence intensities as high as 30%.²⁴ It is typically used in measurement environments where access is limited to provide initial information before applying more complex, multi-component CTA probes.²⁵ The SN-SY method is described briefly as follows.

The effective velocity V_e is the measured velocity obtained via calibration from how much voltage is required to hold a CTA probe element at constant temperature at a specified orientation described by wire pitch (α), yaw (β) and probe stem roll (γ) angles. The diagram in Figure 5 shows how these angles are defined in relation to the coordinates system of the flow facility.²⁴ The relation of this voltage to velocity requires the empirical evaluation of wire yaw and pitch response coefficients k and h , respectively across the expected wire orientation and effective velocity ranges of interest. These coefficients are necessary to determine the response of a CTA probe element with respect to the wire coordinate system as shown in

Equation 1, where subscripts N , T , and B denote unit vectors that are normal, tangent and bi-normal to the wire, respectively as shown in Figure 5. The effective angle calibration procedure described by Bruun, et al.²⁶ has been used to evaluate k and h for $0^\circ < \alpha < 85^\circ$, $0^\circ < \beta < 85^\circ$ at $2 \text{ m/s} < V_e < 90 \text{ m/s}$ for both SN and SY probes.

$$V_e^2 = U_N^2 + k^2 U_T^2 + h^2 U_B^2 \quad (1)$$

The decomposition of the signal content of the effective velocity measurement of a single CTA element is accomplished by use of a coordinate transform of Equation 1 to the probe stem coordinate system at a specified probe orientation.²⁷ The resultant expression is shown in Equation 2, where the coefficients $A_i = f(\alpha, \beta, \gamma, k, h)$. The SY probe has a fixed yaw angle of $\alpha = 45^\circ$, and is rotated about the probe axis using a rigid ceramic sting shown in Figure 6. A X-shaped cross-brace supports the sting in the center of the test section for both divergent duct and subsonic facility configurations. Precise angular positioning of the SY and SN probes is accomplished using a Thor Labs RSP05 rotation stage at the rear of the sting that is accurate to $\pm 0.5^\circ$.

$$V_e^2 = A_1 U_1^2 + A_2 U_2^2 + A_3 U_3^2 + A_4 U_1 U_2 + A_5 U_1 U_3 + A_6 U_2 U_3 \quad (2)$$

Further decomposition of the effective velocity signal can be accomplished by separating each velocity component into mean and fluctuating components as shown by Buresti and Di Cocco,²⁷ where expressions for the mean and variance of the effective velocity to second order for a probe oriented parallel to the mean flow direction (\bar{U}_1) are shown in Equations 3 and 4, respectively. The coefficients B_i and C_i share the same functional dependence as A_i , and result from the series expansion of the Reynolds decomposition of Equation 2. Numerical subscripts are as they appear in Buresti and Di Cocco for reference.

$$\bar{V}_e = B_1 \bar{U}_1 + B_4 \frac{\bar{u}_2^2}{\bar{U}_1} + B_5 \frac{\bar{u}_3^2}{\bar{U}_1} + B_6 \left(\frac{\bar{u}_2 \bar{u}_3}{\bar{U}_1} \right) \quad (3)$$

$$\bar{v}_e^2 = C_1 \bar{u}_1^2 + C_2 \bar{u}_2^2 + C_3 \bar{u}_3^2 + C_4 \bar{u}_1 \bar{u}_2 + C_5 \bar{u}_1 \bar{u}_3 + C_6 \bar{u}_2 \bar{u}_3 \quad (4)$$

Determination of Reynolds stresses via Equation 4 was accomplished obtaining SY V_e records at six angular locations ($0^\circ, 45^\circ, 90^\circ, 180^\circ, 270^\circ, 315^\circ$), where 0° is denoted by the y-axis of Figure 5. Noting the values of C_i at each position, a signal processing routine is used to decompose the SY records into Reynolds stresses. These Reynolds stresses are then applied to Equation 3 to solve for \bar{U}_1 using the SN measurement record.

All measurements were conducted using a DANTEC StreamLine 90C10 frame with 90M10 constant-temperature bridge modules. DANTEC 55P01 and 55P02 gold-plated tungsten SN and SY probes, respectively were chosen for their higher available bandwidth for use in subsonic flows.²⁸ Each probe type has an active sensor width of 1.5 mm and diameter of 5 μm . Probes were calibrated using a DANTEC 90H02 automated laminar jet unit and were set at an overheat ratio of 0.8, resulting in a sensor over temperature of 220°C . This ensures that any fluctuations due to temperature for any measurement do not exceed 0.002 V/C°, or a maximum error 0.1% of the voltage associated with the lowest mean effective velocity measured.²⁹ Data was sampled at 50 kHz and 250 kHz and low-passed at 30 kHz and 100 kHz for divergent duct and subsonic data points, respectively using an analog 5th order Butterworth low-pass filter incorporated in the StreamLine frame. In response to the inability to fine-tune the low-pass analog filter settings and lack of prior knowledge of the turbulence signal frequency bandwidth for a given grid bleed setting, oversampled raw records were then downsampled to a desired new Nyquist frequency. These downsampled records were then low-pass digital filtered using a zero-phase 20th order IIR-type Butterworth low-pass filter before any further processing.³⁰ This eliminated inter-record aliasing with signal content identified as being non-turbulent by spectral analysis of the original oversampled SN records. Filtering criteria derived from the SN measurements were then applied to all SY records at a given shared traverse location and test condition.

Data collection and conversion was accomplished using a PC equipped with DANTEC StreamWare software and a NI 6023E 12-bit DAQ board. Records collected for spectral analysis via the SN probe contained 8.3×10^6 samples. This enabled a FFT frequency resolution of 1 and 5 Hz for divergent duct and subsonic data, respectively. At these resolutions and sample lengths, 300 individual independent records could be extracted from the sample and windowed using 50% overlapped processing. Energy spectra were then computed using the Welch algorithm³¹ while applying a Hanning window, resulting in a maximum

possible error of all spectral-derived quantities of 6%. Use of the Welch method has been validated by confirming that the hypothesis of statistical stationarity is accepted at the 5% significance level using a reverse arrangement test to evaluate all SN records.³⁰ Statistical stationarity and the associated lack of any propagating periodic structures could not be initially assumed due to the unknown nature of the high-bleed blown jet grid.

As previously discussed, the SN-SY measurement method is well-suited for determining the Reynolds stresses of a highly turbulent, statistically stationary flow. However, in a non-isotropic flow field, only scales and spectra along the mean flow direction can be directly evaluated from SN records with associated error assessment. Error assessment of the measured Reynolds stresses would ordinarily use the integral time scale calculated from directly measured u_1, u_2 and u_3 fluctuating velocity records to then select statistically independent data from the raw record for amplitude domain analysis.²⁵ The direct evaluation of such error is not possible using the SN-SY method, as the method cannot produce simultaneously measured independent fluctuating velocity records. However, known confidence intervals and error estimates can be made by using isotropic or RDT relations in the divergent duct and subsonic cases, respectively to estimate $L_{22}(x_1)$ and $L_{33}(x_1)$.¹⁶ Sampling criteria must then be selected to ensure that individual raw data records at a particular rotation angle contain the required signal content assuming amplitude domain analysis could be conducted. The sampling of 1.0×10^6 samples per rotation angle at 50 kHz for all SY measurements ensures that all Reynolds stress measurements are statistically accurate to 3% at a confidence level of 98% for turbulence intensities of 20% and lower.

III. Results and Discussion

A. Divergent Duct Mean and Turbulent Homogeneity

The divergent duct configuration is shown to produce an adequate experimental realization of homogeneous turbulence as shown in Figure 7. Transverse mean and RMS velocity profiles (u') are shown to be flat for both passive and 30% bleed cases, with a maximum deviation of $\pm 5\%$ of the centerline value. It is noted that all of these measurements were taken by a single element SN probe and not a rotating SY probe or multi-element X-probe. Hence, higher order velocity corrections in recovering the true mean velocity are not possible without information regarding contributions from $\overline{u_2^2}$, $\overline{u_3^2}$ and $\overline{u_1 u_3}$, as well as triple fluctuating velocity correlations such as $\overline{u_2^3}$ and $\overline{u_3^3}$ in high-intensity turbulence.²⁷ However, examination of the normalized mean effective velocity \overline{V}_e is an adequate indicator of mean velocity homogeneity, as a homogeneous flow field irrespective of turbulence level should interact with the SN probe element in the same fashion within the homogeneous region.

It is shown that both transverse turbulent and mean homogenization is achieved at $x/M = 30$, where $M = 12.2$ mm in this case. This ensures that a homogeneous turbulent flow-field is produced for study in both divergent duct and subsonic facility configurations. This is in agreement with much larger facilities used in traditional grid turbulence studies.⁹ However, in the case of Run 17, it is shown that homogenization is achieved considerably sooner at $x/M = 15$ ($M = 24.4$ mm), which is traditionally a region where inhomogeneities are present from merging wake structures.¹¹ Further investigation is needed to examine if this is indeed a unique property of the small-scale divergent duct.

The streamwise centerline traverses for all passive cases are shown in Figure 7 to not deviate by more than 5% of the initially measured value. These relatively large spanwise deviations in comparison to traditional larger facilities that have mean velocities that deviate by 1% or less¹³ are challenging to overcome in the case of a diverging duct with small cross-sectional area. In the case of Run 9, the differential static pressure between the first and twenty-eighth traverse points is 3.6 Pa, which is just above the ± 2.5 Pa error range of the differential pressure gauge used to set the diverging angle of the tunnel walls. Additionally, in the case of a highly-turbulent core flow, transient boundary layer interaction has been shown to alter the cross-sectional area of the core flow.²³ Hence, it is demonstrated that a small-scale divergent duct can produce an experimental approximation of homogeneous turbulence.

B. Divergent Duct Reynolds Stress Evolution and Decay

The streamwise evolution of the RMS velocities within the divergent duct for $Ma = 0.0357$ inflow conditions and passive grid reference case is shown in Figure 8. For all bleed settings (Run 10 - 12), the turbulence is

shown to be approximately isotropic for all cases, however it is noted that $u' < v'$. The u'/v' ratios for are shown in Table 2 and are approximately 0.95 for all cases, with the exception of the passive grid reference case (Run 17). The anisotropy ratio $u'/v' = 1.25$ at $x/M = 40.6$ for Run 17, which is in agreement with the reference case. However, as grid turbulence is typically classified as approximately axisymmetric anisotropic turbulence with $u' > v' \approx w'$, these results require further analysis.

As previously described, a signal processing procedure was used involving the downsampling of raw records to a new Nyquist frequency to facilitate digital low-pass filtering at a desired cutoff frequency. Using Taylor's hypothesis, the resultant energy spectra and associated wavenumber relations shown in Equations 5 and 6 could be used to then filter all records irrespective of frequency bandwidth to a cutoff wavenumber $\kappa_{1, cut}$. This facilitated direct comparison between spectra and associated statistics, regardless if the signal originated in a subsonic case or divergent duct case, with a bandwidths on the order of 10^4 Hz and 10^3 Hz, respectively.

$$\kappa_1 = \frac{2\pi f}{U_1} \quad (5) \quad E_{11}(\kappa_1) = \frac{\overline{U}_1}{2\pi} E_{11}(f) \quad (6)$$

However, while this processing procedure yielded common standards for record processing and mitigation or elimination of facility noise, this processing procedure was found to not be a best practice for the SY processing. This is best illustrated by considering a sample equation for the evaluation of $\overline{u_2^2}$ as shown in Equation 7 from the SY fluctuating effective velocity signal v_e at probe stem rotation angles of 0° and 180° degrees denoted by subscripts and superscripts a and b , respectively. The probe directional response coefficients C_i , as well as equations for the third order correlations $\overline{u_i^2 u_j}$ and remaining second order correlations are given in Appendix 1 of Buresti and Di Cocco.²⁷

$$\overline{u_2^2} = \frac{1}{C_2^a} \left[\frac{\overline{v_{e,a}^2} + \overline{v_{e,b}^2}}{2} - C_1^a \overline{u_1^2} - C_7^a \frac{\overline{u_1 u_2^2}}{\overline{U}_1} - C_9^a \frac{\overline{u_1 u_3^2}}{\overline{U}_1} \right] \quad (7)$$

Equation 7 demonstrates that the energy content of $\overline{u_1^2}$, $\overline{u_2^2}$ and $\overline{u_3^2}$ is shared between individual signals from several rotation angles. The use of digital filtering to eliminate facility acoustic noise may force the results to appear "isotropic" or produce results where $u' < v'$. It has been shown experimentally by Ertunç¹⁶ (p. 168) that $E_{22}(\kappa_1)$ has a broader (but less energetic) energy containing range than $E_{11}(\kappa_1)$. If the turbulence intensity is high enough such that an inertial range is present, the filtering of SY records such that $\kappa_{1, cut}$ is in the inertial range may make $\overline{u_1^2} \approx \overline{u_2^2}$. Filtered energy spectra $E_{11}(\kappa_1)$ are shown and discussed in the following subsection to aid in visualizing this effect. Thus, more accurate results using the rotating SY method requires further mitigation of rig noise, as well as some knowledge of the bandwidth of $E_{11}(\kappa_1)$, $E_{22}(\kappa_1)$ and $E_{33}(\kappa_1)$ to avoid losing valuable high-wavenumber signal content.

While the associated RMS velocities are likely slightly anisotropic with $u' > v' \approx w'$, the isotropic decay law can still be approximated using Equation 8, where the turbulent kinetic energy is defined as $k = 1/2(\overline{u_i^2})$, U_o is the mean velocity at the grid, x_o/M is the virtual origin, and A is a fit coefficient. The decay power coefficient n is typically found to be $-1 < n < -1.5$, with the similarity analysis of Mohamed and LaRue¹⁰ placing the value at $n = -1.3$.

$$\frac{2k}{U_o^2} = A \left[\frac{x}{M} - \frac{x_o}{M} \right]^n \quad (8)$$

Equation 8 is evaluated using the algorithm described by Lavoie,¹³ where a "Power Law Decay Region" (PLDR) is explicitly identified to avoid arbitrary determination of the virtual origin. As shown in Figure 8, the PLDR is fully developed for the passive grid reference case (Run 17), and progressively develops by bleed setting. Decay is shown to be irrespective of the grid type or bleed setting, with virtual origins that are similar to traditional studies.⁹ The decay coefficients are shown to be near $n = -1.0$ as shown in Table 2.

C. High-Bleed Blown Jet Grid Scale Comparison

All scales and dissipation estimates are calculated from SN records. As previously discussed, the Welch algorithm was used to calculate the one-dimensional energy spectra $E_{11}(f)$, which is then converted to wavenumber space via Equations 5 and 6. The circular autocovariance algorithm enables ensemble averaged

estimates of the autocovariance, where the autocovariance is defined as $R_{11}(s) \equiv \overline{u_1(t)u_1(t+s)}$, and s is the record lag time.³⁰ Determination of the integral length scale is shown in Equation 9, where the temporal autocorrelation is defined as $\rho_{11}(s) \equiv R_{11}(s)/R_{11}(0)$ and τ_{11} is the integral timescale.

$$L_{11} = \bar{U}_1 \tau_{11} = \bar{U}_1 \int_0^\infty \rho_{11}(s) ds \quad (9)$$

The Taylor length scale λ and mean dissipation $\bar{\epsilon}$ are estimated via Taylor's hypothesis from velocity derivative statistics as shown in Equation 10 and 11, respectively. The Taylor length scale Reynolds number is defined as $Re_\lambda \equiv u'\lambda/\nu$. Determination of the Kolmogorov length scale follows from Equation 11 as shown in Equation 12.

$$\lambda = \left[\bar{U}_1^2 u_1'^2 / (\partial u_1 / \partial t)^2 \right]^{\frac{1}{2}} \quad (10) \quad \bar{\epsilon} = 15(\nu / \bar{U}_1^2) (\partial u_1 / \partial t)^2 \quad (11) \quad \eta = (\nu^3 / \bar{\epsilon})^{\frac{1}{4}} \quad (12)$$

The use of isotropic relations to estimate $\bar{\epsilon}$ at a given point in anisotropic turbulence in this case is driven by current measurement limitations of the experiment. However, Mydlarski and Warhaft show that for $Re_\lambda > 200$ that the assumption for local isotropy in the small scales hold.³ As shown later, this condition is either closely approached or satisfied in this experiment, enabling accurate estimation of λ , Re_λ and η using this assumption.

As shown in Table 2, the high-bleed blown jet grid is capable of generating high-intensity turbulence with large separation of scales. At $x/M = 50$ and 30% bleed, it is shown that the grid produces a flow field that is similar to that of the active vane grid constructed by Makita³² at mesh Reynolds numbers Re_M approximately one-fifth the size of a comparable vane grid case. In comparison to the traditional low bleed (< 10%) blown jet grid of Gad-el-Hak,²¹ it is shown that turbulence intensities in excess of 16% are realized, with integral length scales that are at least twice the size of the characteristic mesh size of the grid or higher.

The claims of Table 2 are further supported by sample Kolmogorov-scaled energy spectra and autocorrelation data at $x/M = 50$ shown in Figure 9. As shown, the high-bleed cases show a prominent inertial range characteristic of $Re_\lambda > 160$, over a large normalized wavenumber region $\kappa_1 \eta$ where a $\kappa_1^{-5/3}$ slope is present.³³

Further support of the scale estimates of Table 2 are shown by the sample autocorrelation data in Figure 9. It is shown that $\rho_{11}(x)$ broadens as required for cases with progressively higher turbulence intensities. Additionally, it is illustrated that the integral length scale shown to be larger than the characteristic mesh size of the grid, whereas the blown jet grid configuration with no bleed (passive) produces an integral scale that is a significant fraction of the characteristic mesh size. This is in agreement with past blown-jet and vane grid active generation studies in larger facilities.

As described previously, a downsampling and digital filtering routine was implemented to set uniform wavenumber cutoffs and to minimize signal content attributed to facility noise. As shown in Figure 9, facility noise is still present at lower wavenumbers, and is more prominent in the currently considered passive and 10% bleed cases. Regardless of this effect, the normalized spectra presented in Figure 9 with a cutoff of $\kappa_1 = 2000 \text{ m}^{-1}$ shown at $\kappa_1 \eta \approx 2 \times 10^{-1}$ suggest that information in the dissipation range cannot be resolved, potentially impacting the validity of Taylor length scale estimates calculated with using Equation 10. However, it is shown by Pope (p. 199) that a necessary condition for the application of Equation 10 is smooth autocorrelation function,³⁴ where $d\rho_{11}(0)/dx = 0$ and $\lim_{x \rightarrow \infty} \rho_{11}(x) = 0$. Hence, if the dissipation range is difficult to recover due to acoustic noise contamination as presently experienced, digital record filtering criteria that can produce a smooth autocorrelation and recover turbulent signal content in all of the energy containing range and most of the inertial range can yield accurate estimates of the Taylor length scale λ , mean dissipation $\bar{\epsilon}$ and Kolmogorov scales. Thus, the presented high Re_λ values that have been previously only seen at laboratory scale at higher Re_M using vane grids are valid.

D. Subsonic Facility Reynolds Stress Evolution

The normalized streamwise mean velocity and mean velocity derivative profiles are shown in Figure 10. Typical experimental results are compared to profiles calculated using isentropic equations ignoring viscous effects such as boundary layer growth. As shown, the facility has a smooth parabolic $d\bar{U}_1/dx_1$ profile within the nozzle, which closely follows that of the isentropic results that are calculated from the nozzle geometry. Additionally, the small test section of square cross-section exhibits core flow acceleration as attributed to boundary layer growth. However, it is shown that this core acceleration does not result in a significant

post-contraction velocity gradient, as $d\bar{U}_1/dx_1 \sim O(10^0)$ or less. This indicates that the effects of mean strain within the subsonic flow facility are limited to the nozzle, and are negligible in the test section.

The streamwise evolution of RMS velocities and turbulent kinetic energy for test section Mach number conditions of $Ma = 0.200$ is shown in Figure 11 for the range of bleed settings considered, as well as a passive case with the blown jet grid configured as shown in Figure 3. As shown in the cases where the bleed ratio is larger than 20%, energy is transferred from the streamwise direction (u') to the spanwise directions (v' and w') and turbulent kinetic energy is produced. As it has been shown in Figure 7 that the inflow turbulence is homogeneous, the effect of the nozzle can be explained by first considering Reynolds stress transport in homogeneous turbulence as described by Equation 13 where the density is given as ρ and p' is the fluctuating pressure. The production, pressure-strain and dissipation tensors are given as \mathcal{P}_{ij} , \mathcal{R}_{ij} , and ϵ_{ij} , respectively.

$$\frac{\partial \overline{u_i u_j}}{\partial t} = \underbrace{-\overline{u_j u_k} \frac{\partial \bar{U}_i}{\partial x_k} - \overline{u_i u_k} \frac{\partial \bar{U}_j}{\partial x_k}}_{\mathcal{P}_{ij}} + \underbrace{\frac{1}{\rho} \overline{p' \frac{\partial u_j}{\partial x_i}} + \overline{p' \frac{\partial u_i}{\partial x_j}}}_{\mathcal{R}_{ij}} - \underbrace{2\nu \overline{\frac{\partial u_i}{\partial x_k} \frac{\partial u_j}{\partial x_k}}}_{\epsilon_{ij}} \quad (13)$$

Examination of the production term \mathcal{P}_{ij} reveals that for an accelerating one-dimensional ($d\bar{U}_1/dx_1 > 0$), incompressible ($d\bar{U}_i/dx_i = 0$) flow with approximately axisymmetric anisotropic turbulence that the turbulent kinetic energy (TKE) production term \mathcal{P}_k represented as half the trace of \mathcal{P}_{ij} is shown in Equation 14 as follows.

$$\mathcal{P}_k = \left(\overline{u_2^2} - \overline{u_1^2} \right) \frac{d\bar{U}_1}{dx_1} \quad (14)$$

Thus, positive TKE production occurs as soon as $\overline{u_2^2} > \overline{u_1^2}$ as shown experimentally. However, for low bleed cases, it is shown that u' decreases slightly halfway through the nozzle, or that u' increases through the nozzle. In the latter case, this can be partially explained by currently experienced acoustic noise that is most prevalent for passive grid cases, as previously illustrated in Figure 9 and further discussed in the following subsection. However in the former case, further analysis is needed with respect to the Reynolds stress transport budget presented in Equation 13 to identify the relative magnitude of components comprising components of the pressure-strain tensor \mathcal{R}_{ij} in relation to production and dissipation terms.

Insight into \mathcal{R}_{ij} is provided from examining the Poisson equation for fluctuating pressure. It is shown by Pope (p. 391)³⁴ that fluctuating pressure in an incompressible, homogeneous turbulent flow is described by Equation 15, where $p'_{(r)}$ and $p'_{(s)}$ denote rapid and slow fluctuating pressure contributions, respectively.

$$\frac{1}{\rho} \frac{\partial^2 p'}{\partial^2 x_i} = \underbrace{-2 \overline{\frac{\partial \bar{U}_i}{\partial x_j} \frac{\partial u_j}{\partial x_i}}}_{\frac{1}{\rho} \frac{\partial^2 p'_{(r)}}{\partial^2 x_i}} - \underbrace{\frac{\partial^2}{\partial x_i \partial x_j} (\overline{u_i u_j})}_{\frac{1}{\rho} \frac{\partial^2 p'_{(s)}}{\partial^2 x_i}} \quad (15)$$

It is seen in the nozzle that the rapid pressure term dominates and serves as a Reynolds stress “redistribution” term. While \mathcal{P}_{ij} is in closed form, analysis of \mathcal{R}_{ij} and ϵ_{ij} is needed to fully understand the Reynolds stress budget in the nozzle. It has been shown previously in this paper via analysis of flow fields generated by the blown jet grid in the divergent duct for shared inflow conditions with the subsonic configuration cases that high Re_λ inflow turbulence has been generated that satisfies the assumption of local isotropy.³ This greatly simplifies experimental measurement and analysis of ϵ_{ij} as previously discussed. However, this assumption may or may not hold within and downstream of the nozzle across all components of the energy spectrum tensor E_{ij} . Hence, analysis of energy spectra components $E_{ii}(\kappa_1)$ corresponding to Reynolds stresses $\overline{u_i^2}$ are needed to gain insight into the behavior of ϵ_{ij} at and after the nozzle to complement rapid pressure strain investigations.

E. The “High Contraction Ratio” Anomaly

It is shown in Figure 11 that for bleed ratios of 20% or greater that an apparent production mechanism is present that causes u' to increase. Decomposition of the production term and pressure-strain term in Equation 13 yields Equation 16 and 17 for \mathcal{P}_{11} and \mathcal{R}_{11} , respectively.

$$\mathcal{P}_{11} = -2\overline{u_1^2} \frac{\partial \overline{U}_1}{\partial x_1} \quad (16)$$

$$\mathcal{R}_{11} = \frac{2}{\rho} \overline{p' \frac{\partial u_1}{\partial x_1}} \quad (17)$$

Equations 16 and 17 show that for such production or pressure strain energy transfer to occur, either (1) $d\overline{U}_1/dx_1 < 0$ or (2) the pressure-velocity correlation terms $\overline{p'(\partial u_1/\partial x_1)} > 0$. It has been shown previously that $d\overline{U}_1/dx_1 > 0$ and $d\overline{U}_1/dx_1 \sim O(10^0)$ in the test section, meaning that $P_{11} \sim \overline{u_1^2}$, making it impossible to reverse the “negative” production effects of the nozzle. Additionally, it has been shown by Ayyalasomayajula and Warhaft experimentally for high-intensity nozzle inflow turbulence where $Re_\lambda = 289 - 412$ and $c = 4$ that the pressure-strain correlation \mathcal{R}_{11} is negative and of the same order as \mathcal{R}_{22} and \mathcal{R}_{33} in the post-contraction region. These results were presented using the framework of Rotta’s return to isotropy model, where \mathcal{R}_{ij} is only composed of slow fluctuating pressure correlations.¹⁷ Hence, the sharp rise in u' is not physical with respect to the turbulence, and must be attributed to non-turbulent phenomena.

The “High Contraction Ratio” anomaly described and experimentally identified by Ertunç¹⁶ is an issue that is present in flow-facilities with nozzle contractions where $c > 4$. It was discovered via considerations of the signal content of a typical CTA measurement, as CTA data had been the basis of numerous classical high-contraction ratio experiments. A typical CTA measurement irrespective of probe type can be decomposed into contributions from the mean velocity, turbulent fluctuations, electronic noise and mass flow fluctuations as shown in Equation 18.

$$V_e(t) = \overline{U}(t) + u_{turb}(t) + u_{elec}(t) + u_{mass}(t) \quad (18)$$

The analysis of Ertunç for incompressible flow has shown that mass flow fluctuations are amplified as per Equation 19, where the subscripts ₀ and ₁ denote a measurement locations immediately before the nozzle and a position downstream from the start of the nozzle. The local contraction ratio $c(x) = A_0/A_1(x)$ follows from this description, where A_0 is the nozzle inlet cross-sectional area.

$$\frac{\overline{u_{1,mass}u_{1,mass}}}{\overline{u_{0,mass}u_{0,mass}}} = c(x)^2 \quad (19)$$

The fluctuating mass flow rate term arises from both mass flow rate perturbations in the facility supply line from the pressure regulator and acoustic disturbances. Similarly, the small cross-sectional area of the test section gives rise to fluctuations in the core flow cross-sectional area as attributed to boundary layer interaction with the core-flow turbulence.²³ Given the current presence of facility noise and the inherent challenges of turbulence study using a small test section, it is seen this problem must be identified and removed in future study.

It is shown in Figure 12 that the “High Contraction Ratio” anomaly has been identified and illustrated via spectral analysis of the nozzle and post-contraction SN records for Run 16. The spectral evolution in the nozzle show that $\overline{u_1^2}$ should decrease as predicted by the Reynolds stress transport equation for two-component anisotropic turbulence. However, it is shown along the nozzle axis that as the cross-sectional area decreases, peaks associated with acoustic noise that are less prevalent at upstream locations are amplified. Additionally, at downstream locations after the contraction, the energy containing range is seen to grow, but grow with the inertial range. This is non-physical, as compared to expected growth in the energy-containing range from higher intensity turbulence as previously illustrated in Figure 9.

The findings of Figure 12 suggest that an extension of the correction method of Ertunç may be possible. The method described by Ertunç requires the use of two SN CTA probes positioned in the same spanwise plane that is perpendicular to the mean flow direction and that are spaced at a distance longer than the transverse integral length scale $L_{11}(x_2)$ to ensure that the turbulent signal content of each individual SN probe are not correlated.¹⁶ This allows for the identification of the spectral contribution of acoustic and mass flow fluctuations independent of the turbulence, which is then subtracted by individual Fourier mode from uncorrected spectra similar to those presented in Figure 12. As access to the subsonic test section volume is restricted, such a method must be implemented within the divergent duct facility at a location upstream of the nozzle for shared inflow conditions with a subsonic case. The access port shown in Figure 4 used for the homogeneity traverses presented in Figure 7 is well-suited for this purpose.

IV. Conclusions

It has been demonstrated that a small scale divergent duct facility can produce an experimental approximation of homogeneous turbulence similar to that of a traditional large scale facility. A novel high bleed blown jet grid has been shown to produce high-intensity turbulence with $90 < Re_\lambda < 298$ and integral scales that are larger than the characteristic mesh width of the grid for bleed ratios ranging from 10% to 30%. The resultant flow-fields are similar to that attained by active vane grids for $Re_M \leq 6580$, which is less than half of the mesh Reynolds number associated with comparable vane grid cases.

The subsonic combustion facility has been shown to exhibit behavior typical of approximately axisymmetric anisotropic turbulence. A nozzle of $c = 8.5$ has been shown to induce anisotropy by virtue of positive production of $\overline{u_2^2}$ and $\overline{u_3^2}$, while exhibiting negative production in $\overline{u_1^2}$. Spectral analysis of the contraction and post-contraction records for inflow conditions studied in the divergent duct facility configuration identify and illustrate the effects of the high contraction ratio anomaly.

This study has identified the presence of facility noise and mass flow fluctuations which is present over turbulent frequency bandwidths of interest. Such issues not only affect current CTA measurements, but would also be present in measurements using optical techniques as well. Facility modifications have since been completed to quiet the facility over frequency bandwidths of interest. Additionally, a correction scheme to remove the effect of acoustical noise and mass flow fluctuations is known. Such developments are in progress to support more accurate turbulence characterization in support of combustion studies.

V. Acknowledgments

This research was supported by the Air Force Office of Scientific Research Energy Combustion and Sciences Program (Dr. Chipping Li Manager, under Contract No. FA9550-12-1-0107/RC657).

References

- ¹Hinze, J. O., *Turbulence*, McGraw-Hill, 2nd ed., 1975.
- ²Kang, H., Chester, S., and Meneveau, C., "Decaying turbulence in an active-grid-generated flow and comparisons with large-eddy simulation," *Journal of Fluid Mechanics*, Vol. 480, 2003, pp. 129–160.
- ³Mydlarski, L. and Warhaft, Z., "On the onset of high-Reynolds-number grid-generated wind tunnel turbulence," *Journal of Fluid Mechanics*, Vol. 320, 1996, pp. 331–368.
- ⁴Lele, S., "Compressibility Effects on Turbulence," *Annual Review of Fluid Mechanics*, Vol. 26, 1994, pp. 211–254.
- ⁵Kwon, S., Wu, M., Driscoll, J., and Faeth, G., "Flame surface properties of premixed flames in isotropic turbulence: Measurements and numerical simulations," *Combustion and Flame*, Vol. 88, 1992, pp. 221–238.
- ⁶Huang, C. C., Shy, S. S., Liu, Y. Y., and Yan, Y. Y., "A transition on minimum ignition energy for lean turbulent methane combustion in flamelet and distributed regimes," *Proceedings of the Combustion Institute*, Vol. 31, 2007, pp. 1401–1409.
- ⁷Barlow, R., "Laser diagnostics and their interplay with computations to understand turbulent combustion," *Proceedings of the Combustion Institute*, Vol. 31, 2007, pp. 49–75.
- ⁸Grady, N. R., Pitz, R. W., Slais, T. A., Berlette, J., Ochs, B., and Menon, S., "OH PLIF Laser Diagnostics of Turbulent, Premixed Flame Kernels," In *52nd AIAA Aerospace Sciences Meeting, National Harbor, MD*, 2013.
- ⁹Compte-Bellot, G. and Corrsin, S., "The use of a contraction to improve the isotropy of grid-generated turbulence," *Journal of Fluid Mechanics*, Vol. 25, 1966, pp. 657–682.
- ¹⁰Mohamed, M. and LaRue, J., "The decay power law in grid-generated turbulence," *Journal of Fluid Mechanics*, Vol. 219, 1990, pp. 195–214.
- ¹¹Roach, P., "The generation of nearly isotropic turbulence by means of grids," *Heat and Fluid Flow*, Vol. 8, 1987, pp. 82–92.
- ¹²Liu, R., Ting, D., and Checkel, M., "Constant Reynolds number turbulence downstream of an orifaced perforated plate," *Experimental Thermal and Fluid Science*, Vol. 31, 2007, pp. 897–908.
- ¹³Lavoie, P., Djenidi, L., and Antonia, R., "Effects of initial conditions in decaying turbulence generated by passive grids," *Journal of Fluid Mechanics*, Vol. 585, 2007, pp. 395–420.
- ¹⁴Antonia, R., Lavoie, P., and Djenidi, L., "Effect of a small axisymmetric contraction on grid turbulence," *Experiments in Fluids*, Vol. 49, 2010, pp. 3–10.
- ¹⁵Uberoi, M. and Wallis, S., "Effect of Grid Geometry on Turbulence Decay," *Physics of Fluids*, Vol. 10, 1967, pp. 1216–1224.
- ¹⁶Ertuğ, O., *Experimental and Numerical Investigations of Axisymmetric Turbulence*, Ph.D. thesis, University of Erlangen - Nürnberg, 2007.
- ¹⁷Ayyalasomayajula, S. and Warhaft, Z., "Nonlinear interactions in strained axisymmetric high-Reynolds-number turbulence," *Journal of Fluid Mechanics*, Vol. 566, 2006, pp. 273–307.
- ¹⁸Sjögren, T. and Johansson, A., "Measurement and modelling of homogeneous axisymmetric turbulence," *Journal of Fluid Mechanics*, Vol. 374, 1998, pp. 59–90.
- ¹⁹Larssen, J. and Devenport, W., "On the generation of large-scale homogeneous turbulence," *Experiments in Fluids*, Vol. 50, 2011, pp. 1207–1223.
- ²⁰Kang, S. K. and Meneveau, C., "Experimental study of active grid generated shearless mixing layer and comparisons with large-eddy simulation," *Physics of Fluids*, Vol. 20, 2008, pp. 125102.
- ²¹Gad-el Hak, M. and Corrsin, S., "Measurements of the nearly isotropic turbulence behind a uniform jet grid," *Journal of Fluid Mechanics*, Vol. 62, 1974, pp. 115–143.
- ²²Tassa, Y. and Kamotani, Y., "Experiments on turbulence behind a grid with jet injection in downstream and upstream turbulence," *The Physics of Fluids*, Vol. 18, 1975, pp. 411–414.
- ²³Fransson, J., Matsubara, M., and Alfredsson, P., "Transition induced by free-stream turbulence," *Journal of Fluid Mechanics*, Vol. 527, 2005, pp. 1–25.
- ²⁴De Grande, G. and Kool, P., "An improved experimental method to determine the complete Reynolds stress tensor with a single rotating slanting hot wire," *J. Phys. E: Sci. Instrum.*, Vol. 14, 1981, pp. 196–201.
- ²⁵Bruun, H. H., *Hot-Wire Anemometry: Principles and Signal Analysis*, Oxford University Press, 1995.
- ²⁶Bruun, H. H., Nabhani, N., Al-Kayiem, H. H., Fardad, A. A., Khan, M. A., and Hogarth, E., "Calibration and analysis of X hot-wire probe signals," *Meas. Sci. Technol.*, Vol. 1, 1990, pp. 782–785.
- ²⁷Buresti, G. and Di Cocco, N., "Hot-wire measurement procedures and their appraisal through a simulation technique," *J. Phys. E: Sci. Instrum.*, Vol. 20, 1987, pp. 87–99.
- ²⁸Jørgensen, F. E., "The computer-controlled constant-temperature anemometer. Aspects of set-up, probe calibration, data acquisition and data conversion," *Meas. Sci. Technol.*, Vol. 7, 1996, pp. 1378–1387.
- ²⁹Bruun, H. H., "Interpretation of hot-wire probe signals in subsonic airflows," *J. Phys. E: Sci. Instrum.*, Vol. 12, 1979, pp. 1116–1128.
- ³⁰Bendat, J. and Piersol, A., *Random Data: Analysis and Measurement Procedures*, John Wiley and Sons, Inc., 4th ed., 2010.
- ³¹Welch, P. D., "The use of fast-fourier transform for the estimation of power spectra: a method based on time averaging over short, modified periodograms," *IEEE Trans. Audio Electroacoustics*, Vol. 15, 1967, pp. 70–73.
- ³²Makita, H., "Realization of a large-scale turbulence field in a small wind tunnel," *Fluid Dynamics Research*, Vol. 8, 1991, pp. 53–64.
- ³³Kistler, A. and Vrebalovich, T., "Grid turbulence at large Reynolds numbers," *Journal of Fluid Mechanics*, Vol. 26, 1966, pp. 37–47.
- ³⁴Pope, S. B., *Turbulent Flows*, Cambridge University Press, 2000.

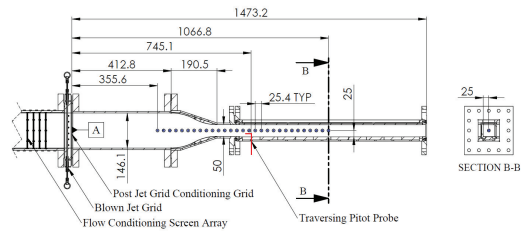


Figure 1. Subsonic facility schematic with centerline traverse locations. All reported x locations are with respect to Datum A, with traverse positions increasing in number in the streamwise direction (Units in mm).

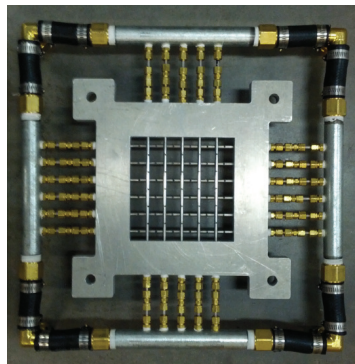


Figure 2. High-bleed active blown jet grid system. The grid with no bleed serves as passive baseline to established data.¹³

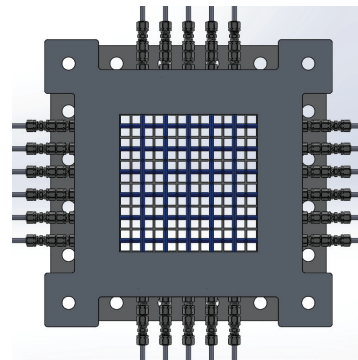


Figure 3. Upstream view of blown jet grid system with post-conditioning grid shown relative to injector rods (blue).

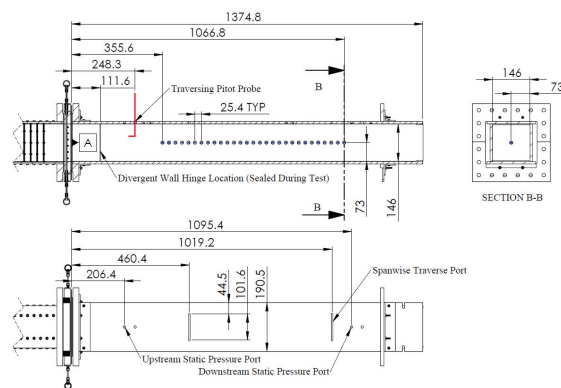


Figure 4. Divergent duct facility schematic with centerline traverse locations and spanwise traverse access ports. Datum A is shared with the subsonic facility shown in Figure 1 (Units in mm).

Table 1. Test matrix of presented study. Individual run information is given with the Mach number (Ma) reported at the pitot probe measuring location for a given facility configuration. The grid mesh size M and tunnel stagnation temperature T_o is given as 12.2 mm and 293 K unless specified otherwise.

Config.	Ma	Total \dot{m} (kg/s)	Re_M	No Bleed	10% Bleed	20% Bleed	30% Bleed
Div. Duct	0.0182	0.103	3280	1	2	3	4
Subsonic	0.100	0.103	3280	5	6	7	8
Div. Duct	0.0357	0.206	6580	9	10	11	12
Subsonic	0.200	0.206	6580	13	14	15	16
Div. Duct [†]	0.0285	0.163	10,400	17	—	—	—

[†]Passive grid reference case: $M = 24.4$ mm

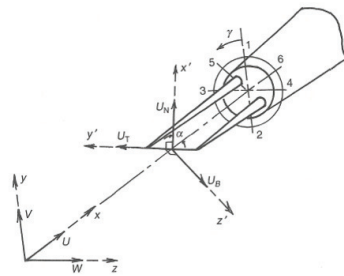


Figure 5. SY Probe wire-fixed coordinate system (x', y', z') in relation to the tunnel coordinate system (x, y, z).²⁵

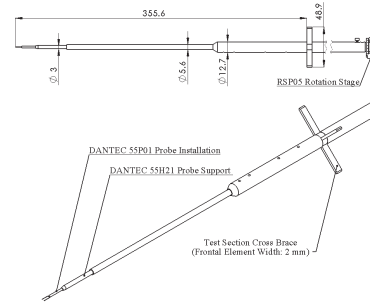


Figure 6. Schematic of rotating CTA probe sting shown in subsonic facility configuration (Units in mm).

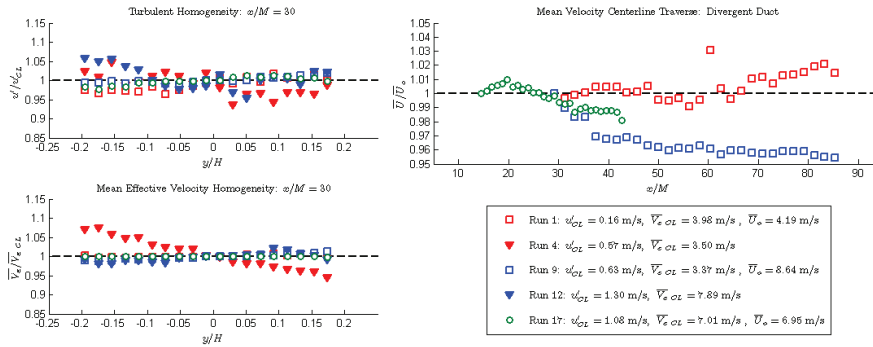


Figure 7. Turbulent and mean effective velocity homogeneity profiles measured by SN probe in divergent duct facility ($H = 0.146$ m). Centerline mean velocity profiles measured by SN probe. (See Table 1 for M Values)

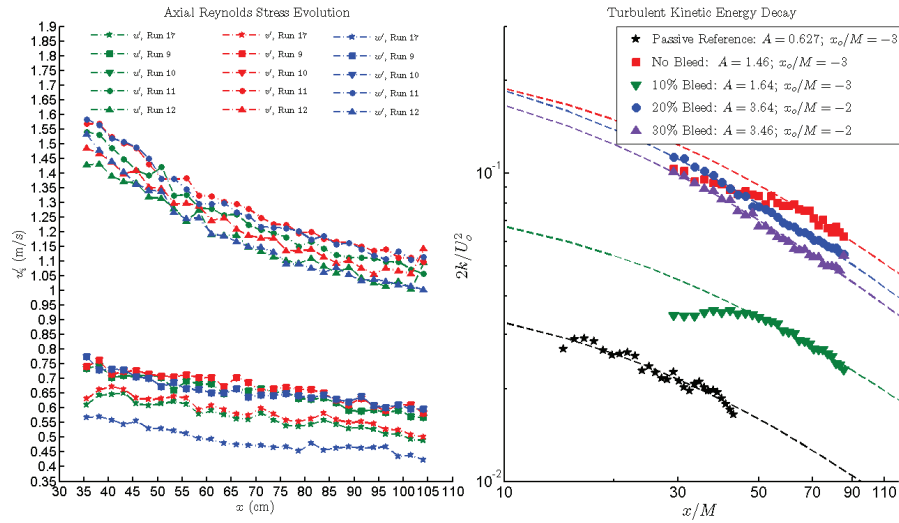


Figure 8. RMS velocity divergent duct centerline traverse and determination of turbulent kinetic energy decay for passive grid baseline case and blown grid settings at $Ma = 0.0357$ inflow conditions. See Table 2 for n values.

Table 2. Scale comparison with noted active and passive grid turbulence studies in literature.

Experiment	U_o (m/s)	M (mm)	x/M	Re_M (10^3)	u'/U_o (%)	u'/v'	L_{11} (mm)	λ (mm)	η (mm)	Re_λ	n
Run 2	4.04	12.2	50	3.28	5.0	0.95	22.8	3.0	0.16	90	1.02
Run 3	4.04	12.2	50	3.28	11.2	0.92	36.0	4.1	0.15	182	1.01
Run 4	4.04	12.2	50	3.28	10.9	0.94	36.7	4.2	0.15	190	1.04
Run 10	8.0	12.2	50	6.58	10.0	0.97	24.8	2.4	0.11	137	0.98
Run 11	8.0	12.2	50	6.58	15.9	0.97	34.6	3.1	0.097	270	1.00
Run 12	8.0	12.2	50	6.58	16.0	0.98	30.7	3.5	0.10	298	1.02
Run 17 [†]	6.4	24.4	40.6	10.4	8.70	1.25	17.0	6.2	0.20	65	1.04
Case 1	5.0	46.7	50	15.6	16.4	1.22	197	8.2	0.21	387	1.43
Case 2	4.2	102.0	46	41.8	3.27	1.11	134.7	9.45	0.39	160	0.97
Case 3	10	50.8	42	34.0	2.22	1.0	24	4.9	0.29	72	1.25
Case 4	6.4	24.8	60	10.4	2.2	1.27	11.0	5.5	0.48	33	1.14

[†]Passive grid reference case

Case	1	2	3	4
Investigators	Makita ³² (Vane Grid, Excited)	Gad-el-Hak ²¹ (Blown Jet Grid)	Compte-Bellot and Corrsin ⁹ (Passive Grid)	Lavoie, "RD-35" ¹³ (Passive Grid)

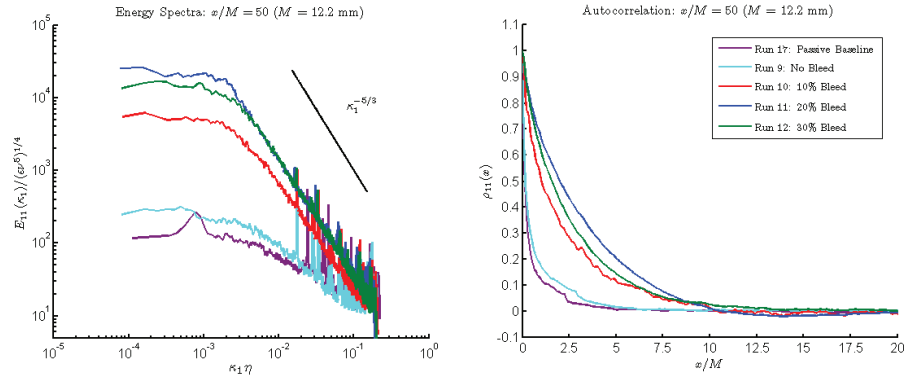


Figure 9. Kolmogorov-scaled energy spectra $E_{11}(\kappa_1)$ and associated autocorrelation $\rho_{11}(x)$ at locations of reported values in Table 2 for the passive grid baseline case and blown grid settings at $Ma = 0.0357$ inflow conditions. Note that for Run 17 the autocorrelation function is normalized by $M = 12.2$ for comparison.

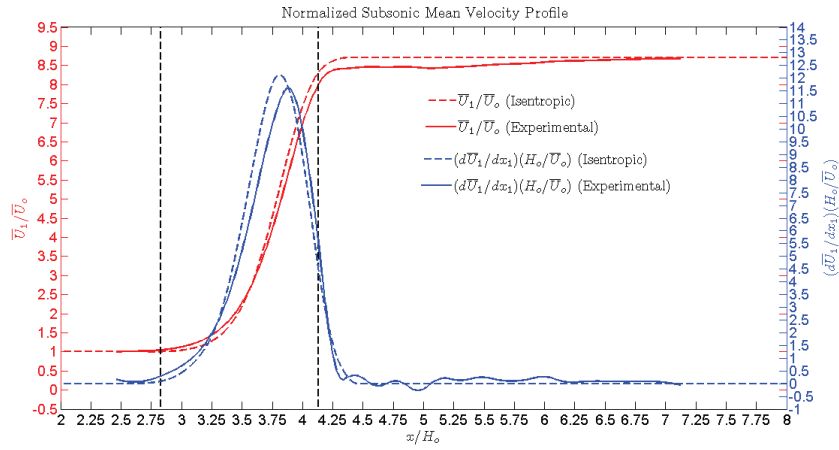


Figure 10. Normalized subsonic facility mean velocity profile and mean velocity derivative. Grid plane mean velocities U_o are given in Table 1 and H_o is the inflow duct height $H_o = 14.6$ cm. The location of the nozzle is shown by the vertical dotted lines.

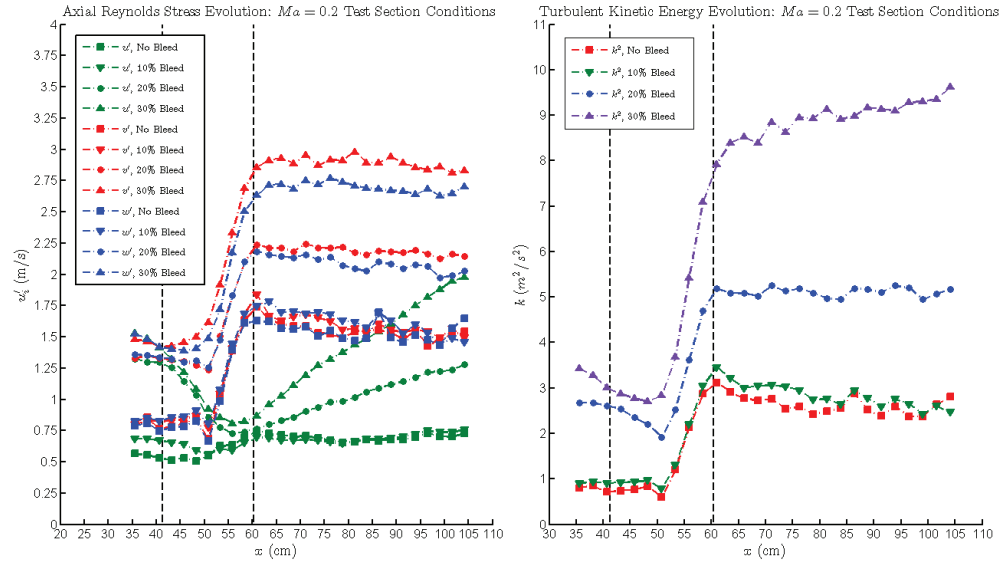


Figure 11. Evolution of RMS velocity and turbulent kinetic energy for blown grid settings associated with test section Mach numbers of $Ma = 0.200$. The location of the nozzle is shown by the vertical dotted lines.

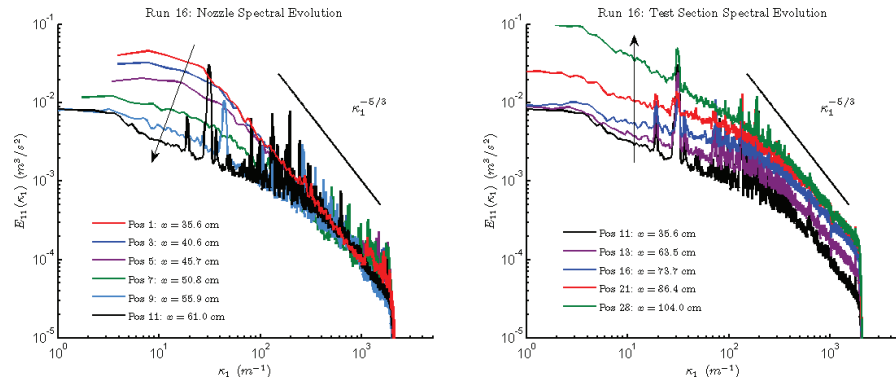


Figure 12. Examination of $E_{11}(k_1)$ evolution for Run 16 in the nozzle (left) and test section (right). The vertical shift in the energy of all scales and lack of collapse in the inertial range illustrates the “High Contraction Ratio” anomaly.¹⁶

D Propagation of Premixed Flame Kernels in High Speed Channel Flows with Moderate Turbulence

AIAA SciTech
5-9 January 2015, Kissimmee, Florida
53rd AIAA Aerospace Sciences Meeting

53rd Aerospace Sciences Meeting, Kissimmee, FL

AIAA-2015-0169

Propagation of Premixed Flame Kernels in High Speed Channel Flows with Moderate Turbulence

Nathan Grady, Robert Pitz
Vanderbilt University

Brad Ochs, Tom Slais, David Scarborough, Suresh Menon
Georgia Institute of Technology

A premixed CH₄/air wind tunnel with active turbulence generated with a vane grid design has been implemented to study turbulent combustion in high speed flows. The current experiment focused on stoichiometric kernels in $M = 0.1$ - 0.3 mean flows with turbulence from 0.4 m/s to 2.0 m/s ($u'/S_L = 1$ and 5 respectively). Flame kernels were laser ignited using ~ 10 mJ/pulse from a 532 nm Nd:YAG laser, and allowed to freely propagate downstream. Combined OH/CH₂O PLIF diagnostics were used to study the flame growth as a function of downstream distance/propagation time. CH₂O images did not indicate any significant local extinction, so the preliminary results shown here only examine the OH PLIF images. Flame surface density was found to decrease with respect to time due to the decaying turbulence in the tunnel. However, flame brush thickness increased resulting in an increase in the consumption rate until the kernel's expansion waves interacted with the wall. Additionally, instantaneous flame lengths determined from single-shot images were found to increase with turbulence as well.

Introduction

Interest in premixed combustion technology, which is generally more efficient and produces lower levels of harmful emissions, has grown in recent years. Additionally premixed combustors are generally smaller and lighter and, therefore, have higher thrust-to-weight ratios than their non-premixed counterparts. However, premixed combustors are also susceptible to flashback, global extinction (blow-out), and combustion instabilities that can be highly destructive to combustion hardware [1]. Finally, non-premixed combustors frequently have locally premixed zones [2] which need to be fully understood for either modelling or design optimization. Since all of these phenomena are related to turbulence, a phenomenological study of turbulence-flame interaction needs to be conducted.

Premixed flame propagation has been studied extensively over a range of turbulence intensities and length scales. However, most of these measurements used burners that imposed "memory effects" on flame propagation due to their particular geometry thus obscuring a fundamental, phenomenological understanding of premixed flame propagation without these large-scale effects. One such way of eliminating "memory effects" is to study freely propagating kernels propagating in a uniform mean flow having significant small-scale turbulence. While experiments studying kernels exist, most are at low turbulence and low mean flow conditions. Additionally, future combustors will have compressible and/or supersonic mean flows and possibly very high turbulence intensities. Therefore, there is a need to study turbulent flame propagation 1) without the use of a stabilization device and 2) with compressible mean flows.

Therefore, a new premixed CH₄-air facility was developed to study the effect of turbulence intensity and mean flow compressibility on freely propagating flame kernels. Previously, freely propagating kernel studies have been conducted by other researchers such as Renou et al. [3] at low mean velocities, 4 m/s, and turbulence levels, up to 0.5 M/s and ignited their kernels using spark igniters. The current facility has also been used to study flame kernels under incompressible flow conditions and with passive grid generated turbulence [4]. These experiments revealed the presence of “artifacts” created during laser ignition of the flame kernel. In the current experiment, an improved spark ignition scheme has been developed to reduce laser artifacts. Additionally, a new active vane stirred turbulence generator [5, 6] has been implemented to increase the turbulence levels from the previous experiments.

Experimental System

A schematic of the wind tunnel facility is shown in Figure 1. Unheated air is supplied to the facility at 1825 kPa and 25°C with controlled stagnation pressures and flow rates ranging from 203 kPa and 208 kPa to 0.09 kg/s and 0.270 kg/s for test section Mach numbers of 0.1 and 0.30, respectively, as shown in Table 1. The incoming air is filtered using a Parker CO2-2362 high-pressure air filter to eliminate particulate contamination with diameters greater than 0.3 μm from building supply lines.

Natural gas is supplied at 170 kPa to a pair of injector manifolds. The average composition of the natural gas mixture includes 98% CH₄, 1.5% N₂, with the remaining 0.5% consisting of CO₂ and heavy hydrocarbons. Flow metering is achieved via a calibrated orifice plate and injector manifold pressure. Fuel is injected via three linear spray bars with an outer and an inner diameter of 13.7 mm and 9.25 mm, respectively. Each spray bar features an array of 10 equally spaced 3.18 mm diameter orifices arranged linearly facing downstream. The mixing section has a square cross-section of the same length of the spray bars and extends 71.1 cm from the plane of injection to the location of the first flow conditioning screens. Shakedown testing using a Foxboro MIRAN 1BX gas analyzer unit verified that this system produced desired homogeneity and stoichiometry in the test section volume.

The turbulence generated by the upstream fuel injector array facilitates mixing. This turbulence is then damped as the flow passes through an array of flow conditioning screens. The flow conditioning array features an upstream perforated plate with 3.96 mm holes oriented in a hexagonal pattern that initiates the break-up of large scale structures created by vortex shedding from the fuel injection rods. As shown in Figure 1, starting 10.2 cm downstream, the flow passes through an array of four fine woven square mesh grids, spaced 2.54 cm apart, each having 1.04 mm diameter holes. The spacing of the grids ensures that each subsequent grid is positioned well after the grid turbulence decay region of the previous grid.

The vane grid generator system used for this study is shown in Figure 1. The grid is constructed of perforated square elements, known as vanes, with a characteristic mesh width M of 24.4 mm. The vanes are actuated via 11 independent rods in a bi-plane arrangement. The rods are 4.76 mm in diameter, giving a geometric solidity of $\sigma = 33\%$ when all vanes are parallel to the flow direction. This enables the grid to be compared in passive mode to classical passive grid turbulence studies. The rods are spun randomly at 2 RPM using DC motors controlled by a LabView algorithm similar to that

described by Larssen et al. [5]. 35 mm downstream of the turbulence generator, a 33% solidity passive grid with 5 mm holes was placed downstream of the vane grid to break up any large scale coherent structures.

The nozzle section features a fused silica glass access window for laser ignition mounted flush with the interior wall. The access port is 5.08 cm upstream from the entrance of the test section. The test section is square (5 cmx5 cm), 19.1 cm long and optically accessible on three sides through Corning 7980 fused silica quartz with a 5x35 cm² viewable area. The tunnel velocity was determined using a 1.59 mm diameter PC-type Pitot probe (United Sensor Corp.) installed in the aft end of the test section.

A schematic of the laser ignition and CH₂O/OH PLIF system is shown in Figure 2. A Spectra Physics Nd:YAG laser (~10 mJ/pulse at 532 nm after focusing lens) was used to ignite the flame kernels. The spark laser was focused into the tunnel using 25 mm aspheric lens situated 75 mm upstream of the test section. A frequency doubled Continuum Powerlite Nd:YAG laser pumping a Continuum ND6000 dye laser with a Continuum UVX frequency doubler provided ~282 nm (10 mJ/pulse) to probe the OH A²Σ⁺(v'=1)←X²Π (v''=0) band. The 282 nm pulse was formed into a sheet by a -150 mm cylindrical lens and a 1 m spherical lens. OH fluorescence was imaged using a PI-MAX 4 ICCD camera with ~100 ns gating. A frequency tripled Continuum Surelite Nd:YAG laser was used to provide 355 nm laser sheet for the CH₂O PLIF sheet using the same optics as the OH PLIF system. The CH₂O fluorescence was imaged on a PI-MAX 2 ICCD camera with ~100 ns second gating. To ensure consistent triggering between the two cameras, the output of the OH PLIF camera was used to trigger the CH₂O camera. This triggering scheme resulted in a ~100 ns delay between the two cameras. The entire system was synchronized with SRS DG645 delay generators and operated at 10 Hz. The raw OH/CH₂O images are then dewarped to account for any perspective distortion and translated to ensure that each pixel has the same physical size (~72.5 μm x 72.5 μm square) and location.

The OH images were used to acquire single shot and averaged images of the flame edge for comparison with previous studies of flame kernels. The flame edge was determined using a *smallest univalue segment assimilating nucleus* (SUSAN) method [7]. Additionally, measurements of flame surface density and flame thickness were acquired from binarized single shot images averaged together to form c-maps similar to previous authors [8-13]. Once the flame edge was found, each image was "binarized" with the value of either 0 or 1 being given to the unburned or burned side respectively. Then each of these binarized images were averaged together to produce a "c-map". From this c-map both flame surface density (FSD) and flame thickness can be derived for each data set.

A 2D dimensional representation of FSD, FSD', can be obtained using the c-map as mentioned in Shepherd and Cheng [9] :

$$FSD'(\bar{c}) = \frac{1}{n_f} \frac{L(\bar{c})}{A(\bar{c})} \quad (1)$$

The terms in Equation 1 are shown pictographically in Figure 3. First, c-map is divided into 20 equidistant bins in progress variable space. Then for a given progress variable bin, A(\bar{c}) is determined

from the area in pixels for a given bin. $L(\bar{c})$ represents the total flame length from all single-shot images within a given bin; this was determined frame-by-frame as shown in Figure 3 by overlaying the flame edge and the current bin, adding all the segments across all frames. Finally, $L(\bar{c})$ is normalized by the number of frames used (i.e. n_f). Typically, profiles of FSD vs \bar{c} form an inverted parabola or bell-shape centered around $\bar{c} = 0.5$ [9, 11, 13].

The flame brush thickness can be calculated by finding the maximum gradient in the c-map by:

$$\delta_T = \frac{1}{(dc/dn)_{max}} \quad (2)$$

The local consumption rate, $S_{T,C}$, can also be shown by using both the brush thickness and the FSD:

$$\frac{S_{T,C}}{S_L} = I_0 FSD_{max} * \delta_T \quad (3)$$

where $I_0 = 1-0.28Ma$ is a stretch correction factor. The displacements speeds can also be calculated from dR/dt and accounting for thermal expansion:

$$S_{T,D} = \frac{dR}{dt} \frac{\rho_P}{\rho_R} \quad (4)$$

Results

Turbulence data was taken using hot wire anemometry (HTA), and the results for the three Mach numbers used are shown in Figure 4. Due to vortex stretching in the nozzle, the turbulence is highly anisotropic in the test section with the streamwise component, u_{RMS} , being ~25% of the other components in the $M = 0.3$ case and ~40% at $M = 0.1$. The streamwise component increases slowly in the streamwise direction due to the tendency of the turbulence to return to isotropy. The square root of the turbulent kinetic energy, k , is also shown in Figure 4 and shows a slow decay of the overall turbulence. The values for $k^{1/2}$ were 0.4, 0.94, and 2.0 m/s ($u'/S_L = 1, 2.35$, and 5 respectively for $S_L = 40$ cm/s) for the $M = 0.1, 0.2$ and 0.3 cases respectively. Estimates of the turbulent length, ℓ , scales are provided in Figure 5, and the regime diagram is shown in Figure 6.

Stoichiometric kernels were observed at three different $M = 0.2$, and 0.3 at 5 streamwise locations and $M = 0.1$ at two different locations to achieve similar kernel propagation times for the three different mean flows. Only two locations are shown at $M = 0.1$ since the kernel takes ~3.5 ms to enter the camera's field of view at upstream location and begins to have significant wall interactions after ~4.5 ms. Raw images for the two PLIF systems are shown in Figures 7 and 8. The CH_2O image in Figure 8 shows a possible break, but the overlap still shows a continuous section. In general there was a continuous CH_2O layer around the OH indicating that local extinctions were rare events. Broadened regions of CH_2O were generally between folds in the kernel although there were regions where preheat zone broadening was apparent such as the rightmost CH_2O image in Figure 7. Given the measured turbulence levels and since there is little evidence of local extinction, local extinction was assumed negligible and preliminary results presented in this paper focus on data from the OH PLIF images only.

Additionally, as can be seen in the regime diagram shown in **Figure 6**, the kernels are propagating in the flamelet regime, there should be no local extinction as confirmed by the combined images.

Example c-maps for $M = 0.2$ and 0.3 are shown in **Figure 9** as determined from the OH images. The peanut like structure in the earlier stages of kernel growth is an artifact from the laser ignition and has been observed in various experiments [4, 14, 15]. From these images, kernel growth was inferred as shown in **Figure 10**. As shown, the growth rates are higher for both $M = 0.2$ and 0.3 than for $M = 0.1$ due to the higher levels of turbulence produced with the $M = 0.3$ profiles growing slightly faster than $M = 0.2$.

To further examine the changes in burning rates due to increased turbulence achieved at higher Mach numbers, FSD was calculated as can be seen in **Figure 11** showing the FSD as a function of time for both $M = 0.2$ and 0.3 . In both Mach numbers, the FSD decreases with time due to the decaying turbulence in the tunnel as shown in **Figure 11**. Comparing the maximum FSD values at $t = 1.842$ ms between the two Mach numbers shows a slightly higher value for $M = 0.2$ than for 0.3 . This can also be seen in **Figure 12** where FSD_{max} is higher for the lower turbulence levels. However, it can be seen that the FSD times the brush thickness is higher for $M = 0.3$ than for 0.2 indicating a faster consumption rate as shown in **Figure 12**. While in general the consumption rate increases with time, the final points for both $M = 0.1$ and 0.2 are slowing perhaps due to the interaction between the tunnel walls and the expansion waves created by the kernels. Additionally, the current results compare well with the results by Renou et al. [3] showing the same trends with respect to both FSD and brush thickness, although the values for both of these are higher in the current experiment as expected from the higher turbulence levels.

Figure 13 shows the instantaneous flame length at $t = 1.842$ ms for $M = 0.2$ and 0.3 as well as the average instantaneous flame length (error bars represent standard deviation) for all Mach numbers and propagation times. Instantaneous flame lengths are determined by finding the total length of the flame edge in a given frame of a single shot image. Longer flame lengths indicate more wrinkling than shorter flame lengths. The trend observed for flame radius was also observed for the mean flame length where the values for $M = 0.1$ were noticeably smaller than for the other two cases. While the mean values at $t = 1.842$ ms were similar between $M = 0.2$ and 0.3 , the distribution was slightly broader for the $M = 0.3$ case than for the $M = 0.2$ case ($\sigma = 1.05$ cm and 0.8 cm respectively). Additionally, the $M = 0.2$ distribution is skewed towards smaller overall flame lengths. These two things are consistent across all propagation times indicating more highly wrinkled flame kernels at the higher turbulence levels. Therefore, the increase in consumption rates is most likely due to the increase in flame area.

Finally, the flame speeds (both $S_{T,C}$ and $S_{T,D}$) are compared with the flame correlation by Peters [16] :

$$\frac{S_T}{S_L} = 1 - \frac{0.39}{2} \frac{\ell}{\ell_F} + \left(\left(\frac{0.39}{2} \frac{\ell}{\ell_F} \right)^2 + 0.78 \frac{u'}{S_L} \frac{0.39}{2} \frac{\ell}{\ell_F} \right)^{1/2} \quad (5)$$

where ℓ_F is the laminar flame thickness (0.6 mm approximated using $S_L = 40$ cm/s and $\alpha_{mix, 1200K} = 2.38$ cm²/s.). The experimental data and theoretical correlation are shown in **Figure 14**. As the kernels grow, the flame speed increases with propagation time, t . In a different experimental work conducted in the same facility by Slais et al. [17], as turbulence propagates down the tunnel it slowly

retains its $-5/3$ decay as expected from isotropic turbulence. However, the turbulence spectra don't retain a well-defined $-5/3$ inertial range until $x \sim 40$ cm into the test section and the furthest downstream distance used in this study was ~ 32 cm. Therefore, it is likely that the increase in flame speed is due in part to the redistribution of energy to the smaller scales which are capable of wrinkling the flame kernel. Furthermore, as the kernel becomes larger more scales can fit inside the kernel to wrinkle the flame front which would also contribute to the observed time dependence. There is decent agreement between $S_{T,C}$ and $S_{T,D}$ for each condition but both are below the estimated theoretical values. Since the theoretical correlation assumes that the burning reached "steady-state", it was not expected to correlate well with the current data. Additionally, the turbulence in the current experiment is neither isotropic or itself steady as assumed for the correlation. However, the correlation provides a reference to show the effects of the developing flow field on kernel propagation.

In the future, studies will be conducted with the turbulence generator placed after the contraction or with the contraction removed all together to eliminate the anisotropy. This will provide for kernel studies in nearly isotropic flows and (in the case of the turbulence generation after the nozzle) much higher turbulence intensities to be studied.

Conclusions

A premixed CH_4/air wind tunnel was developed and used to study laser-ignited, freely-propagating, turbulent premixed flame kernels in a turbulent, subsonic incompressible flow. Turbulence was generated using an active vane grid mechanism. The kernels were imaged at 5 different downstream locations using both OH and CH_2O PLIF to determine flame properties and consumption rates at different mean flow Mach numbers and different turbulence levels. The CH_2O images showed rare local extinction events and occasional preheat zone broadening. Flame surface densities were found to decay with time due to the decaying turbulence in the tunnel; however, the actual consumption rates increased until the expansion waves interacted with the tunnel walls. Analysis of instantaneous flame lengths indicated a higher degree of wrinkling for the higher Mach numbers/turbulence levels, which also explains the observed higher consumption rates at higher turbulence levels.

Acknowledgements

This research was supported by the Air Force Office of Scientific Research Energy Combustion and Sciences Program (Dr. Chiping Li Manager, under Contract No. FA9550-12-1-0107/RC657). The authors also thank technician S. Hutchings and research engineer C. Ballance at Georgia Tech for their assistance.

[1] Swaminathan, N., and Bray, K. N. C., 2011, *Turbulent Premixed Flames*, Cambridge University Press, Cambridge, UK.

- [2] Dhanuka, S. K., Temme, J. E., and Driscoll, J. E., 2011, "Unsteady aspects of lean premixed prevaporized gas turbine combustors: flame-flame interactions," *Journal of Propulsion and Power*, 27(3), pp. 631-641.
- [3] Renou, B., Mura, A., Samson, E., and Boukhalfa, A., 2002, "Characterization of the local flame structure and the flame surface density for freely propagating premixed flames at various Lewis numbers," *Combustion Science and Technology*, 174(4), pp. 143-179.
- [4] Grady, N. R., Pitz, R. W., Ochs, B. A., Menon, S., Scarborough, D. E., Berlette, J., and Slais, T. A., 2014, "OH PLIF laser diagnostics of turbulent, premixed, freely propagating flame kernels," 52nd AIAA Aerospace Sciences Meeting, National Harbor, MD, AIAA-2014-0315.
- [5] Larssen, J. V., and Devenport, W. J., 2011, "On the generation of large-scale homogeneous turbulence," *Experiments in Fluids*, 50(5), pp. 1207-1223.
- [6] Makita, H., 1991, "Realization of large-scale turbulence field in a small wind-tunnel," *Fluid Dynamics Research*, 8(1-4), pp. 53-64.
- [7] Smith, S. M., and Brady, J. M., 1997, "SUSAN - A new approach to low level image processing," *International Journal of Computer Vision*, 23(1), pp. 45-78.
- [8] Cheng, R. K., Shepherd, I. G., Bedat, B., and Talbot, L., 2002, "Premixed turbulent flame structures in moderate and intense isotropic turbulence," *Combustion Science and Technology*, 174(1), pp. 29-59.
- [9] Shepherd, I. G., and Cheng, R. K., 2001, "The burning rate of premixed flames in moderate and intense turbulence," *Combustion and Flame*, 127(3), pp. 2066-2075.
- [10] Sweeney, M. S., Hochgreb, S., and Barlow, R. S., 2011, "The structure of premixed and stratified low turbulence flames," *Combustion and Flame*, 158(5), pp. 935-948.
- [11] Lawn, C. J., and Schefer, R. W., 2006, "Scaling of premixed turbulent flames in the corrugated regime," *Combustion and Flame*, 146(1-2), pp. 180-199.
- [12] Sweeney, M., and Hochgreb, S., 2009, "Autonomous extraction of optimal flame fronts in OH planar laser-induced fluorescence images," *Applied Optics*, 48(19), pp. 3866-3877.
- [13] Shepherd, I. G., 1996, "Flame surface density and burning rate in premixed turbulent flames," *Proceedings of the Combustion Institute*, 26, pp. 373-379.
- [14] Mansour, M., Peters, N., and Schrader, L.-U., 2008, "Experimental study of turbulent flame kernel propagation," *Experimental Thermal and Fluid Science*, 32(7), pp. 1396-1404.
- [15] Bak, M. S., Im, S.-K., and Cappelli, M. A., 2013, "Successive laser-induced breakdowns in atmospheric pressure air and premixed ethane-air mixtures," *Combustion and Flame*, 10.1016/j.combustflame.2013.12.029.
- [16] Peters, N., 1999, "The turbulent burning velocity for large-scale and small-scale turbulence," *Journal of Fluid Mechanics*, 384, pp. 107-132.
- [17] Slais, T., Ochs, B., Scarborough, D., Menon, S., Grady, N. R., and Pitz, R. W., 2015, "An experimental study of homogeneous anisotropic turbulence in channel flow," 53rd AIAA Aerospace Sciences Meeting, Kissimmee, FL, AIAA-2015-1275.

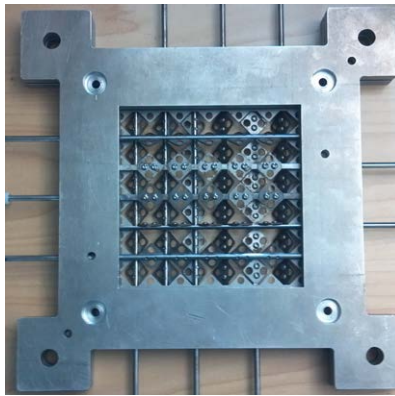
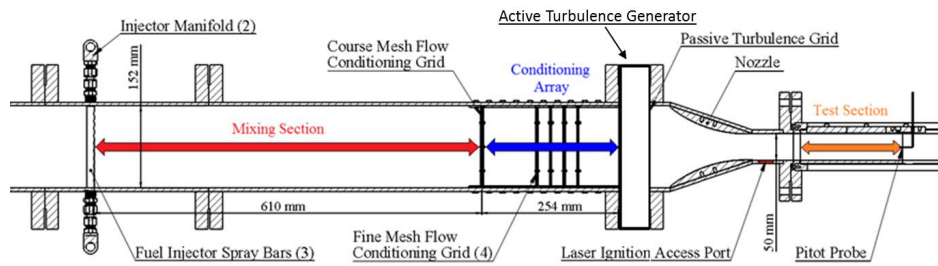
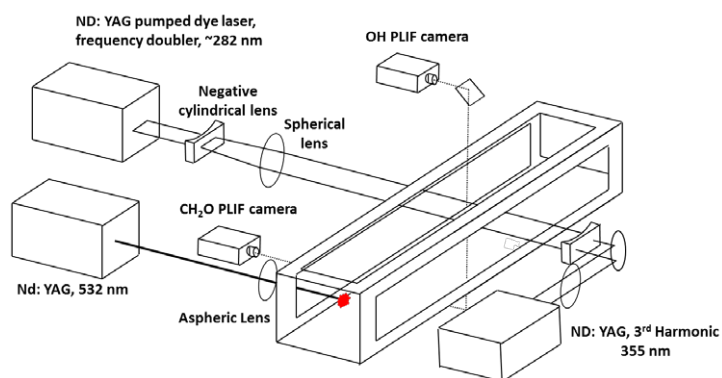
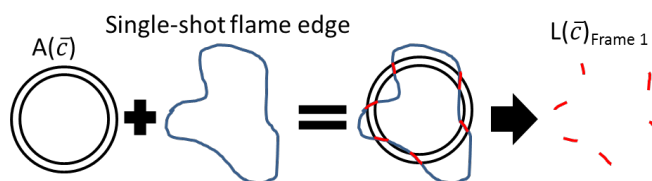


Figure 1: Schematic of wind tunnel facility (top) and active turbulence generator (bottom).

Table 1: Tunnel flow conditions

Mach Number	\dot{m} (kg/s)	U_0 (m/s)	$U_{\text{test section}}$ (m/s)	P_0 (kPa)
0.1	0.103	4	33.5	203
0.2	0.206	8	67.8	205
0.3	0.309	12	97.2	208

Figure 2: Schematic of CH₂O/OH PLIF and laser ignition system.Figure 3: Schematic of FSD' determination from \bar{c} -maps for a given progress variable bin.

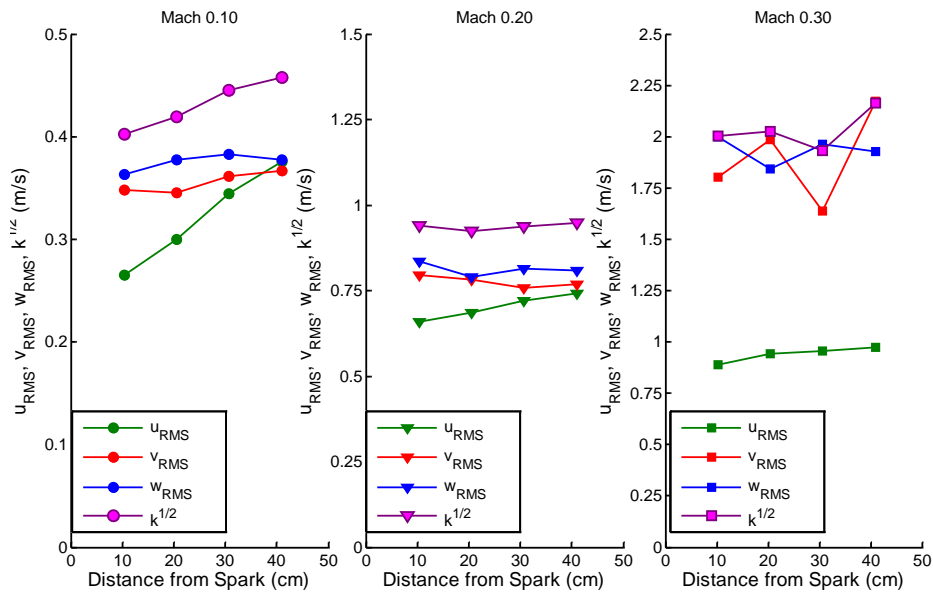


Figure 4: Turbulence levels for M = 0.1 (left), 0.2 (center), and 0.3 (right) as determined via hot wire anemometry

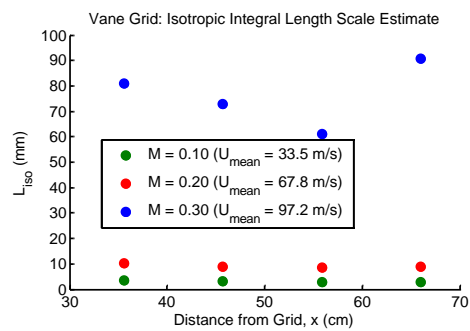


Figure 5: Turbulence length scales for M = 0.1, 0.2, and 0.3 as determined via hot wire anemometry

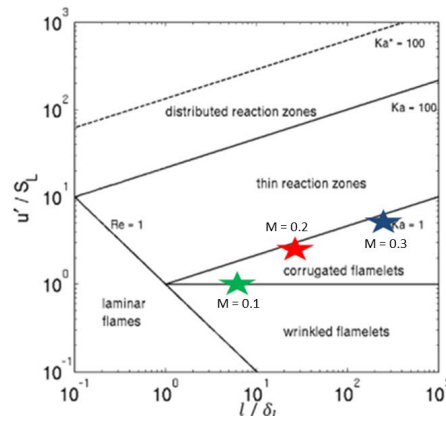


Figure 6: Regime diagram with indicators marking the location of interest for the current study

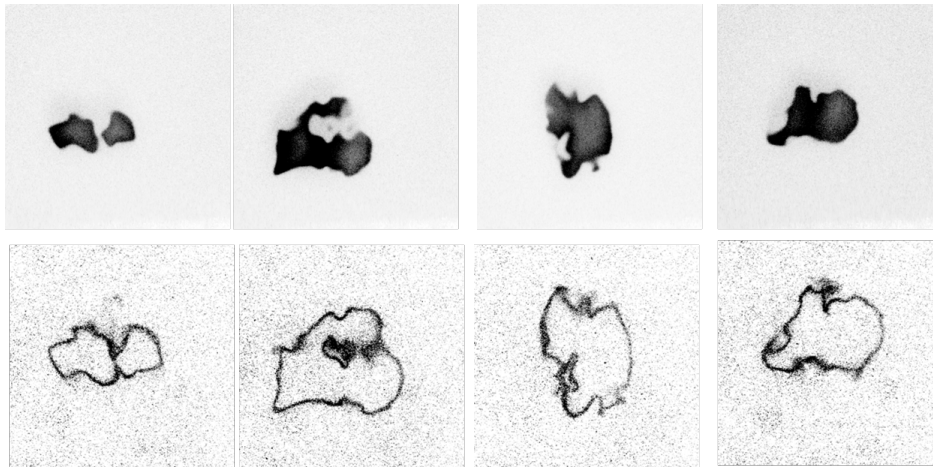


Figure 7: Raw images of OH PLIF (top) and CH₂O PLIF (bottom) taken at M = 0.3 and t = 2.892 ms

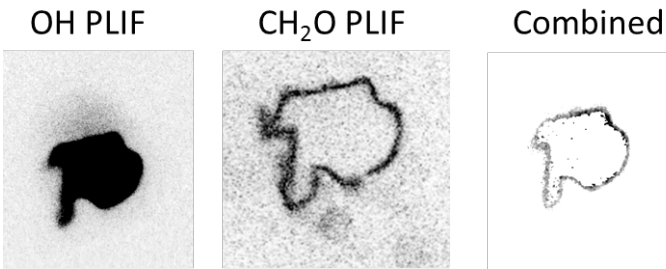


Figure 8: Example raw images of OH and CH₂O PLIF, and the combined image of the two taken at M = 0.3 at t = 1.992 ms.

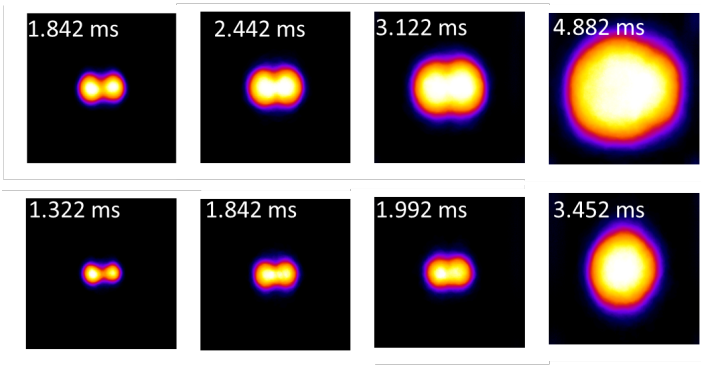


Figure 9 : C-maps for M = 0.2 (top) and M = 0.3 (bottom) at 11.5 cm (left), 15.2 cm, 19.0 cm, and 31.8 cm(right).

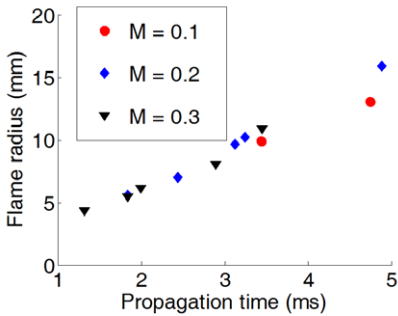


Figure 10: Radius verse time

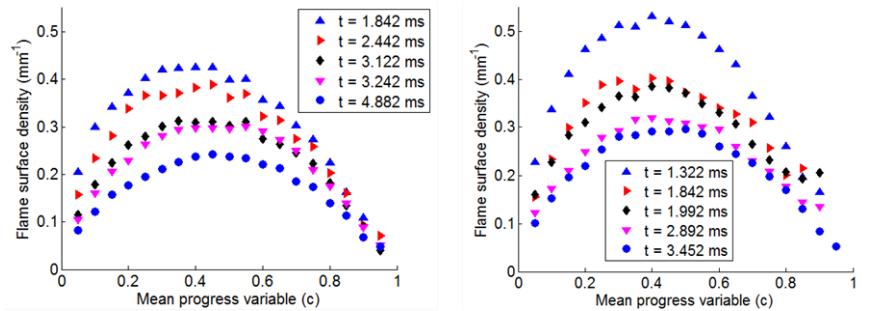
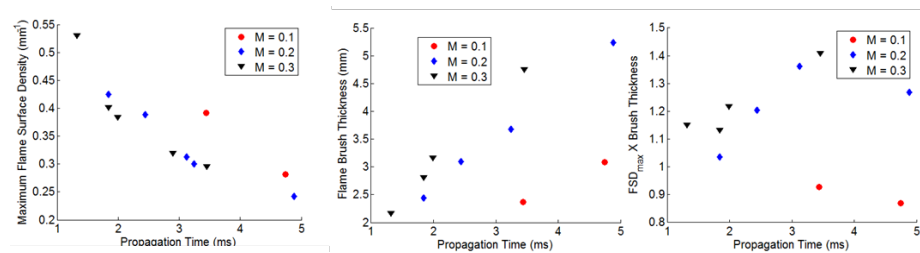
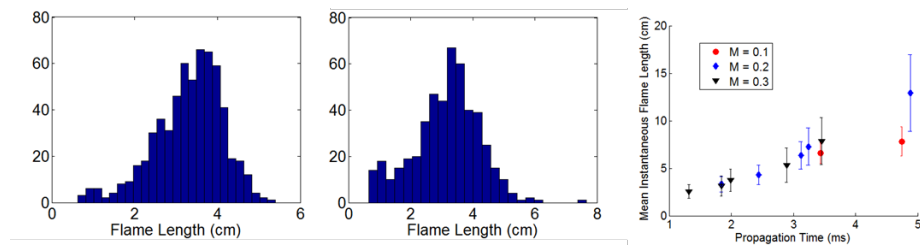
Figure 11: Flame surface density (FSD) vs time for $M = 0.2$ (left) and $M = 0.3$ (right)

Figure 12: Maximum FSD (left), flame brush thickness (center), and the product the maximum FSD and brush thickness (right).

Figure 13: Instantaneous flame length histograms for $t = 1.842$ ms for $M = 0.2$ (left) and $M = 0.3$ (center). Mean flame length verse time is also shown (right) with error bars for standard deviations.

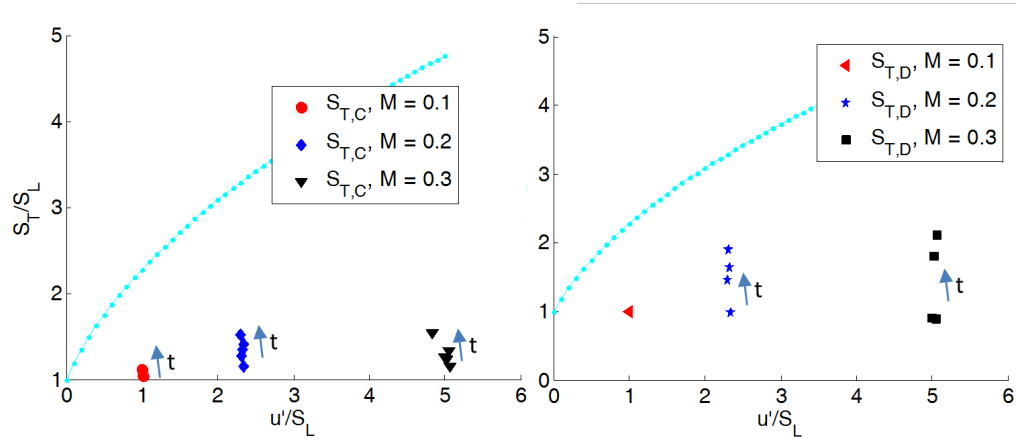


Figure 14: Experimentally determined flame speeds($S_{T,C}$ on the left and $S_{T,D}$ on the right) compared with Peter's theoretical correlation [16] with $\ell = 3$ mm. Arrows indicate increasing flame speed vs propagation time, t .

Characteristics of Freely Propagating Premixed Flame Kernels in Supersonic Turbulent Channel Flow

AIAA SciTech
5-9 January 2015, Kissimmee, Florida
53rd AIAA Aerospace Sciences Meeting

10.2514/6.2015-0928

Characteristics of Freely Propagating Premixed Flame Kernels in Supersonic Turbulent Channel Flows

Bradley A. Ochs,* Thomas Slais,† David E. Scarborough,‡ and Suresh Menon§

Georgia Institute of Technology, Atlanta, GA, 30318, USA

Nathan R. Grady¶ and Robert Pitz||

Vanderbilt University, Nashville, TN, 37235, USA

A new supersonic facility was developed to study the effects of turbulence intensity and mean flow compressibility on freely propagating flame kernels in a $M = 1.5$ channel flow. Two devices, a passive grid of holes and an active grid of rotating vanes, were used to generate turbulence. The $5 \times 5 \text{ cm}^2$ test section was optically accessible on four sides and had variable divergence walls on two sides to account for Fanno and Rayleigh flow deceleration. Methane-air freely propagating flame kernels were ignited with a single pulse of a frequency doubled green (532 nm) Nd:YAG laser and imaged via simultaneous high speed OH* chemiluminescence and high speed Schlieren photography. Planar velocity statistics were measured using particle image velocimetry. The generated turbulence intensity and isotropy are compared for the baseline and passive/active grids. Turbulent burning velocity trends are presented versus turbulence intensity and equivalence ratio. The flame speeds are fit to a functional dependence on the laminar flame speed and RMS velocity fluctuation and compared to classical low speed formulations.

Nomenclature

k	Turbulent Kinetic Energy, m^2/s^2	u', v'	RMS velocity fluctuation, m/s
Le	Lewis number	x, y, z	Cartesian spatial coordinates
M	Mach number	δ	Flame thickness, m
Re	Reynolds Number	ν	Kinematic Viscosity, m^2/s
r	Radius, m	ϕ	Equivalence Ratio
S	Flame speed, m/s	ρ	Density, kg/m^3
U	Mean velocity, m/s		
<i>Subscript</i>			
b	Burned	n	Normal direction
$chem$	OH* Chemiluminescence	sch	Schlieren
gd	Global displacement (velocity)	T	Turbulent
L	Laminar	u	Unburned
l	Integral length scale, m	λ	Taylor micro scale, m

*Ph.D. Student, Aerospace Engineering, AIAA Student Member.

†Master's Student, Aerospace Engineering, AIAA Student Member.

‡Research Engineer, Aerospace Engineering, AIAA Member.

§Professor, Aerospace Engineering, AIAA Member.

¶Ph.D. Student, Mechanical Engineering, AIAA Student Member.

||Professor, Mechanical Engineering, AIAA Member.

I. Introduction

THE desire to access the hypersonic flight regime has introduced requirements for the development of a number of technological advancements. One such requirement is the advancement of the SCRamJet combustor technology. The scramjet engine has been flight demonstrated on several occasions and will likely be the desired propulsion technology for future hypersonic flight. Despite this promise, this technology presents a number of technical challenges and exposes a lack of fundamental understanding in the areas of combustion and fluid dynamics at high Mach number, compressible conditions. For example, the nature of turbulent premixed combustion in the compressible fluid regime at high turbulence levels is almost entirely unexplored, and hence unknown. Additional challenges occur because the very nature of the premixed burning mode in these systems can vary widely depending upon the local turbulence level. Thus, understanding and predicting flame characteristics in the highly turbulent regime remains a challenge.

Studies of low-speed, turbulent premixed flames have established that an increase in turbulence intensity (or more specifically u'/S_L) results in a modification of the fundamental structure and behavior of the flame.¹⁻² Here, u' represents the rms velocity fluctuation and is a measure of the turbulence intensity while S_L is the laminar flame speed determined by the mixture chemistry. Flames within a weakly turbulent flow field are observed to behave like a laminar flame with superimposed wrinkles. An increase in the turbulent intensity results in a corrugated (or strongly wrinkled) flame front. In the limit of extreme turbulence, broken reactions are presumed to exist where the turbulent time scale is on the same order as the chemical time scale. The wide range of behaviors from laminar flamelets to corrugated flamelets to thin reaction zones (TRZ) is well known to exist in classical flame experiments,²⁻³ but the extension of this behavior to flows with mean compressibility is not well understood. In fact, nearly all the research effort has been limited to the flamelet regime in relatively low velocity flows. Only some more recent studies have focused on the thin reaction zone.⁴⁻⁵ In addition, most of these studies employ experimental configurations where the flame has been anchored, e.g., classical Bunsen, slot, or swirl-stabilized burner designs. Although advantageous in that these designs allow stationary flames for long term measurement they are also problematic due to the difficulty in decoupling the effect of large-scale strain from true turbulence-flame interactions. For example, in Bunsen flames $S_{T,gd}$ is observed to vary along the flame length due to flow field development, i.e. the flame is affected by the memory of large-scale structures.⁶ Other issues related to flame holding include heat transfer and preferential diffusion that can also contaminate results. Therefore, the development of experimental apparatus (capable of high speeds and free of large-scale structures) is needed to study the effects of increasing turbulence and mean flow compressibility on flame dynamics.

To address the above concerns, past studies in low speed flows have focused on premixed flame kernel interactions with isotropic turbulence in shear-free ducts and fan-stirred chambers.^{7-8,9,10} In these studies, an ignition kernel was created in a premixed mixture with isotropic turbulence. The propagation and growth of the kernel was investigated to ascertain the relationship between the burning velocity and the turbulent characteristics of the flow. Results have shown that as the turbulence level increases the flame surface undergoes wrinkling and an increase in its radius fluctuation. Propagation of premixed flame kernels in compressible isotropic turbulence has not been experimentally addressed so far, although there have been attempts in the past to generate compressible turbulence.¹¹⁻¹² An accurate measure of velocity statistics is a necessary requirement to compare measured flame behavior on the flame regime diagram. However, velocity measurements in supersonic flows present a particular challenge due to the difficulty of properly time resolving measurements. In addition, achieving faithful particle tracking within the flow field is difficult due to high mean flow momentum and reduced time scales. Despite these challenges, previous studies have demonstrated several techniques for accurate velocity measurements in supersonic flows including: laser Doppler velocimetry,¹³ Doppler shift laser induced fluorescence,¹⁴ and particle image velocimetry.¹⁵

To further the state of the art of SCRamJet combustion technology will require expanding these past studies into the compressible regime. It is expected that as flow speed increases from subsonic to supersonic, compressibility effects will change the nature of the fine-scale structures of turbulence.¹⁶ For example, suppression of mixing efficiency has been observed for highly compressible shear layers. Also, the presence of eddy shocklets has been identified in DNS of high intensity (compressible) turbulence.¹⁶ However, there are still many uncertainties in the flame characteristics in such flows.^{17,18} For example it isn't expected that a flame kernel propagating in a shear-free supersonic mean flow will behave differently than one propagating in an incompressible shear-free mean flow (assuming identical u'/S_L) but this has not yet been experimentally determined. In order to study these aspects of flame kernels in compressible turbulent flow fields, a new optically accessible, supersonic wind tunnel has been developed. The tunnel has been designed to produce

a shock-free $M=1.5$ flow field. In addition, the tunnel cross-section of $5 \times 5 \text{ cm}^2$ allows ample room for kernel growth; hence the methane-air flame kernels propagate downstream free of large-scale structures. Turbulence is added to the free stream by use of a passive grid turbulence generator. The flame kernels are studied via OH^* chemiluminescence and Schlieren photography. Turbulent statistics are collected via particle image velocimetry. This paper will explore measurements of the turbulent flame speed as influenced by the turbulence level and chemistry in this new facility.

II. Experimental Facility

The experimental facility consists of a fuel and air delivery/measurement system, stagnation chamber, fuel mixing section, a flow straightening section, and the supersonic test section (see Figure 1). The air system has the capability to supply 810 K air at up to 5 MPa. Air metering is accomplished via a calibrated orifice plate meter. The fuel system delivers natural gas (98% CH_4 , 1.5% N_2 , with a balance of CO_2 and higher hydrocarbon) and is metered with a calibrated orifice plate meter. The fuel is delivered through an array of co-flowing jets. The horizontal straightening section was designed to be sufficiently long to produce a homogeneous fuel/air mixture at its exit before entering the turbulence generator (discussed below). After the turbulence generator, a 9.3:1 nozzle contraction was needed to accelerate the flow and to allow sufficient geometric room for the turbulence generator. A converging-diverging nozzle then accelerates the flow to $M=1.5$ in the test section. The test section, shown in Figure 1, is nominally $5 \times 5 \text{ cm}^2$ and 1 meter long. The variable walls were set to one degree divergence to maintain a constant velocity in the test section during kernel growth. The test section is optically accessible on three sides via TSC-4 fused quartz glass. Two turbulence generators were investigated in this study. The passive grid turbulence generator consisted of an array of holes (8.89 mm diameter, 33% solidity) machined into a stainless steel plate, see Figure 2 (a). The hole size and solidity were driven by previous studies to ensure spanwise turbulent homogeneity upstream of the contraction.¹⁹ The rotating vane grid consisted of an array of vanes attached to rotating shafts, see Figure 2 (b). The vanes and holes were designed based on results of previous studies with vane grids such as Makita(1991).²⁰ The shafts were coupled to dc gear motors through a gearbox arrangement. The speed and direction of the motors were controlled through a LabVIEW interface. In these studies the motors were set to synchronous rotation and the shafts were driven at approximately two rotations per second.

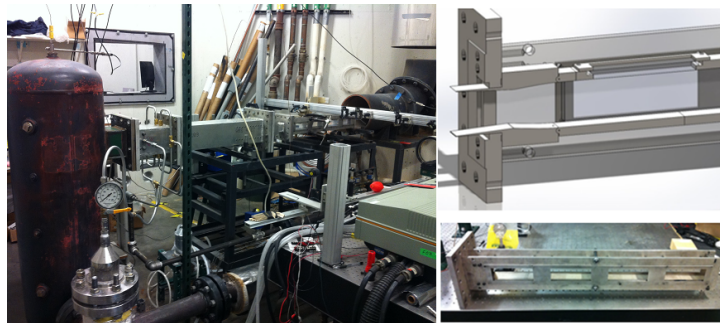


Figure 1. Supersonic reacting facility showing various facility components (left), diverging tunnel section view (top right), and as built diverging tunnel (bottom right).

Velocity measurements were collected with a two-dimensional PIV system. Two frequency doubled Big Sky Nd:YAG lasers (20 Hz) provided particle illumination and a Photron SA5 camera operating at 60 frames per second captured image-pairs. One dark image per image-pair was removed in post processing. Mean and rms velocities were calculated from image pairs via Lavisson's DaVis software. The time between laser pulses was set to 600 ns so that the particles moved approximately 6 pixels (1/4 an interrogation window) on average between images. This value was selected to optimize the measurement by making a trade off between in-plane loss-of-pairs error and resolution error. DaVis's two-image cross correlation with pixel by pixel interpolation has an estimated particle displacement error of 0.1 pixels. For these conditions, this yields

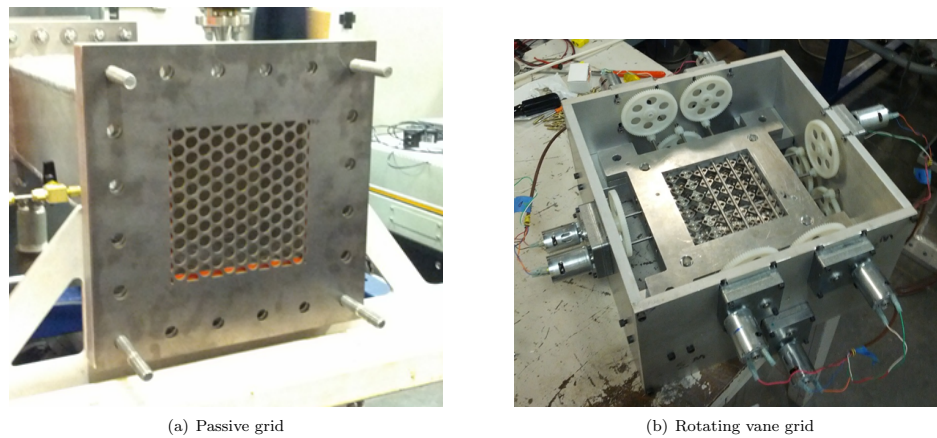


Figure 2. Images of (a) the passive grid turbulence generator and (b) the rotating vane grid turbulence generator.

an error of approximately 5.8 to 10.8 m/s on the instantaneous velocity vectors. Additional error due to particle drag may be present. The sheet size was 50 mm wide by 1 mm thick with 50 μm per pixel resolution. Assuming off-axis homogeneity, the resultant out-of-plane rms velocities were small enough for loss-of-pair error due to out of plane motion to be negligible. The sheet entered the test section through the top window and was imaged from the side window. A seeding system mixed a separate air stream with seed particles and injected the mixture upstream of the fuel inlet. A control valve was used to vary the flow rate through the fluidized bed seeder. The seeded air then mixed with the main air via injection through counter-flowing jets which ensured a homogeneous mixture of seeding particles at the end of the straightening section. The particles used in this study were 1-2 μm Al_2O_3 which were sufficiently small to resolve motion with spectral content under 4000 Hz.

A schematic of the laser ignition, Schlieren, and OH^* chemiluminescence systems is shown in Figure 3. A Continuum Surelite Nd:YAG laser (30 mJ /pulse at 532 nm after focusing lens) was used to ignite the flame kernels. The spark laser was focused into the tunnel using a 35 mm aspheric lens through one of the tunnel side windows. The lens was chosen to prevent damage to the window and limit the effect of back reflections. The ignition system was synced with an eight channel BNC delay generator which ran at 10 Hz.

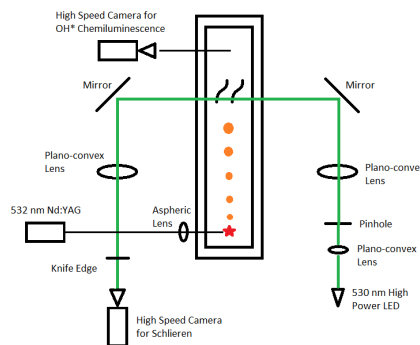


Figure 3. Ignition and flame kernel diagnostics schematic. A 532 nm YAG laser ignites flame kernels while a two Photron SA5 high speed cameras record OH^* chemiluminescence and Schlieren images.

The Schlieren system is depicted in Figure 3. The light source used was a high power continuous 530 nm green LED. A converging lens collected the light and focused it on a 300 μm aperture. A 250 mm diameter, 750 mm focal length plano-convex lens was used to collimate the light. The collimated light passed through the test section before being refocused by a 250 mm diameter, 1000 mm focal length plano-convex lens. A variable iris was used for the knife edge allowing visualization of x-direction and y-direction density gradients. A Photron SA5 high speed camera operating at 50,000 Hz, 3.8 μs exposure and 272×512 pixels captured the kernel images. The camera was triggered to capture 50 frames with every TTL signal from the delay generator. Approximately 822 kernels were captured per dataset providing sufficient samples to generate statistics. The raw Schlieren images are post processed by brightness and contrast adjustment. For each realization, the kernel is located at each instant in time (propagation time from ignition event). For each propagation time, the kernel size is calculated by averaging over all kernel realizations. Cross-stream variation is removed by centering each realization prior to averaging. The adjusted and averaged Schlieren images are then passed through an edge detection algorithm. Finally, the edge is fit to an effective circular diameter. Using the spark-to-image framing time delay, the effective diameter can be plotted against propagation time from the ignition event. Flame growth statistics are derived from this plot.

OH* chemiluminescence was collected at a 22.5° angle to the test section. A Photron SA5 coupled with a HiCATT intensifier at 5 μs gate and 308 nm filter operated at 272×512 pixels and 50,000 frames per second. The camera was triggered using the ignition TTL signal synced to the Schlieren images. The viewing angle dependence was removed in post processing by dewarping the images using a target grid. Approximately 822 kernels were captured per dataset providing sufficient samples to generate statistics. The kernel was located at each instant in time and the size was calculated by averaging over all kernel realizations. Cross-stream variation was removed by centering each realization prior to averaging. A threshold intensity was used to find the edge of the averaged kernel. The resulting kernel area is equal to the averaged line-of-sight OH* chemiluminescence at each time. The area was converted to an effective diameter and plotted versus time in a similar fashion to the Schlieren images. Following the analysis of Smallbone,²¹ the radial growth rate of a freely expanding flame kernel is equal to the global displacement velocity plus the velocity of the expanding burned gas. The global displacement speed is related to the radial growth via Eq. (1).

$$S_n = \frac{\rho_b}{\rho_u} \cdot \frac{dr_{chem}}{dt} \quad (1)$$

III. Results

A. Flow Field Characterization

The pre-combustion flow field was characterized with particle image velocimetry with and without the turbulence grids. Approximately 150 image pairs were processed and smoothed to produce mean and rms velocities for both the streamwise and spanwise velocities. Figure 4 shows the mean axial velocity and out-of-plane vorticity for all three cases. Single point turbulent statistics were produced by selecting a representative center-line value and are shown in Table 1.

Table 1. Turbulence generator properties.

Turbulence Generation	Hole Size (mm)	Solidity	u'	v'	k	$\nu \times 10^{-5}$	Re_l^a	Re_λ^b
Baseline (No Grid)	-	-	1.255	1.907	4.424	1.834	2,341	187
Passive Grid	8.89	33%	2.759	3.511	16.133	2.277	3,601	232
Rotating Vane Grid	5.72	-	5.771	4.393	35.945	2.323	5,269	281

Figure 4(a), (c), and (e) shows the mean velocity profile along the channel centerline. The passive and active grid cases show a mean velocity approximately 80 m/s higher than the baseline. This difference is due to a variation in the stagnation temperature between the datasets. For the baseline dataset, the stagnation temperature was $T_0 = 370$ K, while for the passive grid $T_0 = 450$ K and for the active grid $T_0 = 490$ K. It is

^aIntegral scale estimated as the channel half-width

^bEstimated

expected that a slight error will result when using these rms velocities to generate kernel growth statistics; in the reacting experiments care was taken to maintain a higher stagnation temperature of 550 ± 20 K. Table 1 shows centerline statistics with and without the turbulence grids. Clearly, the installation of the passive grid increases both the axial and tangential rms velocities. The estimated turbulent kinetic energy (TKE), which was calculated assuming cross-stream homogeneity, also increases with the installation of the grid. An even larger increase in both axial and tangential rms velocity fluctuations is achieved with the installation of the active grid system. Also shown in Figure 4(b), (d), and (f) is the mean out-of-plane vorticity for the baseline, passive, and active grid cases. A characteristic strain rate formed with the mean flow velocity and channel half-width is $S \approx \partial u / \partial y \approx 20,000/s$. In all three cases, the mean out-of-plane vorticity is much lower than the characteristic strain rate suggesting that kernels are freely propagating. Previous studies in grid-generated turbulence have shown near isotropy downstream of the grid after a short development distance.²² However, it is well known that contractions modify the turbulence by extracting TKE from axial fluctuations and depositing TKE into off-axis fluctuations.²² The anisotropy ($u'/v' \approx 0.7$) in these experiments is well explained by the 9.3:1 contraction prior to the test section. This significant reduction in area was necessary because the upstream turbulence generator required a large area while achieving long runtimes required a small test section area.

B. Growth Rate of Freely Propagating Flame Kernels

Chemiluminescence and Schlieren measurements were collected at two axial locations corresponding to the tunnel's first and second windows. From these data, global displacement speeds were calculated using Eq. (1). Table 2 summarizes the test conditions and results of this analysis. Six cases are identified: two turbulence settings (baseline and passive grid) and three equivalence ratios. The turbulent statistics for the baseline and passive grid cases are summarized in Table 1. For all cases the stagnation pressure was $P_0 = 320.5 \pm 5$ kPa and the stagnation temperature was $T_0 = 550 \pm 20$ K. Methane-air laminar flame speeds were taken from the bomb data of Andrews and Bradley.²³ An example output of the averaging process is shown in Figure 5 for Case 5 at the upstream axial position.

Figure 5(a) shows the OH* chemiluminescence of the averaged kernel at each propagation time overlaid onto one image. The intensity clearly decreases as the kernel propagates downstream. This is due to the high energy input of the ignition laser and the resulting large luminescence of the initial kernel. The laser energy was set at 30 mJ/pulse to minimize shot to shot variation. The result was an ignition kernel that necessarily over exposes the camera during early propagation times. This phenomena causes an error in the initial size of the kernels measured with the OH* technique. By the third image (approximately 73.3 μs after ignition) this error appears to be gone. Self propagating and growing kernels were achieved with ignition energies as low as 6 mJ/pulse, however a significant portion of these kernels did not grow. Ignition energy may contribute a memory effect to the growth of kernels but the energy was not included as a variable in this study. In fact, ignition in supersonic flows is a relatively unexplored topic that deserves its own study. Brieschenk²⁴ successfully used laser ignition in a scramjet environment but to the authors' knowledge this is the first attempt at ignition of supersonic, freely propagating kernels using laser induced plasma ignition.

Table 2. Summary of test conditions and global displacement velocities.^c

Case	Turbulence Grid	ϕ	$\frac{u'}{S_L}$	$\frac{dr_{chem}}{dt}$	$u_{n_{chem}}$	$\frac{dr_{sch}}{dt}$	$u_{n_{sch}}$
1	No Grid	1.2	2.08	-	-	4.12	0.687
2	No Grid	1.1	1.91	6.86	1.13	2.59	0.427
3	No Grid	1.0	1.98	8.72	1.45	2.54	0.422
4	Passive Grid	1.2	4.58	11.92	1.99	15.3	2.56
5	Passive Grid	1.1	4.21	12.52	2.06	15.8	2.60
6	Passive Grid	1.0	4.36	11.83	1.97	18.5	3.08

Figure 5(b) shows the Schlieren photography of the averaged kernel at each propagation time overlaid onto one image. Unlike the chemiluminescence images, kernels measured with the Schlieren technique have a positive growth rate starting, presumably, at the ignition location (outside the field of view). The kernel

^cLaminar flame speeds from Andrews and Bradley.²³

is at the smallest effective diameter at the first frame. There is also some structure to the kernel which is an artifact of the ignition process. This structure persists downstream and may influence the global growth rate of the flame kernel. Also visible in Figure 5(b) is a spherical shock wave propagating away from the flame kernel. This is the spherical shock resulting from the ignition process. This shock reflects off the side walls of the tunnel and passes through the kernel by the fourth frame (not shown). The ignition laser focusing lens was slightly off-center which caused the reflected shocks to return to the kernel at different times. The effect of this spherical shock on kernel growth is still being explored. There are also two weak oblique shocks in Figure 5(b) that are a result of the variable hinge construction in the tunnel. A slight deviation in the average kernel trajectory can be seen in both the chemiluminescence and Schlieren images due to the location of these shocks and possibly the interaction with the spherical ignition shock.

Figure 6 shows a summary of the measured kernel diameter versus propagation time for both the Schlieren and OH* chemiluminescence techniques. Also shown are linear regression curve fits of the kernel diameter from the first to second window. For both techniques, there is a clear increase in the kernel diameter with propagation time, i.e. the kernels are growing as expected. There is also a clear difference in the growth rate between the baseline and turbulence grid cases. Kernels growing in the flow field with the turbulence grid have a higher final kernel diameter. This is because the increase in turbulence level (u'/S_L) leads to an increase in flame surface density which leads to a larger global displacement velocity and finally a kernel of increased size.

Comparing Schlieren and OH* chemiluminescence, there appears to be a discrepancy in the kernel diameter measured by each technique. The Schlieren technique produces larger kernels than OH* with the turbulence grid but smaller kernels without the turbulence grid. The first of these comments may be explained by the fact that the Schlieren edge is expected to be in the preheat zone of the flame and hence be larger than the OH* edge which is expected to lie in the reaction zone. The second issue, that Schlieren produces much lower kernel diameters downstream than OH* without the grid, may be explained by heat losses. The flame kernels may quench downstream due to radiative heat loss or large rates of scalar dissipation encountered when passing through Mach waves or weak shock waves. Flames growing in higher turbulence may survive these losses better. Luminescence due to chemical excitation of OH has a relatively long lifetime and may survive downstream (despite quenching), explaining the difference between the two measurements. Perhaps a more likely explanation is that the Schlieren technique, as implemented here, suffers from a low signal to noise ratio due to the low irradiance of the chosen light source and relatively long exposure times. These issues were especially problematic when imaging kernels further downstream. The low signal to noise makes edge detection more difficult and resulted in edges that were 15-20% smaller than those of the corresponding OH* measurement at the downstream location.

Measured global displacement velocities, $S_{T,gd}$ were normalized by the laminar flame speed, S_L and plotted versus u'/S_L as shown in Figure 7. Also shown are the classical turbulent flame speed correlations of Damköhler²⁵ (see Eq. (2)), and Bradley²⁶ (see Eq. (3)). Damköhler's correlation is derived by assuming the flame area is increased proportionally to the turbulent velocity resulting in Eq. (2). Bradley's correlation is more complicated in that an attempt is made to correct for thermo-diffusive effects and variations due to the turbulent length scale. Equation 2 is based on a consumption velocity derivation while Eq. (3) combines displacement and consumption velocity data into a single empirical relationship. It should be expected that Eq. (3) more faithfully represents the physics in this study but may fall short of matching these data due to the wide variety of source data used to produce the correlation. In producing these graphs the integral scale l was estimated to be 8.9 mm (which is less than the channel half-width and matches the turbulent grid hole size) and the Lewis number was assumed unity for all cases. Based on these estimates, all of the flames investigated in this study were in the thin reaction zone.

$$\frac{S_T}{S_L} = 1 + \frac{u'}{S_L} \quad (2)$$

$$\frac{S_T}{S_L} = 1 + 0.95Le^{-1} \left(\frac{u'}{S_L} \frac{l}{\delta_L} \right)^{0.5} \quad (3)$$

The same generally upward trend is seen in the experimental data and correlations (Figure 7), however, there is a fairly significant absolute deviation in the data of this study from the correlations. For the baseline tunnel (no grid), $S_{T,gd}/S_L$ is approximately 60% the value of the Damköhler correlation and 40% the value of the Bradley correlation. With the turbulence grid installed, $S_{T,gd}/S_L$ is approximately 60% of

both correlations. A linear fit between the two turbulence levels results in a more gradual slope than the Damköhler correlation. Reasons for these discrepancies fall broadly into two categories: measurement errors and physical phenomena. Based on the PIV error analysis above, there is a relatively small error band on u'/S_L . The measured displacement speeds have a larger error band for reasons discussed above. However, the kernels would need to be 66% larger than measured to explain the difference. This is unlikely to be the case because two different measurement techniques yielded very similar results. Additionally, no single kernel realization came close to the flame speed required to match the correlations. Measurement error alone cannot explain these differences. Heat losses in the form of radiation to the tunnel walls may account for some of the difference between measurement and theory. Heat losses would drive down the laminar flame speed and reduce the burned gas density resulting in a reduced growth rate of the flame kernel. Interaction of the flame kernel with the tunnel walls may also have an effect on kernel growth. The free expansion of the outward propagating gas in front of the flame has the tunnel walls as a physical limit. The expanding gas will have to slow and turn in direction after a certain critical kernel size. This will limit the growth of the kernel and may appear as a kink in the diameter versus propagation time plot. A third possibility is that interaction of the kernel with Mach waves, weak oblique shocks, and the ignition shock may impact its growth, i.e. the classical correlations presented here may do a poor job of predicting turbulent flame speeds in compressible flows. Mean-flow compressibility has a known retarding effect on turbulent phenomena such as mixing in shear layers,¹⁶ but whether or not mean compressibility has an effect on kernels propagating in this shear-free environment is unclear. Further studies with various levels of mean-flow compressibility are needed to elucidate any effects of compressibility on the turbulent flame speed. Finally, the Bradley correlation presented is relatively general in that a variety of experimental configurations and conditions were used to fit the correlation constants and it is not expected to exactly match the data of this study.

IV. Conclusions

A new optically accessible high speed, reacting wind tunnel was built to measure statistics of freely propagating flame kernels in a supersonic $M=1.5$ free-stream with variable turbulence. The baseline tunnel turbulence was modified by installing one of two turbulence generating grids upstream of the converging-diverging nozzle. Particle image velocimetry was used to make velocity measurements. Turbulence statistics from the baseline, passive, and active generators were compared. The passive grid showed a 265% increase in the turbulent kinetic energy over the baseline case. The vane grid showed a further 123% increase in k over the passive grid. Flame kernel diameters were measured at two axial locations via high speed OH* chemiluminescence and Schlieren photography. Global displacement velocities were calculated from these flame images. It was shown that measured values of $S_{T,gd}/S_L$ were 40-60% that of classical low-speed correlations. The discrepancies are due in part to:

1. Heat losses to the walls
2. Wall confinement effects
3. Compressibility effects, i.e. mean-flow compressibility and shock-kernel interaction
4. Differences in experimental configurations and conditions between the data presented and those used to form the classical correlations

Future Work

Subsequent studies will focus on improving measurement techniques and combustor capabilities. Low signal to noise ratios will be improved by replacing the Schlieren light source with a 532 nm Nd:YAG laser. OH planar laser induced fluorescence will replace OH* chemiluminescence to improve accuracy of the OH flame marker location. In addition, kernels with higher turbulence levels will be studied in flow fields utilizing the vane-stirred grid (see Figure 2 b), supersonic jet in cross flow and other turbulence generators in place of the passive grid. The PIV results of the vane-stirred grid have shown an improvement in turbulence intensity and isotropy with $u' = 5.77$ and $v' = 4.393$ (see Table 1), which yields greater than a two-fold increase in u'/S_L up to 9.11. Additional studies on ignition power will be performed to assess any effect of ignition energy on kernel growth rates. Multiple converging-diverging nozzles will be used to repeat these measurements at different Mach numbers to assess any effect of shear-free mean compressibility.

Acknowledgments

This work was supported by the Air Force Office of Scientific Research under basic research grant FA9550-12-1-0107 (Project monitor: Dr. Chiping Li). Special thanks to Ianko Chetrev (Ph.D. student) and Ben Emerson (Research Engineer) for assistance with PIV measurements and Chris Ballance (Research Engineer) for assistance with flame kernel measurements.

References

- ¹Abdelgayed, R. G., Alkhisali, K. J., and Bradley, D., "Turbulent Burning Velocities and Flame Straining in Explosions," *Proceedings of the Royal Society of London Series a-Mathematical Physical and Engineering Sciences*, Vol. 391, No. 1801, 1984, pp. 393–414.
- ²Peters, N., "The turbulent burning velocity for large-scale and small-scale turbulence," *Journal of Fluid Mechanics*, Vol. 384, 1999, pp. 107–132.
- ³Poinsot, T. and Veynante, D., *Theoretical and Numerical Combustion*, Edwards, illustrated ed., 2001.
- ⁴Chen, Y. C. and Mansour, M. S., "Investigation of flame broadening in turbulent premixed flames in the thin-reaction-zones regime," *Twenty-Seventh Symposium (International) on Combustion, Vols 1 and 2*, 1998, pp. 811–818.
- ⁵Mansour, M. S., Peters, N., and Chen, Y. C., "Investigation of scalar mixing in the thin reaction zones regime using a simultaneous CH-LIF/Rayleigh laser technique," *Twenty-Seventh Symposium (International) on Combustion, Vols 1 and 2*, 1998, pp. 767–773.
- ⁶Driscoll, J. F., "Turbulent premixed combustion: Flamelet structure and its effect on turbulent burning velocities," *Progress in Energy and Combustion Science*, Vol. 34, No. 1, 2008, pp. 91–134.
- ⁷Eisazadeh-Far, K., Parsinejad, F., Metghalchi, H., and Keck, J. C., "On flame kernel formation and propagation in premixed gases," *Combustion and Flame*, Vol. 157, No. 12, 2010, pp. 2211–2221.
- ⁸Lim, M. T., Anderson, R. W., and Arpaci, V. S., "Prediction of Spark Kernel Development in Constant Volume Combustion," *Combustion and Flame*, Vol. 69, No. 3, 1987, pp. 303–316.
- ⁹Cheng, T. S., Yuan, T., Chao, Y. C., Lu, C. C., and Wu, D. C., "Premixed methane-air flame spectra measurements using UV Raman scattering," *Combustion Science and Technology*, Vol. 135, No. 1-6, 1998, pp. 65–84.
- ¹⁰Grady, N., Pitz, R., Slais, T., Berlette, J., Ochs, B., and Menon, S., "OH PLIF Laser Diagnostics of Turbulent, Premixed, Freely Propagating Flame Kernels," 52nd Aerospace Sciences Meeting, National Harbor, MD, 2014.
- ¹¹Andreopoulos, Y., Agui, J. H., and Briassulis, G., "Shock wave-turbulence interactions," *Annual Review of Fluid Mechanics*, Vol. 32, 2000, pp. 309–345.
- ¹²Zwart, P. J., Budwig, R., and Tavoularis, S., "Grid turbulence in compressible flow," *Experiments in Fluids*, Vol. 23, No. 6, 1997, pp. 520–522.
- ¹³G., S. J. and Dutton, J. C., "Velocity Measurements of a Jet Injected into a Supersonic Crossflow," *Journal of Propulsion and Power*, Vol. 13, No. 2, 1997, pp. 264–273.
- ¹⁴Gauba, G., Klavuhn, K. G., McDaniel, J., Victor, K., Krauss, R., and Whitehurst, R., "OH Planar Laser-Induced Fluorescence Velocity Measurements in a Supersonic Combustor," *AIAA Journal*, Vol. 35, No. 4, 1997, pp. 1678–686.
- ¹⁵Goyne, C. P., McDaneil, J. C., Krauss, R. H., and Day, S., "Velocity Measurement in a Dual-mode Supersonic Combustor using Particle Image Velocimetry," *AIAA Paper2001-1761*, 2001.
- ¹⁶Lele, S. K., "Compressibility Effects on Turbulence," *Annual Review of Fluid Mechanics*, Vol. 26, 1994, pp. 211–254.
- ¹⁷Poludnenko, A. Y. and Oran, E. S., "The interaction of high-speed turbulence with flames: Global properties and internal flame structure," *Combustion and Flame*, Vol. 157, No. 5, 2010, pp. 995–1011.
- ¹⁸Poludnenko, A. Y. and Oran, E. S., "The interaction of high-speed turbulence with flames: Turbulent flame speed," *Combustion and Flame*, Vol. 158, No. 2, 2011, pp. 301–326.
- ¹⁹Liu, R., Ting, D. S.-K., and Checkel, M. D., "Constant Reynolds number turbulence downstream of an orificed perforated plate," *Experimental Thermal and Fluid Science*, Vol. 31, 2007, pp. 897–908.
- ²⁰Makita, H., "Realization of a large-scale turbulence field in a small wind tunnel," *Fluid Dynamics Research*, Vol. 8, 1991, pp. 53–64.
- ²¹Smallbone, A., Tsuneyoshi, K., and Kitagawa, T., "Turbulent and Stable/Unstable Laminar Burning Velocity Measurements from Outwardly Propagating Spherical Hydrogen-Air Flames at Elevated Pressures," *Journal of Thermal Science and Technology*, Vol. 1, No. 1, 2006, pp. 31–41.
- ²²Comte-Bellot, G. and Corrsin, S., "The use of a contraction to improve the isotropy of grid-generated turbulence," *Journal of Fluid Mechanics*, Vol. 25, 1966, pp. 657–682.
- ²³Andrews, G. E. and Bradley, D., "The Burning Velocity of Methane-Air Mixtures," *Combustion and Flame*, Vol. 19, 1972, pp. 275–288.
- ²⁴Brieschenk, S., O'Byrne, S., and Kleine, H., "Laser-induced plasma ignition studies in a model scramjet engine," *Combustion and Flame*, Vol. 160, 2013, pp. 145–148.
- ²⁵Damköhler, G., "The Effect of Turbulence on the Flame Velocity in Gas Mixtures," *Zeitschrift Electrochem*, Vol. 46, 1940(English translation, NACA TM 1112, 1947), pp. 601–626.
- ²⁶Bradley, D., "How Fast Can We Burn," *Twenty-Fourth Symposium (International) on Combustion, Pittsburgh, PA*, 1992, pp. 247–262.

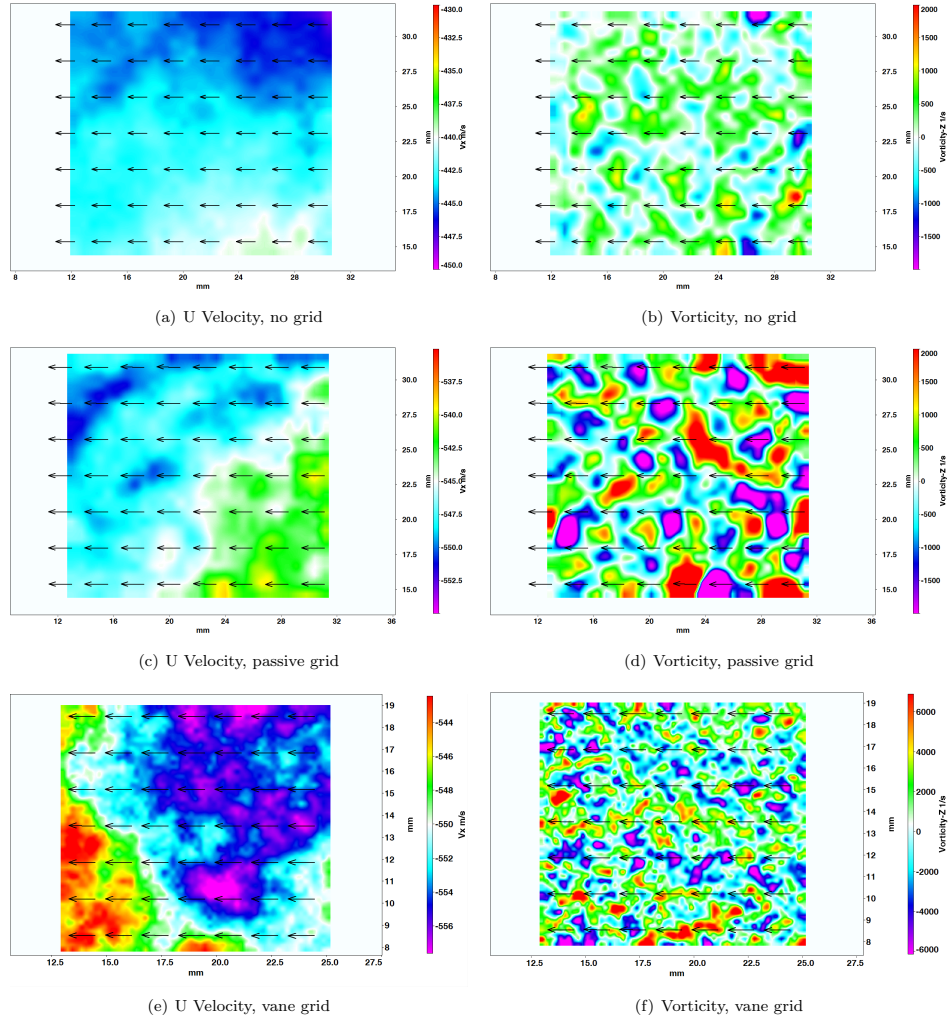
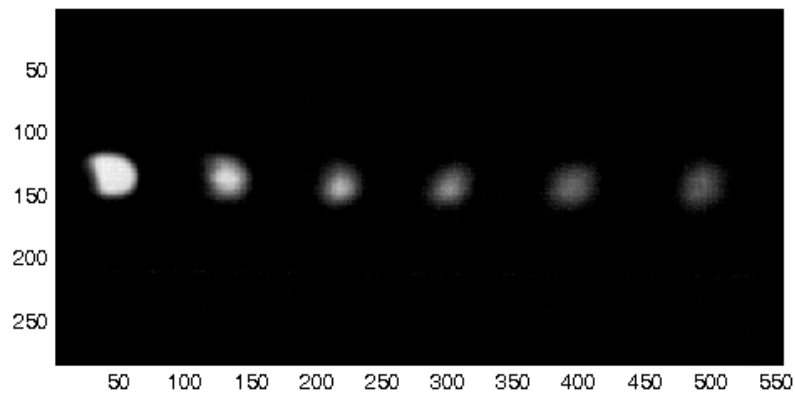
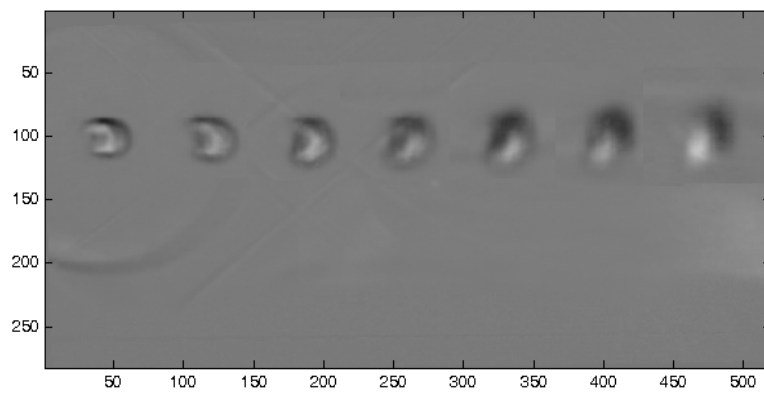


Figure 4. Sample PIV results of (a). average baseline x-direction velocity, (b). average baseline out of plane vorticity, (c). average x-direction velocity with turbulence grid, (d). average out of plane vorticity with turbulence grid, (e). average x-direction velocity with rotating vane grid, (f). average out of plane vorticity with rotating vane grid.



(a) OH*



(b) Schlieren

Figure 5. Sample high speed OH* chemiluminescence and Schlieren images overlaid onto a single image. (a) ~ 7.45 pixels/mm, (b) ~ 5.82 pixels/mm. Images are averaged over 822 independent kernel realizations.

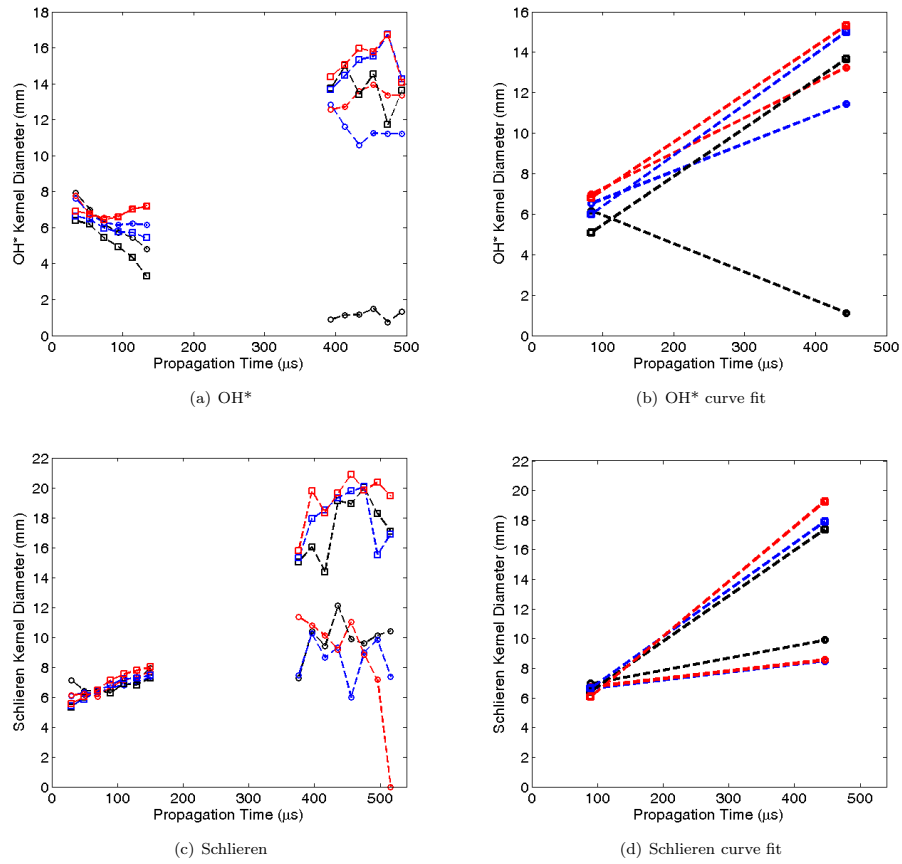


Figure 6. Kernel diameter versus time at $M=1.5$ comparing OH* chemiluminescence and Schlieren methods. Case 1: black circles, Case 2: blue circles, Case 3: red circles, Case 4: black squares, Case 5: blue squares, Case 6: red squares. Case descriptions are in Table 2.

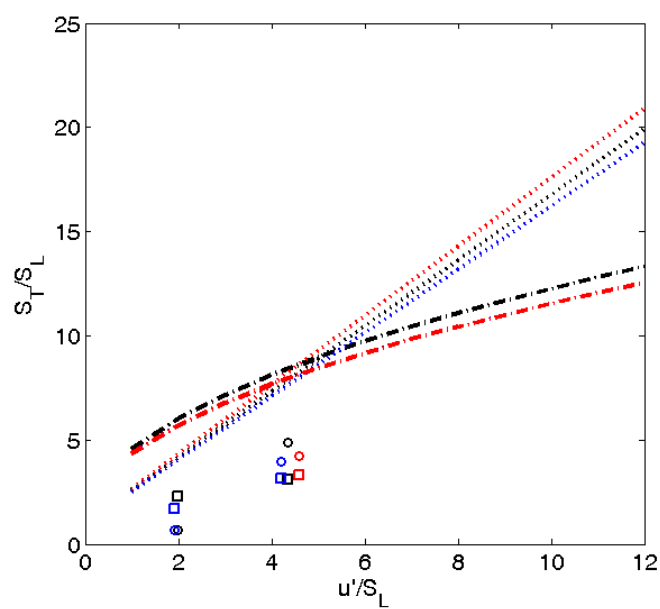


Figure 7. Global displacement velocity versus u'/S_L . Black: $\varphi = 1.0$. Blue: $\varphi = 1.1$. Red: $\varphi = 1.2$. Symbols: data from this study (circles: Schlieren method, squares: OH* chemiluminescence method). Dotted line: correlation of Damköhler,²⁵ Dash-dotted line: correlation of Bradley.²⁶

References

- [1] R. R. Boyce, N. R. Mudford, and J. R. McGuire. Oh-plif visualisation of radical farming supersonic combustion flows. *Shock Waves*, pages DOI 10.1007/s00193-011-0346-7, 2011.
- [2] R. J. Driscoll. Turbulent premixed combustion: Flamelet structure and its effects on turbulent burning velocities. *Progress Energy Combustion Science*, 34:91–134, 2008.
- [3] N. Peters. The turbulent burning velocity for large-scale and small scale turbulence. *Journal of Fluid Mechanics*, 384:107–132, 1999.
- [4] R. G. Abdel-Gayed, K. J. Al-Khishali, and D. Bradley. Turbulent burning velocities and flame straining in explosions. *Proceedings of the Royal Society London A*, 39:393–414, 1984.
- [5] F. Yuen and O. Gulder. Premixed turbulent flame front structure investigation by rayleigh scattering in the thin reaction zone regime. *Proceedings of the Combustion Institute*, 32:1747–1754, 2009.
- [6] F. Yuen and O. Gulder. Investigation of dynamics of lean turbulent premixed flames by rayleigh imaging. *AIAA Journal*, 47:2964–2973, 2009.
- [7] H. Pitsch. Large-eddy simulation of turbulent combustion. *Annual Rev. Fluid Mechanics*, 38:453–482, 2006.
- [8] N. Peters. *Turbulent Combustion*. Cambridge Monographs on Mechanics, 2000.
- [9] T. Poinso and D. Veynante. *Theoretical and Numerical Combustion*. Edwards, Inc., 2001.
- [10] Yung-Cheng Chen and M. S. Mansour. Investigation of flame broadening in turbulent premixed flames in the thin-reaction-zones regime. *Proceedings of the Combustion Institute*, 27:811–818, 1998.
- [11] M. T. Lim, R. W. Anderson, and V. S. Arpaci. Prediction of spark kernel development in constant volume combustion. *Combustion and Flame*, 69:303–316, 1987.
- [12] S. Kwon, M.-S. Wu, J. F. Driscoll, and G. M. Faeth. Flame surface properties of premixed flames in isotropic turbulence: Measurements and numerical simulations. *Combustion and Flame*, 88:221–238, 1992.
- [13] M.S. Mansour, N. Peters, and Y.C. Chen. Investigation of scalar mixing in the thin reaction zones regime using a simultaneous CH-LIF/Rayleigh laser technique. *Proceedings of the Combustion Institute*, 27:767–773, 1998.
- [14] C. C. Huang, S. S. Shy, C. C. Liu, and Y. Y. Yan. A transition on minimum ignition energy for lean turbulent methane combustion in flamelet and distributed regimes. *Proceedings of the Combustion Institute*, 31:1401–1409, 2006.

- [15] K. Eisazadeh-Far, F. Parsinejad, H. Metghalchi, and J. C. Keck. On flame kernel formation and propagation in premixed gases. *Combustion and Flame*, 157:2211–2221, 2010.
- [16] T. S. Cheng, T. Yuan, Y. C. Chao, C. C. Lu, and D. C. Wu. Premixed methane-air flame spectra measurements using uv raman scattering. *Combustion Science and Technology*, 135(1-6):65–84, 1998.
- [17] V. S. Arpaci, Y. Ko, M. T. Lim, and H. S. Lee. Spark kernel development in constant volume combustion. *Combustion and Flame*, 135:315–322, 2003.
- [18] S. Cant. Direct numerical simulation of premixed turbulent flames. *Philos. Trans. R. Soc. A*, 357:3583–3604, 1999.
- [19] K. Jenkins and S. Cant. Curvature effects of flame kernels in a turbulent environment. *Proc. Combustion Institute*, 29:2023–2029, 2002.
- [20] G. Fru, D. Thévenin, and G. Janiga. Impact of turbulence intensity and equivalence ratio on the burning rate of premixed methane-air flames. *Energies*, 4:878–893, 2011.
- [21] S. Menon. Acoustic-vortex-flame interactions in gas turbine combustors. In T. Lieuwen and V. Yang, editors, *Combustion Instabilities in Gas Turbine Engines: Operational Experience, Fundamental Mechanisms, and Modeling*, volume 210, pages 277–314. 2005.
- [22] S. K. Lele. Compressibility effects on turbulence. *Annual Review of Fluid Mechanics*, 26:211–254, 1994.
- [23] A. Y. Poludnenko and E.S. Oran. The interaction of high-speed turbulence with flames: Global properties and internal flame structure. *Combustion and Flame*, 157:995–1011, 2010.
- [24] A. Y. Poludnenko and E.S. Oran. The interaction of high-speed turbulence with flames: Turbulent flame speed. *Combustion and Flame*, 158:301–326, 2011.
- [25] P.J. Zwart, R. Budwig, and S. Tavoularis. Grid turbulence in compressible flow. *Experiments in Fluids*, 23:520–522, 1997.
- [26] Y. Andreopoulos, J. H. Agui, and G. Briassulis. Shock waveturbulence interactions. *Annual Review of Fluid Mechanics*, 32:309–345, 2000.
- [27] G. Briassulis and J. Andreopoulos. Compressibility effects in grid generated turbulence. *AIAA-1996-2055*, 1996.
- [28] H. Pitsch and L. Duchamp De Lageneste. Large-eddy simulation of premixed turbulent combustion using a level-set approach. *Proceedings of the Combustion Institute*, 29:2001–2008, 2002.
- [29] W.-W. Kim, S. Menon, and H. C. Mongia. Large eddy simulations of a gas turbine combustor flow. *Combustion Science and Technology*, 143:25–62, 1999.

- [30] W.-W. Kim and S. Menon. Numerical modeling of turbulent premixed flames in the thin-reaction-zones regime. *Combustion Science and Technology*, 160:119–150, 2000.
- [31] S. Menon and Fureby C. Computational combustion. In R. Blockley and W. Shyy, editors, *Encyclopedia of Aerospace Engineering*. John Wiley and Sons, 2011.
- [32] D. Veynante and Vervisch L. Turbulent combustion modeling. *Proc. Combustion Institute*, 28:193–266, 2002.
- [33] T. M. Smith and S. Menon. The structure of premixed flames in a spatially evolving turbulent flow. *Combustion Science and Technology*, 119(1-6):77–106, 1996.
- [34] T. Smith and S. Menon. One-dimensional simulations of freely propagating turbulent premixed flames. *Combustion Science and Technology*, 128:99–130, 1997.
- [35] S. Menon, P.A. McMurtry, and A. R. Kerstein. A linear eddy mixing model for large eddy simulation of turbulent combustion. In B. Galperin and S. Orszag, editors, *LES of Complex Engineering and Geophysical Flows*. Cambridge University Press, 1993.
- [36] S. Menon and W. Calhoon. Subgrid mixing and molecular transport modeling for large-eddy simulations of turbulent reacting flows. *Proceedings of the Combustion Institute*, 26:59–66, 1996.
- [37] V.K. Chakravarthy and S. Menon. Subgrid modeling of premixed flames in the flamelet regime. *Flow, Turbulence and Combustion*, 65:23–45, 2000.
- [38] V.K. Chakravarthy and S. Menon. Large-eddy simulations of turbulent premixed flames in the flamelet regime. *Combustion Science and Technology*, 162:175–222, 2001.
- [39] V. Sankaran and S. Menon. Structure of premixed turbulent flames in the thin-reaction-zones regime. *Proceedings of the Combustion Institute*, 28:123–129, 2000.
- [40] S. Menon and N. Patel. Subgrid combustion modeling for les of spray combustion in large-scale combustors. *AIAA Journal*, 44(4):709–723, 2006.
- [41] S. Undapalli, S. Srinivasan, and S. Menon. Les of premixed and non-premixed combustion in a stagnation point reverse flow combustor. *Proc. Comb. Inst.*, 32:1537–1544, 2009.
- [42] S. Menon and A.R. Kerstein. The linear eddy model. In T. Echekki and E. Mastorakos, editors, *Turbulent Combustion Modeling*. Cambridge University Press, 2010.
- [43] S. Pfadler, F. Dinkelacker, F. Beyrau, and A. Leipertz. High resolution dual-plane stereo-piv for validation of subgrid scale models in large-eddy simulations of turbulent premixed flames. *Combustion and Flame*, 156:1552–1564, 2009.
- [44] N. R. Grady, R. W. Pitz, T. A. Slais, J. Berlette, B. Ochs, and S. Menon. Oh plif laser diagnostics of turbulent, premixed flame kernels. In *In 52nd AIAA Aerospace Sciences Meeting, National Harbor, MD*, 2013.

- [45] A.L. Kistler and T. Vrebalovich. Grid turbulence at large reynolds numbers. *Journal of Fluid Mechanics*, 26:37–47, 1965.
- [46] G. Compte-Bellot and S. Corrsin. The use of a contraction to improve the isotropy of grid-generated turbulence. *Journal of Fluid Mechanics*, 25:657–682, 1966.
- [47] M.S. Uberoi and S. Wallis. Effect of grid geometry on turbulence decay. *Physics of Fluids*, 10:doi: 10.1063/1.1762265, 1967.
- [48] G. Compte-Bellot and S. Corrsin. Simple eulerian time correlation of full and narrow band velocity signals in grid-generated 'isotropic' turbulence. *Journal of Fluid Mechanics*, 48:273–337, 1966.
- [49] R. Liu, D.S.K Ting, and G.W. Rankin. On the generation of turbulence with a perforated plate. *Experimental Thermal and Fluid Science*, 28:307–316, 2004.
- [50] H. Makita. Realization of a large-scale turbulence field in a small wind tunnel. *Fluid Dynamics Research*, 8:53–64, 1991.
- [51] L. Mydlarski and Z. Warhaft. On the onset of high-reynolds-number grid-generated wind tunnel turbulence. *Journal of Fluid Mechanics*, 320:331–368, 1996.
- [52] H.S. Kang and C. Meneveau. Experimental study of an active grid-generated shearless mixing layer and comparisons with large-eddy simulation. *Physics of Fluids*, 20:doi: 10.1063/1.3001796, 2008.
- [53] J.V. Larssen and W.J. Devenport. On the generation of large-scale homogeneous turbulence. *Journal of Fluid Mechanics*, 50:1207–1223, 2011.
- [54] Corning Incorporated. Corning 7980 data sheet. Accessed: 28/09/2012.
- [55] T. Sjögren and A. Johansson. Measurement and modelling of homogeneous axisymmetric turbulence. *Journal of Fluid Mechanics*, 374:59–90, 1998.
- [56] H. H. Bruun and C. Tropea. The calibration of inclined hot-wire probes. *Journal of Physics E: Sci. Instrum.*, 18:405–, 1985.
- [57] H.H. Bruun. *Hot Wire Anemometry: Principles and Signal Analysis*. Oxford University Press, 1995.
- [58] Y.O. Han, W.K. George, and J. Hjarne. Effect of a contraction on turbulence. part i: Experiment. *AIAA-2005-1119*, 2005.
- [59] G.I. Derbunovich, A.S. Zemskaya, E.U. Repik, and P. Sosedko. Effect of flow contraction on the level of turbulence. *Mekhanika Zhidkosti i Gaza*, 2:146–152, 1987.
- [60] H. S. Ribner. Convection of a pattern of vorticity through a shock-wave. Technical Report 1164, NACA, 1954.

- [61] G. Coppola and A. Gomez. Experimental investigation on a turbulence generation system with high-blockage plates. *Experimental Thermal and Fluid Sciences*, 33:1037–1048, 2009.
- [62] P.J. Zwart. Grid turbulence in compressible flow. Master’s thesis, University of Ottawa, 1996.
- [63] A.C. Nix, A.C. Smith, T.E Diller, W.F. Ng, and K.A. Thole. High intensity, large length-scale freestream turbulence generation in a transonic turbine cascade. In *Proceedings of ASME TURBO EXPO*, 2002.
- [64] R. Liu, D.S.K Ting, and M.D. Checkel. Constant reynolds number turbulence downstream of an orificed perforated plate. *Experimental Thermal and Fluid Science*, 31:897–908, 2007.
- [65] R. Vonlanthen and P. Monkewitz. A novel tethered-sphere add-on to enhance grid turbulence. *Experiments in Fluids*, 51:579–585, 2011.
- [66] P.C. Valente and J.C. Vassilicos. The decay of homogeneous turbulence generated by multi-scale grids. *Journal of Fluid Mechanics*, 687:300–340, 2011.
- [67] N. Mazellier and J.C. Vassilicos. Turbulence without richardson-kolmogorov cascade. *Physics of Fluids*, 22:75–101, 2010.
- [68] R. Liu, D. S.-K. Ting, and M. D. Checkel. Constant reynolds number turbulence downstream of an orificed perforated plate. *Experimental Thermal and Fluid Science*, 31:897–908, 2007.
- [69] J. Fransson, M. Matsubara, and P. Alfredsson. Transition induced by free-stream turbulence. *Journal of Fluid Mechanics*, 527:1–25, 2005.
- [70] P. Lavoie, G. Avallone, F. De Gregorio, G. P. Romano, and R. A. Antonia. Spatial resolution of piv for the measurement of turbulence. *Experiments in Fluids*, 43:39–51, 2007.
- [71] H.S. Kang, S. Chester, and C. Meneveau. Decaying turbulence in an active-grid-generated flow and comparisons with large-eddy simulation. *Journal of Fluid Mechanics*, 480:129–160, 2003.
- [72] R.E.G. Poorte and A. Biesheuvel. Experiments on the motion of gas bubbles in turbulence generated by an active grid. *Journal of Fluid Mechanics*, 461:127–154, 2002.
- [73] R. Hearst and P. Lavoie. High reynolds number grid-generated turbulence. *1000 Islands Fluid Mechanics Meeting*, 2012.
- [74] N. Mordant. Experimental high reynolds number turbulence with an active grid. *American Journal of Physics*, 76:doi: 10.1119/1.2980582, 2008.
- [75] H.E. Cekli and W. van de Water. Tailoring turbulence with an active grid. *Experimental Fluids*, 49:409–416, 2010.

- [76] H. Tennekes and J.L. Lumley. *A First Course in Turbulence*, chapter 3. The MIT Press, 1972.
- [77] S.B. Pope. *Turbulent Flows*, chapter 3-5. Cambridge University Press, 2000.
- [78] H. Makita. Realization of a large-scale turbulence field in a small wind tunnel. *Fluid Dynamics Research*, 8:53–64, 1991.
- [79] DANTEC Measurement Technology A/S. *StreamLine and StreamWare Installation and User Guide*, 2000.
- [80] P. Bradshaw. *An Introduction to Turbulence and its Measurement*. Oxford University Press, 1971.
- [81] F. E. Jørgensen. The computer-controlled constant-temperature anemometer. aspects of set-up, probe calibration, data acquisition and data conversion. *Meas. Sci. Technol.*, 7:1378–1387, 1996.
- [82] DANTEC Measurement Technology A/S. Dantec cta probe catalog. Accessed: 10/01/2013.
- [83] J.O. Hinze. *Turbulence*, chapter 2. McGraw Hill, 1959.
- [84] G. De Grande and P. Kool. An improved method to determine the complete reynolds stress tensor with a single rotating slanting hot wire. *J. Phys. E: Sci. Instrum.*, 14:196–201, 1981.
- [85] A.J. Smits and J.P. Dussauge. Hot wire anemometry in supersonic flows. In *A Survey of Measurements and Measuring Techniques in Rapidly Distorted Compressible Turbulent Boundary Layer*. Agardograph no. 315 edition, 1989.
- [86] H. Fujita and L.S.G. Kovasznay. Measurement of reynolds stress by a single rotated hot-wire anemometer. *Review of Scientific Instruments*, 39:1351–1355, 1968.
- [87] G. De Grande and C. Hirsch. Three-dimensional incompressible turbulent boundary layers. Technical Report VUB-STR-8, Vrije Universiteit Brussel, 1978.
- [88] G. De Grande and P. Kool. An improved experimental method to determine the complete reynolds stress tensor with a single rotating slanting hot wire. *J. Phys. E: Sci. Instrum.*, 14:196–201, 1981.
- [89] H. H. Bruun, N. Nabhani, H. H. Al-Kayiem, A. A. Fardad, M. A. Khan, and E. Hogarth. Calibration and analysis of x hot-wire probe signals. *Meas. Sci. Technol.*, 1:782–785, 1990.
- [90] G. Buresti and N. Di Cocco. Hot-wire measurement procedures and their appraisal through a simulation technique. *J. Phys. E: Sci. Instrum.*, 20:87–99, 1987.
- [91] H. H. Bruun. Interpretation of hot-wire probe signals in subsonic airflows. *J. Phys. E: Sci. Instrum.*, 12:1116–1128, 1979.

- [92] J. Bendat and A. Piersol. *Random Data: Analysis and Measurement Procedures*. John Wiley and Sons, Inc., 4 edition, 2010.
- [93] P. D. Welch. The use of fast-fourier transform for the estimation of power spectra: a method based on time averaging over short, modified periodograms. *IEEE Trans. Audio Electroacoustics*, 15:70–73, 1967.
- [94] J. A. Wehrmeyer, L. A. Ribarov, D. A. Oguss, and R. W. Pitz. Flame flow tagging velocimetry with 193-nm h₂o photodissociation. *Applied Optics*, 38(33):6912–6917, 1999.
- [95] R. W. Pitz, J. A. Wehrmeyer, L. A. Ribarov, D. A. Oguss, F. Batliwala, P. A. De-Barber, S. Deusch, and P. E. Dimotakis. Unseeded molecular flow tagging in cold and hot flows using ozone and hydroxyl tagging velocimetry. *Measurement Science and Technology*, 11(9):1259–1271, 2000.
- [96] L. P. Goss, T. H. Chen, D. D. Trump, and B. Sarka. Flow-tagging velocimetry using uv photodissociation of water vapor, 1991.
- [97] L. R. Boedeker. Velcoity-measurement by h₂o photolysis and laser-induced fluorescence of oh. *Optics Letters*, 14(10):473–475, 1989.
- [98] Kaijun Yuan, Yuan Cheng, Lina Cheng, Qing Guo, Dongxu Dai, Xueming Yang, and Richard N. Dixon. Quantum state-selected photodissociation dynamics of h₂o: Two-photon dissociation via the *c* electronic state. *Journal of Chemical Physics*, 133(13), 2010. Times Cited: 4.
- [99] N.R. Grady, R.W Pitz, C.D Carter, K.-Y. Hsu, C. Ghodke, and S. Menon. Supersonic flow over a ramped-wall cavity flameholder with an upstream strut. *J. of Propulsion and Power (submitted)*, 2011.
- [100] M. D. Lahr, R. W. Pitz, Z. W. Douglas, and C. D. Carter. Hydroxyl-tagging-velocimetry measurements of a supersonic flow over a cavity. *Journal of Propulsion and Power*, 26(4):790–797, 2010.
- [101] Andrew Smallbone, Kousaku Tsuneyoshi, and Toshiaki Kitagawa. Turbulent and stable/unstable laminar burning velocity measurements from outwardly propagating spherical hydrogen-air flames at elevated pressures. *Journal of Thermal Science and Technology*, 1(1):31–41, 2006.
- [102] J. H. Agui, G. Briassulis, and Y. Andreopoulos. Studies of interactions of a propagating shock wave with decaying grid turbulence: velocity and vorticity fields. *Journal of Fluid Mechanics*, 524:143–195, 2005.
- [103] P.E. Roach. The generation of nearly isotropic turbulence by means of grids. *Heat and Fluid Flow*, 8:82–92, 1987.
- [104] J. O. Hinze. *Turbulence*. McGraw-Hill, 2 edition, 1975.

- [105] M. Gad-el Hak and S. Corrsin. Measurements of the nearly isotropic turbulence behind a uniform jet grid. *Journal of Fluid Mechanics*, 62:115–143, 1974.
- [106] O Ertunç. *Experimental and Numerical Investigations of Axisymmetric Turbulence*. PhD thesis, University of Erlangen, 2007.
- [107] O Ertunç and F Durst. On the high contraction ratio anomaly of axisymmetric contraction of grid-generated turbulence. *Physics of Fluids*, 20:025103, 2008.
- [108] M.S. Mohamed and J.C. Larue. The decay power law in grid-generated turbulence. *Journal of Fluid Mechanics*, 219:195–214, 1990.
- [109] G. Briassulis, J. H. Agui, and J. Andreopoulos. The structure of weakly compressible grid-generated turbulence, 2001.
- [110] P. Lavoie, L. Djenidi, and R. A. Antonia. Effects of initial conditions in decaying turbulence generated by passive grids. *J. Fluid Mech.*, 585, 2007.
- [111] T. Kurian and J.H.M. Fransson. Grid-generated turbulence revisited. *Fluid Dynamics Research*, 41:doi:10.1088/0169-5983/41/2/021403, 2009.
- [112] H. Schlichting and K. Gersten. *Boundary Layer Theory*. Springer-Verlag, 8 edition, 2000.
- [113] R. W. MacCormack. The effects of viscosity in hyper-velocity impact cratering. *AIAA Paper 69-354*, 1969.
- [114] Robert S. Rogallo. Numerical experiments in homogeneous turbulence. Technical report, NASA, 1981.
- [115] Robert H. Kraichnan. Diffusion by a random velocity field. *The Physics of Fluids*, 13(1):22–31, January 1970.
- [116] S. Tavoularis, J. C. Bennett, and S. Corrsin. Velocity-derivative skewness in small reynolds number, nearly isotropic turbulence. *Journal of Fluid Mechanics*, 88:63–69, 1978.
- [117] J.C.R. Hunt, A.A. Wray, and P. Moin. Eddies, streams, and convergence zones in turbulent flows. *Center for Turbulence Research Report CTR-S88*, pages 193–208, 1988.
- [118] R Fraser, CJ Pack, and DA Santavicca. An ldv system for turbulence length scale measurements. *Experiments in fluids*, 4(3):150–152, 1986.
- [119] G. Comte-Bellot and S. Corrsin. The use of a contraction to improve the isotropy of grid-generated turbulence. *Journal of Fluid Mechanics*, 25:657–682, 1966.
- [120] James F. Driscoll. Turbulent premixed combustion: Flamelet structure and its effect on turbulent burning velocities. *Progress in Energy and Combustion Science*, 34(1):91–134, 2008. Times Cited: 85 85.

- [121] I. G. Shepherd and R. K. Cheng. The burning rate of premixed flames in moderate and intense turbulence. *Combustion and Flame*, 127(3):2066–2075, 2001. ISI Document Delivery No.: 499ZP Times Cited: 55 Cited Reference Count: 22 Shepherd, IG Cheng, RK 56 Elsevier science inc New york.
- [122] M. Z. Haq, C. G. W. Sheppard, and R. Woolley. Wrinkling and curvature of laminar and turbulent premixed flames. *Combustion and Flame*, 131:1–15, 2002.
- [123] R. G. Abdel-Gayed, D. Bradley, and M. Lawes. Turbulent burning velocities: a general correlation in terms of straining rates. *Proceedings of the Royal Society London A*, 414:389–413, 1987.
- [124] D. Bradley, M. Lawes, and M. S. Mansour. Correlation of turbulent burning velocities of ethanol-air, measured in a fan stirred bomb up to 1.2 mpa. *Combustion and Flame*, 158:123–138, 2011.
- [125] M. Fairweather, M. P. Ormsby, C. G. W. Sheppard, and R. Wooley. Turbulent burning rates of methane nad methane-hydrogen mixtures. *Combustion and Flame*, 156:780–790, 2009.
- [126] S. Chaudhuri, F. J. Wu, and C. K. Law. Scaling of turbulent flame speed for expanding flames with markstein diffusion considerations. *Physical Review E*, 88(3), 2013.
- [127] C Cardin, B. Renou, G. Cabot, and A. M. Boukhalfa. Experimental analysis of laser induced spark ignition of lean turbulent premixed flames: New insight into ignition transition. *Combustion and Flame*, 160(8):1414–1427, 2013.
- [128] S. Chaudhuri, V. Akkerman, and C. K. Law. Spectral formulation of turbulent flame speed with consideration of hydrodynamic instability. *Physical Review E*, 84(2), 2011.
- [129] S. Chaudhuri, F. Wu, D. Zhu, and C. K. Law. Flame speed and self-similar propagation of expanding turbulent premixed flames. *Physical Review Letters*, 108(4), 2012.
- [130] S. Chaudhuri, A. Saha, and C. K. Law. On flame-turbulence interaction in constant-pressure expanding flames. *Proceedings of the Combustion Institute*, 35:1331–1339, 2013.
- [131] Nathan Grady, Robert Pitz, Tom Slais, John Berlette, Bradley Ochs, and Suresh Menon. Oh plif laser diagnostics of turbulent, premixed, freely propagating flame kernels, 52nd Aerospace Sciences Meeting, National Harbor, MD, 2014.
- [132] M. S. Mansour, N. Peters, and L.-U. Schrader. Highly strained turbulent rich methane flames stabilized by hot combustion products. *Experimental study of turbulent flame kernel propagation*, 32:1396–1404, 2008.
- [133] B. Renou, A. Mura, E. Samson, and A. Boukhalfa. Characterization of the local flame structure and the flame surface density for freely propagating premixed flames at various lewis numbers. *Combustion Science and Technology*, 174(4):143–179, 2002. Times Cited: 21 21.

- [134] A. Smallbone, K. Tsuneyoshi, and T. Kitagawa. Turbulent and stable/unstable laminar burning velocity measurements from outwardly propagating spherical hydrogen-air flames at elevated pressures. *Journal of Thermal Science and Technology*, 1(1):31–41, 2006.
- [135] G. E. Andrews and D. Bradley. The burning velocity of methane-air mixtures. *Combustion and Flame*, 19:275–288, 1972.
- [136] S. Brieschenk, S. O’Byrne, and H. Kleine. Laser-induced plasma ignition studies in a model scramjet engine. *Combustion and Flame*, 160:145–148, 2013.
- [137] G. Damköhler. The effect of turbulence on the flame velocity in gas mixtures. *Zeitschrift Electrochem*, 46:601–626, 1940(English translation, NACA TM 1112, 1947).
- [138] D. Bradley. How fast can we burn. *Twenty-Fourth Symposium (International) on Combustion, Pittsburgh, PA*, pages 247–262, 1992.
- [139] S. K. Lele. Compressibility effects on turbulence. *Annual Review of Fluid Mechanics*, 26:211–254, 1994.

1.

1. Report Type

Final Report

Primary Contact E-mail**Contact email if there is a problem with the report.**

suresh.menon@ae.gatech.edu

Primary Contact Phone Number**Contact phone number if there is a problem with the report**

404-894-9126

Organization / Institution name

Georgia Institute of Technology

Grant/Contract Title**The full title of the funded effort.**Experimental Studies of Premixed Flame Structure and
Propagation Characteristics in Compressible Flow**Grant/Contract Number****AFOSR assigned control number. It must begin with "FA9550" or "F49620" or "FA2386".**

FA9550-12-1-0107

Principal Investigator Name**The full name of the principal investigator on the grant or contract.**

Suresh Menon

Program Manager**The AFOSR Program Manager currently assigned to the award**

Chiping Li

Reporting Period Start Date

04/01/2012

Reporting Period End Date

06/30/2015

Abstract

Understanding the nature of premixed combustion in highly turbulent conditions and in compressible flow offers a new paradigm shift in the design of future high-pressure gas turbines and scramjets. Experimental data in these regimes provides hitherto unavailable insight and offer new ways to develop accurate and efficient computational models of turbulent premixed combustion, especially subgrid-scale (SGS) models for large-eddy simulation (LES). In these studies, comprehensive experimental efforts were performed to study turbulent premixed combustion in a configuration that deliberately avoided mean strain effects and focused solely on the interaction of a premixed flame in high Reynolds number, isotropic turbulence over a range of Mach numbers. Two experiments were developed to create this uniform premixed flow with upstream active turbulence generation in the subsonic and supersonic regimes. Turbulent statistics are reported for a variety of conditions using hotwire anemometry and PIV. Flame kernels were generated via laser plasma ignition, and their growth monitored using chemiluminescence, Schlieren, and PLIF imaging. Flame growth statistics show good agreement with classical flame bomb studies in low speeds but deviate with increasing Mach number.

Distribution Statement**This is block 12 on the SF298 form.**

Distribution A - Approved for Public Release

Explanation for Distribution Statement

If this is not approved for public release, please provide a short explanation. E.g., contains proprietary information.

SF298 Form

Please attach your [SF298](#) form. A blank SF298 can be found [here](#). Please do not password protect or secure the PDF
The maximum file size for an SF298 is 50MB.

[AFOSR-PF-SF298.pdf](#)

Upload the Report Document. File must be a PDF. Please do not password protect or secure the PDF . The maximum file size for the Report Document is 50MB.

[FinalReport-FA9550-12-1-0107.pdf](#)

Upload a Report Document, if any. The maximum file size for the Report Document is 50MB.

Archival Publications (published) during reporting period:

Changes in research objectives (if any):

NA

Change in AFOSR Program Manager, if any:

NA

Extensions granted or milestones slipped, if any:

NA

AFOSR LRIR Number

LRIR Title

Reporting Period

Laboratory Task Manager

Program Officer

Research Objectives

Technical Summary

Funding Summary by Cost Category (by FY, \$K)

	Starting FY	FY+1	FY+2
Salary			
Equipment/Facilities			
Supplies			
Total			

Report Document

Report Document - Text Analysis

Report Document - Text Analysis

Appendix Documents

2. Thank You

E-mail user

Jul 09, 2015 18:51:52 Success: Email Sent to: suresh.menon@ae.gatech.edu